Andreev and Spin Transport in Carbon Nanotube Quantum Dot Hybrid Devices

Inauguraldissertation

zur
Erlangung der Würde eines Doktors der Philosophie
vorgelegt der
Philosophisch-Naturwissenschaftlichen Fakultät
der Universität Basel

von

Jörg Benedikt Gramich
aus Renningen, Deutschland

Basel, 2016

Genehmigt von der Philosophisch-Naturwissenschaftlichen Fakultät
auf Antrag von
Prof. Dr. C. Schönenberger
Prof. Dr. C. Strunk
Prof. Dr. R. Deblock

Basel, 19.04.16

Prof. Dr. Jörg Schibler
Dekan

Contents

Introduction

Driven by the ongoing miniaturization of classical silicon transistors due to the unbroken urge for faster and smaller consumer electronics, quantum mechanical concepts have emerged as a major player in future information technology. With the reach of a commercial 14 nm fabrication node in Si-based semiconductors nowadays, even semiconductor industry acknowledges today [1] that traditional miniaturization following Moore's law and classical physics concepts will eventually slow down or even become irrelevant not only due to technological challenges or increased economical costs, but because such nanoscale devices enter the realm of quantum mechanics. The fascinating rules of quantum mechanics do however also pose various opportunities for groundbreaking new concepts, which are exploited in the wide fields of quantum computation and information technology [2–4]. So-called *quantum bits* or *qubits* – quantum mechanical two-level systems – can also be in superposition states of the classical bit states "0" and "1", or even be *entangled* with other qubits. This quantum entanglement is a unique ingredient for the "quantum parallelism" utilized in "quantum algorithms" to solve certain computational problems faster than in classical implementations [4]. The fact that major industrial companies invest into basic and experimental academic research exploiting such topics momentarily can be seen as a sign that quantum information technology is on the brink of a breakthrough.

In this context, superconducting nanostructures and low-dimensional material systems are expected to play a key role [3]. Superconducting qubits based on Josephson junctions, for example, have been at the forefront to realize a quantum computer [5, 6]. From a fundamental point of view, even more intriguing physics is expected when these superconductor structures are combined with gate-tunable low-dimensional systems such as one-dimensional nanowires, or so-called *quantum dots* (QDs) [7]. In QDs or *artificial atoms*

[8], potential candidates of qubits themselves [2], discrete energy levels result from the confinement of electrons in all three spatial dimensions, and nearly all the systems parameters can be tailored at will. This makes such *hybrid devices* [9], in which superconductors are coupled to low-dimensional electron systems, a unique playground to investigate the interplay of correlated electron physics and quantum transport phenomena at the single electron level. Recent examples include for example the quest to reveal and manipulate solid-state versions of Majorana fermions [10–12] – a particle that is its own anti-particle – in hybrid superconductor-nanowire devices [13]. These Majorana bound states obey non-Abelian statistics and are hence a possible ingredient of a topological quantum computer [14]. Other prominent examples are the recent realization [15] of an Andreev qubit [16] with the bound states originating from coherent Andreev reflections in superconducting atomic contacts, or the usage of gate-tunable nanowires as weak links in the Josephson junctions of so-called "gatemon" qubits [17, 18]. A prime example of a hybrid device is also a so-called Cooper pair splitter (CPS) [19–21]: naturally spin-entangled Cooper pairs originating from an s-wave superconductor are split into two arms of the device due to the electron interactions in a QD on each side of the superconductor, potentially providing a continuous source of spatially separated, spin-entangled electrons relevant for quantum cryptography, teleportation and computing [4].

Another key player in the wide area of quantum information technology is the field of *spintronics*, which aims to exploit also the electron spin degree of freedom to control electric currents, or for information processing [22–24]. Ultimately, the spin degree of freedom can also be used for spin qubits and quantum computation [3, 25]. While spin-valve structures, in which a non-ferromagnetic material separates two ferromagnetic components, have become a key concept in the field and revolutionized data storage in hard-drives and magnetoresistive random-access memories (MRAMs) [26], intriguing physics once again comes into play if the non-magnetic spacer is replaced with a gate-tunable nanostructure. Experiments in such hybrid devices have for example already demonstrated an electric field control of spin transport [27], if a QD is connected to two ferromagnetic electrodes.

Motivation of this thesis

In this thesis, we investigate various aspects of such hybrid devices, in which a QD is coupled either to superconducting (S) and normal metal (N) electrodes, or to ferromagnetic contacts (F). We chose to use carbon nanotubes (CNTs) as a host material for the central QD element of our hybrid devices. CNTs, tiny cylinders of about $\sim 1-2\,\mathrm{nm}$ in diameter consisting only of carbon arranged in a hexagonal lattice structure, are an especially suitable platform for such experiments [28]: QDs in CNTs form solely by the patterning of metallic

contacts, which allows to easily couple them to normal, superconducting and ferromagnetic electrodes, which is much harder to achieve in other material systems. The absence of nuclear spin in the main carbon isotope ^{12}C and the negligible influence of spin-orbit interactions make them also very attractive for spin transport experiments [29].

Previous transport studies of hybrid QD devices with superconducting electrodes have predominantly focussed on QDs coupled to two superconducting contacts [9], so that the simple N-QD-S system [30, 31] remains far less well studied. Cooper pair splitting experiments with N-QD-S-QD-N devices have succeeded to demonstrate the expected non-local current [20, 21] and noise correlations [32] due to Cooper pair splitting, also with high efficiencies [33], but a proof of entanglement is still lacking, and many involved and competing transport mechanisms [19, 33] are not yet completely understood. This holds particularly true for transport at energies below the superconducting gap in such N-QD-S devices, which typically comprises quasiparticle tunneling and transport due to Andreev reflections. Also in the context of Majorana bound states, which use very similar device structures, it has become highly relevant to improve our understanding of subgap transport mechanisms in such structures. This thesis hence predominantly aimed at unravelling novel subgap transport phenomena in N-QD-S devices – the most simple element of any more complex device structure – also for varying coupling strength of the QD to the superconductor. Because many of the previous experiments use multiple terminals, we also implement a three-terminal geometry in our devices. Such a three-terminal device, in which ideally a single QD is coupled to one S and two N electrodes, even constitutes a model system for our desired experiments: it does not only allow to analyze competing transport processes originating from different terminals, but also to experimentally assign and determine the coupling strengths of the individual contacts to the QD [34], a major advantage compared to standard two-terminal devices. To acquire the desired high spectroscopic resolution for identifying subgap transport mechanisms, a superconducting gap much larger than the width of the QD resonance is very beneficial – a regime which is not easily achieved in S-QD hybrid devices. We therefore put a particular emphasis also on the goal to achieve large superconducting gaps in our devices, which can be implemented with certain superconducting materials.

In contrast, while experiments on CNT QD spin-valve devices, where a QD is coupled to two ferromagnetic contacts, could already demonstrate clear magnetoresistance (MR) signals and an electrical gate-control of spin transport [27, 35, 36], the devices and signals typically lack a certain reproducibility [37], and spin transport in such devices is far from understood. Hence, a major goal in the second part of this thesis was to improve the device yield, the reproducibility of MR signals, and the understanding of spin transport in such CNT-based spin-valve devices. Such a study should also serve to analyze

the suitability of ferromagnetic contacts for the proposed use as detectors of electron spin entanglement [38–41], e.g. in CPS devices, also by exploiting novel fabrication techniques for future experiments.

Thesis outline and overview

This thesis is structured in the following way: In Chapter 1 and 2, we first discuss concepts common to both topics of this thesis. In **Chapter 1**, we hence introduce CNT-based QDs as most basic element of all our hybrid devices. **Chapter 2** discusses the general device fabrication and the employed measurement techniques in our experiments, but also presents some first, rather technical achievements: Here, we particularly review several clean and ultra-clean fabrication approaches investigated in the course of this thesis, and show how these techniques help to improve the general device quality and yield. According to the two independently treated main topics Andreev and spin transport in CNT QD devices, the rest of this thesis is split into two parts. Each of these parts is structured in a very similar manner, where a first chapter introduces the basics and physical concepts of the respective field, a second chapter contains a study of the relevant material aspects, and the next chapters illustrate the respective main experimental results.

In **Part I**, we first focus on CNT QDs coupled to superconducting and normal metal electrodes. **Chapter 3** thus introduces some of the transport phenomena one can encounter in such N-QD-S hybrid devices. In **Chapter 4**, we discuss the material properties of the investigated and optimized Niobium (Nb) or lead (Pb) based S contacts, summarize their suitability for transport spectroscopy experiments, and review the achieved large superconducting gaps for both material systems. Using this technical progress to our advantage, we then analyze subgap transport in N-QD-S devices in the next three chapters. These chapters treat devices in three very distinct regimes, where different transport mechanisms are dominant, and contain the most important results of this thesis. In **Chapter 5**, we study the dominant quasiparticle transport in devices with a weak coupling of the QD to S, and find that additional subgab features are caused either by thermally excited quasiparticles in S, or by the peculiar three-terminal device geometry. For a device with a slightly more transparent interface to S, we identify in **Chapter 6** for the first time resonant and inelastic Andreev tunneling as spectroscopic features in a N-QD-S device, where two electrons of a Cooper pair tunnel sequentially through the QD. **Chapter 7** is dedicated to devices with a strong coupling to the superconductor, in which Andreev bound states (ABS) form in the QD due to the superconducting proximity effect. For such devices, the QD and S are no longer individual entities, but form an entangled superposition state or ABS, where a Cooper either resides on the QD or in the superconductor. We probe the transport through these ABS in a three-terminal geometry, which

allows to identify the source of the spectroscopic broadening of these levels, to reveal different competing local and non-local transport mechanisms, and to measure the strength of the proximity effect on the QD. To conclude this part of the thesis, **Chapter 8** presents different approaches and some first results to obtain a regular double QD based CPS device with a large superconducting gap, which might not only prove useful in CPS experiments, but offers manifold opportunities for future experiments.

In **Part II**, we analyze spin transport and magnetoresistance signals in CNT QD spin-valve devices, also with the prospective use of ferromagnetic contacts as detectors for electron spin entanglement in mind. After first giving an introduction into this field in **Chapter 9**, **Chapter 10** discusses an optimized fabrication scheme and the characterization of ferromagnetic Permalloy (Py) contacts, useful for nanospintronic magnetoresistance experiments. **Chapter 11** is dedicated to the magnetoresistance signals obtained in conventional CNT QD spin-valve devices on substrate, where we find more stable, but generally negative magnetoresistance signals in a more thorough analysis also compared to previous experiments. To study this surprising characteristics and advance the field further, we suggest in **Chapter 12** to integrate ferromagnetic contacts in ultra-clean fabrication schemes, and demonstrate some first experimental steps towards this challenging goal.

Finally, we revisit the main experimental results of both topics in **Chapter 13**, and provide a summary and an outlook.

1

Carbon nanotube quantum dots

Quantum dots (QDs) – so-called *artificial atoms* [8] and the key ingredient of all electronic devices in this thesis – can be regarded as man-made quasi zero-dimensional condensed matter systems, where the confinement of the electrons to a small size L in all three dimensions leads to a quantized energy spectrum, similar to quantum mechanics well-known particle-in-a-box problem. When the QD is connected to source and drain electrodes, the QD's atom-like properties – i.e. the discrete energy level spectrum, its level spacing δE and a characteristic shell-filling according to Hund's rules – can be conveniently probed by transport spectroscopy experiments at cryogenic temperatures $kT \ll \delta E \propto 1/L^2$. The exquisite tunability of the QD's electrostatic potential and its number of electrons with an external gate allows to study a wealth of transport phenomena, among which Coulomb blockade is the most universal one: due to the QD's small size and non-negligible electron-electron interactions, one has to overcome the charging energy $E_\mathrm{C} = e^2/C$ to add an electron to this small capacitive island.

Most of the QD's properties, including the characteristic shell-filling and spin-orbit interactions, typically depend on the underlying material system. While QDs have been realized in many different solid state systems [7, 8, 42] – including two-dimensional electron gases in semiconductor heterostructures, self-assembled structures, nano-particles, metals, semiconductor nanowires and graphene – carbon nanotubes (CNTs), first discovered by Iijima in 1991 [43], provide a unique and especially versatile platform: CNT QDs can be easily coupled to normal, superconducting and ferromagnetic contacts and combinations thereof, much harder to achieve in other material systems and a playground for unravelling new quantum transport phenomena in these *hybrid devices* [28]

(see Part I and II of this thesis). Their mechanical stiffness allows to freely suspend the CNT and study the electron-phonon interaction in nanomechanical devices [44–48]. Finally, single-wall CNTs represent a model system of a one-dimensional ballistic conductor with only two spin-degenerate transport channels [49].

In this chapter we give a brief introduction into CNT QDs, the key element of our later devices, following the more detailed review articles about transport in CNTs [28, 49–53] and in QDs in general [7, 8, 42]. In Sec. 1.1, we first discuss some structural properties of CNTs and their electronic bandstructure, before we summarize the resulting general electronic transport properties in Sec. 1.2. At last, in Sec. 1.3, we describe a simple picture of transport through CNT QDs, when they are connected to normal-metal source-drain contacts.

1.1. Electronic band structure of carbon nanotubes

Carbon nanotubes (CNTs) are built from carbon, a chemical element with the unique ability to bond to two, three or four neighbouring atoms via single, double and triple bonds. The underlying sp^1-, sp^2- or sp^3-hybridization of the outermost atomic carbon orbitals – occupied by four valence electrons – determines both the electronic and mechanical properties of the various resulting carbon allotropes: this includes the two main crystallographic carbon forms of mechanically hard, large band gap insulator diamond (sp^3-hybridization) and mechanically soft, metal-like graphite (sp^2-hybridization), as well as more fascinating structures like graphene, CNTs or C_{60} bucky-balls [28]. Because a CNT can conceptually be seen as a single graphene sheet rolled up seamlessly into a cylinder with a typical diameter of $d \sim 1 - 2\,\mathrm{nm}$ [Fig. 1.2(a)], one can intuitively derive most of its important electronic properties from a discussion of graphene's band structure [52–54].

Graphene, experimentally discovered by Novoselov *et al.* [55], can be thought of as a single isolated layer of graphite – a one-atom thick layer of carbon atoms arranged in a two-dimensional hexagonal honeycomb lattice. The sp^2-hybridization of one $2s$ and two $2p$-orbitals forms strong covalent σ-bonds between adjacent atoms in the plane, whereas electrical conductivity is determined by the overlapping orbitals from weakly localized π-electrons of the remaining $2p$ orbital [56]. Figure 1.1(a) shows the graphene honeycomb lattice, including the primitive unit cell containing two atoms A and B and the primitive lattice vectors $\mathbf{a_1}$ and $\mathbf{a_2}$. The corresponding reciprocal lattice with reciprocal lattice vectors $\mathbf{b_1}$ and $\mathbf{b_2}$ and the first Brillouin zone is depicted in Fig. 1.1(b). Because some of the corners of the Brillouin zone can be linked by a reciprocal lattice vector, due to Bloch's theorem only two of these six corners are inequivalent, often referred to as valleys K and K' [56]. The electronic band structure of graphene can be calculated in a tight binding model includ-

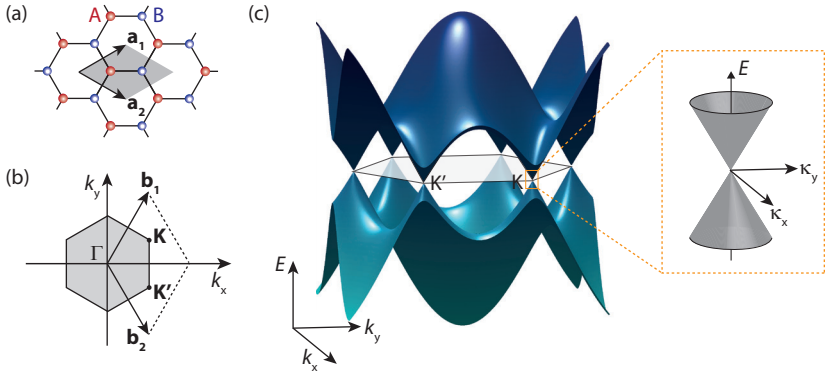

Figure 1.1.: (a) Hexagonal graphene lattice in real-space with unit cell (gray), containing two atoms A (red) and B (blue), and primitive lattice vectors $\mathbf{a_1}$ and $\mathbf{a_2}$. (b) First Brillouin zone of the reciprocal lattice with reciprocal lattice vectors $\mathbf{b_1}$ and $\mathbf{b_2}$ and valleys K, K'. (c) Band structure of graphene in the Brillouin zone, calculated from a tight binding model with nearest neighbor hopping only [54], and the low-energy dispersion or Dirac cone around K.

ing only nearest neighbor hopping (i.e. inter-sublattice A - B) [54, 56, 57], which is plotted in Fig. 1.1(c). At the valleys K and K', the conduction and valence bands touch as cones in so-called charge-neutrality or Dirac points, where the Fermi-energy $E_\mathrm{F} = 0$ lies in the undoped state. Thus, close to these points, the dispersion relation can be approximated linearly as

$$E(\boldsymbol{\kappa}) = \pm\hbar v_\mathrm{F}|\boldsymbol{\kappa}|, \tag{1.1}$$

with $\boldsymbol{\kappa} = \mathbf{k} - \mathbf{K}$ or $\boldsymbol{\kappa} = \mathbf{k} - \mathbf{K}'$ for $|\boldsymbol{\kappa}| \ll |\mathbf{K}|$ and the Fermi velocity $v_\mathrm{F} \approx 8 \cdot 10^5\,\mathrm{m/s}$ [53, 56]. Hence, graphene is a zero-bandgap semiconductor or semimetal with zero density of states at the Fermi level or charge-neutrality point, which can be used for smoothly tuning the induced charge carriers from electrons to holes in a graphene transistor [56]. Due to the connection of this linear dispersion relation to a massless Dirac equation for electrons and holes, one also calls the band structure close to the K, K' valleys a Dirac cone [56], which is shown in Fig. 1.1(c). The Dirac cones describe the low-energy properties of graphene and CNTs sufficiently well, and introduce a new robust quantum number called valley or iso-spin to distinguish energetically degenerate, but inequivalent states at $\boldsymbol{\kappa} + \mathbf{K}$ and $\boldsymbol{\kappa} + \mathbf{K}'$ [53].

The electronic band structure of a CNT can now be calculated in the so-called zone-folding approximation[1] by rolling up a graphene sheet into a closed

[1] The graphene band structure remains to first order approximation unperturbed if the CNT diameter $d \gg a_0 = 1.42\,\text{Å}$, the graphene interatomic spacing [53].

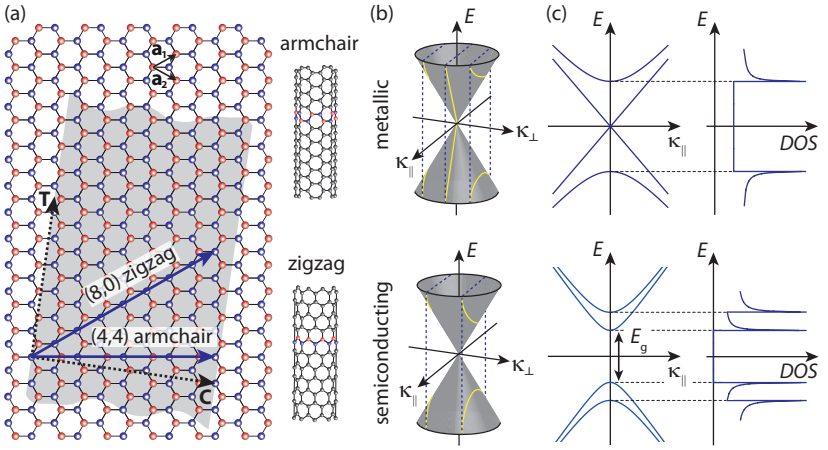

Figure 1.2.: (a) Rolling up graphene into a CNT – the chiral vector $\mathbf{C} = n\mathbf{a_1} + \mathbf{ma_2}$ with chiral indices (n, m) and $n, m \in \mathbb{N}$ determines the CNT's structural and electronic properties. Two examples of a metallic armchair and a semiconducting zigzag CNT are illustrated. (b) The circumferential quantization condition cuts the Dirac cones along the quantization lines $\kappa_\perp^p$, leading to metallic CNTs if $0 \in \kappa_\perp^p$ (top) and semiconducting CNTs if $0 \notin \kappa_\perp^p$ (bottom). (c) Corresponding one-dimensional dispersion relations $E^p(\kappa_\parallel)$ and density of states (DOS) for the lowest subbands in metallic (top) and semiconducting (bottom) CNTs. The peaks in the DOS are van Hove singularities occurring at the respective gap edge of a hyperbola subband. Adapted from Refs. [52–54, 58].

cylinder [Fig. 1.2(a)] and matching the additional periodic boundary condition for the electron wavefunction along the circumference of the CNT [52–54]. While the axial component of the wave vector $\kappa_\parallel$ remains continuous, the periodic boundary condition leads to a quantization of the circumferential component, $\kappa_\perp^p$, where the quantum number $p \in \mathbb{Z}$ denotes the allowed values of $\kappa_\perp^p$. Thus, the one-dimensional dispersion relation of a CNT is a cut of the Dirac cones along the quantization lines $\kappa_\perp^p$, leading to one-dimensional subbands of the form

$$E^p(\kappa_\parallel) = \pm\hbar v_\mathrm{F}\sqrt{(\kappa_\parallel)^2 + (\kappa_\perp^p)^2}, \tag{1.2}$$

which is plotted in Fig. 1.2(b,c). Since the branches or sub-bands closest to E_F determine the CNT's transport properties, we neglect higher subbands. As shown in Fig. 1.2(c), we observe that there are two types of CNTs: if $0 \in \kappa_\perp^p$, the lowest subband $E^p(\kappa_\parallel)$ cuts exactly through the Dirac point and we have a linear dispersion relation, resulting in zero band gap and a constant density of states (DOS) due to the one-dimensionality – the CNT behaves metallic. If, however, the lowest subband bypasses the Dirac point by $|\Delta\kappa_\perp|$,

the dispersion relation is a pair of hyperbolae with band gap $E_g = 2\hbar v_F|\Delta\kappa_\perp|$ – a semiconducting CNT forms. These cases can be derived more exactly from the periodic boundary conditions by introducing a *chiral* or *wrapping vector* $\mathbf{C} = n\mathbf{a_1} + m\mathbf{a_2}$ with $n, m \in \mathbb{N}$ and $|\mathbf{C}| = \pi d$. $\mathbf{C}$ describes the direction along which the CNT is rolled up in a graphene sheet, and its absolute value the later circumference of a CNT with diameter d. The *chiral* indices (n, m) alone determine all properties of a given CNT [52]. Different cases are illustrated in Fig. 1.2(a), where (n, n) CNTs are called armchair, those with $n = 0$ or $m = 0$ zigzag, and CNTs with arbitrary indices chiral [52]. Using Bloch's theorem, one can express the periodic boundary conditions with $\mathbf{C}$ as

$$\psi_{\mathbf{k}}(\mathbf{r} + \mathbf{C}) = e^{i\mathbf{C}(\boldsymbol{\kappa}+\mathbf{K})}\psi_{\mathbf{k}}(\mathbf{r}) = \psi_{\mathbf{k}}(\mathbf{r}). \tag{1.3}$$

From this expression, one finds the quantization condition for $\kappa_\perp^p$ [54] as

$$\mathbf{C}\boldsymbol{\kappa} = \pi d\kappa_\perp^p = 2\pi\left(\frac{m-n}{3} + p\right). \tag{1.4}$$

Hence, when $(n - m) = 3l$ with $l \in \mathbb{Z}$, the CNT is always metallic – which is obviously the case for an armchair CNT and a subset of $(n, 0)$ zigzag CNTs with n multiples of 3. If, however, $(n - m) = 3l \pm 1$ – the second choice for (n, m)-CNTs [52] – the lowest subband misses the Dirac point by $|\Delta\kappa_\perp| = 2/3d$, and a bandgap inversely proportional to the CNT diameter $E_g = 2\hbar v_F|\Delta\kappa_\perp| = 4\hbar v_F/3d \approx 0.7\,\mathrm{eV}/d\,[\mathrm{nm}]$ opens up for these semiconducting CNTs. According to the above conditions, one third of all CNTs should be metallic, while two third should be semiconducting.

1.2. Electron transport in carbon nanotubes

To treat CNTs in a more realistic picture, we will now discuss some important factors determining the transport characteristics of CNT devices. For implementing a CNT in an electronic device, it has to be connected to source (S) and drain (D) contacts, which can for example be patterned by lithographic methods (see Chap. 2). For ideally transparent metal-CNT contacts and a ballistic CNT, one would expect a two-terminal device resistance of $R_{\mathrm{SD}} = h/4e^2 \sim 6.5\,\mathrm{k\Omega}$ in a Landauer picture, due to four conductance channels associated with spin $(\uparrow, \downarrow)$ and valley (K, K') degeneracy. In real devices, one often observes values much larger than this ideal boundary. This can be either due to non-ideal contacts, i.e. a contact resistance $R_{\mathrm{contacts}} \geq h/4e^2$, or diffusive scattering in the CNT, e.g. for long or highly disordered CNT devices. Both contributions can be important depending on the device geometry and add up near room temperature to the device resistance $R_{\mathrm{SD}} = R_{\mathrm{contacts}} + R_{\mathrm{CNT}}$ [49].

Schottky barriers and contact resistances

Non-ideal contact resistances arise from the formation of tunnel-barriers at the CNT-metal interface. These tunnel barriers have two origins: First, imperfect interfaces between metal and CNT play a crucial role for the contact resistance, since this resistance is a function of interface cleanliness and the overlap between CNT-metal electronic states [49]. In Chap. 2, we will present a thorough study and possible solutions to this issue. Second, more fundamental, Schottky barriers can form at the interface between a metal and a semiconducting CNT [59]. When the Fermi level E_F of the metal aligns in equilibrium in the middle of the CNT band gap, a Schottky barrier will exist for injecting electrons and holes. In contrast, if E_F aligns e.g. above the CNT conduction band at the interface, an ohmic contact forms for electrons and a large Schottky barrier for hole injection – resulting in n-type device behavior. This is indeed often observed at room temperature, and experiments with different contact materials support this simple Schottky-Mott rule [59, 60]: While high work-function metals such as Au, Pd or Rh form good p-type CNT contacts, low work-function metals as e.g. Sc or Y yield good n-type contacts – reaching partially the ideal device conductance value of $4e^2/h$ [60–63]. In accordance with a Schottky picture [59], a diameter-dependent contact resistance $R_\mathrm{contacts} \sim 1/d$ was found due to the diameter-dependent band gap [64], and some devices even show a good tunability of the contact resistance with gate voltage due to the changed Schottky barrier width. Unfortunately, this simple picture does not always hold, and theoretical calculations also show the importance of material-dependent wetting properties and chemical bonds [65], determining the electronic hybridization between metal and CNT. Furthermore, CNT devices are very sensitive to the ambient environment, due to chemical doping or a dipole adsorption induced shift of the metal work functions [62]. Because of the various contributing and complex factors, no conclusive picture of the metal-CNT contact has evolved yet [59]. Unfortunately, one can thus not a priori design or tune an arbitrary CNT device to a desired transport regime[2] (i.e. ballistic transport, or the QD regime, see below) due to the very limited experimental control over the contact tunnel barriers.

Are there at all 'metallic' CNTs?

While the correlation between the CNT's chiral indices (n, m) and the DOS could be qualitatively confirmed by scanning tunneling microscopy measurements [66], later transport measurements have surprisingly demonstrated also

[2] In Sec. 2.2, we discuss how this is achieved in ultra-clean processing schemes with low-ohmic contacts only (materials such as Au or Pd), where the band-gap of a semiconducting CNT is utilized in an elaborate gating scheme.

small band gaps $\sim 10 - 100\,\mathrm{meV}$ for nominally metallic CNTs with known chiral indices [53, 67–69]. One typically ascribes the small band gaps to deviations from the zone-folding approximation due to strain, torsion, and the intrinsic curvature of the CNT [52]. All these effects lead to a small, but finite displacement of the Dirac cones away from K, K' so that narrow band gaps appear also for ideally metallic CNTs. Experimentally, only a very small fraction of CNTs ($\lesssim 1\%$) shows quasi-metallic transport characteristics at room-temperature [53, 70]. Some experiments further suggest that physics beyond the simple single-particle picture such as the formation of a Mott gap [69] or an excitonic insulator [71] play a role, because the narrow band gaps could not be closed with an additional Aharanov-Bohm phase acquired by magnetic fields along the CNT axis (the additional phase effectively shifts the position of the cuts $\kappa_\perp^p$ through the Dirac-cone in a non-interacting picture). Finally, theoretical considerations [72–74] and experiments [75, 76] have also shown the importance of spin-orbit coupling in CNTs. While one might at first sight expect negligible spin-orbit coupling as in graphene, the finite curvature of a CNT results in a spin-orbit splitting $\sim 0.1 - 1\,\mathrm{meV}$ of the π-band due to a combination of atomic spin-orbit coupling and interatomic hopping [53]. Thus, due the finite spin-orbit gap also in armchair CNTs [74], there exist no 'metallic' CNTs from a fundamental point of view.

Scattering mechanisms and mean free path

While at room temperature (RT) electron-phonon scattering dominates and limits the mean free path l in CNTs, at low temperatures l is dominated by elastic scattering from defects and can be up to $\sim 10\,\mu\mathrm{m}$ for quasi-metallic CNTs and a few μm for semiconducting CNTs [49]. For higher temperatures (e.g. at RT), one can distinguish acoustic-phonon scattering dominant for small bias voltages, and optical- or zone-boundary-phonon scattering for large source-drain biases ~ 160 meV, the optical phonon energy in CNTs [52]. The latter process limits the maximum current in typical CNT devices to $I_{\max} \sim 25\,\mu\mathrm{A}$ [49], and can be used for a local Joule heating or 'cutting' of suspended CNT devices (see Sec. 2.2). For the purpose of this thesis, all CNT devices are short ($\sim 300\,\mathrm{nm} \ll \mathrm{l}$) and studied at low temperatures, therefore CNTs can be regarded as ideal ballistic conductors.

Transport regimes in the quantum limit

Due to an increased electron phase coherence length or a quantized energy level spacing $\delta E \gtrsim kT$, electron transport in CNTs becomes dominated by quantum mechanical effects at low temperatures, typically for $T \lesssim 10\,\mathrm{K}$. The source-drain contacts on a CNT impose additional potential barriers for the electronic wave function also along the CNT. Due to the small thermal ener-

gies, electrons have to quantum-mechanically tunnel through these barriers. We distinguish two limiting cases: If the barriers are very weak, electron motion in-between is coherent and ballistic with Fermi velocity v_F, and one observes quantum mechanical interference of ballistic trajectories in analogy to a Fabry-Perot cavity [77]. In contrast, if the resistances of the two barriers are similar or larger than the quantum resistance h/e^2 [49], the CNT island in-between becomes strongly isolated and a quantum dot (QD) forms, leading to single-electron charging and Coulomb blockade (see next section).

1.3. Quantum dots in carbon nanotubes

In a quantum dot (QD), the electron wave function is confined in all three spatial dimensions. The required potential barriers to confine the electron wave function also along the CNT can be introduced either directly by the resulting tunnel barriers at the source-drain metal-CNT interface (see previous section), by arbitrary defects along the CNT, or in a more controlled way by utilizing the band-gap of semiconducting CNTs and a gating technique, e.g. in ultra-clean processing schemes (see Sec. 2.2) [53]. As illustrated in Fig. 1.3(a), the discrete energy spectrum of the resulting CNT QD can be estimated from a particle-in-a-box approximation [50, 53] where the parallel momentum component becomes quantized and fulfills standing wave solutions for the boundary conditions

$$\kappa_\parallel = \frac{n\pi}{L} \quad n \in \mathbb{N} \setminus \{0\}, \tag{1.5}$$

with the barrier distance or QD size L. Because typically $L \gg d$ (the CNT diameter), we consider only the lowest subband of the CNT dispersion relation (1.2) for the relevant low energy excitation spectrum. The additional quantization (1.5) leads to a set of discrete energy levels with a level spacing

$$\delta E = \hbar v_\mathrm{F} \frac{\pi}{L} \sim \frac{1.7\,\mathrm{meV}}{L\,[\mu\mathrm{m}]} \tag{1.6}$$

calculated from Eq. (1.2) for metallic CNTs or semiconducting CNTs in the many-electron regime, i.e. where the original dispersion relation $E^p(\kappa_\parallel)$ can be approximated linearly [53]. In a simple non-interacting picture, due to spin- and valley degeneracy, each of these energy levels can be occupied by four electrons.

1.3.1. Coulomb blockade and single electron tunneling

Because QDs are small objects and have a small associated capacitance C, the electron-electron or Coulomb interaction $\sim e^2/C$ is not negligible and can even be the dominating energy scale for low temperatures. The effects of

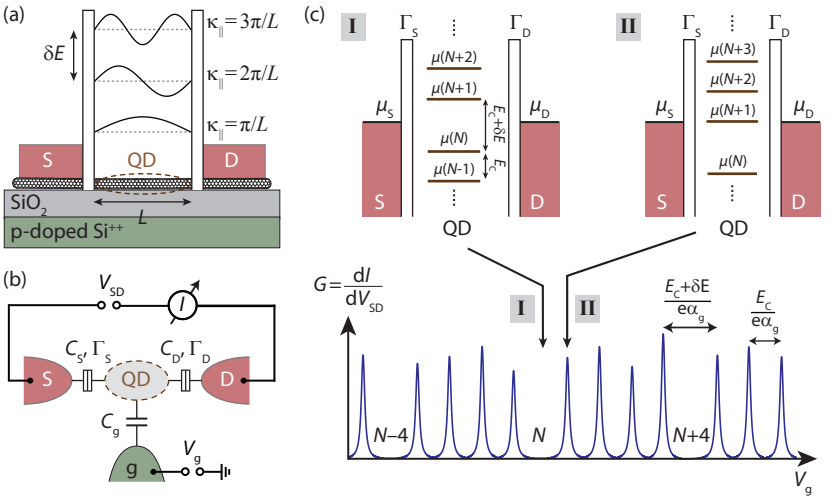

Figure 1.3.: (a) Illustration of the quantization condition for $\kappa_\parallel$ and resulting level spacing δE in a CNT QD with tunnel barriers defined by the source-drain contacts. (b) Capacitor model and typical measurement setup of a QD connected to source (S) and drain (D) electrodes (red), which are both tunnel-coupled with $\Gamma_{S/D}$ to the QD in parallel to their capacitive coupling $C_{S/D}$. A single gate (g, green) allows to tune the electrostatic potential of the QD with voltage V_g via the capacitance C_g - in Fig. (a) a highly doped Si substrate is used as backgate. The current I can be measured when a SD bias voltage V_{SD} is applied. (c) Expected differential conductance G as a function of V_g at $V_{SD} \sim 0$ for a CNT QD with fourfold degenerate energy levels. Situation I and II sketch the alignment of the QD's electrochemical potential μ relative to those of the SD contacts, $\mu_{S/D}$, in Coulomb blockade (I) or on resonance (II). Adapted from Refs. [8, 42, 53, 58, 78].

Coulomb interactions are usually well described within the framework of the *constant interaction model* (CIM) [7]. The CIM assumes that (a) all electron-electron interactions are parametrized by a single constant capacitance C of the island, and (b) that the discrete single-particle energy spectrum of the QD remains unperturbed by electron-electron interactions or the electron number N on the QD [8, 42, 53]. Figure 1.3(b) shows an electrical model of a QD circuit, where a single QD is tunnel-coupled to a source (S) and a drain (D) contact with coupling strengths Γ_S, Γ_D, and in parallel capacitively coupled with capacitances C_S, C_D. A finite source-drain bias voltage $V_{SD} = V_S - V_D$ can be applied between the source-drain contacts while measuring the current I or differential conductance $G = dI/dV_{SD}$, and a voltage V_g is applied to a gate electrode (g) coupled only capacitively to the QD with C_g. In this simple model system, the total capacitance assigned to the QD is $C = \sum_i C_i$ with $i = \{S, D, g\}$, which can be easily extended for additional gates or surrounding

dielectrics. Then the total ground state energy of a quantum dot with N electrons is

$$U(N) = \frac{Q_{\mathrm{tot}}^2}{2C} + \sum_{n=1}^{N} E_n, \tag{1.7}$$

where $Q_{\mathrm{tot}} = -|e|(N - N_0) + \sum_i C_i V_i$ denotes the total charge on the QD, and $N = N_0$ the occupancy for all $V_i = 0$ [8, 42]. The first term in Eq. (1.7) describes the electrostatic energy of the QD, where the quantities $C_i V_i$ can be interpreted as gate-induced charges which allow to change the QD potential continuously (gating). The last term sums up over the occupied 'atomic orbitals' or quantum mechanical energy levels E_n.

In any (transport) spectroscopy experiment, one typically probes energy differences rather than absolute energies. Thus, it is convenient to introduce the electrochemical potential $\mu = \mu_{\mathrm{QD}}$ of the QD,

$$\begin{aligned} \mu(N) &= U(N) - U(N-1) \\ &= \frac{e^2}{C}\left(N - N_0 - \frac{1}{2}\right) - \frac{|e|}{C}\left(\sum_i C_i V_i\right) + E_{\mathrm{N}}, \end{aligned} \tag{1.8}$$

which describes the energy required to add the N-th electron to the dot (the energy difference between two QD ground states or energy levels), and represents a whole 'ladder' of electrochemical potential levels shown in Fig. 1.3(c). The spacing between these electrochemical potential levels is the *addition energy*

$$E_{\mathrm{add}} = \mu(N+1) - \mu(N) = \frac{e^2}{C} + \delta E, \tag{1.9}$$

with the so-called *charging energy* $E_{\mathrm{C}} = e^2/C$ and the quantum mechanical level spacing δE specified in Eq. (1.6) [42, 53]. This ladder of electrochemical potentials can be shifted linearly with the V_i by $e\alpha_i \Delta V_i$, depending on the (gate's) *lever arm* or efficiency factor $\alpha_i = C_i/C$. We now assume linear response (i.e. $V_{\mathrm{SD}} \sim 0$) and low temperatures $kT \ll \delta E, E_{\mathrm{C}}$, so that the Fermi distribution of the lead electrons $f_{\mathrm{S/D}}(E) = 1/(\exp[(E - \mu_{\mathrm{S/D}})/kT] + 1)$ is approximately a step function with a small thermal broadening $\sim kT$ around $\mu_{\mathrm{S/D}}$, the electrochemical potential of the leads. If now $\mu(N) < \mu_{\mathrm{S}} = \mu_{\mathrm{D}} < \mu(N+1)$ as in situation I of Fig. 1.3(c), electron transport is blocked because the lead electrons do not have enough energy to enter the QD state with total energy $U(N+1)$, nor can the QD relax to the $U(N-1)$ ground state due to the occupied lead states around $\mu(N)$. Hence, in this so-called *Coulomb blockade* situation the number of electrons on the QD is fixed [8]. If one increases the gate voltage V_{g} and shifts the electrochemical potential ladder so that $\mu(N+1) = \mu_{\mathrm{S}} = \mu_{\mathrm{D}}$ as in situation II of Fig. 1.3(c), the charge configuration of the QD becomes unstable: the small broadening kT of the Fermi functions allows for both occupied and unoccupied states in the leads, so that the QD

ground state fluctuates between $U(N+1) \leftrightarrow U(N)$. Therefore, a very small bias voltage $-|e|V_{\mathrm{SD}} = \mu_{\mathrm{S}} - \mu_{\mathrm{D}}$ results in a measurable current, where the electrons are sequentially transferred one at a time: *single electron tunneling* occurs [42]. Hence, the gate-dependent differential conductance G shown in Fig. 1.3(c) shows so-called *Coulomb peaks* or *resonances* whenever the QD is resonant, i.e. $\mu(N) = \mu_{\mathrm{S/D}}$, and directly reflects the electrochemical potential ladder or the four-fold degenerate level spectrum of the QD [53]. The Coulomb peaks are separated by E_{add} from Eq. (1.9), and have a four-fold periodic structure: The first electron occupying a new CNT shell or orbital energy needs an addition energy of $U + \delta E$, while for the three following $\delta E = 0$ and $E_{\mathrm{add}} = U$.

1.3.2. Resonance line shapes

So far, we neglected the tunnel couplings or tunnel rates $\Gamma_{\mathrm{S/D}}/h$ and assumed a perfectly isolated QD. Yet a small coupling $\Gamma = \Gamma_{\mathrm{S}} + \Gamma_{\mathrm{D}}$ to source-drain electrodes leads to a finite lifetime τ of the electrons on the QD and allows them to tunnel also slightly off-resonant onto or off the QD within an energy window $\sim h/\tau$ given by Heisenberg's uncertainty relation – resulting in a finite, intrinsic width of the resonances even at $kT \sim 0$. We distinguish two limiting cases for the resonance line shapes: For $kT \ll \Gamma \ll \delta E, E_{\mathrm{C}}$, the so-called *lifetime-broadened*, *intrinsic lineshape* or *strong coupling regime*, tunneling through the QD is well described as double-barrier scattering process of independent electrons, and the conductance peak has a Lorentzian or Breit-Wigner[3] (BW) form [79]

$$G\left(\Delta V_{\mathrm{g}}\right) = \frac{e^2}{h} \frac{\Gamma_{\mathrm{S}}\Gamma_{\mathrm{D}}}{\Gamma_{\mathrm{S}} + \Gamma_{\mathrm{D}}} \frac{\Gamma}{\Delta E^2 + \left(\Gamma/2\right)^2}, \tag{1.10}$$

with the level detuning $\Delta E = -e\alpha_{\mathrm{g}}(\Delta V_{\mathrm{g}} - V_{\mathrm{g}}^{(0)})$ and the position of the resonance $V_{\mathrm{g}}^{(0)}$. The asymmetry of the tunnel barriers $\Gamma_{\mathrm{S}}/\Gamma_{\mathrm{D}}$ determines the conductance maximum, whereas the full width at half maximum (FWHM) of the resonance reflects the tunnel coupling or lifetime broadening Γ.

In the *thermally broadened single-level* or *weak coupling transport regime*, i.e. $\Gamma \ll kT \ll \delta E, E_{\mathrm{C}}$, the lineshape can be described by [80]

$$G(\Delta V_{\mathrm{g}}) = \frac{e^2}{h} \frac{1}{4kT} \frac{\Gamma_{\mathrm{S}}\Gamma_{\mathrm{D}}}{\Gamma_{\mathrm{S}} + \Gamma_{\mathrm{D}}} \cosh^{-2}\left(\frac{\Delta E}{2kT}\right), \tag{1.11}$$

where the maximum conductance depends on the asymmetry $\Gamma_{\mathrm{S}}/\Gamma_{\mathrm{D}}$ and temperature as $\sim 1/kT$, whereas the FWHM $\sim 3.5kT$.

[3] Eq. (1.10) is only valid in the deep Coulomb blockade regime for weak dot-lead coupling, where Coulomb interactions are dominant. For increased dot-lead coupling, the underlying single-particle approximation is invalid.

From the Coulomb peak line shapes one can determine a transport regime and the coupling parameters $\Gamma_{\mathrm{S/D}}$, but cannot assign $\Gamma_{\mathrm{S/D}}$ to individual electrodes in a two-terminal configuration. The tunnel couplings $\Gamma_{\mathrm{S/D}}$ depend on the tunnel barriers and the exact confinement potential, but they can also depend on the electronic charge state of the QD due to the different overlap of the electronic wave function with the leads [see e.g. Fig. 1.3(a)].

1.3.3. Transport spectroscopy with Coulomb diamonds

Applying now a finite source-drain bias voltage V_{SD} and measuring the differential conductance G as a function of V_{SD} and V_{g} results in a so-called *charge stability diagram*, shown in Fig. 1.4. This shows that Coulomb blockade (CB) can also be lifted by a finite bias voltage, because whenever an electrochemical potential level of the QD enters the bias window defined by $-|e|V_{\mathrm{SD}} = \mu_{\mathrm{S}} - \mu_{\mathrm{D}}$, we obtain a step-wise change in current I and therefore a peak in G. In the color-coded charge-stability diagram of Fig. 1.4, we consequently observe a pattern of so-called *Coulomb diamonds* [42]. Inside the diamonds the number of electrons on the QD is fixed and sequential tunneling blocked, whereas outside the number of electrons on the dot is fluctuating because at least one level lies within the bias window. The boundaries of the CB diamonds which mark the onset of charge transport are determined by the condition $\mu_{\mathrm{S/D}} = \mu_{\mathrm{QD}}$, i.e. along the line with negative slope $\beta_- = \frac{\Delta V_{\mathrm{SD}}}{\Delta V_{\mathrm{g}}}$ a level stays aligned with the drain μ_{D}, while for the line with positive slope β_+ $\mu_{\mathrm{QD}} = \mu_{\mathrm{S}}$ holds. The bias voltage at the tip of a diamond where both lines cross hence directly measures the spacing between adjacent electrochemical potentials of the QD [see Fig. 1.4, situation II], the addition energy $E_{\mathrm{add}} = E_{\mathrm{C}} + \delta E$, defined in Eq. (1.9). Whenever a clear four-fold periodic shell filling pattern is observed, this can be used to extract both E_{C} and δE from the diamond tips as indicated in Fig. 1.4.

We now assume asymmetric biasing as in the later experiments, where the drain is grounded ($\mu_{\mathrm{D}} = 0$) and the bias is applied at the S contact only, i.e. $\mu_{\mathrm{S}} = -|e|V_{\mathrm{SD}}$. Then the slopes $\beta_{+/-}$ can be easily calculated: From $\mu_{\mathrm{D}} = 0 = \mu_{\mathrm{QD}}$ for the line with negative slope one finds $0 = -|e|\frac{C_{\mathrm{g}}}{C}\Delta V_{\mathrm{g}} - |e|\frac{C_{\mathrm{S}}}{C}\Delta V_{\mathrm{SD}}$ with Eq. (1.8), i.e. the gate has to compensate for the shift of the QD electrochemical potential due to the capacitive coupling to the S contact. In this case, we obtain $\beta_- = -\frac{C_{\mathrm{g}}}{C_{\mathrm{S}}}$ and similarly $\beta_+ = \frac{C_{\mathrm{g}}}{C - C_{\mathrm{S}}}$ for the positive slope. These can be combined to determine the lever arm of the gate $\alpha_{\mathrm{g}} = \frac{C_{\mathrm{g}}}{C} = \frac{\beta_+|\beta_-|}{\beta_+ + |\beta_-|}$, which is useful to extract energy scales as the addition energy from the spacing of CB peaks in gate voltage. Furthermore, the slopes $\beta_{+/-}$ and α_{g} allow the calculation of all capacitances C_i.

Besides the ground state transitions $U(N+1) \leftrightarrow U(N)$ discussed so far, additional processes and transition lines occur in the charge stability diagrams.

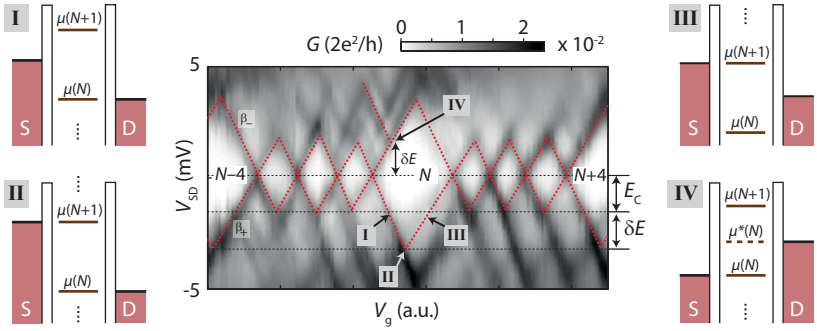

Figure 1.4.: Measured differential conductance G of a CNT QD device as a function of V_{g} and V_{SD} at $T = 1.7\,\mathrm{K}$. The red dashed lines outline the Coulomb diamonds with slopes β_+ and β_-. A clear 4-fold periodicity is apparent, which can be used to extract E_{C} and δE. The small energy diagrams (I-III) represent different biasing conditions indicated in the charge stability diagram. Situation (IV) corresponds to tunneling through the first orbital excited state. Energy diagrams adapted from Refs. [8, 42, 78].

When a bias voltage $|eV_{\mathrm{SD}}| > \delta E$ provides the necessary energy, the N-th electron can also be excited into the orbital level $E_{\mathrm{N+1}}$ and relax back to the ground state $U(N)$ where E_{N} is occupied. One observes these *orbital excited states* whenever an excited state electrochemical potential μ^*_{QD} falls into the bias window [8]. This leads to an additional conductance channel and an extra line in G, running parallel to the ground state diamond edges and terminating there for $|eV_{\mathrm{SD}}| < \mu^*_{\mathrm{QD}} - \mu_{\mathrm{QD}}$, shown exemplary for the first orbital excited state in situation IV of Fig. 1.4.

If the contact coupling $\Gamma_{\mathrm{S/D}}$ is increased, higher order tunneling processes beyond the sequential tunneling limit become likely. For example, in a second order *co-tunneling* process [81], an electron can leave the QD even in Coulomb blockade if another electron co-tunnels simultaneously onto the QD within a time window $\sim h/E_{\mathrm{C}}$ given by Heisenberg's uncertainty principle. This process leads to a background current $\propto V_{\mathrm{SD}}$ and a constant or step-wise increased G in the region of Coulomb blockade [81]. It is called elastic co-tunneling if the QD remains in the ground state after the event, and inelastic co-tunneling if the QD ends up in an excited state. The threshold voltages $|eV_{\mathrm{SD}}| > \mu^*_{\mathrm{QD}} - \mu_{\mathrm{QD}}$ for inelastic co-tunneling events allow for a precise determination of the QD's excitation and level spectrum [76].

In reality, the quantum mechanical level spectrum and shell-filling pattern of a CNT QD often looks much more complex than sketched here. For example, one often observes a separation of the 4-fold periodic CB diamond pattern into groups of two, i.e. a larger $N + 2$ CB diamond [82, 83]. This can be captured

by a subband mismatch $\delta = \sqrt{\Delta_{\mathrm{SO}}^2 + \Delta_{KK'}^2}$, which assumes a lifted fourfold degeneracy of the CNT QD spectrum due to a spin-orbit splitting Δ_{SO} or inter-valley scattering $\Delta_{KK'}$ [53, 75, 76]. The mode spectrum can become very complex, also depending on the band-gap, the exact barrier boundary conditions, and the relative size of different interactions – we refer to Ref. [53] because this is only of minor importance for this thesis and beyond the scope of this introduction.

Resonant tunneling features and transition lines in the charge stability diagrams can also be caused by extrinsic effects [84]. In suspended CNT devices, for example, phonons can couple to the electronic system and additional transition lines and replicas of the ground and excited state transitions appear due to the emission or absorption of phonons in an inelastic tunneling process [44–46, 48, 85]. These lines can be identified by their regular spacing given by the boson energy, and by their characteristic temperature and magnetic field dependence [84]. While the number of populated phonon modes is low at small temperatures and only emission processes are possible, with increasing temperature also absorption processes become likely due to the increased phonon population, and extra absorption replica lines appear in the region of Coulomb blockade [46]. In the case of strong electron-phonon couplings, even current suppression can occur (Franck-Condon blockade) [46]. Similarly, also the electromagnetic environment can provide energy for photon-assisted processes, resulting in discrete QD resonance side bands [86, 87].

2

Device fabrication and measurement set-up

In this chapter, we introduce the fabrication of CNT QD devices with superconducting or ferromagnetic contacts and present fabrication techniques common to both contact materials, and to the respective results presented in Part I and II. Due to the small, nano- to micrometer-scale size of the CNT devices and consequently resulting sample-to-sample variations, only a small fraction of the fabricated devices will typically have desirable characteristics. CNT device fabrication is hence a statistical process, where only the best devices found in an initial sample characterization will finally be investigated at cryogenic temperatures. To eventually obtain an acceptable yield of clean CNT devices with the desired transport characteristics, a considerable amount of time has to be spent to systematically optimize fabrication techniques, and crucial attention has to be paid to even the smallest details for a reproducible process. Most of this work is carried out in a clean room environment to avoid particle contamination of the devices. Here, we will only present the most important and most optimized concepts and techniques used and developed. Some steps are described more accurately in the results section of Part I and II, where also the exact device fabrication is typically summarized briefly. Detailed parameters and recipes of the fabrication, where not found in the main text, are always given in Appendix A. We start the chapter by introducing the standard fabrication and characterization of conventional CNT devices on substrate. Section 2.2 summarizes the most important fabrication approaches developed and used in this thesis to obtain clean conventional devices, or to integrate ferromagnetic or superconducting contacts in so-called ultra-clean fabrication schemes. Finally, the chapter closes with a discussion of the used measurement techniques and set-ups at cryogenic temperatures.

2.1. Standard device fabrication and characterization

We first briefly summarize the general fabrication work-flow of conventional CNT devices on substrate, where metallic contacts are structured in post-processing steps after the CNT growth.

Substrate preparation All CNT devices are prepared on a highly p-doped Si substrate with a 400 nm thick, thermally grown and insulating SiO_2 top layer, which also serves as a backgate (BG). A Si/SiO_2 wafer is carefully cut into $1 \times 1\,cm^2$ substrate pieces and cleaned rigorously by sonication in acetone, isopropanol (IPA) and a final UV ozone treatment, allowing the decomposition of organic surface residues by UV light and oxygen radicals. The thorough substrate cleaning should guarantee an almost particle- and organic residue-free surface, a major prerequisite for clean devices, for an increased resist surface adhesion and for a reduced metal surface diffusion in later processing steps.

CNT growth Single-walled CNTs are grown on the substrate by chemical vapour deposition (CVD) from iron-based catalyst nanoparticles in a CVD reactor [88, 89]. We used both catalyst based on iron molybdenium (FeMo) [89] and iron ruthenium (FeRu) [90, 91]. While the FeRu catalyst should result in a more narrow diameter distribution of the grown CNTs ($\sim 1-2\,nm$) [90, 91] and hence in higher contact resistances (Sec. 1.2) [59, 64], we did not find significantly different CNT device resistances for the two catalysts in the course of this thesis. Thus, we mostly used the FeRu catalyst due the increased chance of growing single-wall CNTs [90]. The catalyst nanoparticles are spin-coated from an IPA-based solution onto the substrate, where the amount of IPA added allows to tune the resulting CNT density. It is crucial to break up catalyst nanoparticle clusters in the catalyst solution beforehand with a high power sonicator, because the nanoparticle size directly influences the diameter of the resulting CNTs [92]. The substrate is placed in the CVD oven and heated to the desired growth temperature $T = 850°C$ (FeRu) or $T = 950°C$ (FeMo) under protective argon (Ar) flow. CNTs are then grown from a methane and hydrogen (H_2) atmosphere with well-defined flow rates for 10 min. (App. A). Methane is catalytically dissociated and serves as carbon feedstock for CNT growth, while hydrogen reacts with excess carbon and reduces the amount of CNT bundles and amorphous carbon [89]. The used CNT growth process generates mainly individual single-wall CNTs with typical lengths of $2-10\,\mu m$ [89, 93]. Finally, the substrate is cooled down to room temperature in a protective and reducing Ar/H_2 atmosphere.

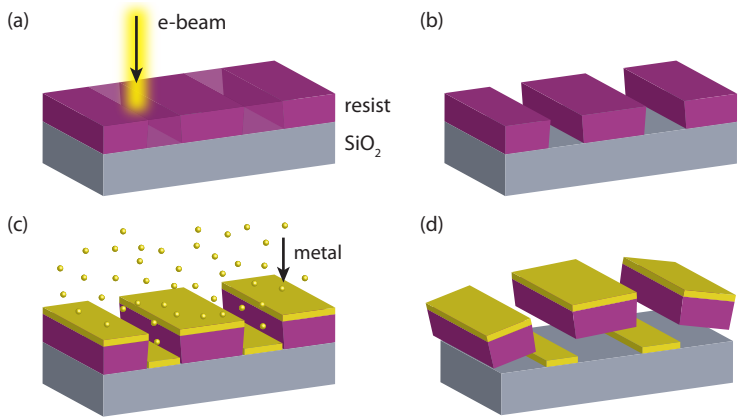

Figure 2.1.: Schematic of a typical e-beam lithography process. (a) A resist is spin-coated on a Si/SiO_2 substrate and exposed by an electron beam that patterns the desired structure into the resist. (b) Development transfers the written pattern into a resist mask. (c) Metal deposition. (d) A lift-off process with a remover dissolves the remaining resist and leaves only the desired metal structure behind.

E-beam lithography For all of the following fabrication steps, an electron-beam (e-beam) lithography (EBL) process is required. Figure 2.1 illustrates the general principle and work-flow of such a process. A thin, e-beam sensitive polymer resist layer is spin-coated onto the substrate and baked for 3 min. at $T = 180°C$ on a hotplate to harden the resist and evaporate any remaining solvents. In this thesis, we mostly use ZEP520A copolymer resist[1] (ZEP) and polymethylmethacrylate (PMMA) with a molecular weight of 950K[2], with typical resist thicknesses of ~ 300 nm. The resist thickness can be adjusted by changing either the rotation frequency of the spinner, or changing the solvent dilution. The desired pattern is then transferred into the resist by exposure of the substrate to the highly focussed e-beam of a scanning electron microscope (SEM) controlled by a pattern generator (Raith Elphy lithography attachment, Raith GmbH) [Fig. 2.1(a)]. In the case of a positive e-beam resist, the exposure to the e-beam results in a chain-scission of the long resist polymer chains into smaller fragments for an appropriate dose or exposure time. A chemical developer, usually a solvent, can then be used to selectively only dissolve the light-weighted short polymer chains, effectively transferring the written e-beam pattern into a resist mask [Fig. 2.1(b)]. We use a 1:3 mixture of methyl isobutyl ketone (MIBK) and IPA as developer for PMMA and n-

[1] Composed of 11% methyl styrene and chloromethyl acrylate copolymer and 89% anisole (solvent) by ZEON corporation.
[2] Solved in chlorobenzene, AR-P 671.09 950K, Allresist GmbH.

amyl acetate for ZEP. The EBL process and the transferred patterns in the resist depend sensitively on the used substrate and resist, the resist thickness, and many parameters including the acceleration voltage and spot size of the e-beam, the working distance, used apertures and beam currents in the SEM, the exposure time and dose, the pattern itself (proximity effect), as well as the used developer, development time and temperature and resist prebaking [94]. An EBL process can be very complex and many parameters can be tuned to engineer the desired results. We will discuss some of these details and the engineering of an optimized EBL process for clean CNT devices based on ZEP in Sec. 2.2.1, and refer to Ref. [94] for a detailed review. The resist structure now acts as a mask for the following metal deposition [Fig. 2.1(c)], and a lift-off process with a resist remover leaves only the desired metal structure, i.e. where the resist was exposed, behind [Fig. 2.1(d)]. Here, we use a 50°C warm acetone bath for PMMA lift-off and a 70°C hot n-methyl-2-pyrrolidone (NMP) bath followed by cleaning in an acetone bath for ZEP lift-off. The lift-off can be supported by the turbulent flow created e.g. with a syringe, but not by sonication due to the otherwise created defects in CNTs.

Alignment markers and CNT localization After CNT growth, a grid of alignment markers used as coordinate system for CNT localization is patterned onto the substrate by EBL. We use a grid of 10×10, $10\,\mu$m spaced, e-beam evaporated Ti/Au (5 nm/45 nm) markers which allow for a ~ 50 nm alignment precision in EBL, visible e.g. in Fig. 2.2(d). Individual CNTs can then be located by SEM imaging on the substrate with respect to the marker grid. We use low acceleration voltages ~ 1 kV and the InLens detector to image the substrate, which allows to resolve the different charging of the insulating substrate below the conducting CNTs due to their additional capacitance [95]. Such a technique hence only images a charge shadow of the CNTs [Fig. 2.2(d)], and does not allow to discriminate between metallic, semiconducting, single-wall, multi-wall or defect-free CNTs. Appropriate CNTs are randomly selected, where the imaging time is kept to a minimum to avoid creating defects and carbon contamination from the e-beam [96].

Fabricating a CNT device After the transfer of the CNT positions to a GDSII-design file, a CNT device layout can be designed on the computer and fabricated using the discussed EBL process repetitively. In such a way, contacts with different materials including normal metals, superconductors and ferromagnets as well as gates and bonding pads can be implemented conveniently in separate EBL steps. In this thesis, we study hybrid CNT QD devices either with superconducting (S) and normal metal (N) contacts in a Cooper pair splitter (CPS) device geometry [see Part I and Fig. 2.2(c)], or with ferromagnetic (F) contacts in a spin-valve geometry [Part II and Fig. 2.2(d)]. In both

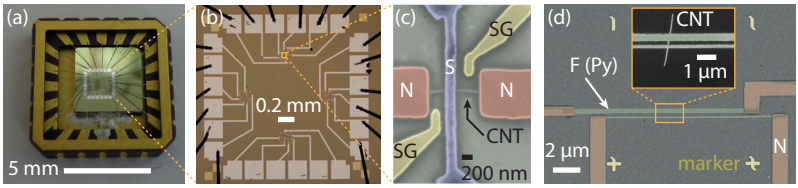

Figure 2.2.: (a) A wire-bonded sample in a chip-carrier. (b) Optical microscope image of the bonded chip, containing four CPS devices with 6 bond pads each. Only 3 devices can be contacted/bonded simultaneously. (c) False color SEM image of a typical CNT device in a CPS geometry with superconducting (S, blue) and normal (N, red) source-drain contacts, including sidegates (SGs, yellow) for tuning. (d) False color SEM image of a CNT spin-valve device with ferromagnetic (F, green) Py source-drain contacts and normal (N, brown) metal leads. One grid square of Ti/Au alignment markers (yellow) is visible.

cases, at least two additional EBL steps with different materials are required. For the normal metal contacts, outer leads, gates and bonding pads shown in Fig. 2.2(b) we use either 50 nm of thermally evaporated Pd or a layer of e-beam evaporated Ti/Au (5 nm/45 nm). In the case of a CPS device geometry, we employed either a sputtered Ti/Nb or an e-beam evaporated Pd/Pb/In layer as S contact, where the $4-6$ nm thick Ti or Pd serves as wetting or contact layer enabling low-ohmic contacts. Details of the sample fabrication, device design and metal deposition are discussed in Part I and Chap. 4. For a CNT spin-valve device, 25 nm thin, long and narrow rectangular Permalloy (Py, $Ni_{80}Fe_{20}$) strips were either e-beam evaporated or sputtered in the first EBL step as ferromagnetic source-drain contacts, which allow to accurately control the easy axis of the magnetization and the respective coercive field by shape anisotropy [36]. Also here, we refer for details of the fabrication and device design to Chap. 10 and Part II. The F contacts are connected to bond pads with Pd leads in a second EBL step [Fig. 2.2(d)], directly after a prior *in-situ* Ar sputtering of the future Py-Pd interface under protection of the lead resist mask. This serves to remove possible ferromagnetic surface oxides and enable a metallic Py-Pd contact. Figure 2.2(c) and (d) show examples of a typical CNT device in a CPS and spin-valve geometry.

Room temperature characterization and wire-bonding To obtain a large enough number of working devices, we fabricated typically 16-20 CNT devices in parallel on a $1 \times 1\,\mathrm{cm}^2$ substrate. To decide which devices should be bonded and measured at low temperatures, we characterize all samples by measuring the two-terminal room temperature (RT) conductance between individual contacts with a needler prober station. Its dependence on the back-gate voltage allows to characterize the contacted CNT as semi-conducting [see

Fig. 12.1(a) for an example], quasi-metallic or narrow band-gap, and to determine a RT device resistance – for the semiconducting CNTs in the 'ON' state of the CNT transistor. In the case of non-working devices or only after successful measurements at cryogenic temperatures, SEM or atomic force microscopy (AFM) imaging gives further feedback on the device quality or the CNT diameter.

Finally, the $1 \times 1\,\mathrm{cm}^2$ substrate is cut into four roughly $4 \times 4\,\mathrm{mm}^2$ pieces, each with up to four working CNT devices [Fig. 2.2(b)], and glued into a 20 terminal chip-carrier with conducting silver-paint. As shown in Fig. 2.2(a), the silver-paint also provides the contact to the backgate, while an ultrasonic Al wire bonding process establishes an electrical connection between the bonding pads and the chip-carrier terminals. The chip-carriers fit into corresponding sockets in the cryogenic measurement setups, thus connecting the CNT devices to the measurement lines.

2.2. Clean and ultra-clean fabrication approaches

Recent years have seen a tremendous increase of research activities based on clean fabrication schemes for CNT QD devices [70, 75, 97–104], enabling the investigation of a variety of fundamental physical phenomena, including tunable QDs in the few electron regime [97, 100–102, 104], Fabry-Perot interference [102, 105], spin-orbit interaction [75, 106], the realization of a one-dimensional Wigner crystal [107] and molecule [108], valley spin-blockade [100] and valley spin-qubits [109], or the interaction between electron tunneling and the mechanical motion of the CNT [48, 85]. All these discoveries, conducted by transport experiments in so-called ultra-clean, suspended CNT QD systems, were made possible by novel fabrication schemes with pristine, as-grown CNTs that are never exposed to an e-beam (deposition of amorphous carbon), resists or solvents, which are believed to contaminate interfaces and the active structure [70, 98]. In these schemes, a pristine CNT is either grown over predefined contacts which are able to withstand high temperatures [70, 75, 97, 105], or mechanically transferred onto the device structure in the last fabrication step [98–101, 103, 104]. This, however, makes it considerably more difficult to integrate also oxidizing materials such as ferromagnets or superconductors in ultra-clean CNT hybrid devices and has thus not been achieved, yet. Nevertheless, the integration of superconducting or ferromagnetic contacts into ultra-clean fabrication schemes seems highly desirable, due to the expected improved device quality, electrical stability and tunability. Such suspended hybrid CNT devices could be used to realize several recent theoretical proposals, including Hanle-type experiments on QDs with ferromagnetic contacts [110], coupling phonons in suspended CNTs either to resonant Andreev tunneling [111], or to spin-polarized currents [112], or an electronic Bell test [113].

Motivated by these proposals, and the unprecedented quality of ultra-clean devices, we developed and used several fabrication techniques in this thesis for clean 'conventional' (on substrate, Sec. 2.1) and ultra-clean hybrid CNT devices with superconducting and ferromagnetic contacts. All of these techniques have the purpose to improve the quality of the CNT devices and of the often limiting metal-CNT interface. Some of these developments were crucial to observe the reproducible superconducting device characteristics presented in Part I, or the spin-valve signals shown in Part II. While we have tested several more approaches, we report here only the most successful ones. CNTs have small diameters, which makes them extremely perceptible to resist residues in conventional CNT devices on substrate. Thus, it is typically much more difficult to achieve low-ohmic contacts to a CNT with superconductors than with normal metals, and even more challenging with ferromagnetic contacts. In Sec. 2.2.1 and 2.2.2, we present two approaches to improve both the interface and general quality of such conventionally fabricated CNT devices. Section 2.2.3 and 2.2.4 summarize two fabrication approaches that aim at implementing superconducting and ferromagnetic contacts in ultra-clean processing schemes.

2.2.1. Optimized e-beam lithography for clean devices[3]

In the standard fabrication scheme for CNT devices (Sec. 2.1), metal contacts are patterned in an EBL step on top of the CNT by using organic e-beam lithography resists. Thus the CNT-metal interface is not pristine, and exposed to chemicals and organic resists. Any interfacial residues from previous processing might therefore diminish the electrical contact yield to CNTs, or even prevent electrical contact at all. As already discussed in Sec. 1.2, the CNT contact resistance and general device quality is thus a direct function of the interface cleanliness. An essentially residue-free, optimized EBL process is hence of crucial importance for CNT devices with desirable characteristics, especially for the superconducting (S) and ferromagnetic (F) contact materials implemented in this thesis: most of these materials form oxides when exposed to air, which greatly diminishes the yield of low-ohmic contacts compared to normal (noble) metals. Further, due to the required narrow contacts in devices with S or F contacts demanded by the shape anisotropy or coherence length (see Part I and II), the interface area between the contact and the CNT is usually very small, which makes the contact very susceptible to resist residues. These residues can compromise the spin and charge transport properties in devices with F contacts, or superconducting properties like the observed transport gap (Part I) in S-QD devices, and also the electrical device stability due to dielectric charge traps.

[3]Parts of this chapter have been published in similar form in Ref. [114].

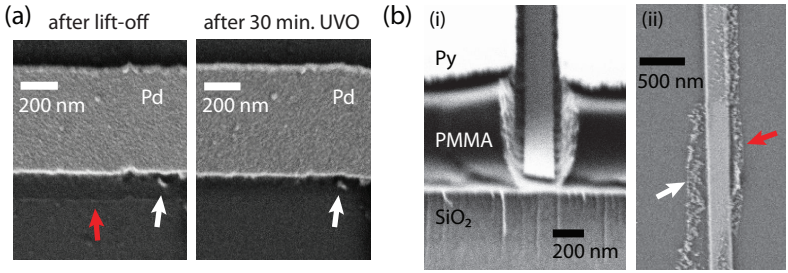

Figure 2.3.: (a) SEM images of a Pd strip fabricated by a standard PMMA-based EBL, before and after a 30 min. long UVO cleaning step. Visible resist residues (red arrow) vanish after the UVO cleaning. (b) SEM images of a Py strip obtained with a 600 nm thick PMMA mask and 30 kV acceleration voltage, (i) cross section of the metallized strip structure, and (ii) top view after the lift-off process. Red arrows point out polymer residues, white arrows metallic particles.

Motivated by the initial problems in contacting CNTs with narrow ferromagnetic Py contacts in the device geometry of Fig. 2.2(d), we have systematically investigated the morphology and contact properties of Py strips fabricated by EBL with different resist systems and beam acceleration voltages. We identified two fundamental problems when a standard, not-optimized EBL fabrication recipe based on PMMA was used: (1) Metallic (Py) nanoparticles form at the side walls of polymer structures with insufficient under-cuts and are deposited nearby or on the Py strips in the lift-off procedure, (2) resist residues lead to a significant decrease in the yield of obtaining low-ohmic electrical contacts to CNTs.

Both problems are illustrated in the SEM images of Fig. 2.3. The red arrow in Fig. 2.3(a,left) points out polymer residues next to a metallic Pd strip processed with a standard EBL recipe based on PMMA and lift-off in warm acetone. We identify the polymer residues by the smaller SEM contrast, and because they are selectively removed in a 30 min. long UV ozone (UVO) cleaning [Fig. 2.3(a,right)]. Remaining resist residues after exposure and development or even after lift-off both in the exposed and unexposed resist areas are a well-known issue not specific to CNT devices [115–117]. Typically, one finds $\sim 0.5 - 3$ nm thick resist residues even for overexposed areas after development and lift-off in a standard PMMA processing scheme [115, 116], which clearly hinder or decrease the contact yield to CNTs. Thus great efforts have already been undertaken to find efficient resist removers [117], whereas in semiconductor device fabrication the more important remaining residues in exposed areas are typically removed before the next metal deposition by standard cleaning procedures like oxygen plasma etching or Ar sputtering. However, most of these procedures also remove or damage the CNT part of a

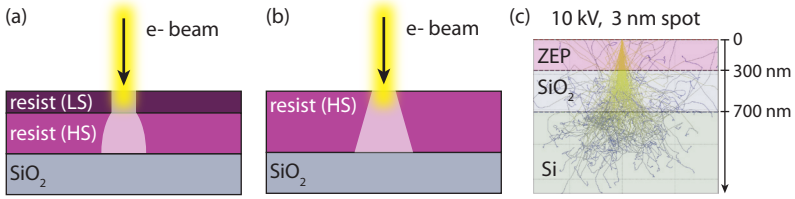

Figure 2.4.: (a) Conventional bilayer resist system to create an under-cut, consisting of a resist with low sensitivity (LS) on top of a highly sensitive (HS) resist. (b) Under-cut achieved in a highly sensitive single layer resist at low e-beam acceleration voltage. (c) Monte-Carlo simulation of electron scattering in a Si/SiO_2(400 nm)/ZEP(300 nm) system at 10 kV e-beam acceleration voltage, calculated with the freely available software CASINO, Université de Sherbrooke.

device and are thus not suitable for carbon-based electronics. Figure 2.3(b,i) shows a tilted side view of a 600 nm thick PMMA mask of a strip after lithography and thermal Py deposition, obtained by dipping a sample into liquid nitrogen and by an instantaneous cleaving. The Py strip forms at the bottom of the polymer trench. However, due to the large beam acceleration voltage of 30 kV used for this structure, the polymer trench is V-shaped with a thin metal film deposited also on the side walls, which often leads to a bad lift-off and large ferromagnetic residues. Subfigure (ii) shows a top view of the resulting Py strip, again demonstrating resist residues (red arrow). While the strip appears well defined, we reproducibly find a large number of Py nanoparticles on top and around the strip, as indicated by the white arrow. Such particles can be magnetic with very large characteristic fields, and can possibly alter the device characteristics [114].

To reduce the number of metallic particles and improve the lift-off, it is desirable to optimize the resist profile, creating a so-called under-cut [94]. Fig. 2.4(a) illustrates the commonly used approach of a bilayer resist system: A thin, less sensitive resist top layer acts as a mask for evaporation and determines the resolution, while a bottom, more sensitive (often lower molecular weight) resist layer is thus overexposed and creates an under-cut. Even more beneficial, one can use a simpler single resist scheme by exploiting the scattering profiles created by low-energy electrons [94]. With a reduced SEM acceleration voltage, the penetration depth of electrons is lowered so that the widening of the e-beam due to forward scattering becomes already significant in the resist. This is demonstrated in Fig. 2.4(c) in a Monte-Carlo simulation for a 300 nm resist layer on a Si/SiO_2 substrate for an acceleration voltage of 10 kV only, where most of the electrons scatter or loose their energy close to the resist/SiO_2 interface. By using a very sensitive e-beam resist, one can thus directly map the electron scattering profile to the resist. This also results in a

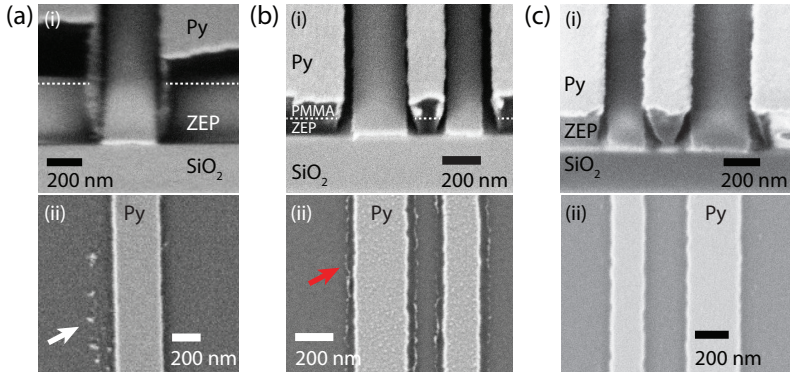

Figure 2.5.: SEM images of (i) cross sections of the metallized strip structures, and (ii) top view of Py strips after the lift-off process. The Py strips were fabricated by thermal evaporation of Py and exposing a (a) 300 nm thick ZEP layer with 20 kV acceleration voltage, (b) 100 nm PMMA (50k)/200 nm ZEP bilayer with 20 kV acceleration voltage, and (c) 300 nm thick ZEP layer with 10 kV acceleration voltage. Red arrows point out polymer residues, white arrows metallic particles.

tunable undercut, which is shown schematically in Fig. 2.4(b).

Finally, to minimize polymer residues in exposed areas, one can increase the exposure dose to larger values [94]. This results in smaller polymer fragments which can be more easily dissolved [94, 118], achievable also by choosing a more sensitive bottom resist in the bilayer system. On the other hand, one can also choose an appropriate resist system and optimize the involved solvent chemistry [119]. For both concepts, especially the previously introduced copolymer ZEP resist is an obvious choice due to its low surface adhesion, low molecular-weight, low clearing-dose and the extremely high sensitivity [120].

To minimize resist residues, improve the electrical contact yield to CNTs, and achieve desirable lift-off results, we have systematically investigated different resist systems and varying e-beam acceleration voltages by SEM imaging. We have tested the bilayer resist systems PMMA/MA (MA: methacrylic acid), PMMA(950k)/PMMA(50k) with different molecular weights, PMMA(50k)/ ZEP and ZEP resist and PMMA(950k) as single layer resist. Figure 2.5(a) and (b) show two examples of this study. While we do not find any disturbing resist residues close to a Py strip fabricated with ZEP alone and 20 kV acceleration voltage, the rather straight resist profile still generates metallic particles close to the strip (white arrows). In contrast, the PMMA(50k)/ZEP bilayer system results in a perfect under-cut and lift-off, but organic residues (removable by UVO cleaning) appear due to the involved PMMA(50k) layer. We find that all resist systems can be optimized to obtain better undercuts

and a significantly reduced number of Py particles on the surface. From this finding we conclude that the particles form at the side walls of V-shaped profiles, which is therefore an essentially geometric effect and independent of the polymer. We however reproducibly find polymer residues (removable by UVO cleaning) for resist systems with a PMMA component, with methyl isobutyl ketone (MIBK) and IPA (1:3) as developer and lift-off in warm acetone. A close to ideal polymer mask cross section and negligible residues can be obtained using the copolymer resist ZEP alone, at 10 kV electron acceleration voltage, and 60 s development in n-amylacetate, stopped in a 9:1 solution of MIBK and IPA, followed by rinsing in IPA. After the metallization, a good lift-off is achieved in a 15 min. NMP bath at 70°C, followed by 30 min. in acetone at 50°C and rinsing in IPA. We use a 300 nm thick ZEP layer, and a typical dose of $\sim 34\,\mu C/cm^2$ at 10 kV acceleration voltage, for which we obtain undercuts with a narrow opening at the top of the polymer film, as demonstrated in Fig. 2.5(c,i). This undercut can be tuned systematically by the dose and acceleration voltage. Subfigure (ii) shows resulting Py strips obtained by thermal Py evaporation. We find no metallic particles or metal flakes and could not detect[4] any resist residues. While the former is due to the optimal polymer mask cross-section, the latter probably originates from ZEP's extremely low clearing dose and the intended resist overexposure at the ZEP/SiO_2 interface at 10 kV acceleration voltage.

The in this thesis developed, essentially residue-free ZEP-based electron beam lithography with optimal polymer mask cross sections [Fig. 2.5(c)] marked a breakthrough. While ZEP resist has been used in EBL for many years, its potential use for CNT devices had to our knowledge not been studied in detail. Using this recipe, we obtained a significantly and reproducibly increased yield of low-ohmic electrical contacts to CNTs for both ferromagnetic and superconducting contact materials compared to fabrication recipes based on PMMA. Further, the improved metal-CNT interface leads to a considerably improved electrical stability of the devices, allowing e.g. for the observation of more stable and reproducible QD spin-valve signals presented in Chap. 11. We also observed reproducibly large and clean superconducting transport gaps in devices with superconducting contacts (Chap. 4), which we also ascribe to cleaner interfaces. While this claim can be justified with the results presented in later chapters, we support the above statement of a higher contact yield by plotting a complete RT device resistance statistics obtained over the course of this PhD thesis in Fig. 2.6. In this statistics, we included all investigated contact materials for the used bottom resist layers PMMA and ZEP. Of the $\gtrsim 500$ conventional CNT devices fabricated, only the devices and sample batches

[4] While we used only SEM imaging in this initial study, later atomic force microscopy images confirmed an extremely low substrate surface roughness ($\lesssim 0.3$ nm) after several ZEP-based processing steps, and negligible resist residues in structured areas. An example is discussed in Sec. 8.1.

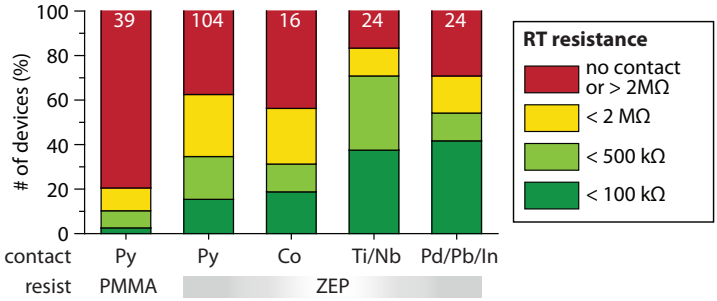

Figure 2.6.: Normalized RT device resistance statistics over the course of this PhD thesis, for the investigated contact materials Py, Co, Ti/Nb, Pd/Pb/In and the different bottom resist layers PMMA or ZEP. The white number on top of the stacked columns denotes the number of devices included in this statistics.

where nothing obvious went wrong were considered, i.e. no EBL errors, a CNT was below the source-drain contacts, only optimized contact materials were used, etc. The measured RT resistances, for semiconducting CNT devices in the 'ON' state of the CNT transistor, were classified into 4 categories to distinguish between no contact ($> 2\,\mathrm{M\Omega}$), high-ohmic ($< 2\,\mathrm{M\Omega}$) and low-ohmic ($< 500\,\mathrm{k\Omega}$ and $< 100\,\mathrm{k\Omega}$ for finer distinction) devices and plotted as normalized, stacked column diagram in Fig. 2.6. For the contact material Py, we can indeed confirm a significantly increased and very useful contact yield of low-ohmic devices for the developed ZEP EBL recipe compared to PMMA resist. Further, for the ferromagnetic material Co a similar yield can be achieved, proving that reproducible contacts can be obtained also with other materials, and emphasizing clean interfaces as most important factor for low CNT device resistances. For the superconducting contacts and junctions Pd/Pb/In-CNT-Pd and Ti/Nb-CNT-Ti/Au even better contact yields could be achieved, corroborating that low-ohmic ferromagnetic contacts are the most difficult to achieve in CNT devices compared to superconducting and normal contacts. Finally, the presented residue-free lithography has become a standard in our group, and has already been successfully applied for graphene spin-valve devices [121], or to achieve clean CNT QDs on hexagonal boron nitride (hBN) as a substrate [122].

2.2.2. Selective hydrogen radical etching of CNTs

While the previous section focussed on minimizing resist residues at the CNT-metal interface by optimizing e-beam lithography, a cleaning method that allows to selectively remove organic residues without damaging the underly-

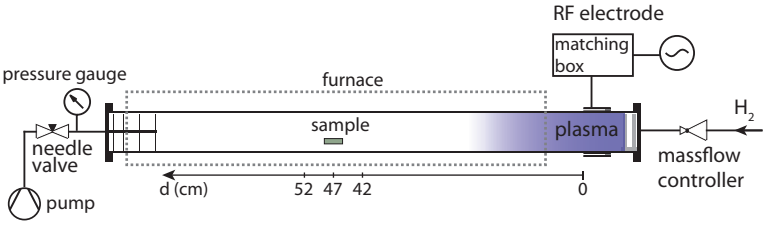

Figure 2.7.: Schematic of the set-up for hydrogen radical etching. An RF generator creates a hydrogen plasma with a capacitively coupled RF electrode inside a vacuum CVD reactor built from a quartz tube. The encircling furnace, a mass-flow controller, needle-valve, pressure gauge and matching box allow to precisely control the process temperature, H_2 flow, pressure and the applied RF power. The sample is placed downstream in the reactor at typical distances $d = 42 - 52\,\mathrm{cm}$ from the RF electrode, far away from the extension of the plasma column. Adapated from Ref. [128].

ing CNTs would also be highly desirable. Recently, it was suggested that catalytically generated atomic hydrogen or hydrogen radicals remove organic resist residues very effectively without damaging an intact underlying graphene lattice [123]. This results in atomically clean graphene, as demonstrated by low-energy electron transmission microscopy [123]. Another series of previous experiments have shown that hydrogen radicals also selectively and anisotropically etch carbon atoms with dangling bonds in the graphene basal plane, i.e. at defect sites, while the intact graphene lattice remains pristine [124–128]. Thus, hydrogen radicals are a potential candidate for a selective cleaning of organic resist residues, and also to selectively etch CNTs with a lattice defect. Following and in close collaboration with J. Schindele [78], we analyzed the effects of hydrogen radicals on CNTs and organic resists with respect to a selective cleaning and etching of CNTs.

Hydrogen (H) radicals are generated with a hydrogen plasma. The plasma is ignited by applying a radiofrequency (RF) signal (power 30 W) with a frequency of 13.56 MHz to the capacitor electrode of a CVD reactor setup, in which a low-pressure hydrogen atmosphere is maintained. This is shown schematically in Fig. 2.7. We use a controlled H_2 flow rate of 20 sccm and a pressure of $p \sim 1.2\,\mathrm{mbar}$, allowing to maintain a stable H_2-plasma [127, 128]. The sample is placed far away from the RF electrode and the extension of the plasma column, which can be roughly estimated by the characteristic glow due to the recombination of high-energetic ions and electrons, typically at a distance of $d = 42 - 52\,\mathrm{cm}$ [127, 128]. At this position, high-energetic hydrogen ions have already recombined, while the H_2 flow is still enriched with low-energetic H radicals due to their different recombination rates [127, 128]. This allows for a selective, chemical etching with H radicals and avoids structural damage of the CNTs by high-energetic ions. Etching rates and the ratio

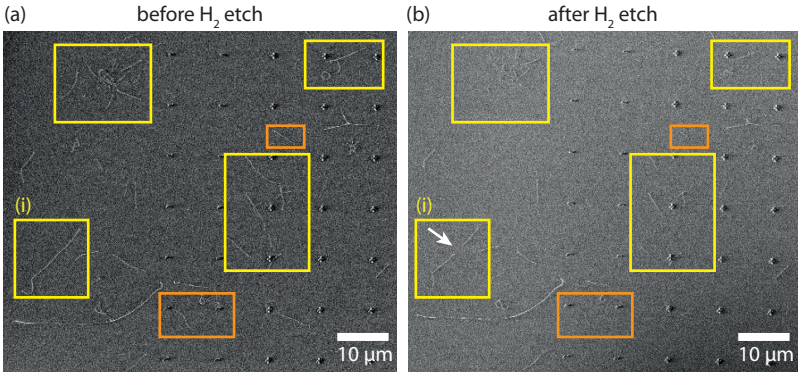

Figure 2.8.: SEM images of CVD-grown CNTs on SiO_2 with a marker-grid (a) before and (b) after a 30 min. long hydrogen radical treatment at $T = 350°C$, for a H_2 flow of 20 sccm, pressure $p = 1.2$ mbar, RF power 30 W and at a sample distance $d = 52$ cm. CNTs are either completely etched away (orange rectangles), others are partially removed (yellow rectangles) and some CNTs are inert to the treatment. The label (i) marks a case where the CNT etching started in the middle of the CNT (white arrow).

of H radicals to high energetic ions can be tuned by changing the sample position relative to the RF electrode. For details we refer to Refs. [127, 128], whose authors developed and studied the home-built plasma etching setup for a selective graphene etching.

We analyze first the influence of H radicals on CVD-grown CNTs, prepared on a SiO_2 substrate with a pre-patterned Ti/Au marker grid. Figure 2.8 shows SEM images of the same CNT sample before and after a 30 min. long hydrogen radical treatment at $T = 350°C$ under the previously mentioned conditions. Similar to Ref. [78], we find that a large portion ($\sim 30\,\%$) of the CNTs is etched away. Generally, a few CNTs are inert to the hydrogen radical treatment within the processing time, some CNTs are partially etched (yellow rectangles), while others are (nearly) completely removed (orange rectangles). Interestingly, one often finds partially etched CNTs where the etching took place in the middle of the CNT, indicated for example with a white arrow in Fig. 2.8(b) for the partially etched CNT (i). This suggests a selective etching mechanism, starting e.g. at defect sites in the CNT. As already mentioned, recent experiments for a similar treatment of graphene have found that hydrogen radicals selectively and anisotropically etch only carbon atoms with dangling bonds in the graphene basal plane, i.e. at defect sites, or at the edges, while the intact graphene lattice remains pristine [124–128]. Most strikingly, this selective etching results in hexagonal hole patterns around an initial defect site, which was attributed to the following etching mechanism [124–128]: H radicals usually lack the required activation energy of 1.2 eV to break the strong C-C

bonds of a pristine graphene lattice. At defects sites or the graphene edge, however, two H radicals can bind to a carbon atom with an unpaired valence electron, a so-called dangling bond – one directly to the unsaturated bond and the other by breaking the weak π-bond to the neighboring C atoms. Thus, the two weakened, remaining C-C bonds can be broken by two further H radicals under removal of the carbon atom as CH_4 molecule. Because two more carbon atoms with an unsaturated bond are hence created, a chain etching reaction sets in around the position of the initial defect site, thus creating a selective and anisotropic etching effect. While we cannot make definite statements due to the lack of an atomically resolved systematic etching study, the observed etching in the middle of CNTs at least suggests a very similar etching mechanism. The etching probably starts at defect sites with dangling bonds in the CNT or at the CNT ends under decomposition to methane – the inverse process of a CNT CVD growth mechanism. The discussed selective H radical etching might hence serve to select defect-free, pristine CNTs for further processing.

Second, we briefly discuss the suitability of the H-radical etching to remove organic polymer residues, e.g. after development to improve the CNT-metal interface for the following metallization. To test this assumption, we measured the etch rates of ZEP and PMMA resist layers exposed to H radicals under the same conditions. We found etch rates of 2 nm/min. for ZEP and 7 nm/min. for an etching temperature of $T = 110°C$ only under application of an RF power, in agreement with Ref. [78]. At higher temperatures, the resist masks melt and decompose even without an RF power applied, while at room temperature no significant etching is observed [78]. This in principle demonstrates the prospect of H radicals for a selective removal of organic polymer residues after development, leaving CNTs previously inert to a first etching process (e.g. to pre-select defect-free CNTs) still intact in a second etching process (to remove resist residues). Nevertheless, we found that a H radical etching after development severely widens and changes the resist mask structures, especially for the optimized one-layer ZEP EBL, and leads to undesirable lift-off results, counteracting the previous efforts of Sec. 2.2.1. Further, in the previous study of Ref. [78] for a PMMA resist system, this H radical residue removal step did not result in reproducible contact properties, and in only a very low yield of superconductivity related transport features. We therefore chose to omit such a H-radical based residue removal step after development, and rather relied on the optimized ZEP EBL discussed in the previous section.

In conclusion, a selective H radical etching step after the CVD growth of CNTs serves most likely to select clean, low-defect CNTs for further processing, even if it is not entirely transparent which factors determine a CNT to remain pristine in the etching. A previous study has already demonstrated a largely increased yield of four-fold shell-filling patterns in transport spectroscopy on CNT QDs, when pristine CNTs are pre-selected in such a way [78]. Four-

fold shell filling patterns are usually ascribed to clean, defect-free CNT QDs on high-quality tubes, thus supporting the above claim. Additionally, such a pre-selection etching step also cleans the surface of a wafer from organic residues, as e.g. amorphous carbon generated during CVD growth. After the etching, samples are annealed for 60 min. in vacuum at $T = 350°\mathrm{C}$ to exclude any possible effects due to a hydrogenation of CNTs, i.e. to dehydrogenate the CNTs [129]. We have employed the above CNT H radical etching step to pre-select inert CNTs for all devices with superconducting contacts presented in this thesis. We also found stable, regular and often four-fold shell filling patterns of the studied CNT QD devices, further corroborating the discussed etching mechanism. In our devices, we reproducibly found signatures of superconductivity, i.e. large superconducting transport gaps (see Chap. 4). We rather ascribe this to the improved metal-CNT interfaces with the employed optimized ZEP EBL, also because in Ref. [78] only a low yield of superconducting transport features was found for H radical pre-selected and cleaned CNTs in a PMMA based EBL process.

2.2.3. Partially suspended CNTs with bottom-gate defined QDs

The clean and stable, disorder-free CNT QDs found in devices fabricated by ultra-clean techniques are commonly attributed to the pristine character of the CNTs, i.e. that CNTs were never exposed to any chemical processing, and to the free CNT suspension between the contacts. Jung *et al.* [102] however found that ultra-clean CNT QD devices of remarkable quality – comparable to the best devices reported so far – can also be obtained with a conventional EBL post-processing step after the CNT growth, when an elaborate electrostatic bottom gating scheme is applied. The central idea behind these findings is sketched in Fig. 2.9(a): A recessed bottomgate and backgate allow to define a single QD in a partially suspended narrow-band gap or semiconducting CNT by electrostatic gating, in contrast to the previously discussed, contact-defined QDs. By applying e.g. a negative gate voltage on the backgate and a positive voltage to the bottomgate, the conduction (CB) and valence band (VB) of the CNT are locally pulled down below the Fermi energy E_F, until an n-type QD forms in the confinement potential of a p*-n-p* junction, where p* (n) denotes the doping of the CNT on substrate (or the suspended part). The so-defined tunnel barrier is a function of the CNT's band gap and the electrostatic confinement potential. Jung *et al.* could form extremely small QDs using multiple gates and normal metal Ti/Au contacts, and observed a transition from Fabry-Perot interferences (open regime, ballistic transport) to ultra-clean single, double and triple QDs of unprecedented quality. The devices are characterized by large charging energies and level spacing due to the small dot size. This probably accounts for the ultra-clean behavior, making the devices immune to remaining small energy-scale disorder potentials

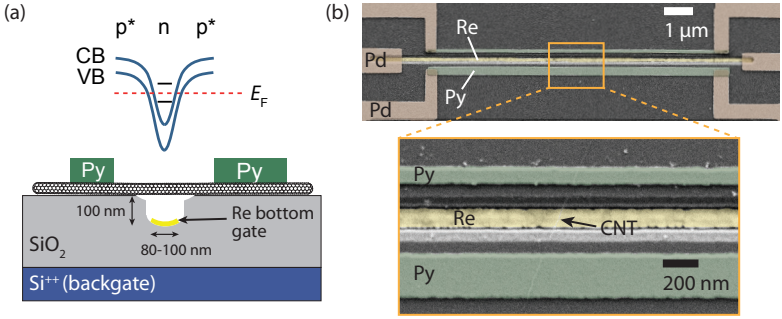

Figure 2.9.: (a) Schematic of a partially suspended CNT device with ferromagnetic Py source-drain contacts (green) and a recessed Re bottomgate (yellow) in the SiO_2 substrate. A QD can be formed for a narrow bandgap or semiconducting CNT by electrostatic gating with two gates as depicted in the energy diagram, i.e. as p*-n-p* junction where p* (n) denotes the doping of the (suspended) CNT, CB (VB) the conductance (valence) band, and E_F the Fermi energy. Adapted from Ref. [102]. (b) SEM image of a partially suspended CNT device with a recessed Re bottomgate (yellow), ferromagnetic Py contacts (green) and Pd leads (brown).

caused e.g. by resist residues [102]. The relatively straightforward inclusion of ferromagnetic or superconducting contacts instead of normal contacts by conventional e-beam lithography, and a possible control over the device tunnel barriers, makes this fabrication approach a potential candidate to realize ultra-clean S-QD or F-QD hybrid devices.

Following the fabrication recipes of Ref. [102], we thus adapted the fabrication scheme for the inclusion of ferromagnetic contacts, shown schematically in Fig. 2.9(a). After the EBL patterning of narrow bottomgate structures and markers into a 250 nm thick PMMA resist mask, $\sim$ 100 nm deep and wide trenches are etched into the SiO_2 substrate as described in the following. Here, one has to explicitly rely on PMMA as resist, because ZEP's poor surface adhesion renders the following steps impossible. Using the resist as a mask, first an anisotropic reactive ion etching (RIE) with CF_4 generates $\sim$ 70 nm deep and wide trenches in the SiO_2. A subsequent isotropic wet etch step in buffered hydrofluoric acid (BHF) creates an undercut below the resist in the SiO_2 to ease the later lift-off procedure and deepens/widens the trenches further. 35 nm of rhenium (Re) is sputtered into the trenches for the bottomgates, again using the initial resist as mask. Re has proven especially useful for this purpose due to its compatibility with a CNT CVD-growth at $T = 850 - 950°C$ [102], originating from its extremely high melting point. With a standard lift-off process, one obtains a substrate with markers and $\sim$ 100 nm wide, recessed Re bottomgates [Fig. 2.9(a) and (b)]. CNTs are then grown randomly over the bottomgate trenches and suitable CNTs are located

by SEM imaging. Finally, using the optimized EBL process based on ZEP resist, ferromagnetic Py source-drain contacts to the CNT and Pd leads are structured. Fig. 2.9(b) shows an SEM image of such a device with a CNT partially suspended over a recessed Re bottomgate. We find similar contact yields and RT resistances than discussed earlier for ZEP, and the results of experiments on these devices are summarized in Chap. 12.

For a sharper confinement potential and to avoid occasionally occurring electrical shorts between the Re and the CNT, more narrow gates and trenches with an increased aspect ratio depth-to-width are desirable. This can be achieved with a cold development of PMMA at $T = 0 - 5°\mathrm{C}$. Typically, resolution in a resist is not limited by the spot size of the e-beam ($\sim 1\,\mathrm{nm}$), but rather due to the electron scattering in the resist and the development sensitivity [94]. As one decreases the development temperature, the development sensitivity is increased and only strongly exposed resist regions with small chain fragments are dissolved, effectively increasing EBL resolution [94]. Using cold development and 20 kV acceleration voltage, one easily achieves a reduced 25 nm-linewidth with an aspect ratio of 1:10 in a 250 nm thick resist after development, while commonly a 1:5 ratio is achieved in RT development. This can be advantageously used for the fabrication of narrow gate structures. Here, we obtain roughly $\sim 50 - 80\,\mathrm{nm}$ wide Re bottomgates due to the widening of the resist mask in the etching process.

2.2.4. Fork stamping of pristine CNTs onto arbitrary contact materials[5]

In this fabrication approach, we try to merge an ultra-clean fabrication scheme with arbitrary contact materials including superconductors or ferromagnets, suspending a pristine, as-grown CNT over the predefined contacts in the last fabrication step. We choose an approach based on the mechanical transfer of the CNT [98–101, 104] termed fork stamping [99, 104]. Compared to a final CNT growth process directly on predefined electrode structures [70, 75, 97], we are not limited to temperature-resistant materials because the CNT growth is performed independently from the actual device structure on a separate 'transfer chip' [101]. This key advantage of fork stamping allows us to process the actual device structure on the 'electrical circuit chip' [101] with arbitrary electrode materials - including temperature sensitive superconductors and ferromagnets - similar to standard devices on substrate. Because the transfer can be optically monitored and controlled, it allows a precise alignment and deterministic transfer of individual CNTs [99], in contrast to the more direct approach of Ref. [103]. To demonstrate our technique, we describe the fabrication of a spin-valve structure with ferromagnetic Py electrodes. We show

[5] Parts of this chapter have been published in similar form in Ref. [130].

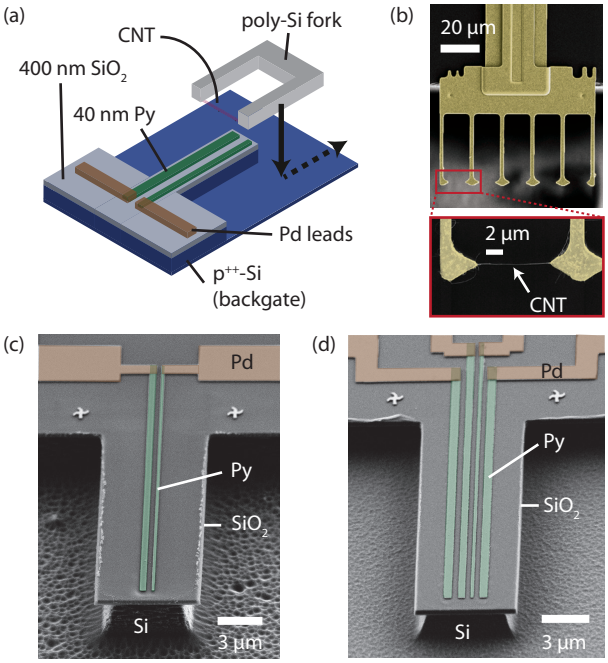

Figure 2.10.: Principle of fork stamping and individual components for the dry transfer. (a) Schematic of the sample layout and CNT transfer onto the electrical circuit chip with mesa structure. (b) False color SEM image of a moveable poly-Si fork (yellow) at the edge of the transfer chip. Individual CNTs are grown across the arms of the fork (zoom-in). (c, d) Tilted SEM images of electrical circuit chips with 6.8 μm wide, 3 μm high SiO_2/Si mesa structure, 40 nm thick ferromagnetic Py electrodes (light green) and connecting Pd leads (brown). The 4-terminal structure allows to electrically cut CNTs between the outer electrode pairs in the pushed-down state of the poly-Si fork.

that single CNTs can be mechanically transferred on top of ferromagnetic contacts, obtaining contact resistances comparable to values published in the literature. This allows magnetoresistance measurements in the QD regime at low temperatures, which we will discuss in Chap. 12.

Figure 2.10(a) summarizes the dry transfer of pristine CNTs onto prefabricated 'electrical circuit chips'. Following Refs. [98–101], the electrical circuit preparation is detached from the growth of the CNTs, done separately on a 'transfer chip'. We transfer the CNTs only in the last fabrication step under a light microscope and ambient conditions in a process called fork stamping, which allows the precise placement of a single CNT onto a suited, predefined electrical circuit [99, 104]. Figure 2.10(c) shows our electrical circuit chip

consisting of a mesa structure with two ferromagnetic Py source-drain (SD) electrodes, a heavily p-doped Silicon (Si) wafer acting as backgate and Palladium (Pd) leads. As schematically depicted in Fig. 2.10(a), a moveable Si fork structure, with ideally a single CNT grown across it, is pushed down on the predefined mesa structure (black arrow) while at the same time monitoring the current through the ferromagnetic SD contacts. Once contact has been detected and established, the fork is retracted (dashed arrow), ideally leaving an individual pristine CNT suspended over the ferromagnetic contacts. To immediately characterize the CNT device, we measure the differential conductance G as a function of the backgate voltage. Undesired CNTs can then be removed by applying large SD bias voltages and the stamping procedure is repeated until an optimal CNT is found.

This work was done in a close collaboration with M. Muoth (C. Hierold group, ETH Zurich), who provided us with the pre-grown CNTs on the elaborate fork structures, and with general guidance for the CNT transfer technique at the micro-manipulator set-up of ETH Zurich during the initial phase of this project. All other steps, particurlarly the development of a suitable electrical circuit chip structure, but also the transfer of the CNTs in the FIRST cleanroom of ETH Zurich in the later phase of the project, were then carried out by the author. We now discuss in some detail the individual fabrication steps.

CNT growth on optimized transfer chip with retractable poly-Si forks CNTs are grown separately from the electrical circuit on a transfer chip with polycrystalline Si fork structures, following previously reported protocols [99, 131]. Figure 2.10(b) shows an SEM image of such a fork structure protruding beyond the edge of the transfer chip. Each fork consists of multiple, 2 μm wide, 1.5 μm thick poly-Si arms and can be retracted beyond the wafer edge, allowing to use different forks on the same transfer chip in one transfer session. CNTs are grown via CVD across the 8 μm wide gaps between the fork arms by using iron-loaded ferritin proteins as catalyst precursors [131, 132]. At best, one obtains maximally one individual CNT spanning each gap between the fork arms as visible in the zoom-in SEM image of Fig. 2.10(b), for which the catalyst concentration has to be optimized on reference forks [99]. Electron microscopy is omitted on the actual transfer chips to avoid carbon deposition, and to maintain the pristine, as-grown character of the transferred CNTs.

Fabrication of mesa structure and electrodes on electrical circuit chip The electrical circuit chip with the mesa structure and the ferromagnetic contacts is fabricated independently of the transfer chip in a five-step EBL process (Fig. 2.11). After the deposition of Au markers on the p-doped Si/SiO_2 substrate acting as a backgate, two 20 μm long, 40 nm thin ferromagnetic Py electrodes of variable width are patterned with a pitch of 400 nm by the previously

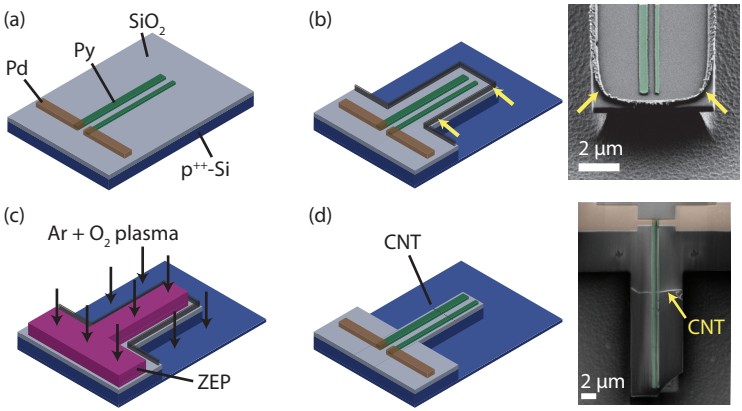

Figure 2.11.: Schematic of the mesa fabrication workflow. (a) 40 nm thick, 160/380 nm wide ferromagnetic Py electrodes with connecting Pd leads are prepatterned in two consecutive EBL steps on a Si/SiO_2 wafer. (b) After the CHF_3/SF_6 mesa etching process and the removal of the PMMA resist mask, hard carbon-fluor polymer residues remain near the resulting mesa edge (arrows in the sketch and SEM image). (c) These undesired etching residues can be completely removed by Ar/O_2 plasma etching, where a patterned ZEP resist mask on the mesa structure exposes only areas with residues to the plasma. (d) Finished device (schematic and SEM image) after CNT transfer and electrical measurements.

discussed ZEP EBL and connected by 50 nm thick Pd leads (3 EBL steps). This results in the spin-valve device geometry shown in Fig. 2.11(a), where the 160 nm and 380 nm wide Py strips allow for well separated switching fields of the electrodes (see Chap. 10 and Part II). For creating the mesa structure in the SiO_2/Si, we first spin-coat a 1.2 μm thick PMMA(950k) resist layer as etching mask. This resist is exposed and developed by EBL, leaving the mesa structure and Py electrodes protected. For etching into the SiO_2/Si around the mesa structure, we use an optimized, anisotropic and selective reactive ion etching (RIE) process [133], resulting in a T-shaped etch profile [compare Fig. 2.10(c)]. A CHF_3 RIE etching is used for the removal of the 400 nm thick SiO_2 layer, while a subsequent anisotropic and very selective SF_6/O_2 RIE process creates a 3 μm deep trench in the p-doped Si. The anisotropic profile stems from a Si sidewall passivation by oxygen species during the etching process [133], which also leads to the observed porous structure in the Si. Before resist removal, the remaining resist mask is typically etched down to a thickness of 300 nm in an Ar/O_2 RIE step to minimize residues from the etch process. After the resist removal procedure in warm NMP or acetone, we typically encounter large carbon-fluor polymer residues close to the edge of the mesa structure [arrows in Fig. 2.11(b)], which severely hinder a successful CNT transfer. These residues originate from polymerization and passivation layers

formed in the CHF_3/SF_6 RIE etching on the side of the resist mask [134] and are not removable by the solvents in the resist removal process. We found that the selectivity of the etch process (Si/SiO_2 relative to resist) is optimal only in a narrow parameter range and cannot be optimized simultaneously to protect the mesa without residues. Sonication to remove the residues mechanically, as used in Ref. [104], typically leads to a partial collapse of the mesa structure and affects the sensitive Py strips. We remove these polymer residues using a 5th EBL step: Spincoating another 450 nm thick ZEP520A resist layer on the wafer covers the entire mesa structure with the Py strips and the residues. We now only expose and develop areas close to the edge of the mesa structure, resulting in a mask open only in the area of the residues, as sketched in Fig. 2.11(c). The residues can thus be reproducibly removed in a standard Ar/O_2 plasma without exposing the Py strips to O_2 plasma. After another resist removal procedure this results in clean, 6.8 μm wide and 3 μm high mesa structures etched into the SiO_2/Si substrate, which allow access for the CNT fork stamping. Figure 2.10(c) and (d) show two different realized geometries, one with two ferromagnetic contact electrodes, the other with four. While in the first geometry only a mechanical transfer of the CNTs can be implemented, the 4-terminal geometry can also be used for an electrical cutting of the CNT described in detail later, or, alternatively, for non-local spin experiments similar to graphene [135]. The comparatively wide mesa relative to the 8 μm fork gap improves the CNT transfer, while the T-shaped underetched mesa profile is beneficial for avoiding CNT-induced electrical shorts from the contacts to the p-doped backgate. To monitor the current through the SD contacts during CNT transfer, all electrical circuit chips are glued into chip carriers and wire-bonded prior to the transfer of CNTs. Figure 2.11(d) shows a schematic and SEM image of a device after successful CNT transfer, demonstrating that single CNTs (yellow arrow) can be transferred onto ferromagnetic contacts.

CNT transfer In the final fabrication step, the CNTs are transferred from the fork structures onto the electrical circuit chip [99]. Immediately prior to the CNT transfer, the electrical circuit chips with the ferromagnetic Py electrodes have to be cleaned from surface oxides in a 25 s long Argon plasma etch. This step is crucial, since without it no electrical contact is formed due to contamination and oxidation of the electrodes. The transfer is done using a micro-manipulator setup under ambient conditions. To reduce further oxidation, a nitrogen flow is applied around the electrical circuit chip. The transfer chip - with the CNT forks protruding beyond the edge of the wafer - is carefully mounted on a three axis piezo controlled transfer arm. Next, the forks with CNTs are carefully aligned with the mesa structure using an optical microscope. Finally, the fork is pressed down over the mesa structure and the contacts [black arrow in Fig. 2.10(a)]. Simultaneously, we monitor

the current through two SD terminals in a voltage-biased setup. In contrast to previous experiments with normal Pd or Au electrodes [99, 101, 104], we have to apply relatively large SD voltages of $1 - 3\,\mathrm{V}$ to electrically register every CNT 'touch-down' event when a CNT bridges the SD contacts, carefully studied by SEM on reference samples following the transfer. When a successful contact is detected, there are two ways to deposit the CNT. First, it can be mechanically torn off by keeping the fork pushed down and retracting it parallel to the chip surface using the built-in mechanism, leaving the CNT in place and suspended over the SD contacts due to van-der-Waals forces. Second, in a 4-terminal device [Fig. 2.10(d)], the CNT can be selectively cut between the outer pair of contacts using large electrical currents, following the approach of Ref. [101]. In the pushed-down state of the transfer fork, the application of a large voltage between the two outer pairs of contacts (while maintaining the inner ones on the same potential) breaks the CNT at a single point between each of the two outer contact pairs due to Joule heating (Sec. 1.2) [101]. The transfer fork can then be lifted, leaving only a part of the CNT suspended over the inner contacts. Typical cutting currents for single wall CNTs are on the order of $15 - 25\,\mu\mathrm{A}$, consistent with Ref. [101]. Usually, we obtain RT device resistances of $R_{\mathrm{SD}} \sim 1 - 10\,\mathrm{M\Omega}$ for a single CNT. The contacts can already be annealed during stamping by driving the SD voltage up and down, a process which will be described in the measurements results presented in Chap. 12. In case that the resistance is too low ($R_{\mathrm{SD}} \ll 500\,\mathrm{k\Omega}$) - meaning that bundles or several CNTs were transferred, as inferred from SEM images of reference samples - the CNTs can be removed by applying a large SD bias voltage. In the cutting procedure for the 4-terminal geometry discussed above, this is immediately evident when one observes several steps in the monitored IV-curves or much higher currents than $25\,\mu\mathrm{A}$ are required to cut the CNT. After the removal of undesired CNTs, the electrical circuit chip can be used again for further transfers until an optimal CNT is found. Already during transfer, we observe that stamped CNT devices on ferromagnetic Py contacts degrade to a much higher device resistance on the timescale of a few minutes, often reaching values as high as $100\,\mathrm{M\Omega}$ when the device had an original resistance of $1\,\mathrm{M\Omega}$. This suggests that the surfaces of the Py contacts oxidize fast. The exposure of samples to air between the CNT transfer under nitrogen flow and the mounting of samples in our cryogenic measurement setup is thus reduced to a minimum.

2.3. Cryogenic measurement set-up for transport spectroscopy

Sufficiently low temperatures are required to resolve the electronic and quantum mechanical transport properties of a CNT QD device in transport spectroscopy experiments (including e.g. single-electron tunneling or coherent ef-

fects like Andreev tunneling, see Chap. 6), i.e. the electronic temperature kT_{el} has to be much smaller than important device energy scales as the charging energy $E_{\mathrm{c}} \sim$ few meV, the level spacing $\delta E \sim 1\,\mathrm{meV} \sim 10\,\mathrm{K}$, the life-time broadening $\Gamma \sim 0.1\,\mathrm{meV} \sim 1\,\mathrm{K}$ and for superconducting devices the energy gap $\Delta \sim 0.5\,\mathrm{meV}$ and critical temperature $T_{\mathrm{c}} \sim$ few K. Thus, a functional CNT device is built into a cryogenic measurement set-up for low temperature characterization, depicted schematically in Fig. 2.12. In the course of this PhD thesis, several cryogenic measurement set-ups with base temperatures between 4.2 K to 20 mK have been used. Liquid ^{4}He has a temperature of 4.2 K (at $p = 1\,\mathrm{bar}$) and can be used for directly dipping the sample inside in transport dewars. By evaporative cooling, i.e. pumping on the He bath and the removed latent heat in the phase transition, temperatures of $\sim 1.4 - 1.5\,\mathrm{K}$ can be reached in a ^{4}He cryostat. Similarly, for the scarce ^{3}He isotope with higher vapour pressure and lower boiling point temperatures of $\sim 220\,\mathrm{mK}$ can be achieved in a ^{3}He cryostat. Finally, in so-called dilution refrigerators a mixture of ^{3}He and ^{4}He allows to reach even lower base temperatures, for the used set-ups typically $\sim 20 - 35\,\mathrm{mK}$. A dilution refrigerator makes use of the ^{3}He/^{4}He mixture's spontaneous phase separation into a ^{3}He-rich and a ^{3}He-poor phase below $\sim 870\,\mathrm{mK}$ described in a mixture phase diagram [136]. An elaborate pumping and mixture cycle creates an osmotic pressure difference that constantly drives ^{3}He from the ^{3}He-rich phase to the ^{3}He-poor phase inside the mixing chamber, where the 'evaporation' or dilution of ^{3}He into ^{4}He through the phase boundary generates the cooling power [136]. All cryostat systems are equipped with superconducting magnets, allowing to study transport under large magnetic fields.

To perform measurements, the device chip-carrier in the cryogenic environment is connected via twisted-pair measurement lines to a break-out box at RT and by BNC cables to the measurement electronics. Electron and phonon temperature decouple for low temperatures [136], so that the phonon lattice of the device cooled by the cryostat cannot absorb all heat originating from the heat leak caused by the measurement lines. At low temperatures thermally well-anchored and strongly filtered measurement lines are therefore of crucial importance to shield from (thermal) high frequency radiation from warmer stages of the setup (e.g. $1\,\mathrm{GHz} \sim T = hf/k \approx 50\,\mathrm{mK}$). We typically use a two- to three-stage filter set-up, where the first filter stage are commercial π-filters from Syfer at RT with a cut-off frequency $f \sim 1\,\mathrm{MHz}$. A specifically designed tape-worm filter [137] with a cut-off $f > 10\,\mathrm{MHz}$ is implemented on the cold finger directly above the sample holder. Optionally, in one setup extra π-filters can be added after the 2nd filtering stage. The sample is shielded from thermal radiation by a Faraday cage and further metal shields. With this setup, we typically reach sufficient electronic temperatures of $T_{\mathrm{el}} \sim 100\,\mathrm{mK}$ in the dilution refrigerators.

Figure 2.12 shows a schematic of a typical cryogenic measurement set-up.

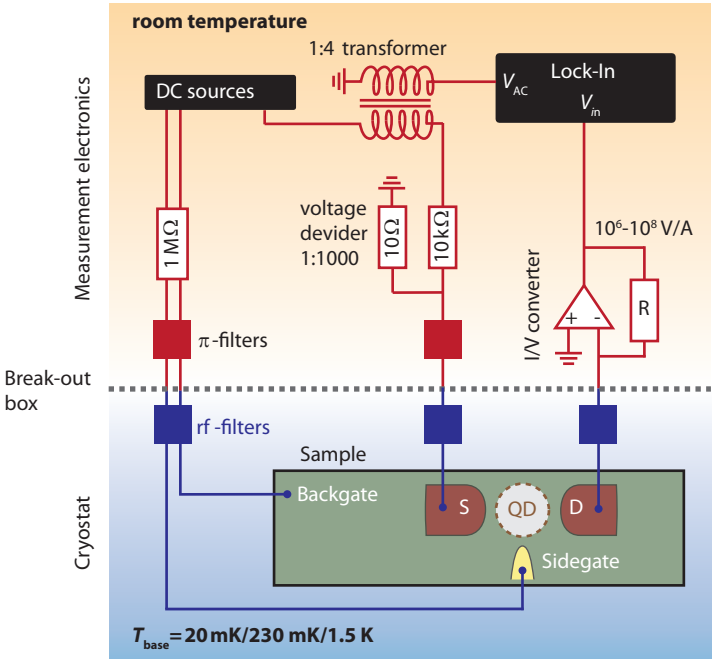

Figure 2.12.: Schematic of a typical set-up for voltage-biased differential conductance measurements at low temperatures using the lock-in technique. Adapted from [58].

Because of the large CNT device impedances, especially in Coulomb blockade, we voltage-bias the devices and measure the current or the conductance using a standard lock-in technique. A small ac excitation bias provided by a lock-in amplifier (*SR830*, Stanford Research Systems) is superimposed on a dc voltage V_{SD} (supplied by a *YK7651*, Yokogawa Electronic Corporation) with a transformer of 1:4 winding ratio and attenuated to the applied ac bias $V_{ac} \sim 10\,\mu V \sim 100\,mK$ at the sample with a 1:1000 voltage divider directly before the π-filter at the break-out box. The frequency of V_{ac} is chosen as high as possible to reduce noise and speed up measurements, typically $f \sim 70-320\,Hz$, and limited depending on the line capacitances and the individual sample impedance. Currents are read out at RT by home-built low-noise current-to-voltage amplifiers (IV-converters) with transimpedances of $10^6/10^7/10^8$ V/A, which also allow to change their offset voltages, useful for applying additional dc bias voltages to a device. Their output voltage is fed back to the phase-locked lock-in amplifier, which allows the direct measurement of the differential conductance $G = dI/dV_{SD} \approx I_{ac}/V_{ac}$. Similarly, a dc measurement setup al-

lows to read out the current directly with a voltage meter (*KY2000*, Keithley Instruments Inc.). Gate voltages are applied and controlled by highly stable low-noise dc voltage sources [*YK7651* or a homebuilt 8-channel low-noise digital to analog voltage source *DAC SP 927*], and a large pre-resistor serves to limit currents in the case of occurring gate leaks. The whole measurement set-up is controlled by RS232 and GPIB interfaces and Labview programs on a computer.

PART I

ANDREEV AND QUASIPARTICLE TRANSPORT IN CNT N-QD-S DEVICES

3

Superconductors coupled to quantum dots

In this chapter, we provide a theoretical basis for the first part of this thesis, in which experiments with superconducting electrodes coupled to CNT QD devices are discussed. We start with a brief introduction into superconductivity, a macroscopic quantum phenomenon, before discussing the relevant transport mechanisms in (mesoscopic) normal metal (N) - superconductor (S) structures (Sec. 3.2). These processes are – on a microscopic level – also responsible for carrying the superconducting proximity effect in mesoscopic systems. In a simple analogy, albeit in a more complex manner, all of the transport mechanisms in metallic N-S structures can also be observed in N-QD-S devices, when a QD is inserted between the two electrodes. This will be treated in detail in Sec. 3.3, where we restrict our discussion to the N-QD-S devices and transport processes relevant for this thesis only, and categorize different dominant transport mechanisms depending on the tunnel coupling strengths of the contacts to the QD.

3.1. Superconductivity

Following partially Refs. [138, 139], we first briefly summarize some basic concepts of superconductivity relevant for this thesis. We rather focus on an intuitive understanding where possible, and refer to the above references for a more detailed review.

Superconductivity – fundamentally seen a coherent quantum many-body phenomenon – can most excitingly be probed at macroscopic length scales due to some of its chief consequences: certain *superconducting materials* or *superconductors*, such as e.g. aluminium, mercury, lead or niobium show an

unmeasurably small, i.e. vanishing electrical resistance below a certain *critical temperature* T_c (typically in the range of a few mK to 10 K for elemental metallic superconductors), which suggests dissipationless currents in the *superconducting state* [139]. A second phenomenon is the perfect diamagnetism or Meissner-Ochsenfeld effect: in the superconducting state, an external magnetic field is expelled from the inside of a superconductor independent of its history, due to induced dissipationless surface (super) currents. This directly implies a certain external *critical magnetic field* $B_c = \mu_0 H_c$, above which a thermodynamic phase transition to the normal state occurs, due to the increased energy cost of the induced supercurrents to expel the magnetic field from the bulk of the superconductor [139]. While these key features of superconductivity could be phenomenologically described by the thermodynamic *Ginzburg-Landau* (GL) theory and the *London equations* [138], a microscopic explanation was only developed in 1957 by Bardeen, Cooper and Schrieffer in the *BCS theory* of superconductivity [140].

This theory is based on Coopers argument that the 'Fermi sea', the fermionic ground state of an electron gas, is unstable against any net attraction between two individual electrons – which can bind the electrons together in a *Cooper pair* obeying bosonic statistics [140]. Such an attractive interaction can be mediated by the phonons of the ion lattice. Intuitively, a moving electron causes a lattice deformation of the positively charged ion cores and effectively creates a retarded positive polarization cloud in its path behind, which in turn attracts a second electron. Crucially, the maximum deformation of the ion lattice is retarded relative to the electrons movement, so that the electron has already moved $\sim v_F T_D = v_F 2\pi/\omega_D \sim 10^6\,\mathrm{m/s} \cdot 10^{-13} s = 100\,\mathrm{nm}$ before the maximum ion displacement is reached, where we used the Fermi velocity v_F and the Debye frequency ω_D to estimate the phonons oscillation period [139]. On this scale, the Coulomb repulsion of the electrons is effectively screened (typically on a few Å) and the interaction hence attractive. Quantum mechanically, one describes this attractive interaction by the exchange of virtual phonons under momentum conservation [138]. The probability of phonon exchange and hence the amount of energy reducing phonon exchange scattering events, i.e. the attractive interaction between electrons, becomes maximal if the two electrons of a Cooper pair have opposite momenta $\mathbf{k_1} = -\mathbf{k_2} = \mathbf{k}$. This implies a symmetric orbital wavefunction, which is the case for conventional (s-wave) superconductors, and a spin singlet state $|\Psi_S\rangle = \frac{1}{\sqrt{2}}(|\uparrow\downarrow\rangle - |\downarrow\uparrow\rangle)$ to obtain the required antisymmetry of the total wavefunction due to Pauli's exclusion principle. Cooper pairs are thus often described by the notation $(\mathbf{k}\uparrow, -\mathbf{k}\downarrow)$, but one has to keep in mind that the electrons of a Cooper pair are maximally spin-entangled. The instability of the 'Fermi sea' in the presence of attractive interactions leads to the formation of a new ground state, where Cooper pairs form until an equilibrium state is reached where further pairing does not lower the energy any more. This *BCS ground state* – described in

the theoretical framework of Ref. [140] – differs enormously from the 'Fermi sea', which has important consequences and implications. First of all, Cooper pairs obey bosonic statistics and can hence condense into a collective macroscopically quantum-coherent ground state. In a GL description, this can be captured by a macroscopic wavefunction of the common Cooper pair ground state $\psi(\mathbf{r}) = \sqrt{\mathcal{N}(\mathbf{r})}e^{i\Phi(\mathbf{r})}$ as an order parameter[1], where $\mathcal{N}(\mathbf{r})$ is the Cooper pair density and $\Phi(\mathbf{r})$ a collective macroscopic phase [138]. Second, the superconducting excitation spectrum is gapped, i.e. a minimum energy of 2Δ is required for elementary excitations of the ground state, i.e. to break up a Cooper pair. We refer to Δ as the *superconducting energy gap*. The coherent excitations differ strongly from simple electronic excitations of a Fermi gas (free electrons), have partially electron and hole character and are hence called *quasiparticles* or *Bogoliubons*. Their dispersion relation is given by

$$E(\mathbf{k}) = \sqrt{\varepsilon(\mathbf{k})^2 + \Delta^2}, \tag{3.1}$$

with the kinetic energy $\varepsilon(\mathbf{k}) = \hbar^2 k^2/2m - E_\mathrm{F}$ of a free electron with respect to the Fermi energy [139]. This dispersion relation has electron ($\varepsilon > 0$) and hole-like ($\varepsilon < 0$) branches, and is hence often plotted in analogy to semiconductor band diagrams for positive (electron-like) and negative (hole-like) excitation energies as depicted in Fig. 3.1(a). Due to the existence of an energy gap, the quasiparticles have only for large kinetic energies $|\varepsilon| \gg \Delta$ free electron (hole) character (dashed lines). Because no states are lost in the phase transition from the normal to the superconducting state ($D_\mathrm{N}(\varepsilon)\mathrm{d}\varepsilon = D_\mathrm{S}(E)\mathrm{d}E$), one can derive the density of states (DOS) $D_\mathrm{S}(E)$ of the quasi-particle spectrum

$$\frac{D_\mathrm{S}(E)}{D_\mathrm{N}(\varepsilon)} = \frac{\mathrm{d}\varepsilon}{\mathrm{d}E} = \begin{cases} \frac{|E|}{\sqrt{E^2-\Delta^2}} & (|E| > \Delta) \\ 0 & (|E| < \Delta) \end{cases}, \tag{3.2}$$

where the normal state DOS $D_\mathrm{N}(\varepsilon)$ is usually assumed to be constant for energies close to the Fermi energy E_F most relevant in transport experiments, i.e. $D_\mathrm{N}(\varepsilon) \approx D_\mathrm{N}(0)$ [139]. This normalized quasiparticle DOS is plotted in Fig. 3.1(b). For $|E| \gg \Delta$ the normal state DOS is recovered, while for $|E| \to \Delta$ the quasiparticle DOS diverges and no quasiparticle states exist for $|E| < \Delta$, where the Cooper pair condensate is located at E_F.

For increasing temperature $T > 0$, quasiparticles are thermally excited and the number of Cooper pairs, directly related to the superconducting order parameter or gap Δ, decreases. Hence, also Δ reduces with increasing temperature and finally vanishes at $T = T_\mathrm{c}$. The temperature evolution of the energy gap can be obtained e.g. from the following approximation of the BCS

[1] It was later shown by Gor'kov, that $\psi(\mathbf{r})$ can be identified with the gap parameter $\Delta(\mathbf{r})$ of the BCS theory [138].

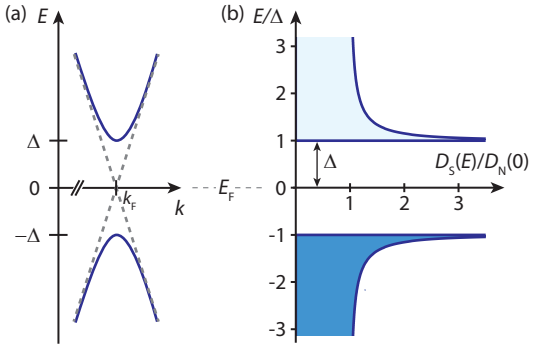

Figure 3.1.: (a) Quasiparticle dispersion relation in the superconducting state (blue solid line) compared to the normal state (dashed lines) close to the Fermi energy, and (b) resulting quasiparticle DOS $D_S(E)/D_N(0)$ in the superconducting state, plotted in a semiconductor representation for positive (electron-like excitations) and negative energies (hole-like excitations). Adapted from Ref. [139].

self-consistency equation [141, 142]

$$\frac{\Delta}{\Delta_0} = \tanh\left(\frac{T_c}{T}\frac{\Delta}{\Delta_0}\right), \tag{3.3}$$

where $\Delta_0 = \Delta(T = 0) \approx 1.764\, kT_c$ for *BCS superconductors* with weak electron-phonon coupling. Another important parameter is the *BCS coherence length* [138]

$$\xi_{(0)} = \frac{\hbar v_F}{\pi \Delta_{(0)}}, \tag{3.4}$$

which can be interpreted as the spatial extent of a Cooper pair $\delta x \sim \hbar/\delta p \sim \hbar p_F/m\delta E \sim \hbar v_F/\Delta$, estimated from the position uncertainty due to an energy uncertainty $\sim \Delta$. Typically, ξ_0 is in a range of a few to a few hundred nanometers, similar to the previous estimation with the retarded ion lattice deformation. Hence, the Cooper pairs will spatially strongly overlap in their collective and coherent many-body ground state, the Cooper pair 'condensate'.

The existence of this coherent Cooper pair ground state and the gapped excitation spectrum finally also account for the vanishing resistance below T_c and the perfect diagmagnetism below B_c. Electrical current in a superconductor is carried by the common motion of Cooper pairs with a center of mass momentum $\mathbf{P}$, where the ground state and particularly its gapped excitation spectrum remain invariant under current flow [139]. Hence, resistance causing scattering events are suppressed due to the existence of a gap Δ, because any change of the common current carrying ground state due to inelastic scattering can only take place by exciting over this gap 2Δ, i.e. by breaking up Cooper pairs. Only when the energy associated with the supercurrent and the Cooper pairs collective center of mass momentum $\mathbf{P}$ reaches 2Δ, Cooper pairs break up and the superconductor is driven to the normal state. Such a *critical current* immediately accounts for the existence of a critical magnetic field B_c,

where the induced supercurrents expelling the external magnetic field from the superconductor reach this critical current value.

3.2. Transport in superconductor/normal metal structures

Coupling a normal metal (N) to a superconductor (S) and studying the transport through such an N-S system rises important questions: How will charge transport occur at the interface between a normal metal, where the current is carried by free electrons (holes), and a superconductor, where Cooper pairs are responsible for a dissipationless supercurrent? We hence briefly discuss the most relevant transport mechanisms in such well-studied N-S structures, which also provide a simple analogy and model picture for the occurring phenomena in the N-QD-S devices of this thesis.

3.2.1. Andreev reflections and proximity effect

Let us first consider a completely transparent N-S interface, and an electron from N impinging on this N-S interface at a subgap energy $|E| < \Delta$ [Fig. 3.2(b)]. At this energy, there are no quasiparticle states available for a transport across the interface, but the electron can also not be normally reflected [Fig. 3.2(a)], because we assumed an ideally transparent interface: The superconductor provides a potential barrier with a maximal height of Δ, and can only exert a momentum $\delta p = \left(\frac{\mathrm{d}p}{\mathrm{d}E}\right)_{p_\mathrm{F}} \delta E = \frac{\Delta}{v_\mathrm{F}}$, orders of magnitude too small to account for a required momentum transfer of $\sim 2p_\mathrm{F}$ for normal reflection [143]. As depicted in Fig. 3.2(b), an *Andreev reflection* process [144] provides the solution to this contradiction: the impinging electron at energy E forms a Cooper pair in S with another electron at energy $-E$ of opposite spin and momentum, under the retro-reflection[2] of a positively charged hole in N due to charge and momentum conservation. Hence, a total charge of 2e is transferred across the interface, which results in twice the conductance value compared to the normal state for energies (or bias voltages) $|E| < \Delta$ and ideally transparent interfaces. Transport across such an N-S interface can be described within the *BTK theory* developed by Blonder, Tinkham and Klapwijk [145]. In this intuitive one-dimensional model, scattering at the N-S interface is captured by a simple delta-distribution potential $V(x) = Z\hbar v_\mathrm{F}\delta(x)$ with a dimensionless barrier strength Z, accounting e.g. for elastic scattering at the interface due to oxide tunnel barriers. A solution of the Bogoliubov-de-Gennes equations [138] for the wave functions by matching the correct boundary conditions allows to derive an expression for the differential conductance G as function of the energy E and barrier strength Z [145]. This is plotted in Fig. 3.2(c) for varying barrier strengths at $T = 0$. As expected, one finds

[2] The reflected hole travels backwards on the path of the incident electron.

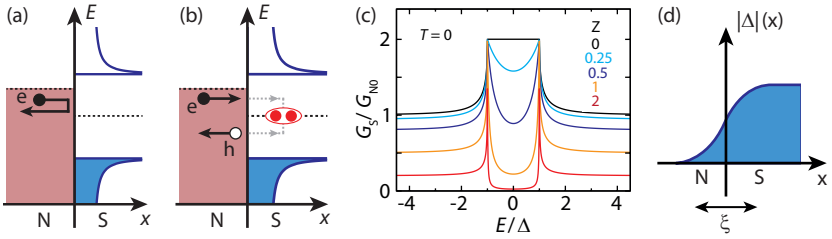

Figure 3.2.: (a,b) Normal reflection (a) for $Z \neq 0$ and Andreev reflection (b) of an incident electron at an N-S interface at $x = 0$, schematically illustrated in an energy-real space diagram with a superconducting ($x > 0$) and a normal metal ($x < 0$) DOS. (c) Differential conductance $G_S(E)$ for an N-S junction according to the BTK model at $T = 0$, for different barrier strengths Z (color coded) and normalized to the conductance G_{N0} in the normal state for $Z = 0$. (d) Qualitatively expected variation of the order parameter $|\Delta(x)|$ across an N-S interface due to the (inverse) proximity effect. Note that it is generally complex to determine the variation of the gap parameter across an arbitrary N-S interface, which usually has to be calculated self-consistently under certain restrictions or approximations.

$G_S = 2G_{N0}$ for $|E| < \Delta$ and $Z = 0$ due to Andreev reflections. In reality always $Z \neq 0$ due to the Fermi velocity mismatch of different materials, and for increasing Z the subgap conductance reduces due to the increased probability of normal reflections [Fig. 3.2(a)], and a 'soft' transport gap starts to appear. For $Z \gg 1$ [cf. $Z = 2$ in Fig. 3.2(c)], Andreev reflection is strongly suppressed for $|E| < \Delta$, and the I-V characteristics represent the quasiparticle DOS in S determining the transport for $|E| > \Delta$. This limit is equivalent to a tunneling spectroscopy experiment in a N-I-S junction, where I denotes a tunnel barrier at the interface.

Already the authors of the BTK theory noticed that the quasiparticle current injected across an ideally transparent N-S interface will be converted to a supercurrent carried by the Cooper pair condensate only on the length scale of the BCS coherence length ξ [145], which forms the microscopic basis of the superconducting *proximity effect*: The density of Cooper pairs does also not change abruptly to zero in N at the N-S interface, but decays continuously in N on a scale $\sim \xi$. In other words, superconducting correlations and Cooper pairs 'leak' into a non-superconducting material in electrical contact with S. Microscopically, this proximity effect is mediated by the phase coherence of the Andreev reflections over a certain distance in N [146, 147]. In the time-reversed version of the previously discussed Andreev reflection process, an incident hole is retro-reflected as an electron under the removal of a Cooper pair from the condensate. Because the Andreev-reflected hole and electron maintain their phase-coherence for a certain time and distance in N, this also corresponds to a finite probability of finding a Cooper pair in N [147]. Macroscopically, the occurrence and decay of superconducting correlations in

the *proximitized* material can be captured by the self-consistently calculated, spatially varying superconducting energy gap $|\Delta(\mathbf{r})|$, the order parameter of the GL theory [138]. This is schematically depicted for an N-S interface in Fig. 3.2(d). Consistently, also a reverse effect takes place: due to the *inverse proximity effect*, the Cooper pair density and energy gap is also reduced in S close to the interface – electrons and holes can enter S before they are converted to a supercurrent on the length scale of $\sim \xi$.

3.2.2. Crossed Andreev reflection and Andreev bound states

In the above discussion, we have so far neglected the fact that Cooper pairs have a spatial extent of $\sim \xi$ also along the interface, and that hence an incident hole can be Andreev-reflected as an electron at a distance $d < \xi$ apart. In multi-terminal devices, e.g. for two normal metal leads attached to S as depicted in Fig. 3.3(a), this can lead to cross-conductances, and the non-local Andreev reflection is then called *crossed Andreev reflection* (CAR). For an incident hole from one normal metal lead, the CAR process corresponds to the splitting of a Cooper pair into two spatially separated leads as shown in Fig. 3.3(a). Due to the phase-coherence of the process, this provides a potential source of spatially separated, but still spin-entangled electrons. Naturally, this triggered a lot of interest, and signatures of CAR were found in metallic N-S-N devices [148–150]. Unfortunately, in metallic structures the competing non-local 'normal' reflection of an incoming electron via a virtual quasiparticle state in S, in analogy to the co-tunneling of QDs called *elastic co-tunneling* (EC), has a similar probability amplitude than CAR which decays exponentially over ξ [151]. This process is depicted in Fig. 3.3(b), and can severely hinder or mask the observation of CAR in purely metallic structures.

There also exists an intimate connection between the superconducting proximity effect in *mesoscopic* systems and Andreev reflections [153]. This connection can be most intuitively described in S-N-S systems, and refines the picture and the link to the more macroscopic view of the proximity effect provided earlier. Let us first consider a mesoscopic S-N-S junction, where the normal metal N has a spatial extension smaller than the phase coherence length and ξ_0, and only few channels are assumed to contribute to transport. Such a system of non-interacting charge carriers can be described within a scattering matrix formalism [153], and stationary state solutions predict the existence of a discrete set of resonances $E(\varphi_2 - \varphi_1)$ at subgap energies $|E| < \Delta$ depending on the macroscopic phase difference $\delta = \varphi_2 - \varphi_1$ between the two superconductors, so-called *Andreev bound states* (ABS) [152]. As schematically depicted in Fig. 3.3(c), these discrete energy bound states originate from the phase-coherence of the Andreev reflection process in such a mesoscopic system, in analogy to a Fabry-Perot interferometer with phase-conjugating mirrors [152]. In a mesoscopic system, these discrete Andreev bound states

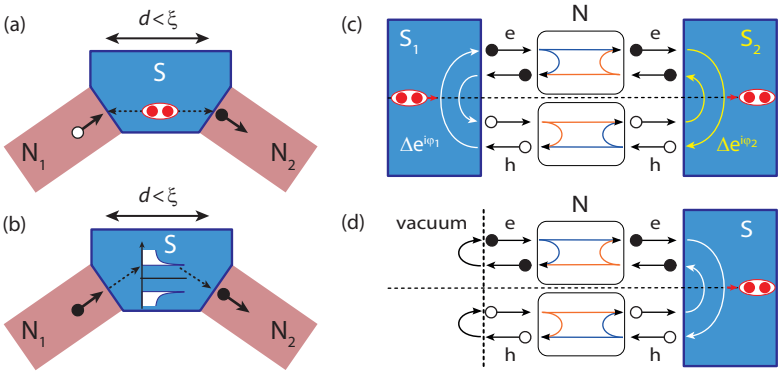

Figure 3.3.: (a,b) Illustration of crossed Andreev reflection (a) and elastic co-tunneling (b) via a virtual quasiparticle state in a three-terminal N-S-N device. (c) Schematic illustration of Andreev bound state forming loops due to virtual Andreev reflexions of electrons (closed circles) and holes (open circles) at the N-S interfaces in a mesoscopic S-N-S device. The rectangles in N represent possible scattering events. (d) Similar illustration as in (c) for a N-S device only, where reflections at the N-vacuum boundary are responsible for the formation of Andreev bound states. Adapted from Refs. [78, 152].

are responsible for carrying a supercurrent through the device architecture [153], often called *Josephson effect*. The phase-coherence of the process can immediately be identified by the current-phase relation of this Josephson current. For a simple single Landauer channel system of transmission T, one finds $E_{\pm}(\delta) = \pm\Delta\sqrt{1 - T\sin^2\frac{\delta}{2}}$ for the Andreev bound state energies [152]. Similarly, as shown in Fig. 3.3(d), one can construct Andreev bound states also with a single superconductor in a mesoscopic N-S junction due to reflections at the N-vacuum interface, which will become relevant and be discussed in detail later. Finally, considering a more macroscopic system with many tranverse contributing transport channels, many of these subgap ABS develop and lead to a modified 'proximity' DOS with a minigap [152, 154], beautifully demonstrated in Ref. [154] by probing the phase- and spatial dependence of the local DOS in a proximitized N metal embedded in a mesoscopic superconducting ring.

3.3. Transport in N-QD-S devices

Inserting now additional QDs between the metallic electrodes, all of the so far discussed transport mechanisms can also be observed, though in a more complex manner. The physics of such *hybrid* S-QD devices [9] is usually governed by a competition between the repulsive interactions of individual electrons

confined in a QD, and the superconducting order favoring a pairing of electrons. Hence, transport through such devices also comprises a competition between single-electron or quasi-particle tunneling and Andreev processes due to Cooper pairs originating from the superconductor. This interplay can be characterized by the relevant energy scales of the system, namely the charging energy E_C of the QD, the superconducting energy gap Δ and the relative coupling strengths of the QD to the individual contacts.

Such hybrid systems, in which a superconductor is coupled (more generally) to low-dimensional electron systems, play a key role to study numerous new transport processes and exotic quantum states of matter, and stimulated thus a lot of interest. Recent examples include the study of Josephson effects [155] and supercurrents [156–164] in S-QD-S systems, the formation of Andreev bound states [15, 31, 165–173] which can be implemented as Andreev qubits [15, 167], and transport signatures possibly due to Majorana fermions [10, 12], which might be used for topological quantum computation [14]. Even more complex devices can be realized, including nano-SQUIDs [162, 163, 165, 174], or Cooper pair splitters [19–21, 32, 33] as a potential source of spin-entangled electrons. A wealth of novel device schemes and transport studies are constantly proposed, and possibly coexisting Kondo correlations [161, 163, 169, 175, 176], multi-terminal effects [177] or spin-orbit interactions [113, 178] diversify this field further.

From this huge spectrum of possibilities, we focus here on N-QD-S devices, much less well studied than the usual S-QD-S geometry. Such a N-QD-S device (pioneered in Ref. [30]), or half a Cooper pair splitter, where a single QD is embedded between an N and an S electrode, also constitutes a model system to understand transport in more complex experiments. Characterizing the device by the relevant energy scales, we categorize three different dominant transport mechanisms or transport regimes with increasing coupling strength of the S contact to the QD, namely quasiparticle tunneling (Sec. 3.3.1), resonant (and inelastic) Andreev tunneling (Sec. 3.3.2), or the formation of Andreev bound states (Sec. 3.3.3). Finally, we briefly discuss Cooper pair splitter devices comprised of two such N-QD-S building blocks, and draw the connections to the previous sections.

3.3.1. Quasiparticle transport[3]

Let us first discuss the most simple N-QD-S system, where a single QD, characterized by its charging energy E_C, level spacing δE and electrochemical potential μ_{QD}, is embedded between a superconducting (S) and a normal metal (N) contact. Such a device with its relevant parameters is depicted in Fig. 3.4(a), where $\Gamma_{S(N)}$ denote the QD's coupling strength to the S (N) lead, $\Gamma = \Gamma_S + \Gamma_N$

[3] Parts of this section have been published in similar form in the supplementary material of Ref. [179] and in Ref. [180].

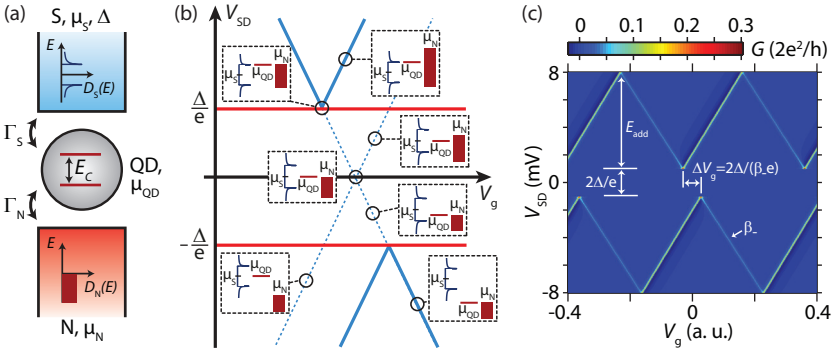

Figure 3.4.: (a) Schematic of a N-QD-S device with all relevant energy scales. (b) Expected charge stability diagram (blue full lines) for a N-QD-S device in the QP tunneling limit, for the bias applied to S. Small diagrams indicate the relative alignment of the electrochemical potentials μ_N, $\mu_S = -|e|V_{SD} + \mu_N$ and μ_{QD} at selected positions in the charge stability diagram. (c) G vs V_{SD} and V_g obtained from Eq. (3.5) with $\Gamma_S = 10\,\mu$eV, $\Gamma_N = 100\,\mu$eV, $E_{add} = 7$ meV and $\Delta = 1$ meV at $T = 100$ mK.

the total coupling, $\mu_{S(N)}$ the electrochemical potential of the S(N) contact, and Δ the superconducting gap in S. In this section, we focus on a regime where transport is dominated by Coulomb repulsion and *quasiparticle (QP) tunneling* only, i.e. we choose[4] $\Gamma_S \ll \Gamma_N \ll \Delta < \delta E \ll E_C$, where Andreev processes are expected to be strongly suppressed due to the small coupling to the superconductor [83, 181]. This limit is equivalent to an opaque N-I-S tunnel junction discussed in the previous chapter (i.e. $Z \gg 1$ in the BTK model), where transport spectroscopy measurements directly reflect the QP DOS in S. Indeed, previous experiments in this transport regime have already found both a characteristically separated CB diamond pattern due to the superconductors energy gap, and an enhanced spectroscopic resolution of e.g. excited states and cotunneling lines due to the sharp peaks in the QP DOS in S [82, 83, 182]. To demonstrate the impact of the energy gap on the CB diamond structure in this transport regime, especially compared to the N-QD-N devices discussed in Chap. 1, we restrict ourselves to a relatively simple description, which will nevertheless be very beneficial for the analysis of the experimental data later.

Figure 3.4(b) qualitatively sketches the expected charge stability diagram for such an N-QD-S device if the bias is applied to S as in the later experiments, where full blue lines correspond to finite differential conductance G. The tips of the CB diamonds mark the onset of QP tunneling, and are hence separated in bias by $2\Delta/e$ due to the superconductors energy gap. The diamond tips will also be shifted horizontally in gate voltage with respect to each other

[4] We also chose a small Γ_N to achieve $\Gamma < \Delta$, though this is not relevant here.

due to the capacitive coupling of the leads to the QD by $\Delta V_\mathrm{g} = 2\Delta/(e\beta_-)$, where $\beta_- = -C_\mathrm{g}/C_\mathrm{S}$ is the (negative) slope of the $\mu_\mathrm{N} = \mu_\mathrm{QD}$ CB resonance. C_S, C_N, C_g, $C = C_\mathrm{S} + C_\mathrm{N} + C_\mathrm{g}$ are the S, N, gate and total capacitances, respectively. If one considers only single electron transport through the system and neglects superconducting correlations and charge dynamics on the QD (e.g. excited states etc.), this charge stability diagram can be understood in a simple resonant tunneling model [181, 183]. Such an intuitive picture was first suggested and derived from a microscopic model for an S-QD-S system in Ref. [181]. Compared to simple tunneling through a N-I-S device captured by Fermi's golden rule, it only introduces an additional energy dependent transmission function $T_\mathrm{QD}(E)$ accounting for the *resonant tunneling* through the QD at $\mu_\mathrm{QD} = \mu_\mathrm{N,S}$ and a broadening due to the QD's finite coupling to the leads. If the bias is applied to S, the current can then be approximated as [181, 184]

$$I = \frac{e}{h}\int dE D_\mathrm{N}(E) D_\mathrm{S}(E + eV_\mathrm{SD}) \cdot T_\mathrm{QD}(E) \cdot [f_\mathrm{N}(E) - f_\mathrm{S}(E + eV_\mathrm{SD})], \quad (3.5)$$

with the constant DOS $D_\mathrm{N}(E) \approx D_\mathrm{N}(0)$ in N and a BCS-type DOS in S normalized to the normal state as in Eq. (3.2), $D_\mathrm{S}(E)/D_\mathrm{N}(0) = |E|/(\sqrt{E^2 - \Delta^2}) \cdot \Theta(|E| - \Delta)$. $f_\mathrm{S/N}(E) = 1/[\exp(E/kT) + 1]$ are the Fermi functions in the respective contacts, and for sufficiently low temperatures, i.e. $kT \ll \Gamma$, we choose a Breit-Wigner (BW) transmission function for the QD of the form [79] $T_\mathrm{QD}(E) = \Gamma_\mathrm{S}\Gamma_\mathrm{N}/(\Delta E^2 + \Gamma^2/4)$ similar to Eq. (1.10). Here, $\Delta E = E - \mu_\mathrm{QD} \pm n \cdot E_\mathrm{add}\,(n \in \mathbb{N})$ accounts for gating of the single QD level by one gate (g, voltage V_g) and all contacts via $\mu_\mathrm{QD} = \mu^0_\mathrm{QD} - e\frac{C_\mathrm{S}}{C}V_\mathrm{SD} - e\frac{C_\mathrm{g}}{C}V_\mathrm{g}$ and the electron filling with the addition energy E_add. The differential conductance $G = \mathrm{d}I/\mathrm{d}V_\mathrm{SD}$ can then be calculated directly as shown for realistic device parameters (caption) in Fig. 3.4(c), which reproduces the qualitative arguments made in Fig. 3.4(b).

3.3.2. Resonant and inelastic Andreev tunneling[5]

We now consider a N-QD-S device as above, but with an increased coupling strength Γ_S of the QD to the superconductor, i.e. $\Gamma_\mathrm{N} \lesssim \Gamma_\mathrm{S} < \Delta < \delta E \ll E_\mathrm{C}$. In this 'intermediate' transport regime Andreev reflection processes become possible [181], but the QD is still weakly (sufficiently well) enough coupled[6] to S (N) so that the QD's energy spectrum is not severely modified by the formation of Andreev bound states (see next section and earlier discussion for N-S devices). We previously discussed Andreev reflection in metallic N-S structures as a process, in which an electron from N can only enter S by forming a Cooper pair with a second electron of opposite spin and momentum.

[5] Parts of this section have been published in similar form in Ref. [179].

[6] In other words, electrons on the QD still have a sufficient probability to 'escape' to N.

This process is slightly more complicated if the two reservoirs are connected by a QD, in which the large charging energy E_C suppresses a double occupation. The resulting *resonant Andreev tunneling* (resonant AT) [185–188] is illustrated in Fig. 3.5(a) as an intuitive sequential tunneling process. At zero bias the two electrons forming a Cooper pair tunnel through the QD at the same energy, which leads to a peak in the differential conductance G. At a finite bias, resonant AT is allowed only for electrons with energies aligned to the electrochemical potential μ_S of S, i.e., only if the QD resonance (μ_{QD}) is aligned to μ_S, see Fig. 3.5(a). This hard condition is due to the energy filtering of the QD transmission, i.e. typically no other QD resonance or state will be available so that electrons can tunnel at arbitrary energies E and $-E$ to form a Cooper pair in S, in contrast to metallic structures. Hence, because two electrons have to be transferred sequentially and phase-coherent through the same QD resonance (a 4th order process in tunnel couplings), one intuitively expects a sharp decay of the probability amplitude for AT away from $\mu_{QD} = \mu_S$, e.g. a line shape similar to a Lorentzian squared (transfer of two electrons). Indeed, very similar to this intuition, the predicted resonant AT conductance line shape in the limit of non-interacting electrons and $kT \ll \Gamma$ is

$$G(\Delta V_g) = \frac{2e^2}{h}\left(\frac{2\Gamma_S\Gamma_N}{4\Delta E^2 + \Gamma_S^2 + \Gamma_N^2}\right)^2, \tag{3.6}$$

first calculated by Beenakker [185] and later confirmed by Refs. [186–188]. $\Delta E = -e\alpha_g(\Delta V_g - V_g^{(0)})$ denotes the QD level detuning, with the lever arm of the gate α_g and the position of the resonance $V_g^{(0)}$. This lineshape is plotted and compared with the BW lineshape of Eq. (1.10) in Fig. 3.5(c,d), for symmetric tunnel couplings $\Gamma_S = \Gamma_N$ (c) and asymmetric couplings $\Gamma_S/\Gamma_N = 10$ (d). In the symmetric case, the AT conductance doubles on resonance compared to the BW conductance, and decays much faster off-resonance as expected. The doubled conductance in the non-interacting regime even for very small, but symmetric $\Gamma_{S/N}$ seems at first surprising, compared to the reduced probability of Andreev reflection for metallic S-N structures with $Z > 0$ in the BTK model. Here, one has to bear in mind that for a mesoscopic N-QD-S system, an electron maintains its phase-coherence during multiple reflections between the two barriers in analogy to a Fabry-Perot interferometer, and the increased electron lifetime leads to the finite probability also for resonant AT [187]. For asymmetric couplings, the AT conductance is suppressed compared to the BW lineshape, but still has a significantly reduced width. Hence, resonant AT can be identified by the distinctive resonance line shape with a sharper decay than when tunneling into a normal reservoir [185]. A second crucial characteristic of resonant AT is its gate and bias dependence depicted as a green line in Fig. 3.5(e), where significant conductance is only expected along the $\mu_{QD} = \mu_S$ line, i.e. on resonance. Because Cooper pairs can either be

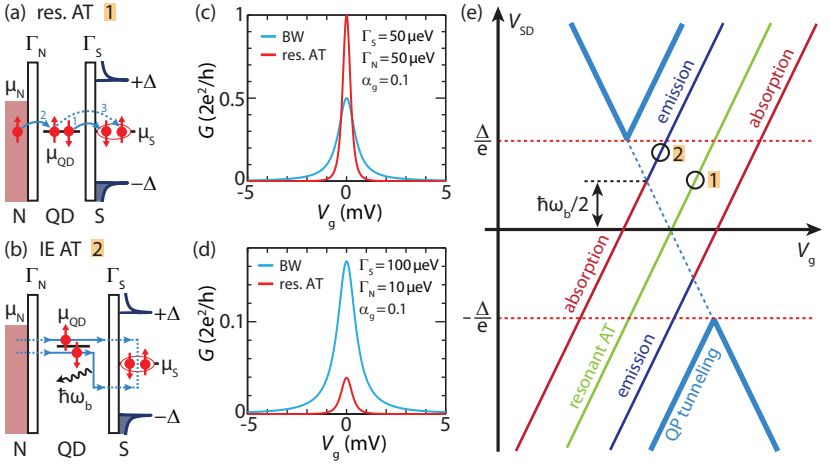

Figure 3.5.: (a) Schematic of resonant AT. Two electrons tunnel through the QD into S for $\mu_{\mathrm{QD}} = \mu_{\mathrm{S}}$ and $\mu_{\mathrm{N}} > \mu_{\mathrm{QD}}$. (b) Schematic of inelastic AT. Two electrons tunnel through the QD into S at $\mu_{\mathrm{QD}} = \mu_{\mathrm{S}} + \frac{n}{2}\hbar\omega_{\mathrm{b}}$ for $\mu_{\mathrm{N}} > \mu_{\mathrm{QD}}$ by emitting multiples of the energy $\hbar\omega_{\mathrm{b}}$ to the environment. (c,d) Comparison of BW and resonant AT lineshapes $G(V_{\mathrm{g}})$ for symmetric (c) and asymmetric couplings (d) Γ_{S} and Γ_{N} (legend). $\alpha_{\mathrm{g}} = 0.1$ denotes the assumed lever arm of the gate. (e) Expected gate and bias dependence of resonant (green line) and boson-assisted AT, deduced from the predictions of Ref. [111]. Replicas of resonant AT can occur due to boson emission (blue lines) and boson absorption (red lines). The numbers mark the position of the diagrams (a,b) in the charge stability diagram.

injected ($\mu_{\mathrm{N}} > \mu_{\mathrm{QD}}$) or removed ($\mu_{\mathrm{N}} < \mu_{\mathrm{QD}}$) from S, the resonant amplitude $G(\mu_{\mathrm{QD}} = \mu_{\mathrm{S}})$ does not depend on the bias.

Inclusion of electron-electron interactions complicates a theoretical description of the process severely, and an analytical treatment is usually only feasible by setting $E_{\mathrm{C}} \to \infty$ or $\Delta \to \infty$ (see also Sec. 3.3.3), but not for the experimentally relevant 'intermediate' regime assumed at the beginning with $\Delta, E_{\mathrm{C}} < \infty$ and $\Gamma_{\mathrm{N}} \lesssim \Gamma_{\mathrm{S}} < \Delta$. In this regime, the resonant AT process will depend on the exact magnitude and relation of all parameters $\Gamma_{\mathrm{N}}, \Gamma_{\mathrm{S}}, \Gamma, kT, \Delta, \delta E$ and E_{C} [188–190], and Kondo correlations can additionally complicate the problem [189–191]. We hence restrict ourselves to a few simple arguments. Because the electrons have to tunnel sequentially in the presence of e-e interactions, the phase-coherence of the AT process requires a timescale $\lesssim \hbar/\Delta$ given by a virtual intermediate quasiparticle state [19, 190]. Hence, the magnitude of the AT process will be determined by the lifetime of the second electron on the QD relative to the size of the gap, i.e. $\sim \Gamma/\Delta$. More precisely, also the ratio $\Gamma_{\mathrm{S}}/\Gamma_{\mathrm{N}}$ plays a role, where an increased probability for resonant AT is

expected for $\Gamma_S > \Gamma_N$. Hence in the regime assumed in the beginning, where $\Gamma_S \gtrsim \Gamma_N$ and Γ_S/Δ is not too small, we still expect a finite probability for resonant AT. Theoretical calculations in different limiting cases predict a similar scenario [19, 188–190, 192], and suggest that even the lineshape (i.e. a reduced width) does not change significantly [187, 188, 192]. These considerations also agree with the optimal operating regime of a Cooper pair splitter device specified in Refs. [19, 78, 193], where resonant AT (local pair tunneling) is competing with Cooper pair splitting (see Sec. 3.3.4). Indeed, Ref. [19] finds $I_{AT} \sim \Gamma_N(\Gamma_S/\Delta)^2$ for the magnitude of the resonant Andreev tunneling current, in the limit $E_C \gg \Delta$ and $\Gamma_N \gg \Gamma_S$ (in contrast to our assumptions), nevertheless supporting our qualitative arguments made above.

In Sec. 1.3, we already discussed for N-QD-N devices how boson-assisted tunneling, in which bosons from the environment are either absorbed or emitted in an inelastic tunneling process, leads to replicas of the elastic tunnel process at higher energies. Similarly, phonon [111] and photon [194] induced discrete replicas of elastic AT were predicted recently for N-QD-S devices. Such *inelastic AT* is illustrated in Fig. 3.5(b): a Cooper pair can only be formed by two electrons of opposite energy with respect to the chemical potential of S, μ_S. If the QD level is aligned at a positive energy, both electrons traverse the QD at the same energy, and, to form a Cooper pair, one relaxes the energy $\hbar\omega_b$ to the environment with a bosonic excitation spectrum. As is evident from Fig. 3.5(b), this condition is met at $\mu_{QD} - \mu_S = \frac{n}{2}\hbar\omega_b$ ($n \in \mathbb{N}$), in contrast to twice this value in boson-assisted processes in devices with normal contacts. The expected gate and bias dependence of the inelastic AT replicas is qualitatively sketched in Fig. 3.5(e). At $T = 0$, there are no boson modes above the ground state populated and hence only inelastic AT processes under the emission of bosons are possible. This introduces an additional bias condition $\mu_S < \mu_{QD} < \mu_N$ ($\mu_S > \mu_{QD} > \mu_N$) for the injection (removal) of a Cooper pair in (from) S [see Fig. 3.5(b)], and only the blue emission lines in Fig. 3.5(e) ending at a finite sub-gap bias will be visible at low temperature [111]. For increasing temperature $kT \gtrsim \hbar\omega_b$, higher modes will be populated in the bosonic environment, and the red lines in Fig. 3.5(b) start to appear due to the now also possible absorption process. The predicted peculiar temperature dependence and shifted weights of the emission and absorption lines [111] hence constitute a clear signature for identifying inelastic AT in an experiment. Furthermore, similar to resonant AT [187], the resonance width of the inelastic AT lines is determined by the QD transmission and hence the tunnel couplings only, i.e. FWHM $< \sqrt{2}\Gamma$ [111], which makes the feature particularly robust and observable also for increased temperature [111]. Another remarkable prediction is the occurence of negative differential conductance (NDC): in contrast to boson-assisted tunneling in N-QD-N devices, the resonance condition is determined by the QD level position and not by the Fermi energy of the normal metal lead, which leads to peaks in the current

[111] and a peak-dip structure in the differential conductance. We note that the gate voltage, bias and temperature dependence is also quite different for boson-assisted quasiparticle tunneling[7] [195], which allows to distinguish the two mechanisms. Neither resonant nor inelastic AT had been observed experimentally in QDs so far, probably because both require the QD resonance width Γ to be smaller than the superconducting energy gap Δ, and a peculiar regime of Γ_S/Γ_N and Γ_S/Δ (see Chap. 4 and 6).

3.3.3. Andreev bound states

Increasing the coupling strength Γ_S of the superconducting electrode in the N-QD-S device even more, so that $\Gamma_N \ll \Gamma_S \sim \Delta < \delta E < E_C$, the superconducting proximity effect strongly affects the QD's energy spectrum [155]. Similar to the metallic N-S system depicted in Fig. 3.3(d), the strong coupling $\Gamma_S/\Gamma_N \gg 1$ of the QD to S and the coupling asymmetry lead to the formation of new sub-gap energy levels called *Andreev bound states* (ABS) [165]. These ABS have recently received a lot of interest both experimentally [15, 31, 165–173, 182, 196] and theoretically [41, 155, 197–207], due to their potential implementation as Andreev qubits [15, 16], and their intimate connection to the supercurrent (reversal) in S-QD-S josephson junctions [156–164], or to the mesoscopic proximity effect [153]. Using a weakly coupled N lead as a tunnel probe, the ABS or Andreev levels can be directly observed in transport spectroscopy. This has been beautifully demonstrated in the landmark experiments of Deacon *et al.* [31] and Pillet *et al.* [165], and further studies have deepened the understanding of their gate, bias, phase and temperature dependence [166–171] and revealed the relevant transport mechanisms [171–173]. In this wide field, we restrict ourselves to a discussion of the relevant transport signatures of ABS in N-QD-S devices, particularly their gate-bias dependence, and refer to Ref. [155] for a detailed theoretical review.

Anderson impurity model with superconducting lead Treating the N lead as essentially decoupled tunnel probe with $\Gamma_N \to 0$, the remaining S-QD system can be described in the (minimal) Anderson impurity model (AIM) with one superconducting lead [155]. This model assumes a Hamiltonian $H = H_{QD} + H_S + H_T$, where

$$H_{QD} = \varepsilon_0(n_\uparrow + n_\downarrow) + U n_\uparrow n_\downarrow \tag{3.7}$$

describes a QD with a single spin-degenerate orbital ε_0, with the number operator $n_\sigma = d_\sigma^\dagger d_\sigma$ and creation (annihilation) operators $d_\sigma^\dagger$ (d_σ) for electrons

[7] One would particularly expect absorption lines for bias voltages below the blue QP tunneling line, and emission lines above the QP tunneling line – hence an inverse temperature dependence. For more details see the supplementary information of Ref. [179].

with spin $\sigma = \{\uparrow, \downarrow\}$, and the Coulomb interaction[8] U for double occupation $n_\uparrow = n_\downarrow = 1$. To first approximation such a model is also valid for CNT QDs with a significantly large level spacing δE and broken valley degeneracy due to disorder or spin-orbit interaction (Sec. 1.3) [169]. The Hamiltonian H_{QD} of the uncoupled QD has the four eigenstates $|0\rangle, |\sigma\rangle = d_\sigma^\dagger |0\rangle, |\uparrow\downarrow\rangle = d_\uparrow^\dagger d_\downarrow^\dagger |0\rangle$, with its energy spectrum depicted in Fig. 3.6(a). In a Coulomb blockade spectroscopy experiment on an isolated QD, one probes exactly the first-order (single electron) transition energies ε_0 and $\varepsilon_0 + U$ of this spectrum (Sec. 1.3). Finally, $H_{\mathrm{S}} = \sum_{\mathbf{k},\sigma} \xi_{\mathbf{k}} c_{\mathbf{k}\sigma}^\dagger c_{\mathbf{k}\sigma} - \sum_{\mathbf{k}} \left(\Delta c_{\mathbf{k}\uparrow}^\dagger c_{-\mathbf{k}\downarrow}^\dagger + \mathrm{h.c.} \right)$ and $H_{\mathrm{T}} = \sum_{\mathbf{k},\sigma} \left(V_{\mathbf{k}} c_{\mathbf{k},\sigma}^\dagger d_\sigma + \mathrm{h.c.} \right)$ denote a BCS mean-field Hamiltonian H_{S} for the S lead and a Hamiltonian H_{T} coupling the QD to S [155]. Here, Δ is the superconducting order parameter, and $c_{\mathbf{k}\uparrow}^\dagger$ ($c_{\mathbf{k}\uparrow}$) the creation (annihilation) operators for electrons with spin σ at the single particle energy level $\xi_{\mathbf{k}}$ measured relative to μ_{S}. The coupling to the reservoir S is usually characterized by a single parameter $\Gamma_{\mathrm{S}} = 2\pi |V|^2 D_{\mathrm{N}}(0)$, assuming a constant normal-state DOS $D_{\mathrm{N}}(0)$ of S around the Fermi level and $V_{\mathbf{k}} \simeq V$ in this range [169, 201, 203].

The solutions for the uncoupled QD form the basis for a discussion of the full Hamiltonian. Unfortunately, the AIM has no full analytical solution [155], and can only be solved with elaborate numerical methods (e.g. numerical renormalization group, NRG [169, 198, 199, 207]), approximations (mean field/Hartree-Fock approaches [171, 204], diagrammatic approaches/perturbation theory [41, 200, 201, 206]), or analytically in certain very limited parameter regimes [197, 198, 201].

Superconducting atomic limit Instructive analytical solutions can be found in the *superconducting atomic limit* [197, 198, 201, 203], where $\Delta \to \infty$ (i.e. a gap much larger than all characteristic QD energies) effectively decouples the QD from the quasiparticle continuum in the S lead, but still allows a finite coupling to the Cooper pair condensate. In this limit, H can be reduced to the effective Hamiltonian [201, 203]

$$H_{\mathrm{eff}} = H_{\mathrm{QD}} - \frac{\Gamma_{\mathrm{S}}}{2} (d_\uparrow^\dagger d_\downarrow^\dagger + d_\uparrow d_\downarrow). \tag{3.8}$$

The second term in H_{eff} describes the superconducting proximity effect on the QD, where virtual Andreev reflections constantly create and destroy Cooper pairs on the QD, and charge is hence shared between the QD and S. This process couples the even charge states $|0\rangle$ and $|\uparrow\downarrow\rangle$ of the decoupled QD, which are thus no longer eigenstates of the system. The odd charge state (doublet)

[8] For conformity with theoretical treatments, and to distinguish from the charging energy E_{C} defined in the constant interaction model valid for many-electron QDs, we use the letter U for the Coulomb interaction in this section. Nevertheless, one should keep in mind that U plays the role of the charging energy E_{C} in the experiments.

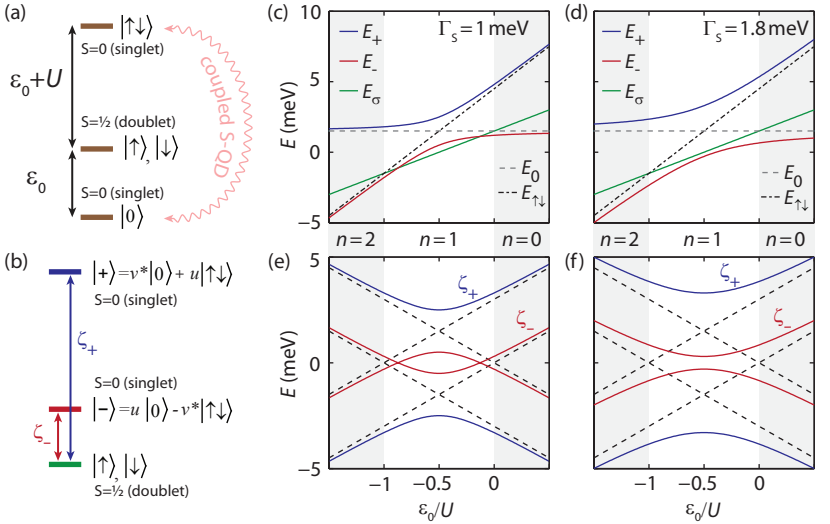

Figure 3.6.: (a) Energy spectrum and eigenstates of an isolated QD with one spin-degenerate orbital. When a finite coupling to S is taken into account, the even charge states mix due to virtual Andreev reflections (faint orange arrow). (b) Energy spectrum and eigenstates of the S-QD system in the superconducting atomic limit. The Andreev resonances $\zeta_\pm$ denote the first-order transition energies of the system. (c-f) Eigenenergies E_σ, E_- and E_+ (top) and transition energies $\pm\zeta_\pm$ (bottom) in the superconducting atomic limit for $U = 3\,\mathrm{meV}$ and $\Gamma_\mathrm{S} = 1\,\mathrm{meV}$ (c/e) and $\Gamma_\mathrm{S} = 1.8\,\mathrm{meV}$ (d/f) as a function of the gate-tunable orbital energy ε_0/U. Shaded areas and n (middle) denote the different charge states. Dashed (dash-dotted) lines correspond to the uncoupled QD's eigenenergies E_0 and $E_{\uparrow\downarrow}$ shifted by $U/2$ (top panels), and the transition energies of the uncoupled QD system (bottom panels). Freely adapted from Refs. [78, 201].

$|\sigma\rangle$ remains an eigenstate, but with a shifted (doublet) eigenenergy $E_\sigma = \varepsilon_0 + U/2 = \xi_\mathrm{d}$ due to electron-hole symmetry [201]. Because of the similarity of H_eff with a BCS Hamiltonian, where Γ_S plays the role of the pairing amplitude, a Bogoliubov transformation yields [201] the BCS-like (singlet) eigenstates $|\pm\rangle$

$$\begin{aligned} |-\rangle &= u\,|0\rangle - v^*\,|\uparrow\downarrow\rangle \\ |+\rangle &= v^*\,|0\rangle + u\,|\uparrow\downarrow\rangle\,, \end{aligned} \tag{3.9}$$

the so-called *Andreev bound states* with amplitudes $u = 1/2\sqrt{1 + \xi_\mathrm{d}/\sqrt{\xi_\mathrm{d}^2 + \Gamma_\mathrm{S}^2}}$ and $v = 1/2\sqrt{1 - \xi_\mathrm{d}/\sqrt{\xi_\mathrm{d}^2 + \Gamma_\mathrm{S}^2}}$ and eigenenergies

$$E_\pm = \frac{U}{2} \pm \sqrt{\xi_\mathrm{d}^2 + \Gamma_S^2} + \xi_\mathrm{d}. \tag{3.10}$$

The corresponding excitation spectrum is depicted in Fig. 3.6(b). Again, in a transport spectroscopy experiment e.g. with a weakly coupled normal tunnel contact (N-QD-S), one probes the transition energies between different states. Transitions with highest probability are the first order (single charge) transitions $|\sigma\rangle \leftrightarrow |\pm\rangle$, with corresponding transition energies $\zeta_\pm$ [Fig. 3.6(b)]. These so-called *Andreev resonances* [172, 208] can be directly observed as additional subgap resonance peaks at exactly $eV_{\mathrm{SD}} = \pm\zeta_\pm$.

In Figs. 3.6(c-f), we plot the eigenenergies of the coupled S-QD system E_σ, E_- and E_+ and the respective Andreev resonances $\pm\zeta_\pm$ as a function of the normalized (gate-tunable) QD orbital energy ε_0/U, for three QD charge states ($n = 0...2$) and different coupling strengths Γ_{S}. We observe that always $E_- < E_+$, and deep in the $n = 0$ and $n = 2$ charge state E_- and E_+ approach the uncoupled $|0\rangle$ and $|\uparrow\downarrow\rangle$ states (dashed/dash-dotted lines) as expected. In the odd charge state $n = 1$, E_- and E_+ obey an avoided crossing with a strength characterized by Γ_{S}. This immediately demonstrates the competing effects of Coulomb repulsion and pairing strength: While the ground state (GS) of the system is always the singlet $|-\rangle$ deep in the even charge states [Figs. 3.6(c-d)], the Coulomb repulsion U favors the doublet GS $|\uparrow\rangle, |\downarrow\rangle$ (i.e. $E_\sigma < E_-$) in the odd charge state for not too large couplings Γ_{S}. The Andreev resonances $\pm\zeta_-$ then form a loop structure [Fig. 3.6(e)], the size of which decreases both horizontally and vertically with increasing Γ_{S}. More precisely, at the points where $\pm\zeta_- = 0$, the QD GS is degenerate, and the QD undergoes a GS transition in the odd charge state from a singlet GS $|-\rangle$ ($E_- < E_\sigma$) to a doublet GS $|\sigma\rangle$ ($E_\sigma < E_-$), and vice versa. This GS transition is sometimes also called a *quantum phase transition* (QPT) [171]. Above a certain critical Γ_{S}, the pairing term in the Hamiltonian 'wins the competition' and becomes so strong that the QD always remains in a singlet GS $|-\rangle$ [Fig. 3.6(d)], even in the odd diamond. In this case, the loop structure of the Andreev resonances $\pm\zeta_-$ vanishes [Fig. 3.6(f)] and an anticrossing is observed instead in the odd charge state.

Qualitative dispersion from numerical solutions For a more realistic scenario and a finite Δ, the interaction with the continuum of quasiparticles in S leads to a level repulsion effect [171], which can be either treated with numerical methods or approximations as discussed previously. This changes the energy spectrum and the resulting dispersion of the Andreev resonances also qualitatively [155]. In Fig. 3.7, we depict the (subgap) dispersion relations $\pm\zeta_\pm(V_{\mathrm{g}})$ of the Andreev resonances expected qualitatively from NRG calculations [152, 155, 169, 199] in N-QD-S charge stability diagrams, for different values of Γ_{S}/U. In contrast to the $\Delta \to \infty$ limit, the energy difference $\zeta_\pm$ between the GS and excited states has an upper limit of Δ and cannot exceed this border. Hence, the Andreev resonances will always approach $\pm\zeta_- = \Delta$

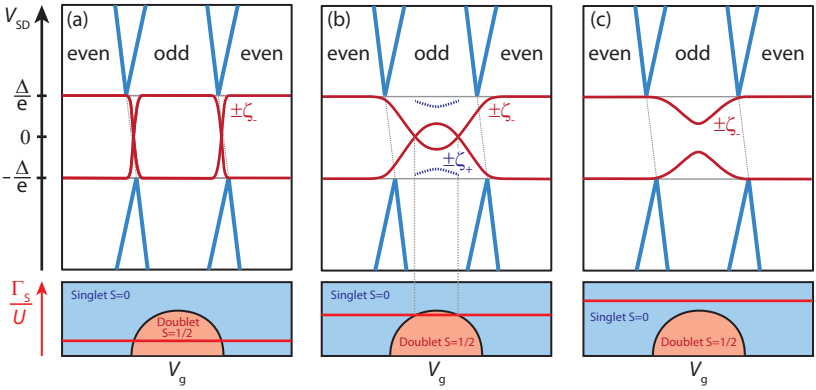

Figure 3.7.: (a-c) Gate-dispersion of Andreev resonances $\pm\zeta_\pm(V_g)$ expected qualitatively from NRG calculations, sketched in N-QD-S charge stability diagrams (top panel) with increasing coupling strengths Γ_S/U (bottom panel) from (a) to (c). Bright blue lines mark the onset of QP tunneling, dark red lines the $\pm\zeta_-$ Andreev resonance, and dashed dark blue lines a possible $\pm\zeta_+$ resonance (only for certain parameters, see text). The bottom panel indicates the respective QD GS as a function of the gate voltage (full red line Γ_S/U), and the singlet-doublet QPT for (a) and (b). Adapted from Refs. [78, 152, 169, 171].

in the even charge states [compare Fig. 3.7(b/c) and Fig 3.6(e/f)]. For the odd charge states (i.e. $n = 1$), the dispersion remains qualitatively similar as discussed for the superconducting atomic limit: Depending on the ratio of Γ_S/U, the QD undergoes a GS transition from a singlet to a doublet state which is characterized by the crossing points $\pm\zeta_- = 0$ and a loop of the ζ_- Andreev resonances. As shown in Fig. 3.7(a) and (b), the size of the loop varies with Γ_S/U [169, 208], which describes the competition between superconducting pairing and Coulomb interaction on the QD[9]. Above a certain critical threshold of Γ_S/U, the singlet $|-\rangle$ is always the ground state, resulting in an anti-crossing of the Andreev resonances ζ_- [Fig. 3.7(c)]. For very small values of Γ_S/U [Fig. 3.7(a)], the singlet-doublet QPT occurs close to the charge degeneracy points, and ζ_- is pinned to the gap edge also in the odd diamond. This singlet-doublet GS transition is also responsible for the 0-π-transition and supercurrent reversal in S-QD-S josephson junctions [159–164]. The Andreev resonances are in principle expected to be infinitely sharp [155], but a finite coupling Γ_N to the N lead [31, 171] and voltage noise [165] results

[9] We note that a qualitatively similar description could also be achieved with the Kondo temperature, kT_K, relative to the size of the gap Δ [170, 176]. Especially for large values $\Gamma_S \gg \Delta$ (not discussed here), the boundary between the BCS-like singlet $|-\rangle$ and a Kondo-like singlet state (many-body state where single spin is screened by reservoir electrons) is not well defined [198]. Such states are also called Yu-Shiba-Rusinov bound states [176].

in an experimentally observed broadening. We finally note that for typical experimental parameters in N-QD-S devices $E_+ > \Delta$ and ζ_+ can usually not be observed. For certain parameter ranges (e.g. for $U \lesssim 1.5\Delta$ and $\Gamma_S/U \lesssim 1$), NRG nevertheless predicts also the occurrence of ζ_+ in the odd charge states [152] as depicted in Fig. 3.7(b) – but only if the GS is a doublet (singlet-singlet transitions are suppressed). The $|+\rangle$ state has however been recently observed in superconducting atomic break junctions [167], and a first implementation of the $|\pm\rangle$ states as Andreev qubit has been demonstrated [15].

Transport through Andreev resonances Finally, we briefly discuss the transport mechanisms responsible for the occurrence of (subgap) Andreev resonances at $|e|V_{SD} = \pm\zeta_-$ in the differential conductance through N-QD-S devices, using the $\Delta \to \infty$ description. This transport occurs again via Andreev reflections [171]: assuming the QD in the odd charge state with a doublet GS $|\sigma\rangle$ as depicted in Fig. 3.8(a), an electron can tunnel onto the QD as soon as $\mu_N = +\zeta_-$ [Fig. 3.8(b)]. This electron excites the QD to the $|-\rangle$-state (E, red arrows), in which charge is shared between S and the QD due to virtual Andreev reflections. The excited state (ES) $|-\rangle$ relaxes back to the GS by transmission of a second electron (R, blue arrow) at a negative energy $-\zeta_-$ [Fig. 3.8(b)], and the transfer of a Cooper pair into S [171, 172]. A complete transport cycle GS→ES→GS (e.g. $|\sigma\rangle \xrightarrow{+1e} |-\rangle$, probability $\propto v^2$ and $|-\rangle \xrightarrow{+1e} |\sigma\rangle$, probability $\propto u^2$ to find the QD empty) hence transfers a Cooper pair into S and reflects an incoming electron at $+\zeta_-$ as a hole at $-\zeta_-$ with a probability (weight) $\propto u^2v^2$ [172]. Similarly, for reverse bias $\mu_N = -\zeta_-$ the inverse process takes place as depicted in Fig. 3.8(c), with the removal of a Cooper pair from S.

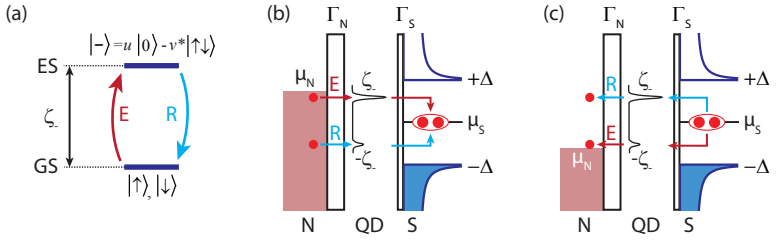

Figure 3.8.: Schematic of transport through Andreev levels. (a) Lowest energy excitation (E) and relaxation (R) for an S-QD system in the odd charge state, assuming a doublet GS in the superconducting atomic limit. (b) For $\mu_N > \zeta_-$, transport through the Andreev levels becomes possible. An Andreev tunneling process with transfer of an electron at ζ_- (excitation) and a subsequent electron transfer at $-\zeta_-$ (relaxation) adds a Cooper pair to S. (c) Process at reverse bias, removing a Cooper pair from S. Adapted from Refs. [171, 172].

3.3.4. Cooper pair splitting

Even if we did not observe *Cooper pair splitting* (CPS) processes in most of our CNT devices, we still briefly discuss this transport mechanism due to the useful links to the previous sections, and for our later discussion in the results chapters. For a more detailed description, we refer to Refs. [78, 193, 209] and the relevant literature (see below).

We saw previously how crossed Andreev reflection (CAR) can provide pairs of spatially separated, but still spin-entangled electrons in metallic N-S-N structures. In these devices, CAR is however often masked due to local transport and elastic cotunneling processes. Recher *et al.* [19] hence suggested to use the electron-electron interactions present in QDs to 'enforce' the splitting of Cooper pairs, respectively suppress the competing processes. Such a *Cooper pair splitter* (CPS) device [19] is shown in Fig. 3.9(a), with the device parameters of the two QDs (QD1 and QD2), normal leads (N1 and N2) and the S contact as introduced earlier[10]. Additionally, Γ_{12} denotes the inter-dot coupling strength, and δr the spatial separation of the tunneling points for the two individual electrons of a Cooper pair.

Figure 3.9(b-d) sketch the central idea of this device scheme, namely that the intra-dot Coulomb interaction or charging energy E_C suppresses a double occupancy of each QD, hereby enhancing the CAR process. In other words, the QD and device parameters are adjusted in such a way that the local pair tunneling (LPT) of Cooper pairs into only one arm of the device is suppressed [19]. The two possible channels for this LPT are illustrated in Fig. 3.9(c) and (d): The two electrons of a Cooper pair can either tunnel simultaneously into N [Fig. 3.9(c)], or sequentially one-by-one via a virtual quasiparticle state in S [Fig. 3.9(d)]. The double occupancy of the QD in the former process is suppressed with the Coulomb interaction $\sim 1/E_\mathrm{C}$, and can hence be controlled easily by the size of the QDs. Making the connection to the previous section, depending on the ratio $\Gamma_\mathrm{S}/E_\mathrm{C}$ and Δ, the coherent repetition of this process leads to the formation of the ABS for $\Gamma_\mathrm{S} \gg \Gamma_\mathrm{N}$. In Sec. 3.3.2, we have already extensively discussed the second process [Fig. 3.9(d)] as *resonant Andreev tunneling*, which corresponds to the sequential tunneling of Cooper pairs via a virtual quasiparticle state $> \Delta$ in S. This process is thus suppressed with $\sim 1/\Delta$. By increasing Δ and E_C, the CPS process [Fig. 3.9(b)] is not affected, and the ratio $I_\mathrm{CPS}/I_\mathrm{LPT}$ between the desired CPS and the parasitic LPT currents can hence be tuned to large values in this device geometry. Indeed, quantitative calculations have shown that $I_\mathrm{LPT} \propto \Gamma_\mathrm{S}^2\Gamma_\mathrm{N}\left(\frac{1}{\pi\Delta}+\frac{1}{E_C}\right)^2$ [19], and that I_CPS is maximal for $\mu_\mathrm{QD1} = -\mu_\mathrm{QD2}$ (for $\mu_\mathrm{S} = 0$) as expected. This situation is depicted for $\mu_\mathrm{QDi} = 0$ in Fig. 3.9(b). In order for the 'filtering' process to remain effective, all relevant energy scales of the system, i.e. the

[10] We assume for simplicity $\Gamma = \Gamma_i = \Gamma_{\mathrm{S}i} + \Gamma_{\mathrm{N}i}$ for $i = \{1, 2\}$, i.e. $\Gamma_\mathrm{S/N} = \Gamma_{\mathrm{S/N}i}$.

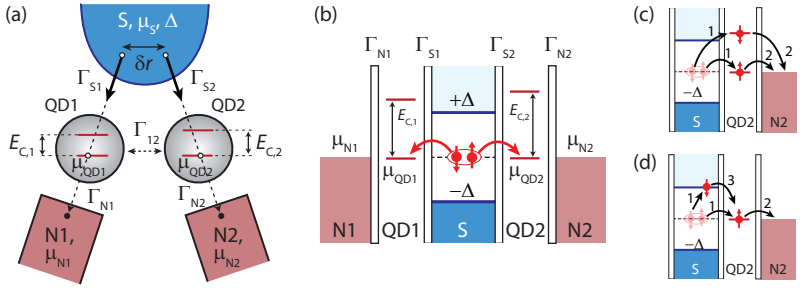

Figure 3.9.: (a) Schematic illustration of a CPS device with its characteristic parameters and energy scales. (b) Schematic of Cooper pair splitting at zero bias, i.e. at $\mu_S = \mu_{Ni} = \mu_{QDi}$. (c-d) Competing LPT processes, where two electrons of a Cooper pair tunnel either simultaneously (c, suppressed $\sim 1/E_C$) or sequentially via a virtual quasiparticle state in S (d, resonant Andreev tunneling, suppressed $\sim 1/\Delta$) into one arm (e.g. N2) of the device. Adapted from Refs. [19, 78, 209].

life-time broadening Γ of each N-QD-S part, the temperature kT and the applied bias $|eV_{SD}|$ have to remain smaller than Δ and E_C. Vanishing occupation probability of the QDs, i.e. $\Gamma_N \gg \Gamma_S$, and a weak interdot-coupling $\Gamma_{12} \ll \Gamma_N$ are also beneficial for a high CPS efficiency [19]. With further considerations [78, 193], the ideal working conditions of a CPS device can be summarized as $E_C, \Delta, \delta E \gg |eV_{SD}| > \Gamma, kT$, with $\Gamma_N \gg \Gamma_S, \Gamma_{12}$, and $\mu_{QD1} = -\mu_{QD2} \neq 0$. Finally, the CPS current is suppressed with a geometry dependent, still heavily debated prefactor [19, 20, 78, 151, 210–212], into which in any case an intuitively plausible term $\sim \exp(-\delta r/\xi_0)$ enters, capturing the spatial extent of a Cooper pair. Hence, in an actual CPS device the width $w \sim \delta r$ of the S contact should be of similarly small magnitude than the BCS coherence length.

After the initial proposal of *Recher et al.* [19], Cooper pair splitting – as a potential source of spin-entangled electrons – has generated a lot of interest. Microscopic theoretical descriptions of CPS devices have been developed [202, 210, 213–215] and the key experiments of Hofstetter *et al.* [20] and Herrmann *et al.* [21] could already demonstrate CPS by charge correlation measurements. This has been exploited further in finite bias [216] and noise correlation experiments [32], a near-unity efficiency of CPS has been achieved [33], and CPS has been unambiguously demonstrated in InAs nanowires [20, 32, 216, 217], CNTs [21, 33], graphene [218, 219] and self-assembled InAs [220] QDs. Nevertheless, a proof of entanglement is still lacking, and different proposals have been made to demonstrate the split electrons entanglement [221], using ferromagnetic detectors [38–40, 222], current and noise correlations [213, 223–225], or different spin projection axes in bent CNTs due to the intrinsic spin-orbit interaction [113].

4

Optimized large gap superconductor contacts[1]

Quantum phenomena in nanostructures with a superconductor (S) and a normal metal contact (N) coupled to low-dimensional electron systems like a quantum dot (QD) [30] have recently gained much attention due to potential applications in quantum technology. Especially prominent are transport phenomena at energies below the superconductor's energy gap, Δ, which typically comprise quasi-particle (QP) tunneling and Andreev processes due to Cooper pair transport (Chap. 3). This results in a large variety of subgap features in such structures, for example Majorana Fermions [10], which might be used for topological quantum computation [14], Cooper pair splitting [19–21, 32, 33] as a source of entangled electrons, resonant and inelastic Andreev tunneling [179], or Andreev bound states (ABSs) [165, 166, 171, 172] which can be implemented as Andreev qubits [15, 167]. Also QP processes can play a crucial role in this regime, which can e.g. lead to additional subgap features [83, 226], or to a poisoning of the bound state parity lifetime [173].

To identify subgap transport mechanisms, a transport gap much larger than the QD life time, $\Delta \gg \Gamma$, is very beneficial – a regime which is not easily achieved in S-QD hybrid devices. In addition, a strong suppression of the QP conductance in the subgap regime is required, which is commonly known as a "clean gap". The widely used superconductor Al [20, 21, 33] has yielded devices with good transport characteristics, long superconducting coherence lengths, ξ_0, and more recently also clean gaps [173, 227], but it's small gap

[1] Parts of this chapter have been published in similar form in Ref. [179] (Sec. 4.1) and Ref. [180] (Sec. 4.2).

usually renders spectroscopic investigations difficult. Since current fabrication technology for S-CNT systems hardly provides control over the coupling strength Γ, we therefore systematically investigated and optimized superconducting materials with large energy gaps Δ as superconducting contacts to CNTs, to achieve $\Delta \gg \Gamma$. Such large transport gaps are also desirable to study competing transport processes (local pair or Andreev tunneling) in Cooper pair splitter devices [19, 33], in finite-bias Cooper pair splitting experiments to reduce entanglement loss [19, 78, 216], or to combine superconducting and ferromagnetic contacts in a QD device [40]. In this chapter, we hence summarize the fabrication, characterization and relevant parameters for transport spectroscopy experiments of the narrow superconducting Niobium (Nb) and lead (Pb) contacts studied in this thesis.

4.1. Nb contacts

Bulk Niobium (Nb) is a type-II superconductor with a large superconducting gap of $\Delta_0 \sim 1.5\,\mathrm{meV}$, a critical temperature and upper critical magnetic field of $T_\mathrm{c} \sim 9.3\,\mathrm{K}$ and $B_\mathrm{c2} \sim 0.4\,\mathrm{T}$, respectively, and a rather small BCS coherence length of $\xi_0 \sim 10 - 40\,\mathrm{nm}$ [228]. Indeed, previous experiments on Nb-based S-QD devices have already shown increased superconducting transport gaps compared to Al devices, typically $0.2 < \Delta < 0.5\,\mathrm{meV}$, which enabled the observation of several fundamental transport processes [83, 164, 172, 182, 217, 226] and new effects due to the large critical field [229]. Nevertheless, most of these devices still exhibit either strongly suppressed (compared to the bulk value) [83, 164, 172, 182, 226] or additionally "soft" gaps [217, 229], and $\Delta \gtrsim 0.5\,\mathrm{meV}$ has not been (reliably) achieved with Nb contacts.

In the later presented experiments on N-QD-S devices (Chap. 6), we fabricate a $\sim 200\,\mathrm{nm}$ wide (in the region of the CNT) and $\sim 2\,\mathrm{mm}$ long Ti/Nb ($3\,\mathrm{nm}/40\,\mathrm{nm}$) superconductor contact to the CNT. For this purpose, clean EBL based on ZEP resist (Sec. 2.2.1) is employed on CNTs preselected by a H radical treatment (Sec. 2.2.2). The Ti/Nb bilayer is sputter deposited without sample rotation in a UHV chamber at a base pressure of $\sim 10^{-9}\,\mathrm{mbar}$. Ti ($3\,\mathrm{nm}$) serves a contact layer to the CNT, and is deposited at a relatively slow rate $\sim 0.04\,\mathrm{Å/s}$ and high background pressure (power $20\,\mathrm{W}$, Ar pressure/flow $15\,\mathrm{mTorr}/35\,\mathrm{sccm}$) to avoid physical damage to the CNT. $40\,\mathrm{nm}$ of Nb are then in-situ sputtered on top at a rate of $\sim 0.7\,\mathrm{Å/s}$ (power $180\,\mathrm{W}$, Ar pressure/flow $4\,\mathrm{mTorr}/40\,\mathrm{sccm}$). The Ti/Nb strips are connected to two bondpads fabricated in the same step, which allows to determine the superconducting properties of the strips in a two-terminal geometry. Figure 4.1(a,b) shows the two-terminal resistance R_strip of such a Nb strip as function of (a) the external magnetic field B applied perpendicular to the substrate (out-of-plane, OOP), and (b) the temperature, with a cryostat line resistance of (a) $415\,\Omega$ and (b)

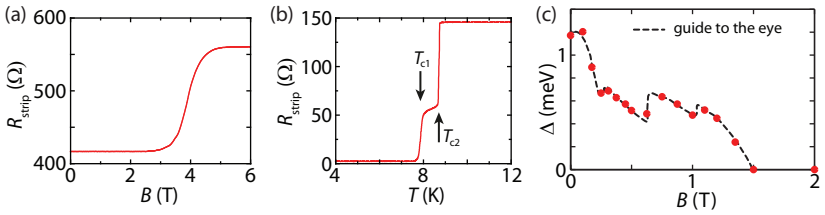

Figure 4.1.: (a,b) Resistance of a Nb strip measured in a two terminal configuration as a function of (a) the out-of-plane (OOP) magnetic field at $T = 110\,\mathrm{mK}$ base temperature, and (b) the temperature in a variable temperature insert (VTI). The two arrows mark two distinct superconducting transition temperatures $T_{c1} \sim 7.7\,\mathrm{K}$ and $T_{c2} \sim 8.7\,\mathrm{K}$. (c) Transport gap Δ vs out-of-plane field B (red points) for the device discussed in Chap. 6, extracted from individual charge stability diagrams similar to Fig. 6.1(c). The black dashed line is a guide to the eye.

$2.5\,\Omega$. The magnetic field dependence in (a) shows a broad transition to the normal state at $\sim 3-4.5\,\mathrm{T}$. In (b) we find two distinct superconducting transition temperatures, most likely due to different widths in the design of the superconductor strip. We ascribe the lower $T_{c1} \sim 7.7\,\mathrm{K}$ to the narrow part of the Nb strip in direct contact to the CNT. All the experiments presented for Nb-based devices in Chap. 6 are well below this T_{c1}, so that a temperature dependence of the superconducting energy gap can be neglected.

Using the above recipe to fabricate CNT N-QD-S devices with Ti/Nb contacts, we obtained a very good yield of low-ohmic contacts (cf. Fig. 2.6), so that different coupling strengths Γ and transport regimes (Sec. 3.3.1-3.3.3) are feasible. As discussed in Sec. 3.3.1, the characteristic separation of the CB diamonds due to the gapped QP DOS in S allows to determine the visible superconducting transport gap at lowest sample temperature and $B = 0$, Δ_0 [see e.g. Fig. 6.1(c)]. In all of the 13 N-QD-S junctions that could be successfully cooled down to low temperature, we reproducibly found a well-defined superconducting transport gap $\Delta_0 > 0.6\,\mathrm{meV}$, for most devices (10/13) $\Delta_0 \approx 1 \pm 0.2\,\mathrm{meV}$. These large gaps enabled us to observe resonant and inelastic AT in a Nb-based N-QD-S device, discussed in Chap. 6, where measurement data of two Nb-based devices with gaps of $\sim 1.2\,\mathrm{meV}$ and $\sim 1\,\mathrm{meV}$ are presented. To our knowledge, the observed gaps are also among the largest in CNT QD devices reported so far.

From individual charge stability diagrams in different external magnetic fields, one can also extract the visible transport gap Δ as function of B, shown exemplary in Fig. 4.1(c) for a device discussed extensively in Chap. 6. We find that the energy gap detected by the QD shrinks fast and monotonically up to $\sim 0.3\,\mathrm{T}$, then stays roughly constant up to $\sim 1.2\,\mathrm{T}$, and disappears around $\sim 1.5\,\mathrm{T}$. We will see in Chap. 6, that even while the visible

transport gap is closed, superconducting correlations still persist up to the critical field $B_{c2} \sim 3.5\,\mathrm{T}$, a value in agreement with the Nb strip measurements shown in Fig. 4.1(a). The detailed characteristics of Δ seems at first somewhat surprising. In the region between 0.3 and 1.2 T, we observe non-monotonic, systematic fluctuations around a constant value. The positions of this opening-closing behavior of Δ are quite reproducible in several repeated measurements and also evident in the V_{SD} vs B map shown in Fig. 6.5(a) of Chap. 6. In addition, we observe a hysteresis in Δ between up- and down-sweeps of B (not shown). We found a very similar characteristics for several Nb-based QD devices. While the exact origin of these fluctuations is not completely understood at present, we tentatively ascribe this behavior to vortices in the superconducting type (II) phase of the narrow Nb strip. Indeed, a first critical field $B_{c1} \sim 0.3\,\mathrm{T}$, marking the initial decay of Δ and the onset of the hysteresis and 'jumps', would be in reasonable agreement with literature values for thin Nb films [230]. For larger magnetic fields, vortices could enter the region of the narrow Nb strip close to the CNT. We speculate that, depending on the position and distance of these vortices relative to the 'sensing' CNT QD region the visible gap Δ could be larger or smaller, thus explaining the sudden jumps in Δ with a vortex rearrangement. Finally, we note that very similar signatures are recently observed for simple N-I-S junctions and subject of further research [231].

4.2. Pb contacts

Motivated by the complex magnetic field characteristics of our Nb leads, we systematically investigated and optimized lead (Pb) as narrow S contact for CNT QD devices. In contrast to Nb, bulk Pb is a type-I superconductor with strong electron-phonon coupling, with a relatively large coherence length and superconducting gap of $\xi_0 \sim 90\,\mathrm{nm}$ and $\Delta_0 \sim 1.3\,\mathrm{meV}$, respectively, a critical temperature of $T_c \sim 7.2\,\mathrm{K}$, and a low critical field of $B_c \sim 80\,\mathrm{mT}$ [228]. Indeed, also in Pb-based devices large transport gaps close to the bulk value have already been demonstrated for CNTs, though only with implemented Al_2O_3 or Pb oxide tunnel barriers [82, 232, 233]. Mostly at the time of this study Pb contacts also allowed the observation of Cooper pair splitting in graphene [219], and high critical currents in graphene and nanowire-based Josephson junctions [234, 235]. The implementation of narrow superconducting Pb contacts with large transport gaps, which enable different coupling strengths Γ to QDs, has however not been achieved.

By evaporating Pb test contacts, we found that a direct, not optimized evaporation of Pb at room temperature (RT) typically results in a strong island growth, where oxidation between the grain boundaries can result in highly resistive normal conducting Pb strips. We also did not achieve low-

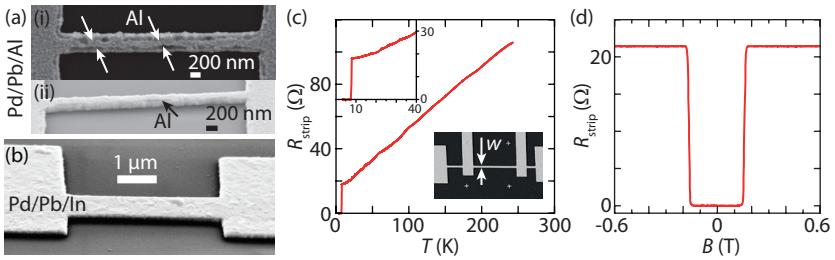

Figure 4.2.: (a) SEM images (i: top view, ii: tilted side-view) of a $\sim$ 400 nm wide Pd/Pb/Al (5/100/5 nm) reference structure. For $w \lesssim 400$ nm, Al does not entirely cover the surface any more (arrows). (b) Tilted side-view SEM image of a Pd/Pb/In strip. (c, d) $R_{\mathrm{strip}}(T)$, $R_{\mathrm{strip}}(B)$ resistance measurements of a $w = 180$ nm wide Pd/Pb/In (4.5/110/20 nm) reference strip, indicating a sharp transition to the superconducting state. The lower inset in (c) shows the used 4-terminal measurement geometry.

ohmic contacts to CNTs with such bare Pb contacts, and hence systematically studied different multi-layer systems to achieve a good coupling to the CNT, while maintaining the superconducting properties also in very narrow, $w \lesssim$ 200 nm strips. To this purpose, we fabricated $L \sim 10\,\mu$m long test strips of varying widths 140 nm $< w < 1\,\mu$m in a 4-terminal measurement geometry [Fig. 4.2(c), lower inset] for each multi-layer system, and characterized the strips by electrical transport measurements at low temperature. We studied the multi-layer systems Ti/Pb/Al, Pd/Pb/Al, Pd/Pb/Pd and Pd/Pb/In with varying Pb thicknesses of $d \sim 50 - 150$ nm. Here, thin Ti or Pd bottom layers enable low-ohmic contacts to CNTs, and Al, Pd or In were tested as top layer to protect from oxidation. To reduce the mobile Pb's surface diffusion and island growth, Pb was evaporated at a sample stage temperature of $\sim -100^{\circ}$C, and the lift-off procedure in the resist remover was carried out at RT ("cold" lift-off). While generally superconducting properties can be observed for $w >$ 400 nm in all multi-layer systems, narrow superconducting Pb strips are more difficult to achieve. We found that a Ti bottom layer is not compatible with a smooth growth of Pb in narrow channels, and an Al top layer does not cover the entire narrow Pb strip surface below a certain w, see Fig. 4.2(a). This hence still results in oxidation between Pb grains from top and highly resistive strips below a certain width. While a 20 nm thick Pd top layer grows smoothly on the Pb strips, it also strongly suppresses superconductivity in narrow strips, possibly due to the inverse proximity effect. In contrast, an optimized Pd/Pb/In multi-layer shows all the desired characteristics, which we summarize exemplary for the fabrication of a CNT-based N-QD-S device.

A $\sim$ 200 nm wide S contact is again defined by optimized ZEP EBL (Sec. 2.2.1) on a CNT preselected by a H radical treatment (Sec. 2.2.2). Most crucially, the

S contact is fabricated last to avoid Pb surface diffusion in (otherwise) subsequent processing and heating steps. We also employ outer normal metal leads and bonding pads for the central narrow S contact (fabricated previously along with the N contacts), to avoid a difficult bonding process on mechanically soft Pb. The optimized Pd/Pb/In (4.5−6/110/20 nm) multi-layer is then deposited *in-situ* using electron beam evaporation[2] at a base pressure $< 10^{-7}$ mbar with a controlled Pb deposition rate of ~ 1.5 Å/s and a sample stage temperature of $\sim -100°$C. These parameters favor a more uniform Pb growth and reduce Pb surface diffusion. In contrast to the tunnel barriers implemented in Refs. [82, 232, 233], the Pd wetting layer to the CNT allows for some tunability of the S contact coupling strengths and for a smooth and homogeneous Pb growth, see Fig. 4.2(b). We employ the superconductor In [228] as a capping layer for oxidation protection, which forms a dense and self-limited native oxide layer [236] covering the upper Pb strip surface [Fig. 4.2(b)]. On metallic 4-terminal test strips [Fig. 4.2(c), lower inset], we find superconducting correlations in resistance measurements for all strip widths down to $w = 150$ nm, and determine approximately the same critical temperature of $T_c \approx 7.2 - 7.4$ K and critical out-of-plane (OOP) magnetic field of $B_c^{OOP} \approx 150 - 200$ mT. Such resistance measurements are shown in Fig. 4.2(c,d) for a 180 nm wide Pd/Pb/In strip. S-CNT-N devices fabricated in this manner have RT resistances of $\sim 12\,\text{k}\Omega - 1\,\text{M}\Omega$ (for a statistics see Fig. 2.6), so that different tunnel coupling strengths of the S contacts are feasible. The device characteristics are stable on the timescale of a day under ambient conditions, but the S contacts are damaged during rapid temperature cycling in the cryogenic setup.

In transport measurements on Pb-based N-QD-S devices, we again reproducibly found very well-defined and large superconducting transport gaps of $\Delta_0 \sim 0.65 - 1$ meV for all 14 measured N-QD-S junctions with Pd interlayer thicknesses of 4.5 and 6 nm. We present the relevant data for such Pb-based devices with different coupling strengths Γ_S in Chap. 5, 7 and 8. Doing a more careful analysis, we find a maximal range $\Delta_0 = 0.86 - 1$ meV with an average $\Delta_0 = 0.93 \pm 0.06$ meV for the 8 N-QD-S junctions with a Pd thickness of $d_{Pd} = 4.5$ nm, and a maximal range $\Delta_0 = 0.65 - 0.8$ meV with an average $\Delta_0 = 0.71 \pm 0.05$ meV for the remaining 6 N-QD-S junctions[3] with a Pd thickness of $d_{Pd} = 6$ nm. Since our devices hence indicate a reduced Δ_0 with increasing Pd thickness, we ascribe the gap reduction from the bulk Pb value to the proximity effect in the Pd interlayer [237, 238] as discussed in Sec. 3.2.1. Most importantly, the observed transport gaps seem **not** to depend on the

[2] Pd deposition rate ~ 0.4 Å/s, In rate $\sim 0.6 - 0.8$ Å/s. Before depositing material on the sample, $20 - 30$ nm of Pb/In are always evaporated off the targets, to remove possible oxides. For Balzers evaporation system: 10 kV e-beam acceleration voltage for Pd, but only 7.5 kV for Pb/In to at all gain control over the deposition rates (Pb already evaporates at extremely small e-gun currents, typically ~ 5 mA).

[3] For device C in Sec. 7.1, we only included the value of Δ_2 in this statistics due to the less clear interpretation of Δ_1.

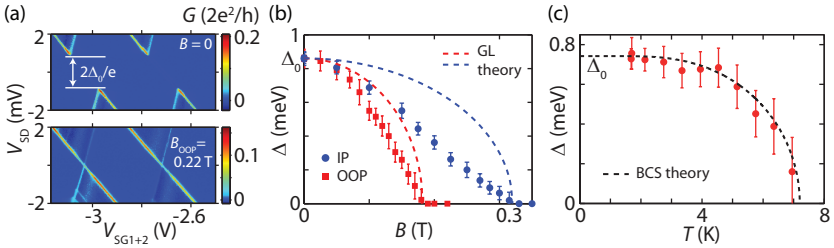

Figure 4.3.: (a) Differential conductance G as function of V_{SD} and a combined sidegate voltage $V_{\mathrm{SG1+2}}$ for one arm of the device discussed in Sec. 5.2, at 30 mK base temperature, $V_{\mathrm{BG}} = -1\,\mathrm{V}$, and applied out-of-plane magnetic fields $B = 0$ and $B_{\mathrm{OOP}} = 0.22\,\mathrm{T}$. (b) Δ of this device as function of the external out-of-plane (OOP, red squares) and in-plane (IP, blue dots) magnetic field B at $\sim 30\,\mathrm{mK}$ base temperature. The dashed lines show the corresponding Ginzburg-Landau (GL) dependence. (c) Δ as function of T for the device discussed in Sec. 5.1. The dashed line is the expected BCS dependence from Eq. (3.3). All data in (b) and (c) are extracted from CB spectroscopy similar to (a), where the error bars indicate the individually estimated read-out and statistical errors from 2-4 datasets.

(very different) coupling strengths Γ_{S} and RT resistances of the devices. This is consistent with the BTK model presented in Sec. 3.2.1, and suggests that we simply probe the superconducting gap of the metallic Pd-Pb system in our experiments. Similar to Ref. [227] for epitaxial Al-semiconductor nanowires, we also find a strong (~ 100 times) suppression of the subgap conductance compared to the normal state ($B > B_{\mathrm{c}}$) or the above-gap conductance in traces along a CB resonance $\mu_{\mathrm{QD}} = \mu_{\mathrm{N}}$ for weakly tunnel-coupled devices measured at $\sim 30\,\mathrm{mK}$ base temperature (see App. B and Fig. B.2), suggesting a clean and hard superconducting transport gap.

To demonstrate the relevant characteristics of our superconducting Pb contacts, we also plot the temperature- and magnetic field dependence of Δ in Fig. 4.3(b) and (c). This data is extracted from individual CB measurements [see e.g. Fig. 4.3(a)] on two different N-QD-S devices. For the device discussed in Sec. 5.2, which was measured in a dilution refrigerator at a base temperature of 30 mK, the B-dependence of Δ is plotted in Fig. 4.3(b). At zero field we find $\Delta_0 = 0.86\,\mathrm{meV}$ for this device. The field is either applied in-plane (IP) with an angle of $\sim 15^\circ$ to the Pb strip long axis, or out-of-plane (OOP), i.e. perpendicular to the Pb film. Figure 4.3(a) demonstrates that the CB diamonds close at fields larger than the critical field B_{c} of the superconducting Pb strip. $\Delta(B)$ closes monotonically with increasing B for both cases and we extract the critical fields $B_{\mathrm{c}}^{\mathrm{OOP}} \sim 180\,\mathrm{mT}$ and $B_{\mathrm{c}}^{\mathrm{IP}} \sim 320\,\mathrm{mT}$ for the OOP and IP configuration, respectively, which are of similar magnitude as the bulk Pb value and coincide with the resistance measurements on metallic Pb reference strips [Fig. 4.2(d)]. $B_{\mathrm{c}}^{\mathrm{IP}} > B_{\mathrm{c}}^{\mathrm{OOP}}$ is expected for a long, slab-like Pb strip geometry with $L \gg w > d$, where the screening currents can reach higher val-

ues in the IP configuration before the critical current density is reached. The data do not agree[4] well with the standard Ginzburg-Landau (GL) expression $\Delta = \Delta_0 \cdot \sqrt{1-(B/B_c)^2}$ for a type I superconductor [239], plotted with the respective device parameters (dashed lines). This is most likely due to the nonconformity of the Pb strip dimensions with the assumptions for the above GL expression [239–241], where also the exact local Pb growth configuration and the proximitized Pd layer may play a significant role. Figure 4.3(c) shows the temperature dependence of Δ, for the device discussed in Sec. 5.1. The data agree well with the energy gap obtained from Eq. (3.3) (dashed line), the BCS dependence with $\Delta_0 = 0.74\,\mathrm{meV}$ and $T_c = 7.2\,\mathrm{K}$. This BCS dependence of Δ is expected to be also approximately valid for the superconductor Pb with a strong electron-phonon coupling [242]. Hence, the ideal temperature dependence of Δ and its monotonic reduction with magnetic field demonstrate that sub-micron Pb contact strips are ideally suited for transport experiments in S-QD devices.

4.3. Conclusions

In conclusion, we demonstrated the optimized growth and fabrication of well-defined, narrow Ti/Nb or Pd/Pb/In multilayer-based S contacts for CNT devices. These contacts allow for different coupling strengths Γ_S to the QD, and lead to reproducibly large and "clean" superconducting transport gaps in S-QD devices. Hence, the relevant condition $\Gamma \ll \Delta$ for subgap transport spectroscopy experiments in S-QD devices can be reliably achieved, a crucial prerequisite for the experiments presented in the following chapters. We ascribe the reproducibly large values of Δ in our devices to an improved CNT-metal interface quality with optimized ZEP EBL, as discussed in Sec. 2.2.1 and 2.2.2. The observed complex magnetic field characteristics of Nb contacts, in agreement with previous findings [217, 229], make normal state control experiments difficult, and the rather short coherence length might pose a disadvantage for Cooper Pair splitting experiments [19]. In contrast, the optimized Pd/Pb/In contacts have ideal characteristics for transport spectroscopy experiments in S-QD devices. Our fabrication scheme for Pb contacts can also be easily transferred to other material systems, and has already been successfully applied to graphene and InAs nanowires in our group with support of the author. Our findings of a large gap Δ, depending rather on the wetting interlayer thickness than on the coupling strength Γ_S of S to the QD, might also contribute to the discussion about "hard gaps"/"soft gaps" and the superconducting proximity effect in mesoscopic QD or nanowire structures [227, 243–245].

[4] Very recently and without sufficient time to still address this, the author became aware that a comparison with GL theory might not be completely appropriate for our narrow and thin Pb contacts. Since this has no implications on all results presented later, we postpone a detailed discussion to the corrected and final version of the thesis.

5

Subgap resonant quasiparticle transport in N-QD-S devices[1]

We have seen in Chap. 3, that depending on the tunnel coupling strength of the S contact to the QD, transport phenomena in N-QD-S devices are typically governed by a competition between single-electron or quasi-particle (QP) tunneling and Andreev processes due to Cooper pairs in S. At bias voltages below the superconductor's transport gap, this competition leads to a variety of subgap features. While most studies have focussed on features due to Andreev processes, recent experiments have also highlighted the importance to understand in detail the QP excitations in such structures, which, for example, lead to additional subgap features [83, 226], or to a poisoning of the bound state parity lifetime [173]. Especially in N-QD-S systems [30], these quasiparticle processes remained relatively unexplored so far, mostly due to the required large superconducting gaps in the experiments.

In this chapter, we hence discuss N-QD-S devices in which transport is dominated by QP tunneling only, and analyze the resulting subgap features. To achieve a high spectroscopic resolution in the subgap region, i.e. $\Gamma \ll \Delta$, we employ optimized Pd/Pb/In multi-layer S contacts (cf. Sec. 4.2). This allows us to also experimentally demonstrate the impact of the superconducting gap on the CB diamond structure in N-QD-S devices, sketched previously in Sec. 3.3.1. In the first section we report subgap transport resonances that originate from tunneling of thermally excited QPs through a CNT QD. Such features were predicted recently [183, 246] and reported for experiments in S-

[1] Parts of this chapter have been published in similar form in Ref. [180] (Sec. 5.1), or will be published elsewhere (Sec. 5.2, manuscript in preparation).

QD-S devices [83, 226], whereas the lack of a large superconducting transport gap prohibited the observation in N-QD-S devices. In Sec. 5.2, we describe transport experiments on a three-terminal, single QD connected to one S and two N contacts. While many subgap transport phenomena are predicted in such three-terminal devices due to Andreev processes [177, 200, 247, 248], we demonstrate here that already QP transport and the multi-terminal geometry can generate additional subgap transport resonances, also clarifying the interpretation of the debated features [246] in earlier experiments [82].

5.1. Thermally activated quasiparticle transport

We first study in some detail the thermally activated QP transport in the transport gap Δ of a N-QD-S device, i.e. for bias voltages $|V_{\mathrm{SD}}| < \Delta/e$. If the temperature of a superconductor becomes comparable to the size of the superconducting gap, $kT \sim \Delta$, QPs are excited thermally across the gap with an occupation probability given by the Fermi distribution in S. These QPs can tunnel through the QD to the normal contact and lead to additional subgap transport features, as proposed in Refs. [183, 246] and found in experiments on S-QD-S devices for both, the sequential [83] and the cotunneling [226] regime. While similar sequential tunneling resonances due to thermally excited QPs have been proposed theoretically also for N-QD-S devices [246], no such features were reported so far.

Figure 5.1(a) shows a false color SEM image of the studied N-QD-S device, including a schematic of the measurement setup. Using our optimized ZEP EBL (Sec. 2.2.1) on a highly p-doped Si/SiO_2 substrate used as a backgate (BG), we fabricate a single sidegate (SG), and a $\sim 200\,\mathrm{nm}$ wide S contact separated by $\sim 300\,\mathrm{nm}$ from an N contact on a CVD-grown CNT preselected with the use of a H radical treatment (Sec. 2.2.2). We use 50 nm of e-beam evaporated Pd for the N contact, the SG, and for the outer leads and bonding pads of the narrow S contact. For the S contact fabricated last, we employ a Pd/Pb/In (6/110/20 nm) multi-layer discussed in Sec. 4.2. This N-CNT-S device had a RT resistance of $\sim 30\,\mathrm{k\Omega}$. All experiments presented here employed standard lock-in techniques to measure $G = \mathrm{d}I/\mathrm{d}V_{\mathrm{SD}}$ and were performed in a variable temperature insert, allowing experiments at temperatures of $1.5 - 300\,\mathrm{K}$. The sample temperature T is determined by a standard resistance thermometer coupled to the device by a copper bridge.

In Fig. 5.1(b) the differential conductance $G = \mathrm{d}I/\mathrm{d}V_{\mathrm{SD}}$ of the device is plotted as a function of the bias V_{SD} applied to S and of the sidegate voltage V_{SG}, at $T = 1.68\,\mathrm{K}$ and the backgate voltage $V_{\mathrm{BG}} = -2.987\,\mathrm{V}$. We observe regular CB diamonds that are separated due to a well-defined superconducting transport gap Δ_0 (see Sec. 3.3.1), where transport is suppressed for $|V_{\mathrm{SD}}| < \Delta_0/e$, with $\Delta_0 \approx 0.74\,\mathrm{meV}$ at the lowest sample temperature. The regular,

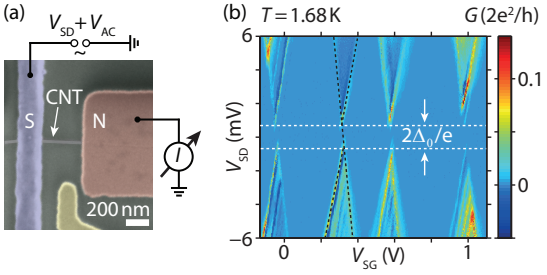

Figure 5.1.: (a) False-color SEM image of the studied N-QD-S device with a Pd/Pb/In S contact and schematic of the measurement setup. (b) G as function of V_{SD} and V_{SG} at $T = 1.68\,\mathrm{K}$ and $V_{BG} = -2.987\,\mathrm{V}$. The white dashed lines mark the onset of QP tunneling and thus the superconducting transport gap Δ_0.

2-fold periodic structure of the CB diamonds in Fig. 5.1(b) indicates a clean, defect-free CNT QD, for which a rich substructure of excited states can be resolved due to the sharp QP peaks in the Pb DOS [82, 83, 182]. We extract a charging energy of $E_C \sim 8.7\,\mathrm{meV}$ and a spacing of the lowest excited states of $\delta E \sim 1.6\,\mathrm{meV}$. From CB spectroscopy in the normal state at $T = 1.68\,\mathrm{K}$, $V_{SD} = 0$ and $B_{OOP} = 0.6\,\mathrm{T} > B_c$, we determine a typical CB resonance width $\sim 0.5\,\mathrm{meV}$. Fits with a Breit-Wigner (BW) line shape (1.10) due to life-time broadening agree well with these data, in spite of the relatively large temperature, with typical tunnel couplings $\Gamma_1 \sim 1-10\,\mu\mathrm{eV}$ and $\Gamma_2 \sim 500\,\mu\mathrm{eV}$ (not shown). Since we do not observe Andreev bound states [165, 166, 171, 172], we tentatively ascribe the smaller coupling to S, i.e. $\Gamma_S = \Gamma_1$. This places the device in a regime $\Gamma_S \ll \Delta_0 < \delta E \ll E_C$, in which transport is dominated by Coulomb repulsion and quasi-particle tunneling [83, 181], while Andreev tunneling (Chap. 6) is strongly suppressed.

We now analyze thermally activated QP transport resonances, which appear also at subgap bias voltages $V_{SD} < \Delta/e$. Figure 5.2(a) shows a detailed map of G for a CB region as function of V_{SD} and the gate voltage V_{SG} at $T = 1.68\,\mathrm{K}$ (left) and for an increased temperature of $T = 3.95\,\mathrm{K}$ (right). While we observe only the standard CB diamond edges separated by Δ_0 at the lowest T, additional lines (arrows) labeled TL (left) and TR (right) appear for elevated temperatures besides the expected thermal broadening of CB features. At a finite bias V_{SD}, the conductance maxima of TL and TR are accompanied by regions of negative differential conductance (NDC, dark blue). We study the temperature dependence of these extra lines TL and TR in cross-sections $G(V_{SG})$ at $V_{SD} = 0$ and $V_{SD} = \pm 1\,\mathrm{mV}$ ($+1\,\mathrm{mV}$ for TR and $-1\,\mathrm{mV}$ for TL). This is shown explicitly only for $V_{SD} = 0$ in the waterfall plot of Fig. 5.2(b), but we perform an equivalent analysis also for $V_{SD} = \pm 1\,\mathrm{mV}$. In Fig. 5.2(b), each curve is an average over a small bias window $\Delta V_{SD} = \pm 8\,\mu\mathrm{eV}$ in individual CB spectroscopy measurements using a moving average filter. With increasing temperature the amplitude of the features TL and TR increase, while the

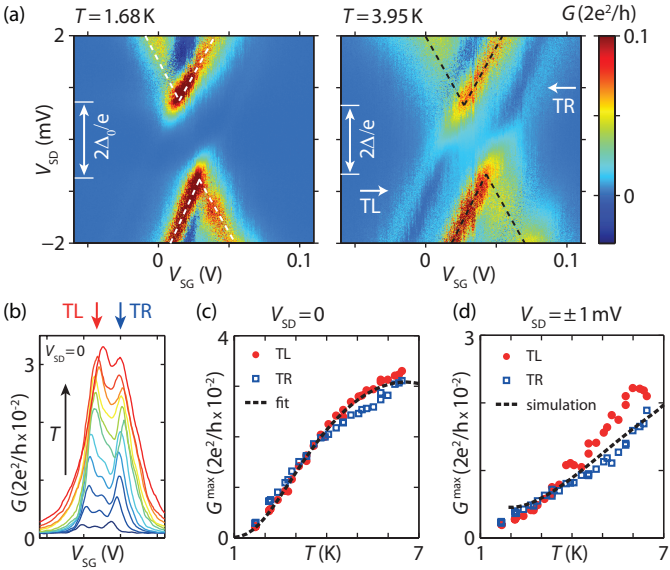

Figure 5.2.: (a) G as function of V_{SD} and V_{SG} at $T = 1.68\,\mathrm{K}$ (left) and $T = 3.95\,\mathrm{K}$ (right), for $V_{\mathrm{BG}} = -2.987\,\mathrm{V}$. Extra thermal lines (TL/TR, arrows) appear at higher temperatures. (b) Waterfall plot of cross-sections at $V_{\mathrm{SD}} = 0$ in (a) for $T = 1.68\,\mathrm{K}$ (dark blue) to $6.45\,\mathrm{K}$ (red), extracted from CB spectroscopy with an averaging procedure (text). (c,d) Maximum conductance G^{max} of TL (red points) and TR (blue squares) as function of T for (c) $V_{\mathrm{SD}} = 0$ and (d) $V_{\mathrm{SD}} = \pm 1\,\mathrm{mV}$. The dashed line in (c) represents a best fit with Eq. (3.5) and fit parameters $\Gamma_1 = 33\,\mu\mathrm{eV}$, $\Gamma_2 = 490\,\mu\mathrm{eV}$, the line in (d) a model simulation with the same parameters.

background is zero due to CB.[2] To compare with the model discussed below, we extract the maximum conductance of TL and TR from such averaged curves both for $V_{\mathrm{SD}} = 0$ (see waterfall plot) and for $V_{\mathrm{SD}} = \pm 1\,\mathrm{mV}$ (not shown). This temperature dependence of the maximum conductance G^{max} of TL (red points) and TR (blue squares) is plotted in Fig. 5.2(c) and (d) for $V_{\mathrm{SD}} = 0$ and $V_{\mathrm{SD}} = \pm 1\,\mathrm{mV}$, respectively, which show a qualitatively different, but distinctive monotonic increase in G^{max} with increasing temperature.

We ascribe the resonance lines TL and TR to the sequential tunneling of thermally excited QPs in the superconductor, as shown schematically in Fig. 5.3(a): at elevated temperatures of $kT \sim \Delta$, the quasi-electron population at $E > +\Delta$ in S (light red) is finite. When the QD's electrochemical

[2] We ascribe the small central subgap conductance peak between TL and TR to the thermally broadened DOS in the S contact, coinciding with $\mu_{\mathrm{QD}} = \mu_{\mathrm{N}}$. The analysis at $V_{\mathrm{SD}} = \pm 1\,\mathrm{mV}$ shows that this finite subgap conductance at elevated temperatures has no influence on our analysis.

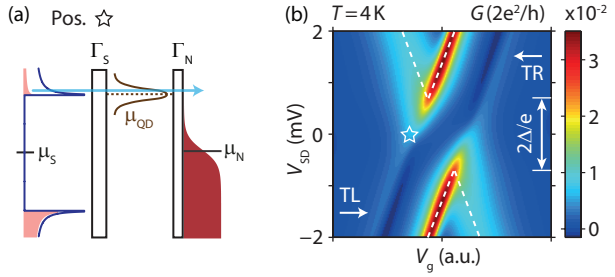

Figure 5.3.: (a) Schematic of thermally activated quasiparticle transport for $kT \sim \Delta$. Thermally excited quasiparticles in S (light red) tunnel through the QD if $\mu_{\rm QD} = \mu_{\rm S} + \Delta$ even for $\mu_{\rm S} \sim \mu_{\rm N}$. (b) Model simulation of $G(V_{\rm SD}, V_{\rm g})$ with Eq. (3.5) (text). Similar to the experiment, extra thermal lines TL and TR (arrows) appear. The star indicates the position of the schematic in (a).

potential $\mu_{\rm QD}$ is aligned with this population, i.e. $\mu_{\rm QD} = \mu_{\rm S} + \Delta$, a current flows even for a bias smaller than Δ/e, resulting in the additional resonance TL tuned by the bias and the gate voltages via the QD resonance condition. Similarly, the resonance TR is due to the condition $\mu_{\rm QD} = \mu_{\rm S} - \Delta$ for quasi-hole excitations.

We model these QP processes in the simple resonant tunneling picture discussed in Sec. 3.3.1, using Eq. (3.5) to calculate the differential conductance G. Figure 5.3(b) shows the resulting G for $\Delta = 0.7\,\text{meV}$, $T = 4\,\text{K}$, $\Gamma_1 = 10\,\mu\text{eV}$ and $\Gamma_2 = 500\,\mu\text{eV}$. The model captures the gate voltage and bias dependence of the experiment very well, including the peak-dip structure with negative differential conductance (NDC) next to the TL/TR resonances due to the non-monotonic DOS of S. These results also agree with previous calculations using a microscopic model [246].

To substantiate that the observed subgap features are due to thermal QP tunneling, we now analyze the temperature dependence of TL and TR's resonance amplitudes at zero bias. The corresponding data are plotted in Fig. 5.2(c). For a zero-width QD resonance $T_{\rm QD}(E) = \delta(\Delta E)$ in Eq. (3.5), one finds $G_{\rm T}^{\rm max} \propto 1/kT \cdot \cosh^{-2}(\Delta/2kT)$ at $V_{\rm SD} = 0$ for $T \ll T_{\rm c}$. Thus, in agreement with a microscopic description [83], we expect a low-temperature thermally activated characteristics of $G^{\rm max}$ as $\sim \cosh^{-2}(\cdots)$ and a $\sim 1/kT$ decay at larger temperatures, $kT \gg \Delta$, well known for sequential tunneling processes. Due to its large superconducting gap, the device is in the regime dominated by the $\cosh^{-2}$ term. It is important to note that in the studied temperature range $kT \sim \Delta \sim kT_{\rm c}$, the closing of the transport gap for $T \lesssim T_{\rm c}$ plays already a significant role. To take into account both, the finite width Γ of the resonance and the temperature dependence of Δ, we fit Eq. (3.5) to the zero-bias data using the BCS temperature dependence of the gap Δ obtained from Eq. (3.3).

Figure 4.3(c) shows that the assumption of a BCS temperature dependence $\Delta(T)$ is justified for this device. Using $\Delta_0 = 0.74\,\mathrm{meV}$ and $T_\mathrm{c} = 7.2\,\mathrm{K}$ determined independently from a resistance measurement of the Pb strip, we obtain the tunnel couplings $\Gamma_1 \approx 33\,\mu\mathrm{eV}$ and $\Gamma_2 \approx 490\,\mu\mathrm{eV}$ as the only adjustable parameters for the best fit to the data. The fit is shown in Fig. 5.2(c) as a dashed line, which describes the data very accurately. The extracted coupling parameters agree well with the ones found from independent CB line shape fits in the normal state. This model also reproduces the finite-bias data: Inserting the tunnel couplings obtained from the zero bias fit into Eq. (3.5), we obtain the $V_\mathrm{SD} = \pm 1\,\mathrm{mV}$ amplitudes in a model simulation without additional fit parameters. The resulting curve is plotted as dashed line in Fig. 5.2(d) and also agrees well with the experiment. We note that for a given temperature, both, the experiment and the model exhibit only a very weak dependence of G^max on V_SD for $|eV_\mathrm{SD}| > kT$ in the direction away from the CB diamond edge, see e.g. Fig. 5.2(a) and Fig. 5.3(b). This is expected from the sketch in Fig. 5.3(a), because the Fermi function $f_\mathrm{N}(E)$ changes significantly only in an interval kT around μ_N.

To summarize the two-terminal experiments, we report thermally activated transport resonances for biases below the superconducting energy gap in a CNT QD device with a superconducting Pb and a normal metal contact. These resonances are due to the superconductor's finite quasi-particle population at elevated temperatures and can only be observed when the QD life-time broadening is considerably smaller than the gap, which is achieved by using a Pd/Pb/In multi-layer contact. The accurate description of the subgap resonances by a simple resonant tunneling model furter illustrates the ideal characteristics of the optimized Pd/Pb/In contacts, corroborates a BCS-type S DOS, and gives an alternative access to the tunnel coupling strengths in a QD.

5.2. "Subgap" transport due to a three-terminal QD

In many experiments with S-QD devices, three- or even multi-terminal geometries are used [20, 21, 33, 82, 169, 170, 229]. Theoretical works predict novel subgap transport phenomena due to the multi-terminal geometry already for the simplest case of a single QD connected to one S and two N contacts [177, 200, 247, 248], of which not all might be due to Andreev processes [82, 246]. While three-terminal QDs with only N contacts have been studied extensively both in theory [249, 250] and experiments [34, 251–253], there exists, to our knowledge, only one experiment with one S and two N contacts coupled to a single QD. In this visionary experiment, Dirks *et al.* [82] performed transport spectroscopy with a weakly tunnel-coupled superconducting probe on a CNT QD coupled to two N terminals, and found novel

subgap lines when an additional bias voltage was applied between the two N contacts, even if transport was dominated by quasiparticle tunneling only. To interpret these surprising subgap features, Dirks *et al.* suggested that they might be due to an inelastic scattering of electrons [82], while others proposed thermally excited quasiparticles in S (Sec. 5.1) as origin [246], even if $kT \ll \Delta$ in the experiment. Using a similar, three-terminal single QD system with one S and two N contacts, we show that such transport resonances can be solely caused by QP transport and the three-terminal device geometry. Here, we also make use of a peculiar advantage of three-terminal devices, which allows one to determine absolute coupling parameters to each contact in the limit of low T, $kT \ll \Gamma$, in the normal state of S [34].

5.2.1. Three-terminal N-QD-S system

We use a CNT contacted with one weakly coupled, $\sim$ 200 nm wide central superconducting (S) Pb contact (Sec. 4.2) and two normal (N) metal contacts at a distance of $\sim$ 300 nm from S to investigate (subgap) transport processes in a three-terminal or Cooper pair splitter geometry [33], with two sidegates (SGs) for individual electrical tuning of the two CNT sides. Figure 5.4(a) shows a schematic of such a three-terminal geometry for a single QD forming between the N contacts, and Fig. 5.4(b) a false color SEM image of the device on which the experiments were performed. As in the previous section, the contacts are structured on a CVD-grown CNT preselected with a H radical treatment (Sec. 2.2.2) by means of optimized ZEP EBL (Sec. 2.2.1), on a highly p-doped Si/SiO_2 substrate used as a backgate (BG). For the N contacts, SGs, outer leads and bonding pads also of the narrow S contact we use 50 nm of e-beam evaporated Pd. As S contact, we employ a Pd/Pb/In (4.5/110/20 nm) multi-layer, which results in large superconducting transport gaps (Sec. 4.2). The employed CNT device had S-CNT-N1(N2) RT resistances of $\sim 1\,\mathrm{M}\Omega$. All experiments were carried out in a dilution refrigerator with a base temperature of $\sim$ 30 mK. Figure 5.4(b) shows the used measurement setup: A dc voltage, V_S, with a small superimposed ac excitation $V_\mathrm{AC} \sim 10\,\mu\mathrm{V}$ is applied at the S contact, while measuring simultaneously either the current $I_{1,2}$ or by standard lock-in techniques the differential conductance $G_{1,2} = \mathrm{d}I_{1,2}/\mathrm{d}V_\mathrm{S}$ in the two N contacts. Additional dc bias voltages $V_{1,2}$ can be applied to the N contacts, or they can be individually set floating (fl) with a switch $S_{1(2)}$ at RT. In the three-terminal setup, we define voltage differences as $V_{ij} \equiv V_i - V_j$, for $i \neq j$ and $i, j \in \{\mathrm{S}, 1, 2\}$.

In Fig. 5.4(c), the simultaneously measured differential conductance G_1 and G_2 are plotted as a function of the bias applied to S, V_S, and as a function of the SG1 voltage only, V_SG1, at fixed voltages of $V_\mathrm{BG} = -1\,\mathrm{V}$ and $V_\mathrm{SG2} = -2\,\mathrm{V}$. With a separate reference measurement (cf. Sec. 5.2.2), the electrical potentials of the two N contacts are adjusted to the same value during this

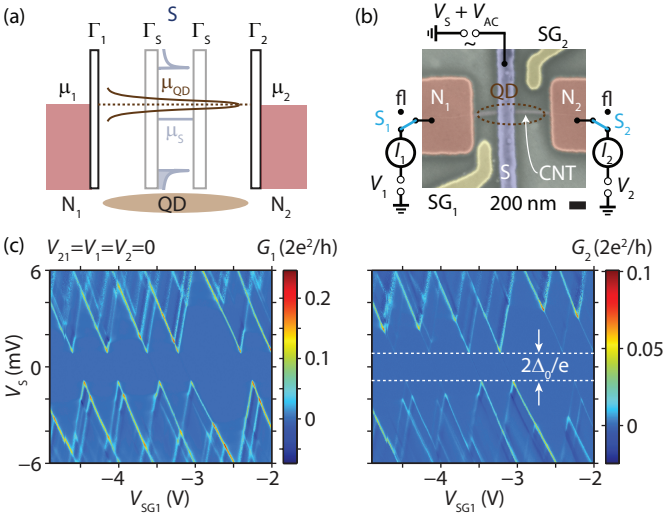

Figure 5.4.: (a) Schematic of a three-terminal QD coupled to one S (faint, overlain) and two N contacts. (b) False-color SEM image of the studied device and schematic of the measurement setup. Currents I_1 and I_2 are measured at the two N contacts, and DC bias voltages V_S, V_1, V_2 can be applied individually to the contacts. The two N contacts can be individually set floating (fl) with a switch $S_{1(2)}$. (c) Simultaneously measured differential conductance G_1 and G_2 of the device as a function of the bias V_S applied to the S contact and the sidegate voltage V_{SG1}, at fixed voltages of $V_{BG} = -1\,V$ and $V_{SG2} = -2\,V$. The two N contacts have the same potential, i.e. $V_{21} = V_1 = V_2 = 0$. The dashed lines mark the onset of QP tunneling and thus the superconducting transport gap Δ_0.

measurement, i.e. $V_{21} = 0$. Again, we observe the same regular CB diamond structure separated by a well-defined superconducting transport gap $\Delta_0 \approx 0.86\,meV$ in both conductance maps, closely resembling the data in Sec. 5.1. The twofold or fourfold periodicity of the CB diamonds – depending on the gate voltage region – suggests a clean CNT QD, whereas the rich substructure of excited states, elastic and inelastic cotunneling lines is due to the enhanced spectroscopic resolution with the sharp quasiparticle peaks in the Pb DOS [82, 83, 182, 226]. Most strikingly, we observe conductance maxima in both G_1 and G_2 at the same gate voltage and bias position when using only one sidegate voltage for tuning. These findings remain intact when tuning the other sidegate (not shown). Hence, we deduce that there is only a single, large QD forming in the CNT between the two N contacts at low temperatures, as sketched in Fig. 5.4(b). This is further supported by measuring G_1 and G_2 as a function of V_{SG1} and V_{SG2} at zero bias in the normal state of the device, where we observe only one slope in the gate-gate conductance maps (see App. B

and Fig. B.1). These characteristics are surprising, because typically central superconducting contacts separate the CNT into two separately tunable QDs [21, 33, 172, 179]. Hence, our Pb contact is non-invasive and does not create substantial defects in the CNT, in agreement with previously reported results for Pb contacts with Al_2O_3 tunnel barriers [82]. We observe this behavior on different CNT samples also for low-ohmic Pb contacts (see Chap. 7), indicating a generic origin. This can be possibly ascribed to the clean ZEP e-beam lithography (Sec. 2.2.1), combined with a gentle e-beam deposition of the material. Also the mechanical softness or the largely different workfunction[3] of Pb (dominating the S contact) compared to the normal metal Pd contacts and the CNT might play a role [166]. From CB diamonds measured over a larger gate voltage region and in finite magnetic fields $B > B_c^{OOP} \sim 180\,\mathrm{mT}$ to suppress superconductivity (not shown), we extract an average charging energy of $E_C \sim 3.5\,\mathrm{meV}$ and an average level spacing of $\delta E \sim 1.3\,\mathrm{meV}$. The small values indicate a large QD. From the level spacing we estimate a QD size of $L \sim 1\,\mathrm{meV}/\delta E \sim 800\,\mathrm{nm}$ [50], fitting roughly to the lithographically defined contact separation between the N contacts.

Due to the particular three-terminal nature of our device, following Refs. [34, 252], we can directly determine and assign values of the individual Γ_i from lineshape fits of independent differential conductance measurements. Since the full width half maximum (FWHM) of our resonances is considerably larger than the estimated electronic temperature of $100\,\mathrm{mK} \sim 10\,\mu\mathrm{eV}$, we use a generalized 3-terminal conductance matrix (valid for linear response) [34] in the lifetime-broadened limit ($kT \ll \Gamma$) and in the single-level transport regime ($kT \ll E_C, \delta E$) to extract the Γ_i from independent conductance measurements. In this case, the conductance matrix can be written as

$$\begin{pmatrix} I_1 \\ I_2 \\ I_S \end{pmatrix} = \boldsymbol{G} \begin{pmatrix} V_1 \\ V_2 \\ V_S \end{pmatrix} = \begin{pmatrix} G_{11} & G_{12} & G_{1S} \\ G_{21} & G_{22} & G_{2S} \\ G_{S1} & G_{S2} & G_{SS} \end{pmatrix} \begin{pmatrix} V_1 \\ V_2 \\ V_S \end{pmatrix}, \tag{5.1}$$

with off-diagonal elements [34, 250]

$$G_{ij}(E) = \frac{e^2}{h} \cdot \frac{\Gamma_i \Gamma_j}{(\Gamma_1 + \Gamma_2 + \Gamma_S)^2/4 + (E - E_0)^2} \tag{5.2}$$

for $i \neq j$ and $i, j \in \{S, 1, 2\}$, where E_0 denotes the gate-tunable position of the resonance. This conductance matrix obeys two sum rules, i.e. (1) due to current conservation $\sum_i G_{ij} = 0$ for all j, and (2) if $V_1 = V_2 = V_3 = V$ no current flows so that $\sum_j G_{ij} = 0$ for all i [252]. Hence, due to this current conservation and the symmetry $G_{ij} = G_{ji}$ valid for zero [see e.g. Eq. (5.2)] and possibly also small magnetic fields [34], the conductance matrix has only three independent matrix elements from which all parameters can be deduced. Setting

[3] Tabulated workfunctions: $\phi_{Pb} = 4.25\,\mathrm{eV}$, $\phi_{Pd} = 5.4\,\mathrm{eV}$, $\phi_{CNT} = 4.8\,\mathrm{eV}$ [59, 254].

now boundary conditions $V_1 = V_2 = V_S = 0$ and applying a small ac bias at S only yields for example the zero-bias conductances $G_{1S} \equiv G_1$ and $G_{2S} \equiv G_2$ measured in the experiment. Additional, independent measurements with the ac bias applied at one of the N contacts then allow to determine also e.g. G_{12} and G_{S2}. Combining these two datasets, we have three independent measurements G_{1S}, G_{2S} and G_{12} for the same QD resonance, which allows to unambiguously identify all three Γ_i. Thus, from such CB measurements with no applied dc bias and small magnetic fields $B^{OOP} = 0.3\,\mathrm{T}$ to suppress superconductivity (not shown), we determine typical tunnel couplings in the studied gate voltage region of $\Gamma_S \sim 10\,\mu\mathrm{eV}$, $\Gamma_1 \sim 80\,\mu\mathrm{eV}$ and $\Gamma_2 \sim 8\,\mu\mathrm{eV}$, yielding a combined $\Gamma = \sum_i \Gamma_i \approx 100\,\mu\mathrm{eV}$. The asymmetry of the extracted tunnel couplings explains for example the observed lower conductance maxima in G_2 compared to G_1 [cf. Fig. 5.4(c)]. We also obtain the relevant capacitances of the contacts and gates to the QD from the slopes of the resonances in individual conductance measurements, yielding $C = 45.8\,\mathrm{aF}$, $C_{BG} = 3.2\,\mathrm{aF}$, $C_{SG1+2} = 0.5\,\mathrm{aF}$, $C_1 = 6.7\,\mathrm{aF}$, $C_2 = 2.1\,\mathrm{aF}$ and $C_S = 33.3\,\mathrm{aF}$. Hence, because $\Gamma_S \ll \Delta_0 < \delta E \ll E_C$ for this device, transport is dominated by Coulomb repulsion and quasi-particle tunneling from the S contact, whereas Andreev processes are strongly suppressed (Sec. 3.3.1). Indeed, as also apparent from Fig. 5.4(c), for $V_1 = V_2$ no current (within measurement accuracy) flows within the superconducting gap as expected for a device dominated by quasiparticle transport only. We find a conductance suppression of ~ 100 for bias voltages $|eV_S| < \Delta_0$ along the resonance line where $\mu_{QD} = \mu_N$ (see App. B and Fig. B.2), suggesting a clean and hard transport gap for this device.

5.2.2. Additional bias voltages at the N contacts

Following the visionary experiments of Ref. [82] described in the introduction to this section, we now discuss experiments with an additional voltage applied between the N contacts, i.e. $V_{21} = V_2 - V_1 \neq 0$. We choose to bias asymmetrically, i.e. we keep $V_1 = 0$ and vary V_2, so that $V_{21} = V_2$ in the setup of Fig. 5.4(b). In contrast to the experiments of Ref. [82], we measure both differential conductances G_1 and G_2.

Figure 5.5(a) shows conductance maps of G_1 and G_2 as function of the combined sidegate voltage $V_{SG1+2} = V_{SG1} = V_{SG2}$ and as a function of V_{21}, when no dc voltage is applied to the S contact ($V_S = 0$). We observe a "rotated" CB diamond with the bias voltage on the horizontal and the gate voltage on the vertical axis, with lines of positive and negative differential conductance, perfectly anti-correlated between G_1 and G_2. In Fig. 5.5(b), we show G_1 and G_2 as a function of V_S and V_{SG1+2}, when V_{21} is fixed at $V_{21} = +0.8\,\mathrm{mV}$ [indicated by a red dashed line in Fig. 5.5(a)]. In these experiments, i.e. when V_{21} is fixed at a certain value, we observe additional lines of positive and nega-

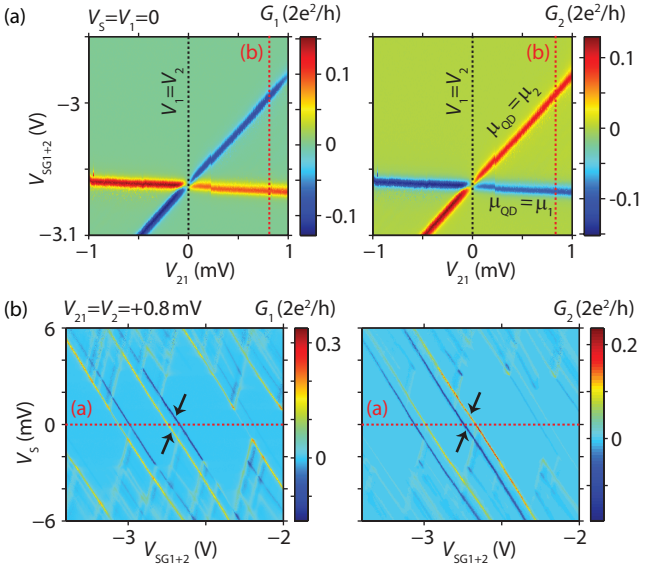

Figure 5.5.: G_1 and G_2 at a fixed BG voltage of $V_{BG} = -1\,V$ as a function of (a) V_{21} and a combined sidegate voltage $V_{SG1+2} = V_{SG1} = V_{SG2}$ at $V_S = 0$, (b) V_S and V_{SG1+2} at $V_{21} = +0.8\,\text{mV}$. The black dashed line in (a) marks the position of equal electrical potential at both N contacts for $V_1 = V_2 \approx 0$. Black arrows in (b) point at the discussed 'subgap' lines. The red dashed lines in (a) and (b) mark equivalent measurements in the three-dimensional parameter space (V_S, V_{21}, V_{SG1+2}).

tive differential conductance both in the subgap region (black arrows) and for larger bias voltages V_S, which are again perfectly anti-correlated between G_1 and G_2. These lines vanish for $V_{21} = 0$ [cf. Fig. 5.4(c)], and have the same negative slope determined by the capacitances of the system (see Sec. 1.3). Because the red dashed lines in Fig. 5.5(a) and (b) correspond to equivalent line measurements in the three-dimensional parameter space (V_S, V_{21}, V_{SG1+2}), we measure the same anti-correlated 'subgap' lines in Fig. 5.5(a) and (b), but map them as a function of different parameters.

These experimental findings agree very well with those of Ref. [82]. In Fig. 5.5(b), for example, we observe similar subgap peak-dip structures (black arrows), and are also able to spectroscopically determine the applied bias voltage V_{21} from a shift in the set of CB diamond tips. Since we simultaneously measure G_1 and G_2, we are able to interpret also these "subgap" structures. Here, one first has to remember that for example the current I_1 measured in N1 is $I_1 = I_{1S} + I_{12}$, and consists of a "gapped" QP current I_{1S} originating from the S contact, and an "ungapped" electron current I_{12} originating from

the N2 contact. We hence ascribe the extra "subgap" lines [black arrows in Fig. 5.5(b)] to the additional transport channel between the two normal contacts. For an additional bias V_{21}, electrons can tunnel from N2 to N1 for $\mu_1 < \mu_{\rm QD} < \mu_2$ independent of the S-N1 channel, i.e. even if $\mu_{\rm S} = \mu_1$ or $V_{\rm S1} = 0$. This situation is depicted schematically in Fig. 5.6(c), and results in a current "band" present in the "subgap"[4] region [black arrows in Fig. 5.5(b)], which is restricted to $\mu_1 < \mu_{\rm QD} < \mu_2$ (for the case $\mu_2 > \mu_1$). We observe this current "band" also in independent dc current measurements (not shown). Thus, the measurement of Fig. 5.5(a) exactly maps the 'opening' of this bias window $\mu_2 - \mu_1 = -|e|V_{21}$ – or in other words, it represents a CB diamond measurement between the two N contacts. In G_2, for example, we observe a peak (dip) exactly at $\mu_{\rm QD} = \mu_2$ ($\mu_{\rm QD} = \mu_1$). The peak-dip structure in differential conductance can be explained by the fact that we apply the ac bias at the S terminal, while transport occurs between the N terminals only. For example, when one differentiates the "subgap" current band in I_1 originating from the N2 contact with respect to $V_{\rm S}$, one will obtain a peak and a dip as observed in Fig. 5.5(b) [see e.g. also the simulation in Fig. 5.6(b) discussed below]. The completely anti-correlated differential conductance maxima and minima in G_1 and G_2 are also in agreement with this interpretation: the two conductance maps G_1 and G_2 in Fig. 5.5(a) add up to zero within measurement accuracy. This means that all current in the "subgap" region flows from N2 to N1, and vice versa. This picture is further substantiated by analyzing the slopes of the lines in Fig. 5.5(a) [determined by the capacitances of the system given in Sec. 5.2.1], which are consistent with the ones observed in independent measurements where the ac bias is applied at one of the N contacts (not shown). Figure 5.5(a) also serves as a reference for following experiments: it allows to experimentally determine the position of equal electrical potential $V_1 = V_2$ or $V_{21} = 0$ (black line) at both N contacts, which we find at $V_2 \approx 0$. At exactly $V_{21} = 0$, i.e. perfect compensation also of small intrinsic offset voltages at the employed current-voltage converters, no subgap features are observed any more [see Fig. 5.4(c)]. We note that a V_{21} as small as $V_{21} \sim 10\,\mu{\rm V} \leq V_{\rm AC}, kT/e$ results in clearly observable "subgap" lines.

For a simple description of these "subgap" features in such a three-terminal device, we extend the resonant tunneling model for quasiparticle transport introduced in Sec. 3.3.1 to the case of three contacts. Within this simple model, for the bias applied to S (to compare with our measurements in Fig. 5.5), the current measured in a particular N contact $i = 1, 2$ is

$$I_i = \sum_{\rm j \neq i} I_{ij}. \tag{5.3}$$

The individual contributions I_{ij} originating from the S and other N contact

[4] Here, "subgap" refers to as "seen" by the N1 electrode.

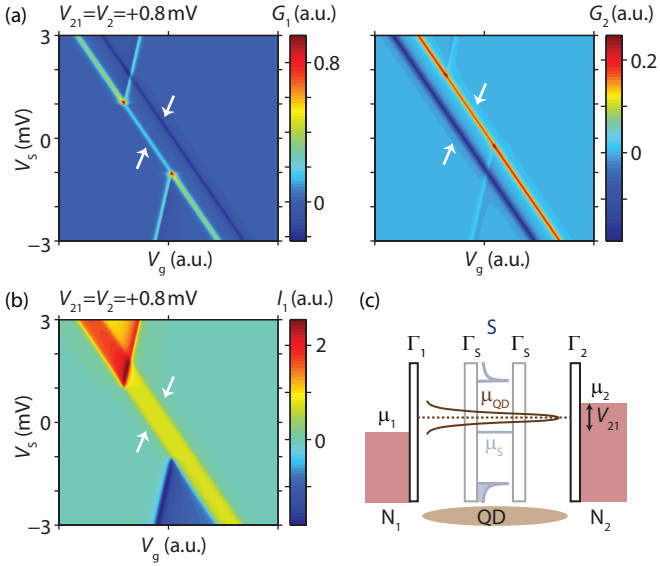

Figure 5.6.: (a) G_1 and G_2 calculated from Eqs. (5.3) and (5.4) as a function of the gate voltage, V_g, and bias V_S, for $V_{21} = +0.8\,\mathrm{mV}$. This situation corresponds to the measurements plotted in Fig. 5.5(b), and results in similar 'subgap' lines (white arrows). Here, we used $\Delta = 1\,\mathrm{meV}$, $T = 100\,\mathrm{mK}$ and Γ_i-s as in the experiment. (b) Current $I_1(V_\mathrm{S}, V_\mathrm{g})$ calculated with the same parameters. (c) Schematic of the three-terminal QD system with an additional bias voltage V_{21} applied between the two N contacts. In the depicted situation $\mu_1 < \mu_\mathrm{QD} < \mu_2$, electrons can flow from N2 to N1 even if $\mu_\mathrm{S} = \mu_1$, i.e. $V_{\mathrm{S}1} = 0$.

are

$$I_{ij} = \frac{e}{h} \int dE D_i(E) D_j(E + eV_{ji}) T_{ij}^{\mathrm{QD}}(E) [f_i(E) - f_j(E + eV_{ji})]. \qquad (5.4)$$

From this expression, the resulting differential conductance $G_i = \mathrm{d}I_i/\mathrm{d}V_\mathrm{S}$ can be calculated. In Eq. (5.4), $f_i(E)$ denotes the Fermi function in contact $i = 1, 2, \mathrm{S}$ and $D_\mathrm{i}(E)$ the respective DOS in the S and N contacts as introduced in Sec. 3.3.1. $T_{ij}^{\mathrm{QD}}(E) = (\Gamma_i\Gamma_j)/(\Delta E^2 + (\Gamma_1 + \Gamma_2 + \Gamma_S)^2/4)$ is a Breit-Wigner transmission function for the QD of the same form as the off-diagonal conductance matrix elements from Eq. (5.2), where the QD level detuning ΔE (Sec. 3.3.1) accounts for gating of the single QD level by one gate (g) and all contacts with the capacitances C_S, C_1, C_2, C_g and $C = C_\mathrm{S} + C_1 + C_2 + C_\mathrm{g}$.

Figure 5.6(a) and (b) show the differential conductance G_1 and G_2 and the current I_1 as a function of the bias voltage V_S and a gate voltage V_g calculated within this model, at a fixed bias voltage $V_{21} = +0.8\,\mathrm{mV}$. These conductance

maps qualitatively reproduce the experimental features of Fig. 5.5(b), which confirms our previous arguments and interpretation. Particularly, we also find a current "band" present in the "subgap" region (white arrows) in Fig. 5.6(b), which accounts for the lines of positive and negative differential conductance in Fig. 5.6(a).

In conclusion, we are able to reproduce the already observed "subgap" features of Ref. [82] in a three-terminal N-QD-S system, when an additional bias voltage V_{21} is applied between the two N contacts. With our measurements and a simple resonant tunneling model, we show that the so-called "subgap" features can be simply explained by considering the three-terminal device geometry and the additional transport channel between the two N contacts. Hence, our analysis also demonstrates that "subgap" transport resonances due to thermally activated quasiparticle tunneling (Sec. 5.1) and the ones due to a multi-terminal device geometry can be clearly distinguished experimentally. Specifically, this picture also accounts in a very natural way for the findings in Ref. [82].

5.2.3. Transport spectroscopy with a floating N contact

We now illustrate transport spectroscopy experiments with one floating N contact, i.e. where one of the switches S_1 or S_2 in the measurement setup depicted in Fig. 5.4(b) is set to 'fl'.

Figure 5.7(a) shows the differential conductance G_1 as a function of V_S and V_{SG1+2} at $V_{BG} = -1\,V$, with the terminal N2 floating. While the overall structure of the CB diamonds does not change significantly, we observe a new subgap feature. The dashed region of Fig. (a) is plotted in more detail in Fig. 5.7(b), where we observe a double line (DL, arrow) at subgap bias voltages. This double line runs parallel to the above-gap resonance maximum, the negative slope of which is determined by the condition $\mu_{QD} = \mu_1$. DL consists of a peak-peak structure in $\mathrm{d}I_1/\mathrm{d}V_S$, with a gate spacing of the individual lines of $\Delta V_{SG1+2} = \Delta V_{21}^{ind}/\alpha_G \sim 10\,\mathrm{mV}$. The individual lines of DL appear centered around the line given by the above-gap conductance maximum with negative slope, and have a significantly reduced linewidth ($\sim 1/3$) compared to the above-gap resonance. If we measure the dc current I_1 in this region, which is plotted in Fig. 5.7(c), we observe a current 'band' of $\sim 1 - 2\,\mathrm{pA}$ in this subgap region. Both the spacing $\Delta V_{21}^{ind}/\alpha_G$ (the lines are parallel) and the intensity of DL in Fig. 5.7(b) do not depend on V_S applied to S, nor on the gate voltage V_{SG1+2} in a given charge state. While we observe similar DL features also for different gate voltages [Fig. 5.7(a)], we find, however, that the spacing depends on the charge state of the QD, though not in a systematic or predictable manner.

Feature DL is completely symmetric and reproducible under a swap of N2 $\leftrightarrow$ N1 in the measurement setup (N1 floating). The DL in a given state of the QD

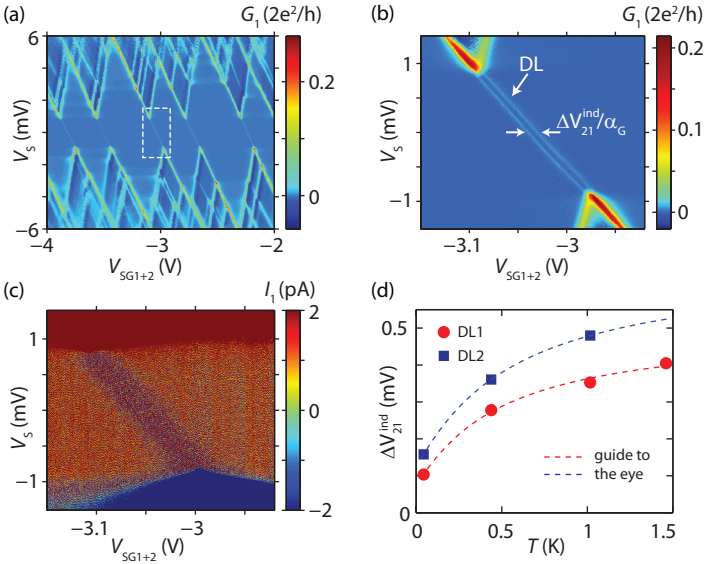

Figure 5.7.: (a) Conductance G_1 as a function of V_S and V_{SG1+2}, for a floating terminal N2 at $V_{BG} = -1\,V$. (b) Zoom-in of the indicated region in (a). DL denotes a double subgap line (DL1) parallel to $\mu_{QD} = \mu_1$, with a spacing $\Delta V_{21}^{ind}/\alpha_G$, where ΔV_{21}^{ind} is the induced voltage difference between N1 and N2 (text) and α_G a leverarm of the SGs. (c) Measured dc current I_1 for the same region as in (b). The colorscale has been limited to $|I_1| < 2\,pA$ to emphasize a visible subgap current 'band'. (d) Temperature dependence of the induced voltage difference ΔV_{21}^{ind}, for two studied double lines: DL1 from (b) and DL2 at $V_{SG1+2} = -2.71\,V$. The dashed lines represent guides to the eye.

does not depend on the magnetic or electric field, i.e. neither the spacing nor the intensity of DL changes when varying B or V_{SG1+2} and V_{BG} while staying on the same resonance (not shown). The spacing also does not depend on the applied ac voltage V_{AC}. An increased sample temperature, however, does not only lead to a smearing of the conductance peaks, but also to an increased spacing between the double lines. This is shown in Fig. 5.7(d), where we plot the extracted peak-peak spacing $\propto \Delta V_{21}^{ind}$ (see below) as a function of the sample temperature T for two studied double lines: DL1 from Fig. (b) and (c) and a DL2 at $V_{SG1+2} = -2.71\,V$.

For interpreting these findings, we first refer to the similarities with the experiments of Sec. 5.2.2, where a constant voltage V_{21} was applied between the two N contacts. In this case, we observed a subgap current band in I_1 and a peak-dip structure in G_1 due to the additional transport occurring between the N contacts. In the experiments with a floating terminal discussed here, we

observe a very similar structure with a current band in I_1, but a peak-peak structure in G_1.

We tentatively ascribe these subgap features to the same mechanism as in Sec. 5.2.2, i.e. to a transport between the two normal terminals, due to reasons we discuss in the following. First, we observe the same voltage dependences of the position of the DL or the current band as in Sec. 5.2.2, i.e. a very similar overall structure. Second, one has to bear in mind that the electrical potential of the floating contact is not fixed, but determined by the boundary condition $I_2 = 0$, so that the net current in contact N2 vanishes. An 'induced' potential offset $\Delta V_{21}^{\mathrm{ind}}$ of the floating N2 terminal relative to the N1 terminal, $\mu_2 = \mu_1 + e\Delta V_{21}^{\mathrm{ind}}$ would again result in a current band for $\mu_1 < \mu_{\mathrm{QD}} < \mu_2$, as already depicted in Fig. 5.6(c) and similar to what is observed in the experiment. Third, the observed peak-peak structure in G_1 for DL further supports this claim: an ac bias modulating μ_2 of the floating terminal, might create such a structure similar to transport through a two-terminal N-QD-N device ("standard diamonds" between N1 and N2 with a peak-peak signature). It is important to note the distinct difference between the experiments of the previous section and the floating case discussed here: In Sec. 5.2.2, all contact potentials were fixed, while here the potential of N2 is explicitly not fixed and can have an ac contribution. This ac contribution could for example be caused via capacitive[5] "cross-talk" or via a transport process between S (where the ac bias is applied) and N2. Using this interpretation, the reference measurements of Sec. 5.2.2 and Fig. 5.6(a) allow us to directly extract values for the additional, induced dc voltage offset $\Delta V_{21}^{\mathrm{ind}}$ from the gate spacing $\Delta V_{21}^{\mathrm{ind}}/\alpha_{\mathrm{G}}$ of the double line in the experiments, where α_{G} denotes the sidegates leverarm. We obtain a value of $\Delta V_{21}^{\mathrm{ind}} \sim 100\,\mu\mathrm{V}$ for DL1 at base temperature, and typical values between $\sim 50 - 200\,\mu\mathrm{V}$ for other double lines.

The induced dc voltage offset $\Delta V_{21}^{\mathrm{ind}}$ can in principle originate both from intrinsic sources (i.e. transport in the three-terminal QD itself) and extrinsic sources (e.g. gate leaks or measurement setup). We believe that $\Delta V_{21}^{\mathrm{ind}}$ has an origin intrinsic to the three-terminal QD system, because any external voltage source at the floating lead is most likely to depend on the used measurement configuration N2 $\leftrightarrow$ N1, which we do not find in the experiment. Furthermore, we exclude gate leaks as a possible extrinsic origin of $\Delta V_{21}^{\mathrm{ind}}$, because the spacing of the DL feature does not increase as a function of gate voltage, and is constant for a given DL when tuning V_{BG} and $V_{\mathrm{SG1+2}}$ simultaneously in a range of $\sim 1\,\mathrm{V}$ to track the resonance in the gate-gate parameter space. The fact that $\Delta V_{21}^{\mathrm{ind}}$ depends on the exact electronic state of the QD, and the temperature dependence of $\Delta V_{21}^{\mathrm{ind}}$ are further hints for an internal process.

Internally, one could suspect an extra current originating from S charging

[5] We estimated the stray capacitance between S and N2 to $\sim 1\,\mathrm{aF}$. This small value rather suggests a negligible effect of capacitive "cross-talk".

up the N2 terminal, compensated by the transport between N2 and N1 so that $I_2 = 0$. Since no subgap current (within measurement accuracy) is observed in the reference measurements of Sec. 5.2.2 for $V_1 = V_2$, we exclude Andreev processes as a possible source for this extra current. Together with our findings from the previous section, the temperature dependence of $\Delta V_{21}^{\mathrm{ind}}$ hints at a thermally activated process as the source of the induced voltage difference and extra current, such as e.g. a cotunneling of thermally excited quasiparticles from the superconductor [226]. In principle, such an induced voltage difference $\Delta V_{21}^{\mathrm{ind}}$ at the floating terminal can be captured in the three-terminal description introduced earlier: from $I_2 = 0$ in Eq. (5.3), one can self-consistently determine the electrochemical potential μ_2, and then calculate current maps for I_1. We implemented such an approach using the resonant tunneling model, but could so far not generate similar structures as in the experiment. The resonant tunneling model is however not able to capture cotunneling or higher order transport processes in a consistent manner, nor the possibly relevant charge dynamics of the QD. These more complex transport mechanisms go clearly beyond a simple resonant tunneling picture, and need a more accurate, microscopic modeling to be addressed in the future.

We thus conclude that transport spectroscopy experiments in multi-terminal N-QD-S devices with a floating N contact can result in extra subgap features. We speculate that these additional resonances could possibly give more insight into higher-order transport mechanisms in QD devices with S contacts, thus providing a novel spectroscopic tool to study such processes. The floating contact potential possibly acts as a sensitive probe for detecting small currents in such a three-terminal geometry, and allows to convert such small currents to easily measurable voltage signals.

5.2.4. Conclusions to Section 5.2

In conclusion, we studied quasiparticle transport and subgap transport resonances in a three-terminal superconductor/normal metal quantum dot, using Pb as a superconducting contact. We show that the multi-terminal geometry can generate apparent 'subgap' transport resonances, which do not originate from true subgap transport, but are e.g. simply caused by a small voltage drop and transport between the normal metal contacts. Finally, transport spectroscopy with a current-sensitive floating contact potential also generates subgap transport resonances, which could possibly help to unravel higher-order subgap transport processes in quantum dot devices with superconducting contacts.

6

Resonant and inelastic Andreev tunneling observed on a CNT QD[1]

In Chap. 3, we introduced Andreev reflection as the most fundamental low-energy transport process between a metallic N and an S reservoir. Though the equivalent resonant Andreev tunneling (AT) process in an N-QD-S device has long been predicted [185, 187, 188] and often been cited to account for a background subgap conductance e.g. in Cooper pair splitter devices [21, 33, 217], its spectroscopic observation in a transport experiment had been lacking so far, probably due to the required high spectroscopic resolution $\Gamma \ll \Delta$ and an "intermediate" coupling strength Γ_S. In Sec. 3.3.2, we already introduced this resonant AT as an intuitive sequential tunneling process of two electrons through the same QD resonance, which can be identified by its distinctive resonance lineshape and gate-bias dependence. We also discussed the predicted signatures of inelastic AT, in which an energy exchange with a bosonic bath leads to discrete replicas of resonant AT [111].

In this chapter, we report the observation of these two fundamental subgap transport processes on a CNT QD contacted with a superconducting Nb and a normal metal contact. The large energy gaps Δ observed in our Nb-contacted CNT devices (cf. Sec. 4.1) allow us to perform bias spectroscopy with $\Gamma \ll \Delta$, which is crucial to identify these processes. After the initial device characterization in Sec. 6.1, we carefully analyze and interpret the occurring subgap features in Sec. 6.2 and 6.3. First, we find a single resonance with position, shape and amplitude consistent with the theoretically predicted resonant AT through a single QD level [185, 188]. Second, we observe a series of discrete

[1] Parts of this chapter have been published in similar form in Ref. [179].

replicas of resonant AT, with a gate, bias and temperature dependence characteristic for boson-assisted, inelastic AT. While the nature of these bosons is difficult to assess in our experiments, this spectroscopic observation of resonant and inelastic AT contributes to a coherent picture of transport through N-QD-S devices, and opens up new questions and possibilities (Sec. 6.4).

6.1. Device characterization

Figure 6.1(a) shows a false-color SEM image of a Nb-based N-QD-S device, including a schematic of the measurement setup. The studied device was fabricated as discussed in Sec. 2.1, using ZEP EBL (Sec. 2.2.1) on a suitable CVD-grown CNT preselected with a H radical treatment (Sec. 2.2.2), where the Si^{++}/SiO_2 substrate serves as a backgate (BG). We fabricate a central $\sim$ 200 nm wide and $\sim$ 2 mm long Ti/Nb (3 nm/40 nm) S contact (Sec. 4.1) and two normal metal Ti/Au (5 /65 nm) contacts (N) on either side of S at a distance of $\sim$ 300 nm, in a Cooper pair splitter geometry [33] with sidegates (SGs) for individual electrical tuning of the two CNT sides. Between the contacts two separate QDs form, but no signals could be found that depend on both QDs. We discuss this in more detail in App. C, and further demonstrate that the two QDs are well decoupled, so that the capacitive inter-dot coupling is negligible and no hybridization of the QD levels occurs [255–257]. Hence, the QDs can be treated as individual objects, and we focus here solely on experiments on QD1. The experiments were carried out in a dilution refrigerator at a base temperature of $\sim$ 110 mK, with an estimated electron temperature of $T \sim 150$ mK. To minimize thermal radiation from warmer stages of the setup and the effects due to quasi-particles, the electrical lines are heavily filtered using three filter stages (Sec. 2.3), and the sample is shielded from the helium bath by a Faraday box and two additional copper shields. Since the electronic temperature is considerably lower than the critical temperature of the Nb strip (Sec. 4.1) and the observed energy gap (see below), the generation of quasi-particles is strongly suppressed. Furthermore, three independent cool-downs of the device in two different measurement set-ups allow us to exclude any spurious effects from the electronic set-up on the features reported below.

In Fig. 6.1(b) the differential conductance G through QD1 is plotted as a function of the backgate voltage, V_{BG}, and the bias applied to S, V_{SD}. We find very clear CB diamonds, and extract a leverarm of the global backgate of $\alpha_{\mathrm{BG}} \approx 0.09$ and an addition energy of $E_{\mathrm{add}} \approx 6.6$ meV. A well-defined superconducting transport gap $\Delta_0 \approx 1.2$ meV, illustrated in Fig. 6.1(c) at $B = 0$, separates the CB diamonds in a characteristic way due to the gap in the QP DOS in S (see Sec. 3.3.1). This gap is reduced monotonically with a magnetic field B applied perpendicular to the CNT and the substrate[2] and

[2] Since only an out-of-plane field could be applied, we use $B \equiv B_{\mathrm{OOP}}$ as notation here.

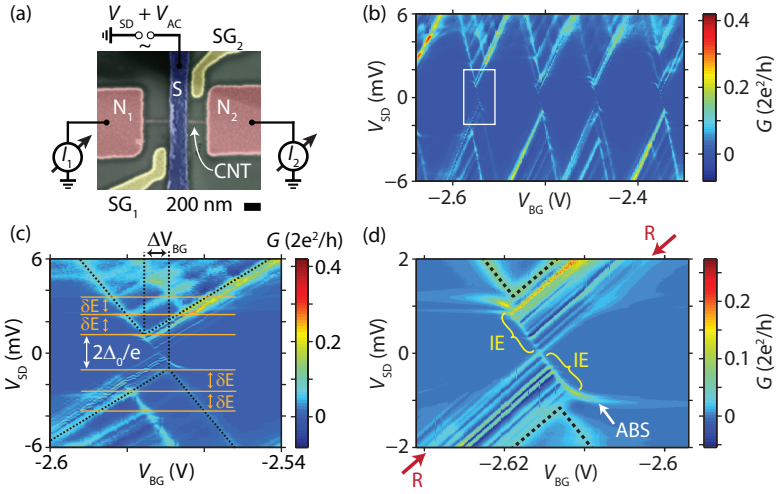

Figure 6.1.: (a) False-colored SEM image of a representative device and schematic of the measurement setup. (b) Differential conductance of QD1 as function of V_{SD} and V_{BG} at $T = 110\,\mathrm{mK}$ and $B = 0$. (c) Close-up of the conductance map around the region indicated in (b), to determine the spacing of the (electronic) excited states δE (orange lines), and the superconducting transport gap Δ_0 (white arrow). Black dashed lines mark the shifted CB diamonds. (d) Detailed conductance map of the region indicated in (b). The resonant AT line and the inelastic AT are labeled R and IE, respectively. The dotted lines point out the CB diamond edges and ABS an Andreev bound state. A small discrepancy in gate voltage compared to (b,c) is due to a gate charge rearrangement between the measurements.

vanishes at $B \approx 1.5\,\mathrm{T}$ (see Fig. 4.1(c) and App. C). In Fig. 6.1(c), we find conductance resonances running in parallel to the edge of the diamonds for $|eV_{\mathrm{SD}}| > \Delta_0$. These are due to (electronic) excited states of the QD, which exhibit a Zeeman splitting in an external magnetic field [84] (see App. C). From their roughly equidistant spacing in energy (orange horizontal lines), we find a level spacing of $\delta E \sim 1.2\,\mathrm{meV}$.

Figure 6.1(d) shows G plotted in the region indicated by the rectangle in Fig. 6.1(b). Here we find up to 7 weak but very sharp parallel resonance lines with the same positive slope as the CB diamonds. Similar features appear in all other CB diamonds (see App. C), independent of the QD charge state. The average spacing between the lines (see detailed analysis below) is $\langle \delta\varepsilon \rangle \sim 145 \pm 30\,\mu\mathrm{eV} \ll \delta E$, much smaller than the QD's electronic level spacing, and with some resonances showing significant deviations from this value. Only one of these parallel lines (R) crosses the entire transport gap, while the other lines (IE) end at a finite sub-gap bias. Pronounced negative differential conductance (NDC) values occur between the conductance maxima. An ad-

ditional structure arises due to a (weak) Andreev bound state [labeled ABS in Fig. 6.1(d)], which leads to some amplitude modulation, but will not be discussed in more detail here.

6.2. Signatures of resonant and inelastic Andreev tunneling

In the following, we interpret the subgap features R and IE by carefully analyzing and comparing their gate voltage, bias, temperature and magnetic field dependence with the predicted signatures of resonant and inelastic Andreev tunneling, previously introduced in Sec. 3.3.2.

6.2.1. Gate voltage and bias dependence

Resonant Andreev tunneling Line R we identify with resonant AT. To demonstrate this, we compare the line shape of the zero-bias CB resonance measured in the normal state at $B = 5\,\mathrm{T}$ shown in Fig. 6.2(a) to the resonance at zero field, i.e. in the superconducting phase of S, which is plotted in Fig. 6.2(b). For the following fits we added an identical background determined by the data points far off resonance (not shown). In the normal state we expect a Breit-Wigner (BW) line shape due to life-time broadening, described by Eq. (1.10). This expression fits the observed line shape in Fig. 6.2(a) very well (blue curve) for the tunnel coupling parameters $\Gamma_1 \approx 9.0\,\mu\mathrm{eV}$ and $\Gamma_2 \approx 96.5\,\mu\mathrm{eV}$. As a comparison, we also plot the best fit using the expression for thermally broadened resonances (dotted green line), Eq. (1.11), which does not describe the data well. For resonant AT in the limit of non-interacting electrons the expected line shape is given by Eq. (3.6) [185, 188], which also deviates strongly from the data. In contrast, the resonance at zero magnetic field plotted in Fig. 6.2(b) is described best by the expression for resonant AT: the measured conductance values decay faster away from the maximum than in the normal state, one of the hallmark features of resonant AT (Sec. 3.3.2). The extracted values for the tunnel coupling using the BW expression are a factor of $3-7$ smaller than in the normal state, while the values extracted from the resonant AT expression, $\Gamma_1 \approx 8.4\,\mu\mathrm{eV}$ and $\Gamma_2 \approx 66.5\,\mu\mathrm{eV}$, are very similar to the ones in the normal state. We find very similar values also in gate sweeps at a small bias (see App. C), which allows to exclude an influence of the (weak) observed Andreev bound state on the analysis. Due to the observation of this ABS and the higher probability of AT, we tentatively attribute the larger tunnel coupling to the superconducting contact, i.e. $\Gamma_\mathrm{S} = \Gamma_2$, and $\Gamma_\mathrm{N} = \Gamma_1$, in agreement also with the regime of AT considered in Sec. 3.3.2. Finally, we note that this resonance occurs exactly when the QD level is aligned to the electrochemical potential of S, i.e. $\mu_\mathrm{QD} = \mu_\mathrm{S}$, another key signature of resonant AT (cf. Fig. 3.5 and Sec. 3.3.2). From the analysis of the line shapes and the gate-bias dependence

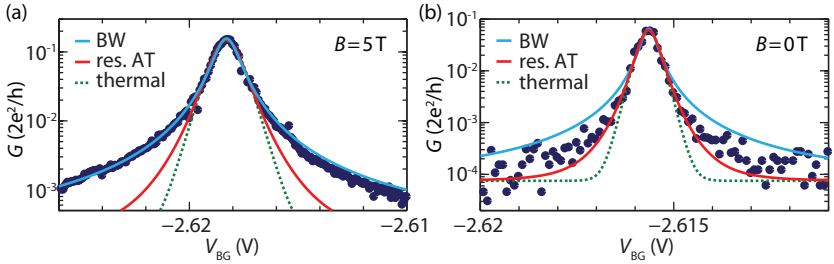

Figure 6.2.: Resonance line shapes: G as function of V_{BG} (points) at zero bias (a) in the normal state at $B = 5\,\mathrm{T}$ and (b) at zero field in the superconducting state. The blue, red and dotted green lines are best fits to the data using the expressions for a Breit-Wigner (BW) [Eq. (1.10)], resonant AT [Eq. (3.6)] and a thermally broadened [Eq. (1.11)] QD resonance, respectively.

we hence conclude that resonance R running through the full energy gap of the superconductor is due to resonant AT.

Inelastic Andreev tunneling The replicas (IE) parallel to the resonant AT line (R) found in Fig. 6.1(d) we attribute to the emission and absorption of energy from or into a bosonic reservoir in an inelastic Andreev tunneling process. The bias condition for the at low temperatures only possible emission process is $\mu_{\mathrm{S}} < \mu_{\mathrm{QD}} < \mu_{\mathrm{N}}$ and $\mu_{\mathrm{S}} > \mu_{\mathrm{QD}} > \mu_{\mathrm{N}}$ [111] (Sec. 3.3.2), which results in the lines ending at a finite sub-gap bias, as observed in Fig. 6.1(d). Indeed, the observed gate-bias dependence closely resembles the predicted structure for inelastic AT [111], sketched previously in Fig. 3.5(e).

To further substantiate our interpretation and extract all relevant parameters, we first carefully analyze these inelastic replicas (IE) of the resonant Andreev line (R) at $B = 0$ and $T = 110\,\mathrm{mK}$. In Fig. 6.3(a), we explicitly illustrate the extraction of the energies (positions) ε_n of the IE replica lines (labeled with $n \in \mathbb{N}$ for increasing energy) relative to the resonant line R from conductance maps. The vertical conductance cross-section, marked with an asterisk in Fig. 6.3(a), is used for the analysis of the conductance maxima G_{max} and the full width at half maximum (FWHM) of the IE replicas. This cross-section clearly demonstrates the pronounced negative differential conductance (NDC) between the peaks and the Fano-like linehape of the IE features. NDC is expected from the predictions for inelastic AT in Ref. [111], since the resonance condition is determined by the QD level position (Sec. 3.3.2) and not by the Fermi energy of the normal metal lead, which leads to peaks in the current and a peak-dip structure in the differential conductance. In Fig. 6.3(b) and (c), we plot the extracted energies ε_n of the IE replicas and their spacing $\delta\varepsilon = \varepsilon_n - \varepsilon_{n-1}$ as a function of the replica number n. A linear

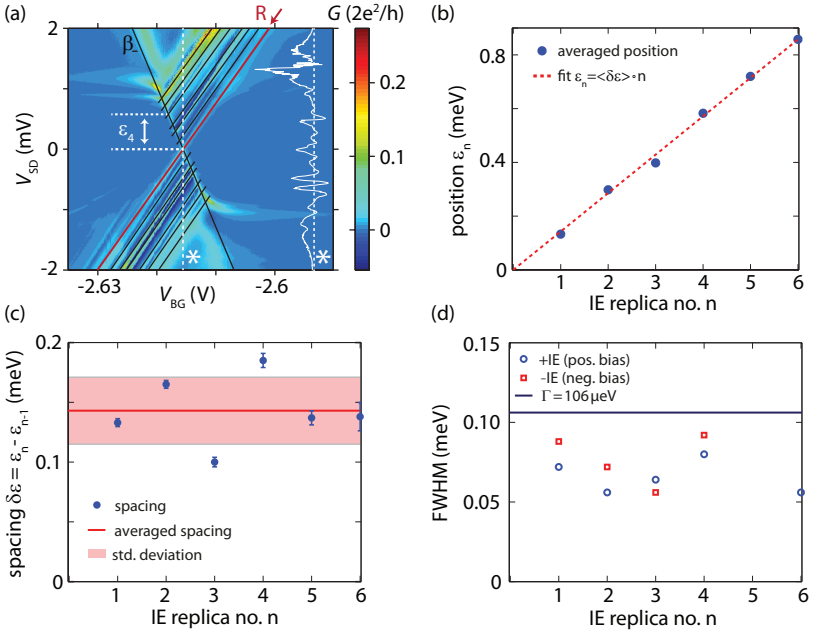

Figure 6.3.: (a) Schematic illustration for the extraction of the energy ε_n (and spacing) of the IE replica lines labeled with $n \in \mathbb{N}$ relative to R (red line) from a $G(V_{\mathrm{BG}}, V_{\mathrm{SD}})$ map, shown exemplary for the IE4 replica ($n = 4$) at positive bias. The white curve (asterisk) shows a vertical cross-section at the backgate voltage indicated by a dashed line. (b) Extracted position ε_n vs. the IE replica number n, data averaged from 2 datasets for positive and negative bias. The red dashed line shows a linear fit $\varepsilon_n = \langle\delta\varepsilon\rangle \cdot n$ with $\langle\delta\varepsilon\rangle = 143\,\mu$eV. (c) Spacing $\delta\varepsilon = \varepsilon_n - \varepsilon_{n-1}$ of the IE lines as function of n, data averaged over 2 datasets for positive and negative bias. The red line and area mark the averaged spacing $\langle\delta\varepsilon\rangle = 143\,\mu$eV and standard deviation determined in (c). (d) FWHM of the IE features as a function of n, for positive (blue circles) and negative bias (red squares), where the dark blue line marks the value of $\Gamma = 106\,\mu$eV.

fit of the positions in Fig. 6.3(b), $\varepsilon_n = \langle\delta\varepsilon\rangle \cdot n$, allows to extract an average spacing (over all n) between the IE lines of $\langle\delta\varepsilon\rangle = 143 \pm 28\,\mu$eV. For an inelastic AT process, this spacing corresponds to an average boson energy of $\hbar\omega_{\mathrm{b}} = 2\langle\delta\varepsilon\rangle = 286\,\mu$eV (Sec. 3.3.2). The averaged spacing (red solid line) and its standard deviation (light red area) are also plotted in Fig. 6.3(c). While the IE replica energies scale roughly linear with n in Fig. 6.3(b), we find in the more careful analysis of Fig. 6.3(c) that some replicas significantly deviate from the average spacing. This is most likely due to a different bosonic origin of the resonances, as discussed in more detail below. Here, one also has to bear in mind that the position of $G_{\max}$ might not completely agree with the

position of the current maximum predicted for boson-assisted tunneling [111], maybe partially explaining the deviations due to the overlap and slightly different widths of neighboring IE replica lines. To obtain an estimate for the width of the IE replica lines, we neglect the influence of NDC and determine the FWHM from $G_{\max}$ to $G = 0$, plotted in Fig. 6.3(d) as function of the IE replica number n. We note that the FWHM stays roughly constant and smaller than the determined Γ from the fits, i.e. also FWHM $< \sqrt{2}\Gamma$ as predicted for inelastic AT [111] (see Sec. 3.3.2). We obtain an average FWHM of $\sim 70\,\mu$eV for the IE lines. Hence, the IE replicas are characterized by an average boson frequency of $f_\mathrm{b} \approx 69\,$GHz, a FWHM $\approx 17\,$GHz and an IE resonance Q factor of $Q \sim f_\mathrm{b}/\mathrm{FWHM} \approx 4$. We can thus summarize the characteristic energies in our system as $kT \ll \Gamma < \hbar\omega_\mathrm{b} \ll \delta E \approx \Delta_0 \ll E_\mathrm{add}$, where we deduced $\Gamma_\mathrm{S} > \Gamma_\mathrm{N}$ in the previous paragraph. All these findings are in very good qualitative agreement with the predictions of inelastic AT, in which the excess energy of the tunneling electrons is emitted into a bosonic bath [111]. Similar to Ref. [46], one can also study the maximum conductance of the IE replicas $G_{\max}$ as a function of the replica line number n, the number of emitted bosons. We observe a varying $G_{\max}$ (not shown), with the maximum for the negative bias e.g. at the $n = 2$ and $n = 3$ lines [see Fig. 6.3(a)], reminiscent of a Franck-Condon blockade scenario [46].

6.2.2. Temperature dependence

Following the predictions of Ref. [111] for phonons, Fig. 6.4(a) shows G as a function of V_SD and V_BG for different temperatures $T = 110\,$mK, $T = 500\,$mK and $T = 950\,$mK. At higher temperatures, $kT \sim \hbar\omega_\mathrm{b}$, the conductance maximum of the resonant Andreev line and the emitted-boson replicas start decreasing and sidebands due to boson absorption appear [white arrows in Fig. 6.4(a)]. We study this behavior also in cross-sections at fixed V_SD values, indicated by white dashed lines in Fig. 6.4(a). To reduce noise occurring at higher temperatures, 12 cross-sections around the desired V_SD value were averaged (blue shaded bias range), including the compensation of the horizontal shifts due to gating. Two of the studied cross-sections are shown in Fig. 6.4(b) and (c). The zero-bias curves in Fig. 6.4(b) are symmetric with respect to the central resonant AT peak indicated by the black arrow. The amplitude of this peak is reduced considerably with increasing temperature, while the width increases because of side peaks (red arrows) emerging as weak shoulders between 0.5 K and 1 K. The amplitudes of the indicated features are plotted in the inset of Fig. 6.4(b) for the three temperatures, which shows that resonant AT is reduced with increasing temperature ($\sim 1/kT$) due to the thermal broadening of the Fermi functions in the normal metal contact. In contrast, the absorption side peaks increase in amplitude at higher temperatures due to the thermal population of the boson states [$\sim 1/kT(\mathrm{e}^{\hbar\omega_\mathrm{b}/k_\mathrm{B}T} - 1)^{-1}$, red guide to the

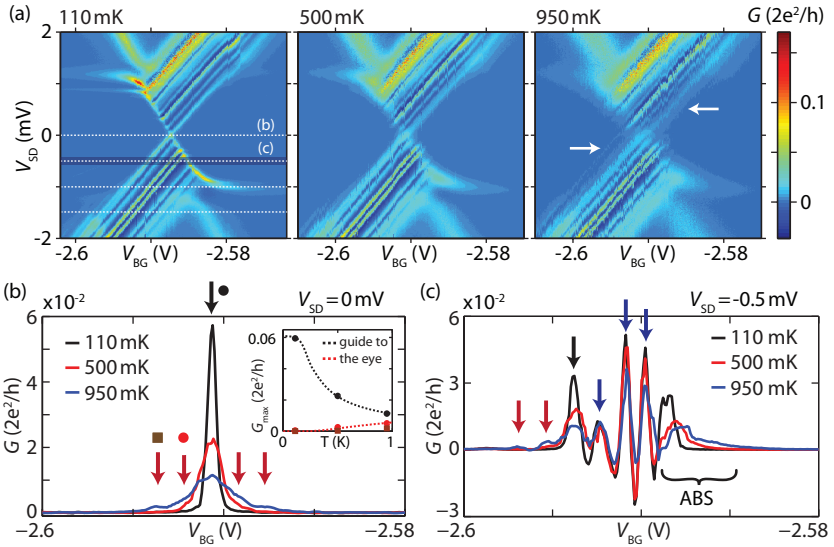

Figure 6.4.: Temperature dependence of resonant and inelastic AT. (a) $G(V_{\mathrm{BG}}, V_{\mathrm{SD}})$ maps at $T = 110\,\mathrm{mK}$, $T = 500\,\mathrm{mK}$ and $T = 950\,\mathrm{mK}$. The white dashed lines in the $T = 110\,\mathrm{mK}$ map indicate the analyzed horizontal cross-sections at a fixed bias, for each of which a small bias window (blue shaded area) was used for averaging (text). White arrows in the $T = 950\,\mathrm{mK}$ map point to appearing sidebands due to boson absorption. (b,c) G as function of V_{BG} for the three indicated temperatures at (b) $V_{\mathrm{SD}} = 0\,\mathrm{mV}$ and (c) $V_{\mathrm{SD}} = -0.5\,\mathrm{mV}$, obtained from the cross-sections indicated in (a). The black arrow points out the resonant AT line, the red arrows the boson-absorbing and the blue arrows the boson-emitting resonances. The inset in Fig. (b) shows the peak amplitudes of the features indicated in the main panel.

eye in Fig. 6.4(b)], in good qualitative agreement with the predictions for phonon-assisted AT [46, 111]. Backgate sweeps at the bias $V_{\mathrm{SD}} = -0.5\,\mathrm{mV}$ are plotted in Fig. 6.4(c) for the same temperatures, which again shows the reduction of the resonant AT amplitude (black arrow) and the onset of boson-assisted inelastic AT at more negative gate voltages due to boson absorption (red arrows). At more positive voltages, i.e. $\mu_{\mathrm{S}} < \mu_{\mathrm{QD}}$, resonances occur with slightly decreasing amplitudes due to boson emission (blue arrows). An important finding is that these resonances have essentially constant widths even for increasing temperature, immediately evident also in the conductance maps in Fig. 6.4(a), and analyzed in more detail in App. C. This finding is again in very good qualitative agreement with inelastic AT [111], where the IE AT resonance width is mainly determined by the tunnel couplings, which we do not expect to change greatly with temperature. Other cross-sections indicated

in Fig. 6.4(a) show the same features as the $V_{SD} = -0.5\,\mathrm{mV}$ cross-section (not shown). We note that the gate voltage, bias and temperature dependence is also quite different for boson-assisted quasiparticle tunneling, which allows to distinguish the two mechanisms [179].

6.2.3. Magnetic field dependence

We now investigate the resonant and inelastic AT as a function of an external magnetic field B applied perpendicular to the substrate plane. Figure 6.5(a) shows G as a function of V_{SD} and B at the backgate voltage at which the elastic AT resonance (R) crosses $V_{SD} = 0$ (see App. C and Fig. C.5). We find that the energy gap detected by the QD shrinks monotonically up to $\sim 0.3\,\mathrm{T}$ and is then roughly constant up to $\sim 1\,\mathrm{T}$ and diappears around $\sim 1.5\,\mathrm{T}$ [for a detailed discussion see Sec. 4.1 and Fig. 4.1(c)]. Here we focus only on the subgap features: the resonant AT line R is essentially unaffected at fields below $B \approx 0.7\,\mathrm{T}$ and splits at higher fields due to Zeeman shifts of the resonances (see App. C). These do not affect the following analysis since we extract all values directly from Coulomb diamond experiments, which is shown in App. C. We

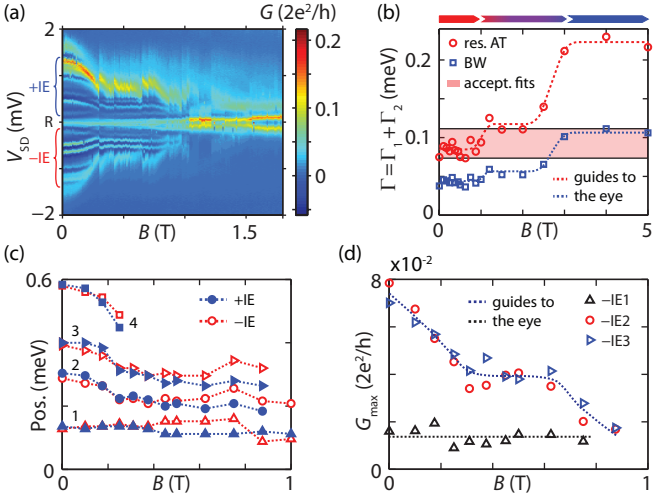

Figure 6.5.: Magnetic field dependence of resonant and inelastic AT. (a) G as a function of the bias V_{SD} and the external magnetic field B at a fixed backgate voltage where the resonance (R) crosses $V_{SD} = 0$. (b) Tunnel coupling $\Gamma = \Gamma_1 + \Gamma_2$ of resonance (R) extracted from the resonant AT and the Breit-Wigner expressions as a function of B. The fits are obtained from colorscale images always at the same relative position (see App. C). (c) Energy and (d) amplitude of the inelastic AT peaks (IE) as function of B. The resonances are labeled in Fig. (c) for increasing energy.

can visualize the transition from resonant AT to a Breit-Wigner characteristics with increasing field by plotting the extracted tunnel parameter, $\Gamma = \Gamma_1 + \Gamma_2$, as a function of B, which is shown in Fig. 6.5(b) and analyzed in more detail in App. C. We assume that the tunnel couplings stay roughly constant with increasing B. While up to $B \approx 1\,\mathrm{T}$ the expression for resonant AT reproduces nicely the large-field values of the BW fit (light red band), it overestimates the coupling by more than a factor of 2 at high fields. At intermediate fields between 1 T and 3 T both line shapes deviate considerably from the expected values, which suggests that normal electron tunneling and AT co-exist at fields where the visible transport gap is reduced to zero. The evolution of a resonant AT lineshape from $B = 0$ to a BW lineshape for $B > 3.5\,\mathrm{T}$ agrees very well with the upper critical field determined in resistance measurements on the Nb strip, shown in Fig. 4.1(a).

Figure 6.5(c) and (d) show the magnetic field dependence of the position (energy) and the peak amplitude of the inelastic AT lines, respectively, extracted from CB spectroscopy as shown in Fig. 6.3 and App. C. We plot the position of the conductance maxima relative to the resonance R at negative and positive bias up to 1 T and label the lowest resonances in energy in Fig. 6.5(c). While the energy of resonance IE1 is essentially constant in this field interval, the positions of IE2, IE3 and IE4 are all reduced and scale similarly with increasing field, but not linear with the energy gap [Fig. 4.1(c)]. For the latter resonances the spacing stays roughly constant. Even more pronounced is the difference in the field dependence of the resonance amplitudes, plotted in Fig. 6.5(d): the amplitude of IE1 is independent of B within experimental error, but the amplitudes of IE2 and IE3 decay continuously on the scale of 1 T. This characteristics might give a further indication which bosonic systems are responsible for the inelastic AT process in our CNT device, which we want to discuss in the following section.

6.3. Discussion

Inelastic AT is mediated by the absorption or emission of bosons. In our system, three types of bosons might be responsible for these sub-gap processes: (I) phonons, e.g. mechanical oscillations in the CNT [111], (II) plasma modes in the millimeter scale superconducting contact [258], or (III) photons, i.e. electromagnetic modes of the resonator formed by the inductance of the S-contact and its capacitance to the backgate, which are damped by ohmic dissipation in normal metals. We used simple estimates to approximate the resonance frequencies for all three bosonic systems. For CNT phonons, using a CNT diameter $d \sim 1.5\,\mathrm{nm}$ determined from atomic-force microscopy on our device, we find that longitudinal acoustic modes in the doubly-clamped CNT [45], or the CNT squash mode [259] can yield quantized energies of the

observed energy scale. Using e.g. the estimation given in Ref. [45] for longitudinal stretching modes, we find a 'vibrating' CNT length of $\sim 380\,\mathrm{nm}$ for our bosonic energies, matching the S-N contact separation. For the analysis of plasma and electromagnetic modes, it is crucial that the S-contact has a length of $\sim 1\,\mathrm{mm}$ and extends all the way out to the bond wires. We obtain very similar resonance frequencies as in the experiment using the estimates given in Ref. [258] for plasma modes, and with simple estimates and a numerical finite element simulation (software Sonnet) of the exact Nb-contact geometry for the electromagnetic modes. Hence, all three scenarios are plausible and cannot be distinguished from the energy scales alone. Phonons naturally account for the temperature dependence of the inelastic AT lines, but it is not straight-forward to explain a magnetic field dependence. Photons would, at least qualitatively, account for both the field and temperature dependence: since the kinetic inductance L_k of S diverges with decreasing energy gap and reduced Cooper pair density [260], this results in a reduced resonance frequency $\propto (L_\mathrm{k}C)^{-\frac{1}{2}}$ (C is the capacitance to the backgate) possibly similar to what is observed in the experiment [see Fig. 6.5(c)]. Indeed, similar electromagnetic modes have also been found to be responsible for excess subgap current (peaks) in S-I-S Josephson junctions [261, 262], making this a very plausible scenario. The fact that we find qualitatively different magnetic field characteristics for the lowest energy inelastic AT peak compared to the resonances at higher energies might however indicate that even two different bosonic baths are coupled to our QD, severely complicating a more detailed analysis.

6.4. Conclusions and outlook

In summary, the large superconducting transport gap found in our Nb-contacted CNT QDs and the sharp QD resonances allow us to identify resonant (elastic) and inelastic Andreev tunneling in a QD-superconductor structure. The temperature dependence of the inelastic replicas of resonant AT is consistent with bosonic excitations that open additional transport channels. However, from our experiments the nature of the bosons is difficult to assess. The magnetic field dependence might even hint at the possibility of two different bosonic systems coupling to the QD. Our experiments demonstrate that, in contrast to normal metal systems, such excitations can become the dominant transport mechanisms in S-QD systems. We note also that a smearing of the discrete resonances observed here might be an alternative origin of the heavily discussed 'soft gaps' [227, 244, 245] in superconductor nanostructures. Indeed, Ref. [263] has already demonstrated both experimentally and theoretically a formal equivalence between a 'smeared' Dynes-DOS and (environmental) photon-assisted quasiparticle tunneling in N-I-S structures, making the above scenario plausible.

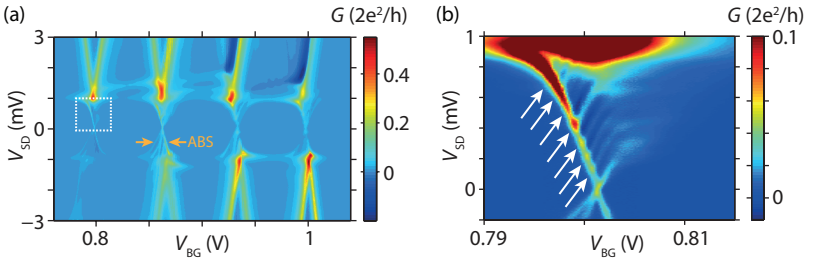

Figure 6.6.: (a) Differential conductance map $G(V_{\mathrm{BG}}, V_{\mathrm{SD}})$ of QD1 for a second, similar Nb-based CNT device, recorded at $B = 0$ and at a base temperature of 60 mK. Orange arrows mark more pronounced Andreev bound states (ABS). (b) Detailed conductance map of the region indicated in (a), where the colorscale has been deliberately limited to $0.1 \times 2e^2/h$ to enhance the visibility of subgap features. White arrows point out additional subgap features with a similar gate-bias dispersion as the ABS.

In addition, the coupling to bosonic reservoirs is also expected to result in replicas of other sub-gap features, for example ABSs [264]. The large energy gaps found in our CNT QD devices should enable the spectroscopic analysis of such features, e.g. due to multiple replicas of ABSs. Figure 6.6(a) shows a conductance map measured at a base temperature of 60 mK for a second Nb-based CNT device fabricated in the same geometry, exhibiting a clear 4-fold symmetry on QD1 (not shown) and an energy gap of ~ 0.9 meV. For this device ABS features, marked by orange arrows in Fig. 6.6(a), are more pronounced. A detailed conductance map of the region indicated in (a), which is plotted in Fig. 6.6(b), demonstrates multiple subgap features with a similar gate-bias dispersion as the ABS (white arrows), but crucially a different (positive) slope than the respective CB diamond edge. While we refrain here from speculating on the origin of the observed features due to the less clear experimental signatures for this device[3], these findings demonstrate that QD devices with large gaps permit to study such novel subgap transport phenomena spectroscopically.

We hence propose to employ similar devices with engineered bosonic environments for further studies, which could shed more light on the nature of the observed processes and lead to hybrid quantum systems with a controlled coupling to the superconductor. For example, novel techniques allow the fabrication of suspended CNTs with superconducting and other contact materials (see e.g. Sec. 2.2.4), which should give access to well-controlled CNT phonons [48]. Using the same technique, a radio-frequency cavity can be coupled to the CNT QD, which results in a well-controlled electromagnetic environment with discrete modes [104].

[3] For an alternative interpretation to the boson-assisted scenario, see also Chap. 7.

7

Andreev bound states probed in a three-terminal geometry[1]

In this chapter, we investigate CNT QD devices more strongly coupled to a superconductor (S), so that Andreev bound states (ABS) form (Sec. 3.3.3). Because these ABS can be implemented as an Andreev qubit [15, 16] and constitute a model system to investigate the superconducting proximity effect in QD systems [155], they recently attracted a lot of attention [15, 31, 165–173]. While previous experimental studies in S-QD systems have focussed mostly on the gate, bias, phase, magnetic field and temperature dependence of these ABS [31, 165–171], only very few experiments have analyzed transport through Andreev levels in a multi-terminal device geometry [172, 173]. Due to the interplay of non-local and local transport mechanisms, novel transport signatures are expected in such systems, as e.g. a triplet blockade [202] or other non-local effects [41, 177, 200, 207]. The additional freedom of more than two terminals, e.g. for a three-terminal device geometry, allows one to identify these transport processes and to access the coupling strengths of the individual contacts to the QD (Sec. 5.2). The latter sheds more light on the question of the broadening and spectroscopic linewidth of the Andreev resonances[2] in the QD regime [165, 171].

[1] Parts of this chapter will be published in similar form elsewhere. Manuscript in preparation.

[2] As introduced in Sec. 3.3.3, we use here the term Andreev resonance (AR) for the observed transition lines in the transport spectroscopy experiments, whereas we employ ABS to refer to the quantum mechanical state. This language becomes important in the context of this chapter, where AR should not be confused with the in the literature often used abbreviation for Andreev reflection (which we do not employ in this thesis).

Here, we use three different CNT QD devices strongly coupled to one S and more weakly to two N contacts to address such questions. The employed Pb contacts allow us to study subgap transport with a high spectroscopic resolution. In Sec. 7.1, we first characterize each device by transport measurements. Using the extracted parameters and taking advantage of the three-terminal geometry, we find in Sec. 7.2 that the Andreev resonances are mainly broadened by the finite coupling to the two normal metal contacts. One device shows replicas at higher energies of the lowest Andreev resonance, which we ascribe in Sec. 7.3 to the additional transitions to energetically closely spaced single-particle energy levels. Finally, in Sec. 7.4, we analyze transport between the two normal metal contacts through Andreev resonances. The competing local and non-local transport mechanisms give rise to characteristic conductance sign changes, which can be captured by a simple rate equation model. When the S contact remains floating, we observe signatures of transport through Andreev resonances only for a sufficiently strong coupling of the QD to S, providing a novel view on the superconducting proximity effect in QD systems.

7.1. Device characterization

Pb-based CNT devices have been fabricated in the same manner as discussed in Sec. 5.2, in a three-terminal Cooper pair splitter geometry shown in Fig. 5.4(b), with a central, $\sim 200\,\mathrm{nm}$ wide Pd/Pb/In S-contact, two N contacts and two sidegates. Here, we employ the same measurement set-up and terminology as introduced and depicted in Sec. 5.2 and Fig. 5.4(b). All measurements were performed in a dilution refrigerator at a base temperature of $\sim 35\,\mathrm{mK}$. We discuss three CNT devices A, B and C, which showed transport through Andreev bound states, i.e. Andreev resonances (Sec. 3.3.3) could be observed. In device A the Pd wetting layer is 4.5 nm thick, while in the devices B and C it was 6 nm thick. The samples had N-CNT-S room temperature resistances of $\sim 30-40\,\mathrm{k\Omega}$ (A) and $\sim 20\,\mathrm{k\Omega}$ (B and C), respectively. We now characterize each device in detail, taking advantage of the three-terminal geometry.

7.1.1. Device A

In App. D and Fig. D.1, we deduce in detail that transport between all three terminals of device A is governed by a single, large QD. In a region of Coulomb blockade (cf. Fig. D.1), we measure the differential conductance G_1 and G_2 at both terminals N1 and N2 as a function of the combined sidegate voltage $V_{\mathrm{SG1+2}} = V_{\mathrm{SG1}} = V_{\mathrm{SG2}}$ and the bias applied to S, V_{S}, while keeping $V_1 = V_2 \sim 0$. This is plotted in Fig. 7.1(a-d), for both S in the normal state for an external magnetic field $B = 0.4\,\mathrm{T} > B_{\mathrm{c}} \sim 0.2\,\mathrm{T}$ (a-b) applied perpendicular to the substrate, and in the superconducting state of S at $B = 0$ (c-d). In the normal state experiments depicted in Fig. 7.1(a-b), we observe the same

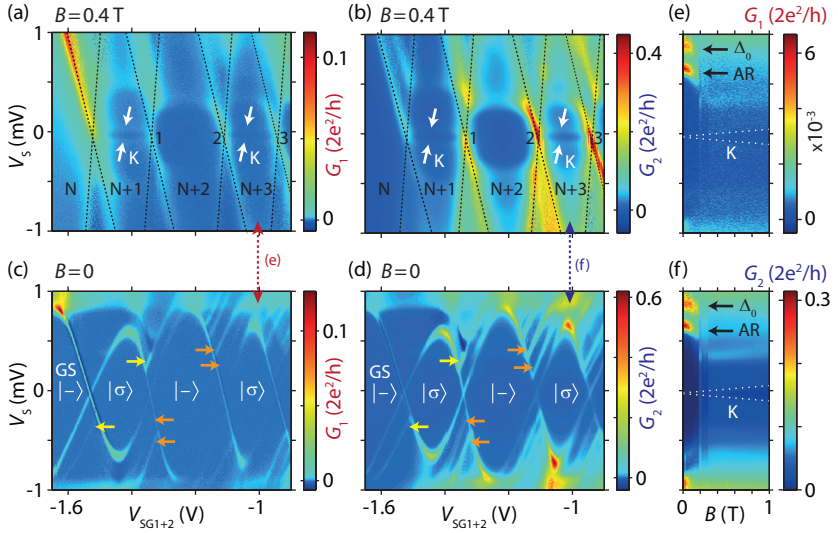

Figure 7.1.: (a-d) Differential conductance G_1 and G_2 of device A as a function of the bias applied to S, V_S, and a combined sidegate voltage V_{SG1+2} at $V_{21} = 0$ and $V_{BG} = 0$, for an external magnetic field $B = 0.4\,T$ applied out-of-plane (a-b) or $B = 0$ (c-d). The white arrows in (a-b) label Zeeman-split Kondo (K) resonances, and numbers next to the dashed CB diamonds the fitted zero bias resonances (main text). GS denotes the QD groundstate in (c-d), and yellow (orange) arrows "excited" Andreev resonances (AR). (e-f) G_1 and G_2 as a function of V_S and B, at a fixed sidegate voltage of $V_{SG1+2} = -1.02\,V$ indicated by red and blue dashed arrows in (a-d). K, AR and Δ_0 mark the Zeeman-split Kondo ridge, the Andreev resonance, or the superconducting transport gap, respectively.

diamond pattern (dashed lines) with a clear even-odd shell-filling sequence in both simultaneously measured conductance maps. In the odd diamonds, we find horizontal conductance lines (K, white arrows) characteristic for a Zeeman-split Kondo resonance [265, 266]. To substantiate this interpretation, we plot the conductance G_1 and G_2 as a function of the bias V_S and the applied magnetic field in Fig. 7.1(e-f), for a fixed gate voltage in the middle of the $N+3$ diamond (indicated by red and blue dashed arrows). We observe a Zeeman-splitting of this Kondo resonance with a g-factor of $g \approx 2.1$ above the critical field $B_c \sim 0.2\,T$ of S, which extrapolates to zero (dashed white lines). From additional conductance measurements in different biasing configurations (e.g. bias applied at one of the N terminals, not shown) and using the advantage of a three-terminal geometry [251], we find that the Kondo resonance originates from the S contact only. From the charge stability diagrams in the normal state of S, we deduce a leverarm $\alpha_{SG1+2} \approx 0.01$ of the combined sidegate to the QD, a charging energy $E_C \sim 2.5\,meV$, and from excited state and

inelastic cotunneling lines the lowest visible excitation energies $\sim 0.3\,\mathrm{meV}$ and $\sim 0.5\,\mathrm{meV}$. As introduced in Sec. 5.2, the three-terminal geometry allows one to determine the coupling strengths Γ_i of the individual contacts to the QD by fitting a Breit-Wigner lineshape to the normal state conductance data in different measurement configurations. This is shown exemplary for one resonance in App. D. From these fits, we obtain $\Gamma = 204\,\mu\mathrm{eV}$, $\Gamma_\mathrm{S} = 150\,\mu\mathrm{eV}$, $\Gamma_1 = 1\,\mu\mathrm{eV}$ and $\Gamma_2 = 53\,\mu\mathrm{eV}$ for resonance 1 in Fig. 7.1(a), $\Gamma = 220\,\mu\mathrm{eV}$, $\Gamma_\mathrm{S} = 173\,\mu\mathrm{eV}$, $\Gamma_1 = 1\,\mu\mathrm{eV}$ and $\Gamma_2 = 46\,\mu\mathrm{eV}$ for resonance 2, and $\Gamma = 151\,\mu\mathrm{eV}$, $\Gamma_\mathrm{S} = 118\,\mu\mathrm{eV}$, $\Gamma_1 = 3\,\mu\mathrm{eV}$ and $\Gamma_2 = 30\,\mu\mathrm{eV}$ for resonance 3. An estimate of the Kondo temperature can be obtained from $kT_\mathrm{K} \sim \sqrt{\frac{E_\mathrm{C}\Gamma}{2}} \exp\left(-\frac{\pi E_\mathrm{C}}{8\Gamma}\right)$ at the electron-hole symmetry point in the middle of the odd diamonds [31, 168, 267], yielding e.g. $kT_\mathrm{K} \sim 6\,\mu\mathrm{eV}$ or $T_\mathrm{K} \sim 70\,\mathrm{mK}$ with $E_\mathrm{C} \sim 2.5\,\mathrm{meV}$ and $\Gamma \sim 0.22\,\mathrm{meV}$ (for resonance 2). This value is in reasonable agreement with the observation of a Kondo resonance in the normal state of S at base temperature.

In the superconducting state of S [Figs. 7.1(c-d)], we observe a suppressed conductance and pronounced resonances for bias voltages below $\Delta_0 \sim 0.95\,\mathrm{meV}$, the superconducting transport gap. Also here we find the same features in both G_1 and G_2, though with varying and partially anti-correlated amplitudes. The subgap lines we interpret as Andreev resonances (AR), i.e. as spectroscopic transitions to or from an ABS: The lowest-energy AR at $eV_\mathrm{S} = \pm\zeta_-$ shows a qualitatively similar dispersion as discussed in Sec. 3.3.3. Consistent with the spin filling identified in the normal state measurements, we observe loops of the Andreev resonance $\pm\zeta_-$ for odd occupation, where Coulomb repulsion favors the doublet ground state (GS) $|\sigma\rangle$. A ground state transition to the singlet GS $|-\rangle$ occurs at $\pm\zeta_- = 0$ for even occupation, for which ζ_- converges to Δ_0. Such a dispersion with a singlet-doublet quantum phase transition (QPT) is expected for the device energy scales, i.e. $kT_\mathrm{K} \ll \Delta_0$ or $\Gamma_\mathrm{S}/E_\mathrm{C} \sim 0.06$ not too large with $\Gamma_\mathrm{S} \gg \Gamma_\mathrm{N}$ [31, 168, 169, 171]. We observe replicas [e.g. yellow and orange arrows in Figs. 7.1(c-d)] of the lowest energy AR $\pm\zeta_-$ at a higher energy with a similar bias-gate dispersion. These "excited" Andreev resonances are typically shifted by a constant value of $\sim 0.2 - 0.3$ or $\sim 0.5\,\mathrm{meV}$ from the lowest energy mode, energies consistent with the lowest excited state spacing found in the normal state measurements. In contrast to IE AT (Chap. 6), we do not observe pronounced negative differential conductance between these excited AR, and they smear out with increasing temperature. This suggests a different physical origin of the excited AR than for the IE AT replicas discussed in Chap. 6. We postpone a more detailed discussion to Sec. 7.3.

7.1.2. Device B

Using a similar analysis as for the previous device in App. D, we find that also transport through device B can be described by a single QD. For this device,

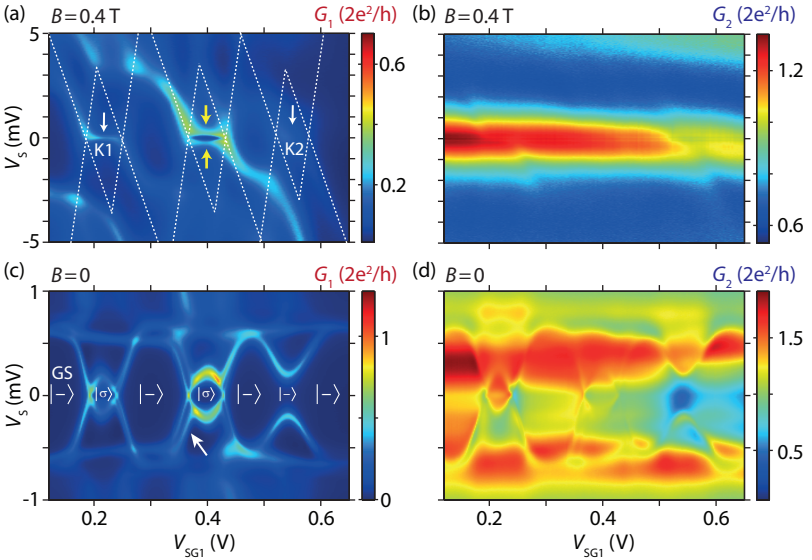

Figure 7.2.: G_1 and G_2 of device B as a function of V_S and V_{SG1} at $V_{21} = V_{BG} = V_{SG2} = 0$, for $B = 0.4\,T$ (a-b) or $B = 0$ (c-d). The white arrows in (a) label Kondo (K) ridges, and dashed lines qualitatively sketch the CB diamonds, where small (large) diamonds correspond to odd (even) occupation. GS denotes the QD groundstate in (c), and the white arrow points to a second Andreev resonance visible at a higher bias $|V_S|$.

the QD is mostly located between S and N1, while the piece of CNT between S and N2 acts as a CNT lead (in an open regime, see App. D). We therefore measure G_1 and G_2 as a function of V_S and V_{SG1} only to keep the other side unperturbed, which is plotted in Fig. 7.2 for S in the superconducting state at $B = 0$ (c-d) and in the normal state of S for $B = 0.4\,T > B_c \sim 0.38\,T$ (a-b). The critical field of devices B (and C, see below) is slightly larger compared to other devices and the reference measurements (Sec. 4.2), possibly due to the thicker Pd layer and a therefore altered Pb growth. In the normal state of S, we observe a conductance pattern in G_1 typical for a more strongly coupled QD, where a CB diamond pattern with an even-odd filling sequence can still be deduced from cotunneling lines [white dashed lines in Fig. 7.2(a)]. In contrast, G_2 shows only a weak conductance modulation in the measurement region as expected for a CNT with strongly coupled contacts, i.e. for highly transparent barriers. Focussing on G_1, we again observe Kondo ridges in the odd charge states (K, arrows). Here, the Kondo ridges are too broad to resolve a Zeeman splitting. The apparently split horizontal lines at $V_S \sim \pm 0.2\,mV$ in the odd charge state in the middle of the conductance map (yellow arrows) do not

agree with the expected Zeeman splitting of a (spin) Kondo resonance for $g = 2$. We speculate that these features are due to inelastic cotunneling lines, possibly in agreement with the observation of a second Andreev resonance in the same charge state at $B = 0$, or related to a valley Kondo effect [268]. From the charge stability diagram in Fig. 7.2(a), we estimate a leverarm of $\alpha_{\mathrm{SG1}} \approx 0.05$, a charging energy of $E_{\mathrm{C}} \sim 3.0\,\mathrm{meV}$, and a level spacing of $\sim 2.5\,\mathrm{meV}$ consistent with a smaller QD located between S and N1. Due to the pronounced Kondo ridges and the stronger coupling to the leads, fits of CB resonances are not possible. We therefore estimate the coupling strength Γ and the Kondo temperature at K1 and K2 from the half width at half maximum (HWHM) of the Kondo ridges [31, 168, 175]. We obtain $kT_{\mathrm{K}} \sim 0.24\,\mathrm{meV}$ or $T_{\mathrm{K}} \sim 2.8\,\mathrm{K}$ for K1, and estimate $\Gamma \sim 0.8\,\mathrm{meV}$ from $kT_{\mathrm{K}} \sim \sqrt{\frac{E_{\mathrm{C}}\Gamma}{2}} \exp\left(-\frac{\pi E_{\mathrm{C}}}{8\Gamma}\right)$ [168]. For K2, we determine $kT_{\mathrm{K}} \sim 0.8$ meV or $T_{\mathrm{K}} \sim 9.3\,\mathrm{K}$, and $\Gamma \sim 1.7\,\mathrm{meV}$. These values are consistent with estimates of Γ obtained from the width of CB features at a finite bias.

Figure 7.2(c-d) shows G_1 and G_2 at $B = 0$, i.e. in the superconducting device state, where we observe pronounced Andreev resonances in G_1 for bias voltages V_{S} below the superconducting transport gap, $\Delta_0 \sim 0.65\,\mathrm{meV}$. Imprints of these Andreev resonances can also be found on a large conductance background in G_2. Due to the stronger coupling to S, we observe a qualitatively different dispersion of these Andreev resonances than for device A. Consistent with the extracted energy scales $kT_{\mathrm{K}} < \Delta_0$, we find a crossing of Andreev resonances in the two leftmost states of odd occupation due to a singlet-doublet GS transition [Fig. 7.2(c)]. In contrast, in the rightmost state of odd occupation (K2), the Andreev resonances do not cross. Here, the QD remains in the $|-\rangle$ ground state due to the increased coupling to the superconductor, consistent with $kT_{\mathrm{K}} > \Delta_0$ for K2 [31, 168, 169, 171]. A second Andreev resonance (arrow) visible in close proximity to the lowest-energy AR might be due to a broken valley degeneracy of the CNT [170], and is possibly related to the inelastic cotunneling lines found in the normal state of S in the same charge state.

7.1.3. Device C

In contrast to the previous devices, device C shows clear characteristics of a double quantum dot with strong inter-dot coupling and level hybridization (see App. D for details). In the measurements and analysis presented here, we focus on features due to QD1. By using sidegate 1 only and setting $V_{\mathrm{SG2}} = 0$, we tune mostly QD1 and keep QD2 in an even, Coulomb-blockaded charge state (App. D). Such measurements are shown in Fig. 7.3, where G_1 and G_2 are plotted as a function of V_{S} and V_{SG1}, for S in the superconducting state at $B = 0$ (c-d) and in the normal state of S for $B = 0.4\,\mathrm{T} > B_{\mathrm{c}} \sim 0.38\,\mathrm{T}$ (a-

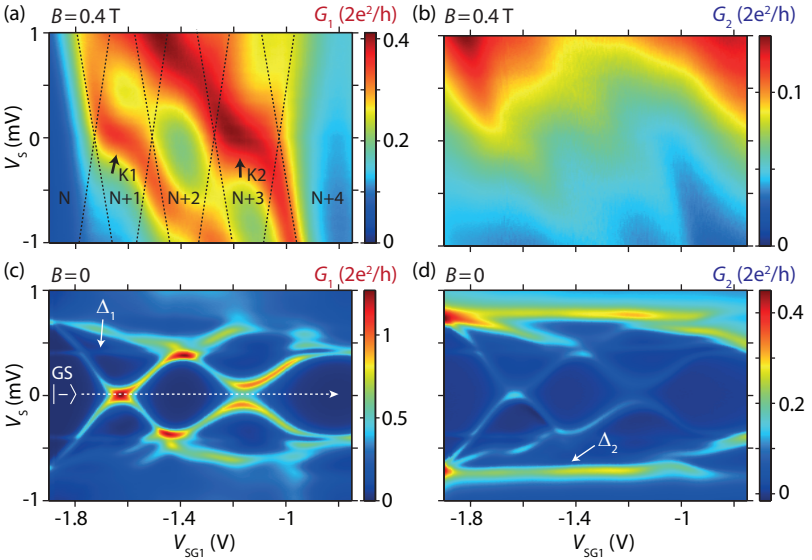

Figure 7.3.: G_1 and G_2 of device C as a function of V_S and V_{SG1} at $V_{21} = V_{BG} = V_{SG2} = 0$, for $B = 0.4\,T$ (a-b) or $B = 0$ (c-d). The black arrows in (a) label Kondo (K) ridges, and dashed lines qualitatively sketch the CB diamonds. GS denotes the QD groundstate in (c), and $\Delta_{1(2)}$ the two assumed superconducting transport gaps.

b). Similar to the previous samples, we find conductance maps characteristic for a more strongly coupled QD, with strong cotunneling lines, and Kondo ridges (K, arrows) for odd occupation in the normal state of S [Fig. 7.3(a)]. From such charge stability diagrams, we estimate the leverarm of SG1 to QD1 $\alpha_{SG1} \approx 0.01$, and a charging energy $E_C \sim 2.4\,meV$ and level spacing $\sim 1.3\,meV$ of QD1. Similar to device B, we estimate the Kondo temperature and Γ from the HWHM of the Kondo ridges. We obtain $kT_K \sim 0.3\,meV$ or $T_K \sim 3.5\,K$ and $\Gamma \sim 0.8\,meV$ for K1, and $kT_K \sim 0.35\,meV$ or $T_K \sim 4\,K$, and $\Gamma \sim 0.88\,meV$ for K2.

In the superconducting state of S [Figs. 7.3(c-d)], we observe again pronounced Andreev resonances visible both in G_1 and G_2. In these conductance maps, two horizontal lines are visible at $\Delta_1 \approx 0.42\,meV$ and $\Delta_2 \approx 0.75\,meV$, which we tentatively interpret as two superconducting transport gaps in the individual CNT arms (QD1 and QD2). For the lowest energy Andreev resonance in Fig. 7.3(c), we find that the ground state always remains a singlet $|-\rangle$, in agreement with the energy scales $kT_K \sim \Delta_1$ [31, 168, 169, 171].

We note, however, that one could interpret Δ_1 also in an alternative man-

ner, and that the origin of this line and the features between Δ_1 and Δ_2 are at present not entirely understood. For example, the lowest-energy AR (presumably originating from QD1) forms an anti-crossing with Δ_1 e.g. at $V_{\mathrm{SG1}} \approx -1.8\,\mathrm{V}$, and continues for $|eV_{\mathrm{S}}| > \Delta_1$. Hence, one might also speculate that Δ_1 is an Andreev resonance originating from QD2, which hybridizes with the Andreev resonance of QD1 e.g. due to crossed Andreev reflection or elastic cotunneling processes. Such a process could possibly lead to the observed anti-crossing at $V_{\mathrm{SG1}} \approx -1.8\,\mathrm{V}$. While such an interpretation is tempting (see also App. D and the description of the Andreev molecule in Chap. 8), this goes beyond the intended scope of this thesis and will not be analyzed further here.

7.2. Spectroscopic linewidth of the Andreev resonances

Using the device parameters extracted in Sec. 7.1 and taking full advantage of the three-terminal geometry, we can now address the broadening and spectroscopic linewidth of the Andreev resonances in our experiments. While the observed broadening of the AR and its origin has already been debated in previous transport experiments [165, 171], theory predicts that the spectroscopic linewidth of the AR should be determined by Γ_{N} only in a N-QD-S device [155], respectively by $\Gamma_{\mathrm{N}} = \Gamma_1 + \Gamma_2$ in our three-terminal N-QD-S devices [177]. This has never been demonstrated so far to our knowledge, mostly due to the lack of a multi-terminal device geometry.

For device A with a not too strong coupling of the superconductor to the QD, the three-terminal device geometry allowed us to determine exact values of the tunnel couplings Γ_i from Coulomb blockade lineshape fits in the normal state of S, with typical values of $\Gamma_{\mathrm{S}} \sim 150\,\mu\mathrm{eV}$ and $\Gamma_{\mathrm{N}} = \Gamma_1 + \Gamma_2 \sim 50\,\mu\mathrm{eV}$. For this device, we find a typical spectroscopic linewidth of the Andreev resonances of FWHM $\sim 50-70\,\mu\mathrm{eV}$, much smaller than the total coupling strength $\Gamma \sim 0.2\,\mathrm{meV}$. This value agrees however very well with the extracted coupling $\Gamma_{\mathrm{N}} \sim 50\,\mu\mathrm{eV}$. Hence, in agreement with the theoretical prediction, our experiments show that the Andreev resonances in N-QD-S devices are indeed mainly broadened by the finite coupling of the QD to the (two) normal metal contacts.

In the limit of large gaps and small electronic level separation as for device A, this reduced effective broadening Γ_{N} for bias voltages below the superconducting transport gap ("turned off Γ_{S}") also allows to observe a manifold of excited Andreev resonances, in agreement with the measurements presented in Figs. 7.1(c-d). In contrast, above the gap or in the normal state the broadening is given by Γ, and hence only few excited states can be resolved in the normal state measurements [Figs. 7.1(a-b)]. In Sec. 7.3, we will use this finding to our advantage, and employ a serial measurement configuration ("Γ_{S} turned off")

device	gap (meV)	E_C (meV)	$\Gamma_1 + \Gamma_2$ (meV)	Γ_S (meV)
A	0.95	2.5	~ 0.05	~ 0.15
B	0.65	3.0	~ 0.2	$\sim 0.6 - 1.5$
C	0.42 (and/or) 0.75	2.4	~ 0.1	~ 0.7

Table 7.1.: Extracted parameters for devices A, B and C.

to probe the transport and excited states between the two N contacts.

For devices B and C, the stronger coupling of the QD to S did not permit to extract exact values of the tunnel couplings Γ_i from Coulomb blockade lineshape fits, but only allowed to estimate the total coupling strength Γ from the width of the Kondo resonances. Here, we can now use the experimentally determined linewidth of the Andreev resonances to first estimate $\Gamma_N = \Gamma_1 + \Gamma_2$, and then $\Gamma_S = \Gamma - \Gamma_N$. For device B, we estimate a linewidth of $\sim 100-200\,\mu$eV for the Andreev resonances. Hence, using $\Gamma_1 + \Gamma_2 \cong 200\,\mu$eV and the total coupling strengths Γ from Sec. 7.1, we deduce a coupling strength between S and the QD of $\Gamma_S \sim 0.6$ meV for the Kondo resonance K1 and $\Gamma_S \sim 1.5$ meV for K2. Similarly, we find a width ~ 0.1 meV of the AR for device C, and estimate $\Gamma_S \sim 0.7$ meV for the Kondo resonances K1 and K2. To summarize our findings, table 7.1 shows some typical device energy scales for all three samples.

7.3. Excited Andreev resonances

In Sec. 7.1, we observed multiple replicas of Andreev resonances (or "excited" AR) for device A, while such features were mostly absent for devices B and C. We found that the spacings between these "excited" AR are consistent with the lowest excited state spacings found in the normal state measurements of the device. Hence, we suggest that these excited AR must be intimately connected to the QD energy level spectrum with small level spacings $\delta E \ll \Delta_0$, consistent with a large QD for device A. Such small level spacings could also originate from a broken KK' degeneracy due to disorder or spin-orbit interactions [75, 76], or a complex and non-uniform confinement potential over the whole QD. In contrast, the level spacings for device B and C are substantially larger, i.e. $\delta E > \Delta_0$ due to the smaller geometrical extension of the QDs, which does not allow the observation of such excited AR.

To substantiate our interpretation and unambiguously identify the origin of these excited AR, we performed three-terminal experiments on device A with an additional bias voltage applied between the normal contacts, i.e. $V_{21} = V_2 - V_1 = V_2 \neq 0$, while still applying the ac excitation to S. Figure 7.4(a) shows conductance maps of G_1 and G_2 as function of V_{SG1+2} and as a function of V_{21}, when no voltage is applied at the S contact ($V_S = 0$). In Sec. 5.2.2,

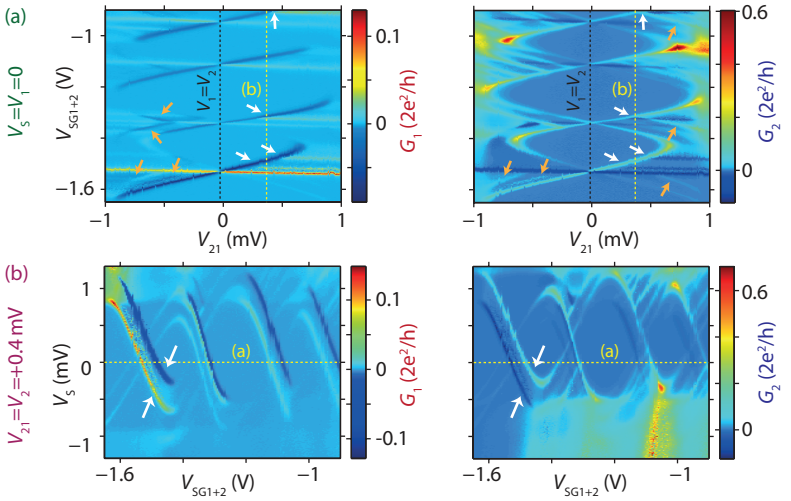

Figure 7.4.: G_1 and G_2 of device A at $V_{BG} = V_1 = 0$ as a function of (a) V_{21} and a combined sidegate voltage V_{SG1+2} at $V_S = 0$ (b) V_S and V_{SG1+2} at $V_{21} = V_2 = +0.4\,\mathrm{mV}$. The black dashed line in (a) marks the position of equal potential at both N contacts for $V_1 = V_2 \approx 0$. White arrows in (a) denote straight lines originating from transport between the N contacts, which partially coincide with the spacing of "excited" Andreev resonances (orange arrows). White arrows in (b) point at the transport boundaries through AR set by the external bias V_{21} (text). The yellow dashed lines in (a) and (b) mark equivalent measurements in the three-dimensional parameter space (V_S, V_{21}, V_{SG1+2}).

we have already analyzed similar experiments for a single QD device with no subgap transport channel (Fig. 5.5), and found that we only probe the transport between the two N contacts. Here, we use the same technique: Due to the additional transport path between S and N via Andreev resonances, one probes both the transport between the two normal contacts and between N and S at the same time. In agreement with this interpretation, we find both straight lines and AR with a curved dispersion, visible best in G_2 [Fig. 7.4(a)]. Because $|eV_S| < \Delta_0$, the resolution of the transport resonances between N1 and N2 is determined by $\Gamma_1 + \Gamma_2$ only, and not by $\Gamma = \Gamma_1 + \Gamma_2 + \Gamma_S$ (see Sec. 7.2). This allows us to map also excited state lines originating from transport between the two N contacts with a high resolution. In Fig. 7.4(a), we find that these excited state lines (straight lines labelled with white arrows) obey a similar spacing or even end at the same bias as corresponding excited AR (marked by orange arrows), which allows to directly support our earlier claim. Hence, we conclude that the excited AR indeed originate from the detailed energy level spectrum of the QD.

In the simplest approximation, one can understand the origin of these ex-

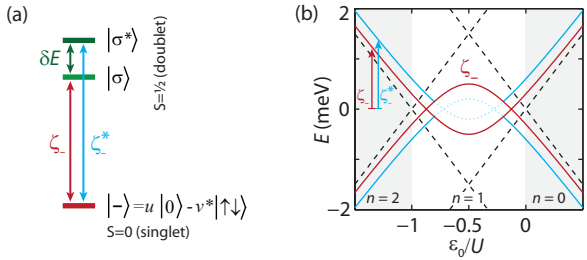

Figure 7.5.: (a) Expected lowest-energy transitions in the superconducting atomic limit, for two spin-degenerate single-particle energy levels $|\sigma\rangle$ and $|\sigma^*\rangle$ with a level spacing of δE. Neglecting ABS originating from $|\sigma^*\rangle$ and considering only first order transitions, an extra excited AR ζ_-^* will occur in addition to ζ_- in the spectrum. (b) Transition energies ζ_- (red) and ζ_-^* (blue) as a function of the gate-tunable orbital energy ε_0/U for the situation sketched in (a), for $U = 3\,\mathrm{meV}$, $\Gamma_\mathrm{S} = 1\,\mathrm{meV}$ and $\delta E = 0.3\,\mathrm{meV}$. n denotes the different charge states, dashed lines the transition energies of the uncoupled QD system.

cited AR qualitatively from the $\Delta \to \infty$ limit of the ABS for a single spin-degenerate orbital (Sec. 3.3.3). Adding a second spin-degenerate single-particle energy level $|\sigma^*\rangle$ to the model system, separated from $|\sigma\rangle$ by δE, we neglect the additional ABS due to the zero and double occupation of $|\sigma^*\rangle$, and consider only first-order transitions $|-\rangle \leftrightarrow |\sigma\rangle$ or $|-\rangle \leftrightarrow |\sigma^*\rangle$ [Fig. 7.5(a)]. More precisely, as depicted in Fig. 7.5(a) for a $|-\rangle$ GS, we suggest that also $|\sigma^*\rangle$ can be populated as an alternative to $|\sigma\rangle$ (both single particle states). The corresponding transition energies ζ_- (red lines) and ζ_-^* (blue lines) are plotted in Fig. 7.5(b). ζ_-^* replicates ζ_- at higher energies exactly as in the experiment, i.e. with a constant energy separation of δE. We call the resonances ζ_-^* *excited Andreev resonances*, because they correspond to a first order transition between a single ABS and an excited single-particle state. Now also the use of our language becomes clear: while in the literature the terms ABS and Andreev resonances are often used equivalently, it is important to distinguish multiple Andreev resonances originating from one and the same ABS here. The illustrated situation of a $|-\rangle$ GS in Fig. 7.5(a) and (b) corresponds to the excited AR marked by yellow arrows in the experimental data of Fig. 7.1(c-d). To be conform with the experimental observations, ζ_-^* also ends at the intersection with ζ_- (red lines) in Fig. 7.5(b). We speculate that this is due to the occurring GS transition to the lower-lying doublet $|\sigma\rangle$: If we assume a fast relaxation rate from $|\sigma^*\rangle$ to $|\sigma\rangle$, and that the excited single-particle state $|\sigma^*\rangle$ is not thermally populated, only transitions $|\sigma\rangle \leftrightarrow |-\rangle$ will occur for a $|\sigma\rangle$ GS, in agreement with the experimental data. Here, for a doublet GS $|\sigma\rangle$ no subgap resonance stems from the $|\sigma\rangle \leftrightarrow |\sigma^*\rangle$ transition, because both states have the same odd electron number. This line of argument follows also

Ref. [171], which found a Zeeman splitting of Andreev resonances only for a singlet GS. Similarly, when one considers additionally lower-lying states $|\sigma^*\rangle$ in the QD level spectrum (not shown), one can qualitatively reproduce also the excited AR marked by orange arrows in Fig. 7.1(c-d). For a better comparison with the experiment, however, one needs to consider a more elaborate model, taking into account all ABS and transitions originating from all excited states of the QD level spectrum.

To complete our comparison with the experiments of Sec. 5.2.2, Fig. 7.4(b) plots G_1 and G_2 at a fixed bias of $V_{21} = +0.4\,\mathrm{mV}$ between the N contacts as a function of V_S and $V_{\mathrm{SG1+2}}$. The yellow dashed lines in Fig. 7.4 correspond to equivalent line measurements in (a) and (b) in the three-dimensional parameter space (V_S, V_{21}, $V_{\mathrm{SG1+2}}$). In these maps, we observe a shifted set of Andreev resonances which is mostly anti-correlated in G_1 and G_2 (white arrows). The region between these AR of positive and negative differential conductance corresponds exactly to the applied bias voltage $V_{21} = +0.4\,\mathrm{mV}$. We find similar characteristics for device B and C. Referring to our previous interpretation in Sec. 5.2.2, this suggests a current band "bordered" by these AR, and a transport process via Andreev bound states between the two normal contacts. Here, the interpretation is however less trivial: both transport processes between S and N or between the two N contacts compete. In the next section we will deepen this discussion, and suggest a possible transport mechanism via Andreev resonances between the two normal contacts.

7.4. Transport via Andreev bound states between two N contacts

In the previous section, we have seen that transport can occur through Andreev resonances between the two normal contacts. To probe this and the underlying transport mechanisms more directly, we now analyze experiments where the ac excitation and dc bias are applied at one of the normal metal contacts, and the differential conductance is measured at the opposite N contact.

7.4.1. Sign changes in the conductance between two N contacts

We first apply the bias voltage $V_{12} = V_1$ at N1, while measuring the conductance G_S at S and G_2 at N2 as a function of the gate voltage V_{SG1} at $V_\mathrm{S} = 0$. This is plotted in Fig. 7.6(a-b) for device B. While G_S shows the pattern of Andreev resonances discussed before (see e.g. Fig. 7.2), we observe very clear and different amplitudes in G_2 at the same gate voltage and bias positions of the Andreev resonances in G_S. This shows that N2 is a separate terminal to the ABS, and that we probe the same Andreev resonances in G_2 and G_S. The conductance G_2 along these Andreev resonances shows however pronounced

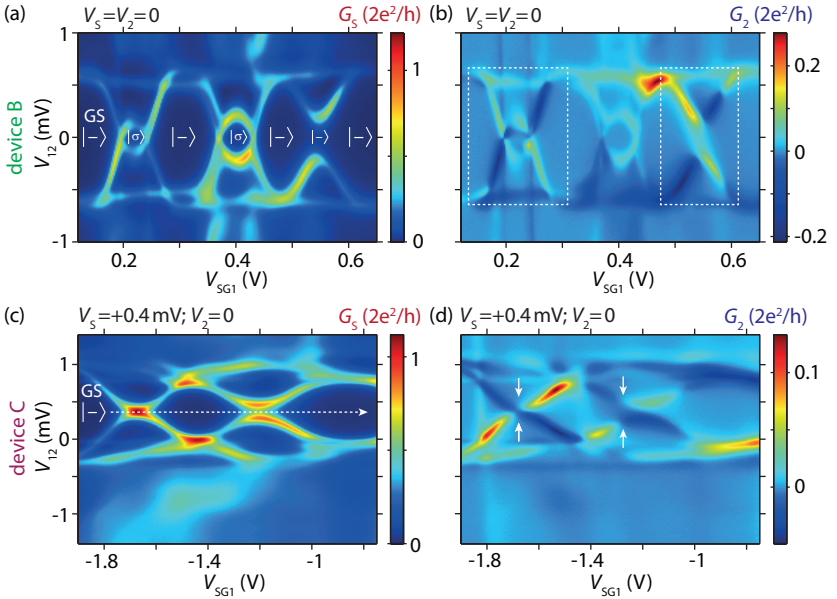

Figure 7.6.: G_S and G_2 as a function of the applied bias voltage $V_{12} = V_1$ and gate voltage V_{SG1}, for (a) device B and $V_S = 0$, (b) device C and $V_S = +0.4\,\mathrm{mV}$. Arrows and dashed rectangles mark regions of sign changes discussed in the main text.

sign changes from positive to negative differential conductance. Both the positive and negative differential conductance of the Andreev resonances found in G_2 have a similar magnitude of $\sim \pm 0.1 \times 2e^2/h$. The conductance sign changes of the AR occur mostly at the electron-hole (e-h) symmetry point or at the singlet-doublet QPT, and are inverted for opposite bias. This is best visible in the regions marked by rectangles in Fig. 7.6(b), i.e. for the leftmost $|\sigma\rangle \leftrightarrow |-\rangle$ GS transition, and for the second rightmost $|-\rangle$ GS. The middle $|\sigma\rangle \leftrightarrow |-\rangle$ GS transition shows a deviating characteristics from these findings, most likely due to the overlapping second AR in this orbital (Sec. 7.1). We find a qualitatively similar characteristics for device A and device C. In Fig. 7.6(c-d), G_S and G_2 of device C are plotted with an additional bias offset $V_S = +0.4\,\mathrm{mV}$ at S. This offset leads to a shift of the AR observed in G_S and G_2 by exactly $V_S = +0.4\,\mathrm{mV}$. Nevertheless, we still find sign changes in G_2 along the position of the Andreev resonances, which again occur at or close to the e-h symmetry points [white arrows in Fig. 7.6(d)]. From further measurements with varying V_S, we conclude that the sign changes are robust with the applied bias V_S.

7.4.2. Rate equation model and comparison with the experiment

To interpret our findings, we first refer to the similarities with the experiments of Ref. [172]. Schindele *et al.* observed similar sign changes at the GS transitions and the e-h symmetry points in the non-local conductance correlations of a double QD CPS device, where ABS existed only on QD1, and QD2 could be tuned independently. These sign changes were found to originate from the competition between a local and non-local (Cooper pair splitting and elastic cotunneling through S) excitation and relaxation of the ABS. In Ref. [172], the non-local current reflects the Bogoliubov-de-Gennes (BdG) amplitudes u and v of the ABS, and allows to qualitatively follow the average charge distribution of the ABS.

Our results suggest a similar competition of transport mechanisms between the S and the two N contacts. We hence introduce a similar rate equation model as in Ref. [172] to describe the transport through our system, using the superconducting atomic limit for the ABS (Sec. 3.3.3). We note however already here, that the obtained equations and the underlying transport mechanism causing the sign changes are different from Ref. [172]. We model our system as illustrated in Fig. 7.7(b), as a single QD coupled with Γ_S to S and with $\Gamma_{1(2)}$ to N1 (N2), and consider transport only through the Andreev resonances $\pm\zeta_- \equiv \pm\zeta$. A bias $V_{12} = V_1$ is applied to N1 as in the experiment, whereas S and N2 are kept on the same potential, i.e. $\mu_\mathrm{S} = \mu_2 = 0$. We choose the (technical) current direction for the individual contacts as depicted in Fig. 7.7(b), so that $I_1 + I_2 + I_\mathrm{S} = 0$. Transport through the Andreev resonances is described by the two level rate equation depicted in Fig. 7.7(a), where $t_{\mathrm{e(r)}}$ denotes the total rate of the excitation (relaxation) by electrons from N1 and N2, and GS (ES) the systems ground state (excited state). The steady state occupation probabilities P_GS and $P_\mathrm{ES} = 1 - P_\mathrm{GS}$ of the GS and ES can be calculated by

$$\frac{d}{dt}P_\mathrm{ES} = t_\mathrm{e}P_\mathrm{GS} - t_\mathrm{r}P_\mathrm{ES} = 0, \tag{7.1}$$

which yields $P_\mathrm{GS} = t_\mathrm{r}/(t_\mathrm{r} + t_\mathrm{e})$ and $P_\mathrm{ES} = t_\mathrm{e}/(t_\mathrm{r} + t_\mathrm{e})$.

Both rates t_e and t_r are composed of all possible excitation and relaxation processes, graphically illustrated by red (excitation) and blue (relaxation) arrows in Fig. 7.7(b). In these individual rates $t_{\mathrm{e(r)}}^{1(2)+(-)}$, a superscript 1(2) denotes the contacts N1 or N2, respectively, and $+(-)$ or the arrow direction denote if an electron is added (removed) from the S-QD system. In contrast to Ref. [172], where the QD2 resonance acted as an energy filter for electrons from N2, we cannot neglect any of the depicted processes. The individual excitation and relaxation rates can then be calculated using Fermi's golden rule [172, 203, 269]. Assuming e.g. the doublet GS $|\sigma\rangle$ and the ES $|-\rangle$ as illustrated

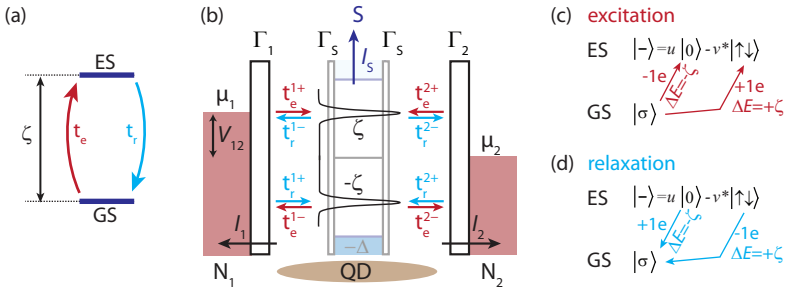

Figure 7.7.: (a) Two-level rate equation model with excitation (relaxation) rate t_e (t_r). (b) Schematic of the three-terminal N-QD-S system, with a faint superimposed S contact, and a negative bias voltage $V_{12} = V_1$ applied at N1. Transport is only considered through the AR $\pm\zeta$, with color-coded rates $t^{1(2)+(-)}_{\mathrm{e(r)}}$ (text). I_1, I_2 and I_S denote the technical current direction in the respective contacts (arrows). (c-d) Intuitive diagrams of the possible excitation (c, red) and relaxation (d, blue) processes and non-vanishing transition matrix elements, if $|\sigma\rangle$ is the GS. We consider only first order transitions (+1e/-1e) with the energy conditions $\Delta E = \pm\zeta$.

in Fig. 7.7(c-d), the rate t_e^{1+} for the excitation with an electron from N1 is

$$|\sigma\rangle \xrightarrow[\mathrm{N1}]{+1e} |-\rangle : \; t_\mathrm{e}^{1+} = \Gamma_1 \underbrace{|\langle -|d_{\bar\sigma}^\dagger|\sigma\rangle|^2}_{v^2} f_1(\zeta), \tag{7.2}$$

where $f_{1(2)}(E)$ denotes the Fermi function of contact N1 (N2), and $d_\sigma^\dagger$ (d_σ) the creation (annihilation) operator for an electron on the QD with spin σ (opposite spin $\bar\sigma$), and v (u) the (real) BdG amplitudes of the ABS (Sec. 3.3.3). Similarly, we find

$$|-\rangle \xrightarrow[\mathrm{N2}]{-1e} |\sigma\rangle : \; t_\mathrm{r}^{2-} = \Gamma_2 \underbrace{|\langle\sigma|d_{\bar\sigma}|-\rangle|^2}_{v^2} (1 - f_2(\zeta)) \tag{7.3}$$

for the relaxation rate with an electron leaving to N2. For the doublet GS $|\sigma\rangle$, all these rates can be obtained from the diagrams in Fig. 7.7(c-d), which depict all non-vanishing transition matrix elements and the respective energy conditions in an intuitive, graphical manner. From such diagrams, we obtain the total excitation and relaxation rates

$$\begin{aligned} t_\mathrm{e} &= \underbrace{\Gamma_1 v^2 f_1(\zeta)}_{t_\mathrm{e}^{1+}} + \underbrace{\Gamma_2 v^2 f_2(\zeta)}_{t_\mathrm{e}^{2+}} + \underbrace{\Gamma_1 u^2 (1 - f_1(-\zeta))}_{t_\mathrm{e}^{1-}} + \underbrace{\Gamma_2 u^2 (1 - f_2(-\zeta))}_{t_\mathrm{e}^{2-}} \\ t_\mathrm{r} &= \underbrace{\Gamma_1 v^2 (1 - f_1(\zeta))}_{t_\mathrm{r}^{1-}} + \underbrace{\Gamma_2 v^2 (1 - f_2(\zeta))}_{t_\mathrm{r}^{2-}} + \underbrace{\Gamma_1 u^2 f_1(-\zeta)}_{t_\mathrm{r}^{1+}} + \underbrace{\Gamma_2 u^2 f_2(-\zeta)}_{t_\mathrm{r}^{2+}} . \end{aligned} \tag{7.4}$$

For the case of a singlet GS $|-\rangle$, all rates can be obtained from Eq. (7.4) with the replacement $u \leftrightarrow v$, because the initial and final states in the transition matrix elements are simply interchanged. The total currents in the contacts N1 and N2 are then given by [172]

$$\begin{aligned} I_1 &= \frac{e}{h}\left((t_{\mathrm{e}}^{1+} - t_{\mathrm{e}}^{1-})P_{\mathrm{GS}} + (t_{\mathrm{r}}^{1+} - t_{\mathrm{r}}^{1-})P_{\mathrm{ES}}\right) \\ I_2 &= \frac{e}{h}\left((t_{\mathrm{e}}^{2+} - t_{\mathrm{e}}^{2-})P_{\mathrm{GS}} + (t_{\mathrm{r}}^{2+} - t_{\mathrm{r}}^{2-})P_{\mathrm{ES}}\right), \end{aligned} \tag{7.5}$$

and $I_{\mathrm{S}} = -(I_1 + I_2)$. We note that the bias voltage V_1 enters also in the Fermi functions in these equations. The differential conductance can then be obtained from $G_i = \mathrm{d}I_i/\mathrm{d}V_1$.

Figure 7.8 shows such conductance maps as in the experiments, i.e. as a function of the bias V_{12} applied to N1 and the normalized (gate-tunable) QD orbital energy ε_0/U, calculated from Eq. (7.5) and (7.4) with the transition energies $\pm\zeta$ and BdG amplitudes from Sec. 3.3.3 in the limit of $\Delta \to \infty$. Comparing Fig. 7.8(b-c) with the equivalent experimental data plotted in Fig. 7.6, we find that the model at least qualitatively reproduces our experimental results. Here, we assumed a Γ_{S} in the model that leads to a singlet-doublet QPT, as e.g. for device B in Fig. 7.6(a-b). Whereas the calculated differential conductance G_{S} in the S contact reproduces the typical AR pattern with solely positive conductance as in the experiment, we find sign changes in the calculated conductance G_2 at the contact N2 [Fig. 7.8(c)]. As in the experiment [Fig. 7.6(b)], these sign changes occur at the GS transition and the e-h symmetry point ($\varepsilon_0/U = -0.5$), or for a reversed bias. Similarly, for the case in which the system's GS is the singlet $|-\rangle$ for all gate voltages, i.e. for larger couplings Γ_{S}, we find sign changes only at the e-h symmetry point

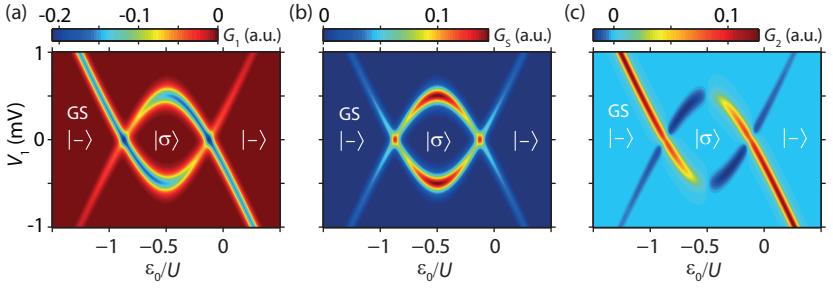

Figure 7.8.: Model calculation of the differential conductance according to Eqs. (7.5) and (7.4) in the $\Delta \to \infty$ limit, for $\Gamma_{\mathrm{S}} = 1\,\mathrm{meV}$, $U = 3\,\mathrm{meV}$ and $\Gamma_1 = \Gamma_2 = 0.1\,\mathrm{meV}$. (a) G_1, (b) G_{S} and (c) G_2 as a function of the bias voltage V_1 applied to N1 and the QD orbital energy ε_0/U, for $V_2 = V_{\mathrm{S}} = 0$ as in the experiment. To simulate a broadening of the AR, a small finite temperature of $T = 0.5\,\mathrm{K}$ was assumed.

$\varepsilon_0/U = -0.5$ in the model (not shown), which is also consistent with the experiment shown in Fig. 7.6(b) and (d). In addition, the sign changes in the model are independent of the applied bias voltages $V_S \neq 0$ or $V_2 \neq 0$ as in the experiment (not shown).

In our model and for the situation depicted in Fig. 7.7(b) with $V_S = V_2 = 0$ and $\mu_1 > +\zeta$, we obtain non-vanishing rates only for t_e^{1+}, t_r^{1+}, t_r^{2-} and t_r^{2+} due to the Fermi functions. The sign change in G_2 is therefore caused by the competition of the two relaxation processes t_r^{2-} and t_r^{2+} from contact N2 [see e.g. Eq. (7.5)], and only occurs in the model simulations if both processes are considered. Hence, the current I_2 is proportional to the difference between the BdG amplitudes, $I_2 \propto \pm(u^2 - v^2)$, where the prefactor changes the sign at a singlet-doublet GS transition or for a reversed bias V_1. Note that this proportionality applies also for a finite bias V_2 or V_S as in the experiment, even when in this case different processes (determined by the Fermi functions, e.g. of N2) cause this dependence. Similar to Ref. [172], but in a more direct way, the conductance G_2 allows us to monitor the gradual charging of the ABS $|-\rangle$ with the gate voltage, which evolves from a mean excess QD charge of $0e$ in the $n = 0$ state to an average QD charge of $2e$ in the $n = 2$ state. Exactly this charge distribution of the ABS, expressed by the BdG amplitudes, leads to the sign change at the e-h symmetry point in the $n = 1$ charge state. Combined with the excitation t_e^{1+}, the processes t_r^{2-} and t_r^{2+} correspond to the direct transfer of one electron from N1 to N2 via the ABS, similar to an 'elastic cotunneling' process through the AR, and the 'non-local' creation of a Cooper pair in S, an inverse CPS process. Both of these "non-local" transport processes are sketched schematically in Fig. 7.9. For the reverse bias V_1, instead of a Cooper pair creation a splitting of a Cooper pair from S can occur [t_e^{1-} and t_r^{2-} in Fig. 7.7(b)]. Compared to Ref. [172], these processes are significantly different, because all three terminals have the full bandwidth and are not energy-filtered by a second QD. Only this allows us to observe the 'cotunneling' process through the AR, which we will call *"resonant ABS tunneling"* in the following.

In our model, the processes are considered sequentially. The good overall qualitative agreement with the experimental findings show that our descrip-

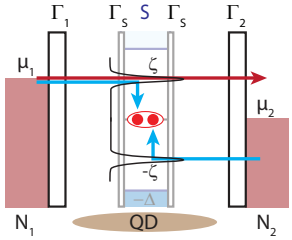

Figure 7.9.: Schematic of the "non-local" transport processes for $\mu_1 > +\zeta$. The red arrow depicts "resonant ABS tunneling", i.e. a direct transfer of one electron from N1 to N2 via the ABS, whereas the blue arrows show an inverse CPS process, i.e. the "non-local" creation of a Cooper pair in S.

tion of the experiments by a single large QD is sufficient, and that both a 'non-local' CPS and a 'resonant ABS tunneling' process occur in the experiments to account for the observed sign changes. This interpretation of our experimental findings is also unambiguously supported by the recent more elaborate calculations for such a three-terminal N-QD-S system [177, 200], all in qualitative agreement with our experimental findings and model results. Ref. [177] states for example explicitly, that sign changes in the 'non-local' subgap conductance are due to the "competition between the ballistic electron transfer and crossed Andreev reflection processes". Hence, Cooper pair splitting is indeed occurring in our three-terminal N-QD-S devices, whereas the also present 'resonant ABS tunneling' between two normal terminals has to our knowledge not been observed before. Unfortunately, in our model the relative magnitude of both processes is determined by Γ_2 only and hence fixed. We therefore did not quantify the relative and absolute strengths of the two processes from the conductance amplitudes in the experiments yet, but will address this in future.

Finally, we note that for a better agreement with the experiment, both a finite Δ and interactions with quasiparticles (e.g. by NRG calculations), and additionally occurring normal transport processes (without involvement of ABS) between the two N contacts would have to be taken into account. Such more elaborate models could possibly also capture additional sign changes of the conductance sometimes observed close to the superconducting gap edge Δ (Fig. 7.6). The fact that our model captures the main experimental findings, however, already demonstrates that transport through the Andreev resonances is the dominant transport mechanism also between the two N contacts.

7.4.3. Probing the proximity S-QD system with a floating S contact

To study this intriguing finding further, we analyze transport between the two normal metal contacts when the S contact is left floating. Such experiments are directly equivalent to Ref. [173], where bound states in a proximitized S-QD hybrid InAs nanowire were probed through transport between two N contacts. Figure 7.10 shows such conductance measurements as a function of bias and gate voltage in the same gate voltage region as discussed previously, for device A (a), C (b), and B (c). The devices and measurements are ordered according to increasing Γ_S (red arrow), extracted previously in Sec. 7.1 and Sec. 7.2.

For device A with a weak coupling Γ_S and small Γ_S/E_C, we observe CB diamonds [dashed lines in Fig. 7.10(a)] in the conductance between the two normal metal contacts, as if the superconductor were not present. For this device, we do not find any superconductivity-related conductance features in G_1, i.e. no signatures of Andreev resonances, even if these could be clearly observed when the superconductor was grounded (see e.g. also Fig. 7.4). In

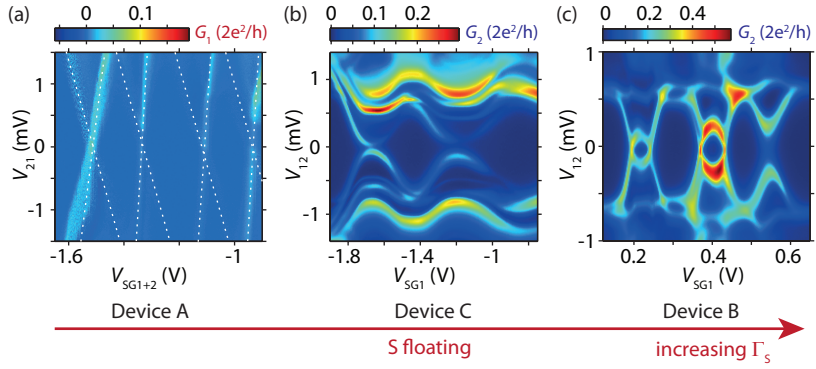

Figure 7.10.: Conductance between the two normal contacts N1 and N2 with the S contact floating. (a) $G_1(V_{21}, V_{SG1+2})$ for device A, (b) $G_2(V_{12}, V_{SG1})$ for device C, and (c) $G_2(V_{12}, V_{SG1})$ for device B. The measurements are ordered for increasing coupling strengths Γ_S of the devices (bottom arrow).

contrast, device C and B with an increased coupling strength Γ_S show clear signatures of Andreev resonances in the transport between the two N contacts. For both devices, the previously observed sign changes when S was grounded [Fig. 7.6] have completely vanished, and we observe solely positive differential conductance. For device B, this experiment directly matches the previously observed dispersion [Fig. 7.2], whereas for device C we observe additional bent lines at higher energies [cf. Fig. 7.3]. The fact that the AR are centered around zero bias suggests a negligible charging of the superconductor (voltage on S was not measured).

For interpreting these findings, we first note that all experiments correspond to the boundary condition $I_S = 0$. In Sec. 3.3.3, we introduced ABS as new sub-gap energy levels of the QD, that emerge from a strong coupling of the QD to the superconductor, and concluded that this superconducting proximity effect severely modifies the QD's energy spectrum. In the experiments discussed here, one expects to probe exactly this modified energy spectrum in the transport between the two N contacts, at least for sufficiently small (sub-gap) bias voltages. This energy spectrum allows transport between the two normal contacts with the creation and annihilation of a Cooper pair in S and the excitation (relaxation) of ABS with electrons from different normal contacts, so that $I_S = 0$ is satisfied. Additionally, the 'resonant ABS tunneling' discussed in the previous section might play an important role. In agreement with this intuition, we observe clear signatures of Andreev resonances in the conductance between the two normal contacts for devices B and C with a sufficiently strong coupling Γ_S to the superconductor. Device A, with a smaller

coupling Γ_S, however contradicts this expectation. While we did observe clear signatures of ABS also for this device in the previous experiments, the CB diamonds found in Fig. 7.10(a) map only the unperturbed QD energy level spectrum, and suggest a "normal" transport channel between the N contacts as if the S contact were not present. This suggests that our initial picture is not entirely correct, where we assumed that the superconductor and the QD are no longer individual entities for a sufficiently strong coupling Γ_S, i.e. that the ABS "live" on the QD. One might speculate that the regime of an intermediate coupling Γ_S is not very well described by the $\Delta \to \infty$ limit of the ABS, so that a set of normal, unperturbed QD states is still available below S. While a more detailed analysis, also based on models, is required for a detailed explanation of the observed phenomena and to support or refute our interpretation, we conclude that such experiments provide a novel experimental probe for the superconducting proximity effect in S-QD systems, and possibly probe the strength of the coupling between S and the QD.

7.5. Conclusions

In conclusion, we studied transport through Andreev bound states in a three-terminal N-QD-S geometry. This geometry allowed us to identify the finite coupling to the normal metal leads as main source for the broadening of the Andreev resonances. We could identify 'excited' Andreev resonances at higher energies with the transitions between Andreev bound states and excited single-particle QD states, and observed clear sign changes in transport through the Andreev resonances between the two normal metal contacts. These sign changes could be explained in an intuitive rate equation model by the competition of the non-local creation of a Cooper pair in S and the transport of a single electron through the Andreev resonance. Our results show that novel non-local transport features occur in a single QD coupled to one S and two N contacts, and agree qualitatively also with the predictions of Ref. [177]. Finally, our experiments with a floating S contact are a novel experimental probe for the superconducting proximity effect in S-QD systems, which could possibly provide a measure for the coupling strength between S and the QD.

8

Towards Cooper pair splitting with large gap superconductors in double QD devices

In this chapter, which is intended purely as an outlook, we present our efforts and progress to achieve Cooper pair splitting (CPS) in "regular" CNT double QD (DQD) based Cooper pair splitter (CPS) devices (Sec. 3.3.4) also with large superconducting transport gaps. While such experiments are desirable to gain a deeper understanding of the CPS process itself and its relation to competing subgap transport mechanisms (local pair or Andreev tunneling) [19, 33, 179], the possibility of finite-bias CPS experiments [216] with $\Gamma < |eV_{\mathrm{SD}}| \ll \Delta$ allows to reduce entanglement loss due to electron-hole pair excitations from the N metal leads [19, 78]. S contacts with large superconducting transport gaps and higher critical magnetic fields should also be beneficial for combining a CPS device with ferromagnetic contacts, e.g. for entanglement detection [39, 40], due to the increased subgap resolution also at finite (stray and external) magnetic fields. Finally, if the two QDs are strongly coupled to S and weakly to the N contacts, a novel molecular state coined *Andreev molecule* [78] could form. This state is conceptionally very similar to the molecular states in conventional inter-dot tunnel-coupled DQDs, where the charge states (1,0) and (0,1) hybridize [257]. For a strong coupling to S, CPS processes also mediate a coupling between the two QDs and mix the (1,1) and (0,0) charge states to a novel "non-local bound state", an Andreev molecular state. To observe the characteristic anti-crossings for such molecular states, a large superconducting transport gap is certainly also beneficial.

In the previous chapters, we did however not achieve ideal working conditions for the envisioned experiments. For Nb-based CPS devices (e.g. Chap. 6)

we achieved two clearly decoupled QDs – possibly due to defects in the CNT created by sputter deposition of the Nb contacts – but did not observe CPS. A possible explanation might be the short superconducting coherence length of Nb, much smaller than the width of the superconducting contacts, leading to a geometrical suppression of CPS as discussed in Sec. 3.3.4. We note that the observed resonant AT does not suffer from such a suppression factor [19]. In contrast, for Pb-based CPS devices we found that mostly a single, large QD or sometimes a very strongly interdot-coupled double QD forms in a non-predictable manner between the two normal contacts, independent of the coupling strength Γ_S to the superconductor. In Sec. 5.2, we ascribed this rather surprising characteristics to the clean ZEP EBL, the softness of Pb combined with a gentle material deposition, or the largely different workfunction of Pb. While we already found rather indirect signatures of CPS for a strong coupling of a single QD to S (Chap. 7), the three-terminal Pb-based devices were not suitable to realize a regular DQD-based Cooper pair splitter. Sec. 8.1 hence summarizes our efforts to obtain two QDs in Pb-based CPS devices in a more controlled manner, while Sec. 8.2 presents preliminary measurement results obtained on such a device. Finally, Sec. 8.3 illustrates different CPS device geometries that could be relevant for future experiments.

8.1. Approaches to obtain two QDs in Pb-based devices

In general, there exist various possibilities to define a DQD in a Pb-based CNT CPS device in a more controlled manner. This could possibly be achieved by changing the material properties (e.g. work function), a modified Pb deposition (e.g. sputtering), electrostatic gating, by cutting the CNT below the S contact or even contacting two individual CNTs of a 'CNT cross' (Sec. 8.3). Apart from the sputter deposition, we tested all of these approaches.

A thickness change of the Pd wetting layer below the Pb or a different material choice (e.g. Ti) could possibly influence the S contact's workfunction. The compatibility with a smooth Pb growth in narrow strips (Sec. 4.2) however severely limits the choice of suitable materials, and a thicker Pd interlayer (decreases also Δ) does not result in a more reproducible DQD formation (Chap. 7, devices with 6 nm Pd instead of 4.5 nm). Defining a DQD with electrostatic gates (e.g. sidegates, backgate) worked only very limited for our Pb-based CNT devices on substrate (see App. B and D), and typically also strongly depends on the respective sample (e.g. semiconducting CNT). Such gate-defined DQDs in conventional CNT devices show usually also strong inter-dot couplings [257], making CPS experiments more challenging [21].

We hence focussed our attention on cutting the CNTs below the S contact prior to the Pb evaporation, therefore separating the contacted CNT into two individual pieces. A focussed ion beam (FIB) based on Ga allows to cut the

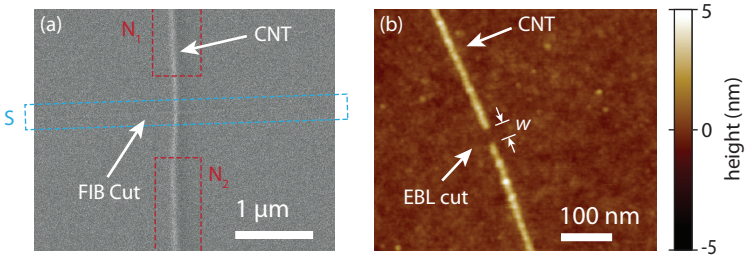

Figure 8.1.: (a) SEM image of a FIB-cut CNT. Dashed rectangles mark the intended CPS device geometry, where the S contact is placed over the cut. (b) AFM image of a CNT cut by EBL and a successive plasma etch. w denotes the width of the cut in the CNT.

CNTs with a line width of $w \sim 30 - 50\,\text{nm}$, which is shown in the SEM image of Fig. 8.1(a). Unfortunately, for all 14 Ga-FIB cut CNT devices, we did not obtain measurable contact to the CNT with an evaporated Pb contact [aligned on top of the cuts, Fig. 8.1(a)] any more, even if the cut area was cleaned with hydrofluoric acid prior to the Pb evaporation to remove possible SiO_2 residues from FIB milling. We hence assume that the FIB milling sputters residues such as carbon, Ga, or Si directly on top of the $\sim 1\,\text{nm}$ thick CNT in the vicinity of the cut, rendering good contacts to the CNT almost impossible. A similar study, which used He-FIB cut CNTs as electrodes for molecular electronics, found significantly increased contact resistances for the less invasive milling with He ions, also supporting our findings [270]. To circumvent these problems, we developed a cutting procedure based on an Ar/O_2 RIE plasma etch. In an additional EBL step, $\sim 30\,\text{nm}$ wide lines are patterned[1] into a 100 nm thick ZEP resist layer using cold development at $T = 5°\text{C}$. A 30 s long RIE Ar/O_2 etch[2] is enough to remove the carbon in the developed area, leaving the rest of the CNT protected by the resist mask. After removal of the resist, the superconducting Pb strip can then be patterned on top of the cut in the CNT as usual. Figure 8.1(b) shows an atomic force microscopy (AFM) image recorded in tapping mode of such an EBL defined cut in a CNT. The method works reliably, in three test devices we always obtained $w \approx 30\,\text{nm}$ wide cuts in the $1-4\,\text{nm}$ thick CNTs. In Fig. 8.1(b), we note also the relative cleanliness of the substrate (mean surface roughness 0.25 nm) after several ZEP resist based processing steps, even in the area of the cut. This also supports our previous claim of the improved cleanliness for a ZEP EBL process (Sec. 2.2.1). It is possible to contact such cut CNTs, though with a clearly reduced yield than for normal processing (possibly due to smaller contact overlap).

[1] Acceleration voltage 10 kV, line dose 220 pC/cm, development as in App. A.
[2] Parameters Oxford Plasmalab 80 Plus: $p = 250\,\text{mTorr}$, flow 16 sccm (16 %) Ar/8 sccm (8 %) O_2, power 30 W, ZEP etch rate $\sim 40\,\text{nm/min}$.

8.2. Pb-based CNT double QD device

In this section, we briefly summarize our first measurement results obtained on a Pb-based CPS device processed on a (possibly) cut CNT. The device was fabricated as described in Sec. 5.2, except for the additional plasma etch-based CNT cutting procedure directly prior to the Pb evaporation. There is a high chance that the contacted CNT was partially etched/cut, because the three successful CNT reference cuts discussed in the previous section were processed on the same sample, in the same step, and imaged with the AFM after the measurements of this device. The device had S-CNT-N room temperature resistances of $\sim 250\,\mathrm{k\Omega}$, and all measurements were carried out in a dilution refrigerator at a base temperature of $\sim 50\,\mathrm{mK}$ in the set-up of Fig. 5.4(b).

Figure 8.2 shows the zero-bias differential conductance G_1 and G_2 measured at N1 and N2 as a function of the sidegate voltages V_{SG1} and V_{SG2}, for equal potentials of the two N terminals, i.e. $V_{21} = 0$. Focussing first on the measurements in Fig. 8.2(a) and (b) at $B = 0.6\,\mathrm{T} > B_{\mathrm{c}}$ in the normal state of S, we observe a charge stability diagram with a honeycomb pattern typical for a double QD. One finds two different slopes in this DQD charge stability diagram, the conductance of which are either only strong in G_1 or G_2. This indicates that QD1 (QD2) is located between S and N1 (N2). While the separation of the triple points [TP, Fig. 8.2(b)] hint at a significant capacitive inter-dot coupling, the curved resonances in the vicinity of the triple points suggest a level hybridization due to a non-vanishing inter-dot tunnel coupling [255–257]. This is further supported by a serial measurement through the DQD system (not shown), which shows weak conductance along honeycomb borders also away from the strong conductance at the triple points [257]. These results contradict our expectation to find two decoupled QDs for a completely cut CNT. In contrast, the facts that (i) all reference CNTs on the same sample showed clear cuts in AFM images, and (ii) that we observed for the first time a clear and regular DQD conductance pattern with a single QD located in each arm at least suggest that the CNT plasma etching must have partially worked. One might speculate that the plasma etching removed the CNT only partially, or only created defects in the CNT at the intended position of the cut, which could possibly explain the finite inter-dot coupling. To resolve this uncertainty in future devices, it would be beneficial to control the CNT cut either with an AFM image or by measuring the conductance between the two N contacts already prior to the Pb deposition.

In the superconducting state of S, we observe a transport gap of $\Delta_0 \approx 0.9\,\mathrm{meV}$, but no features due to ABS. Hence, such a DQD geometry should already be sufficient for CPS experiments [21]. In Fig. 8.2(c), the zero-bias conductances G_1 and G_2 are plotted as a function of V_{SG1} and V_{SG2} at $B = 0$. Astonishingly, instead of a regular CPS signal with an increased conductance at the anti-crossings or positive conductance correlations [21, 33], we observe

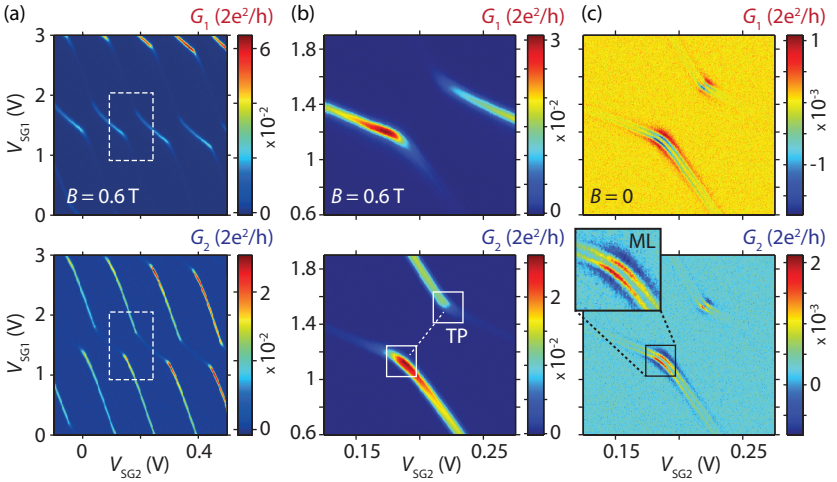

Figure 8.2.: Conductance G_1 and G_2 as a function of V_{SG1} and V_{SG2}, at $V_S = V_{21} = 0$ and $V_{BG} = -12\,V$: (a,b) For $B = 0.6\,T$ in the normal state of S for (a) a larger gate voltage range or (b) in the region indicated by rectangles in (a), and (c) in the superconducting state of S at $B = 0$ in the gate region of (b). Rectangles in (b) indicate the triple points (TP) of the DQD charge stability diagram, the inset in (c) the multi-line (ML) feature.

multiple lines [ML, Fig. 8.2(c)] of positive and negative differential conductance. These conductance features are completely anti-correlated, i.e. we observe positive conductance in G_1 while obtaining the same negative conductance value in $G_2 = -G_1$ and vice versa. The features are strongest at the position of the anti-crossing, i.e. where the two dot levels mix strongest, and vanish in the normal state of S [Fig. (b)]. Corresponding features are observed in dc current measurements. We controlled that ML is not due to a small bias offset $V_{21} \neq 0$ between the N contacts, i.e. ML does not vanish for increasing $|V_{21}|$, but only changes the respective weights or asymmetry of ML. In a finite bias experiment ($V_S \neq 0$, not shown), ML is aligned with the chemical potential of the normal metal leads, i.e. $\mu_{ML} = \mu_N$. When one measures in series through the double QD, i.e. with a bias voltage applied at the N1 contact and recording G_S and G_2, we do not observe any features in G_S within the energy gap of the superconductor. The ML features are however at present not understood, and a more detailed analysis goes beyond the scope of this thesis, but will be addressed in future.

Nevertheless, the developed CNT cutting procedure and the possible formation of DQDs also in Pb-based devices is a step towards realizing DQD-based CPS experiments in CNT devices with large superconducting transport gaps.

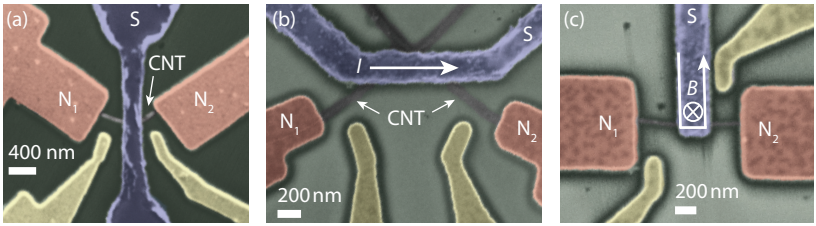

Figure 8.3.: False-color SEM images of CPS devices in various geometries. (a) CPS device on a bent CNT to realize the entanglement detection proposal of Braunecker *et al.* [113]. (b,c) Geometries suitable for an enhancement of CPS by 'current-driving' [271] (text).

8.3. Device geometries for future experiments

In this section, we present some SEM images of CPS devices in various geometries that provide an interesting route for future experiments. We did however not obtain working devices in any of these geometries yet.

We will see in Part II of this thesis, that it is quite challenging to integrate ferromagnetic contacts as detectors for spin-entanglement in CPS experiments. A different, more promising approach to demonstrate the spin-entanglement of the split Cooper pairs was proposed by Braunecker *et al.* [113]. Figure 8.3(a) shows a possible implementation of this proposal, in which an external magnetic field and a bent CNT are used to obtain different spin quantization axes due the spin-orbit interaction in the two arms of a CPS device. Here, the two QDs act as spin-selective filters and allow to probe a violation of the Bell inequality by current cross-correlation measurements.

Figure 8.3(b) and (c) show two device geometries possibly suitable for a 'current-driving' of CPS: according to Ref. [271], a supercurrent component parallel to the CNT junction could enhance the CPS efficiency, providing an 'on-demand' source of CPS. Here, the finite momentum of the Cooper pairs opens a bias window, in which CPS is possible without any geometrical suppression factor even for widths of the S contact larger than the coherence length ξ_0, while elastic cotunneling is suppressed. In (b), two individual CNTs of a CNT 'cross' are contacted to obtain a sizeable supercurrent component along the CNT junction. Supercurrents I with a value below the critical current density, e.g. $j_c \approx 1.3 \cdot 10^7\,\mathrm{A/cm^2}$ in our Pb strips, could then be driven through S. Fig. (c) shows a possible realization if the superconductor's edge is aligned to the CNT within London's penetration depth ($\sim 40\,\mathrm{nm}$ for Pb [228]), where the screening current induced by an applied out-of-plane magnetic field could provide the necessary parallel momentum component of the Cooper pairs.

With the methods developed in this and the previous chapters, we are very well prepared to carry out such intriguing experiments in future.

PART II

SPIN TRANSPORT IN CNT QD SPIN-VALVE DEVICES

9

Magnetoresistance and spin-polarized electron transport

In this chapter, we provide the theoretical basis for the experimental results presented in the following chapters, where we study CNT QDs coupled to ferromagnetic electrodes for magnetoresistance experiments in a spin-valve geometry. We start with some relevant principles of ferromagnetism and magnetic anisotropies, useful to engineer the coercive fields of micron-size ferromagnetic contacts, followed by an introduction to some important concepts of the field of spintronics. After discussing the most relevant magneto-resistive effects for this thesis, we briefly review magnetoresistance effects in CNT QDs and previously published results to provide an introduction to this broad field.

9.1. Ferromagnetism and magnetic anisotropies

Ferromagnetism is one of the few phenomena where an underlying quantum mechanical effect – the collective ordering of the electrons' magnetic moment – can be observed in the finite magnetization $\mathbf{M}$ of a permanent magnet even at room temperature[1] and on macroscopic length scales. This finite $\mathbf{M}$ is caused by a ferromagnetic ordering with favored parallel alignment of the electrons' magnetic moments, which arise from the electron's orbital motion and spin. Microscopically, this ordering can be understood as a consequence of the so-called *exchange interaction*, a purely quantum mechanical effect caused by the electrons indistinguishability and Coulomb repulsion [272, 273]. Due to

[1] If the Curie temperature T_{Cu}, which measures the strength of the ferromagnetic ordering or exchange interaction, is sufficiently large, as e.g. for Fe, Co and Ni.

the required anti-symmetric wavefunction under two-particle exchange (Pauli exclusion principle), the spatial component of the wavefunction and its symmetry directly depend on the electrons spin configuration and vice versa. The reduced Coulomb repulsion (exchange integral) for an antisymmetric spatial wavefunction of the electrons favors a parallel spin configuration for a ferromagnetic material. The ferromagnetism of strongly localized electron systems (e.g. magnetic insulators) is well-described within such a *Heisenberg model* of direct exchange between localized electrons, whereas it cannot be applied to metallic ferromagnets (e.g. Fe, Ni, Co) in which the electrons responsible for the ferromagnetism are *itinerant* [273]. These metallic ferromagnets can be treated in the *Stoner band model* of ferromagnetism, which assumes a spin-split band structure and considers the energy gain due to a spontaneous magnetization in case of ferromagnetic ordering [272, 273]. If the *Stoner criterion* $UN(E_\mathrm{F}) \geq 1$ is fulfilled, the system's energy reduction due to exchange interaction calculated in a mean field approach outweighs the increase in total kinetic energy, and spontaneous ferromagnetic behavior occurs. This requires a large strength of the exchange interaction U and a large density of states[2] (DOS) $N(E_\mathrm{F})$ at the Fermi energy E_F. For the transition metals Fe, Co and Ni that condition is fulfilled due to the large DOS $N(E_\mathrm{F})$ caused by the narrow 3d band [272]. In these ferromagnets, the spin-up and spin-down bands are split by the exchange splitting ΔE_ex and a spontaneous *magnetization* $M \propto (n_\uparrow - n_\downarrow)$, proportional to the difference between the total number of spin-up ($n_\uparrow$) and spin-down ($n_\downarrow$) electrons, occurs without an externally applied magnetic field. This is schematically depicted in Fig. 9.1(a).

While the Stoner model accounts for the microscopic origin of the magnetization $\mathbf{M}$, the vector field that describes the density of magnetic dipole moments, it cannot explain the local variations $\mathbf{M}(\mathbf{r})$ and its anisotropy observed in bulk ferromagnets. This can be captured by a minimization of the ferromagnets total free energy $G = \int_V dV\, g_\mathrm{tot}(\mathbf{M}(\mathbf{r}), \mathbf{H})$, and considering all competing relevant energy terms and built-in *magnetic anisotropies* of the system in a micromagnetic theory [273, 274]. These anisotropies lead, for example, to the alignment of the magnetization $\mathbf{M}$ along a preferred orientation or *easy axis* in zero external magnetic fields $\mathbf{H}$, for which the system's total free energy G is minimal, whereas the orientation with maximal energy is called a *hard axis*. Following Refs. [273, 274], we briefly discuss the most relevant energy terms and magnetic anisotropies $f_\mathrm{ex}, f_\mathrm{Z}, f_\mathrm{mc}, f_\mathrm{d}$ contributing to the total energy density $g_\mathrm{tot} = f_\mathrm{ex} + f_\mathrm{Z} + f_\mathrm{mc} + f_\mathrm{d}$ of the ferromagnet, and determining its magnetic properties. A Zeeman energy term $f_\mathrm{Z} = -\mu_0 \mathbf{HM}$ describes the preferred alignment of the magnetization parallel to external fields, while a short range internal exchange energy term $f_\mathrm{ex} \propto (\nabla \mathbf{M})^2$ accounts for the

[2] In contrast to part I of this thesis, we use in part II the symbol N for the DOS; for conformity to literature and to not confuse D with the later introduced diffusion constant.

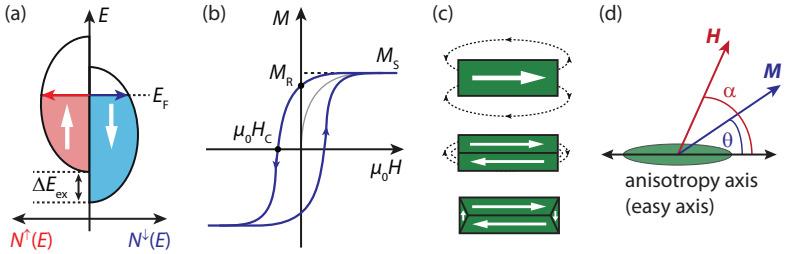

Figure 9.1.: (a) Schematic of spin-split bands shifted by the exchange splitting ΔE_{ex} in the Stoner model. Different DOS $N^{\uparrow}(E_{\mathrm{F}})$ (red arrow), $N^{\downarrow}(E_{\mathrm{F}})$ (blue arrow) and a spontaneous magnetization $M \propto (n_{\uparrow} - n_{\downarrow})$ (light red and blue) result. (b) Magnetization curve of a multi-domain ferromagnet. (c) Illustration of reduced stray fields by forming multiple domains, for closure domains the stray field vanishes (bottom). (d) Elliptical single-domain nanomagnet and angles between easy axis, **M** and **H** in the Stoner-Wolfarth model. Adapted from Ref. [58].

preferred microscopic ferromagnetic ordering of magnetic moments. The *magneto crystalline anisotropy* energy $f_{\mathrm{mc}} = K \sin^2(\theta) + \mathcal{O}(\sin^4(\theta))$, written as leading term of an expansion in $\sin^2(\theta)$ for uniaxial anisotropy with the angle θ between **M** and the easy axis [Fig. 9.1(d)], describes the favored alignment of the magnetic moments along a crystallographic easy axis. The origin of this anisotropy is the spin-orbit interaction, coupling the electron spins responsible for the magnetism to the anisotropic orbitals in a crystalline structure [273]. One of the most important energy terms is the dipolar energy density $f_{\mathrm{d}} = -\mu_0 \mathbf{H}_d(\mathbf{r})\mathbf{M}(\mathbf{r})$, which describes the dipole-dipole interaction of the local magnetization in the *demagnetizing field* $\mathbf{H}_d$ (inside the sample) or *stray field* (outside of sample) created by the sample itself. The minimization of stray field energies leads to a preferred in-plane magnetization in magnetic thin films, and is responsible for the formation of magnetic domains [273]. One also refers to this anisotropy as *shape anisotropy*, because by a chosen shape of the ferromagnetic sample one can directly influence or engineer the magnetization direction due to the energetically preferred reduction of surface magnetic charges. For larger ferromagnetic strips or samples, as schematically depicted in Fig. 9.1(c), the stray fields can be reduced by introducing uniformly magnetized areas or *magnetic domains* with a parallel orientation of magnetic moments, separated by *domain walls* over which the magnetic moments orientation changes continuously. Such a multi-domain[3] ferromagnet will exhibit a hysteresis loop in a magnetization curve $M(H)$ similar to the one depicted in Fig. 9.1(b). For increasing external magnetic field, the domains with ferromagnetic moments ordered parallel to the field grow until all

[3]Below we discuss that already a single domain is sufficient to observe a hysteresis loop.

moments are aligned parallel, and the saturation magnetization M_S is reached. In the absence of external fields, a non-zero or remanent magnetization M_R remains, and an external *coercive field* $B_C = \mu_0 H_C$ is required to overcome this ferromagnetic ordering and to reverse the magnetization. Ferromagnets with a small (large) H_C are called *soft (hard)* magnets [272]. For very small ferromagnetic samples (typically $\lesssim 100 - 500\,\mathrm{nm}$ [275]), the energy cost for domain wall formation outweighs the gain due to stray field reduction, and the exchange term dominates – a single-domain magnet results [9.1(c),top]. In this case, the magnetic easy axis is usually determined by a competition between shape and crystalline anisotropy. The response of such a system to external fields can be described by the *Stoner-Wolfarth model* [275, 276], which assumes a ellipsoidal shaped single-domain magnet of uniaxial anisotropy and a constant magnetization $|\mathbf{M}|$. Within this model, the direction of $\mathbf{M}$ is determined by a competition between the uniaxial anisotropy term originating from either magneto crystalline or shape anisotropy, and the Zeeman energy of the magnetization in the external field. It can be found from minimizing

$$g_{SW} = f_{mc} + f_Z = K \sin^2(\theta) - M_S \mu_0 H \cos(\alpha - \theta). \tag{9.1}$$

As depicted in Fig. 9.1(d), $\mathbf{M}$ is restricted to a 2-dimensional plane, in which θ (α) denote the angle between easy axis and $\mathbf{M}$ ($\mathbf{H}$). As the applied external field H is changed, $\mathbf{M}$ aligns with an axis of minimal energy either by a smooth rotation in the plane or a sudden sharp switching. If the magnetic field is applied parallel to the easy axis, i.e. $\alpha = 0$, the magnetization reverses abruptly its sign by jumping to the second energy minimum of g_{SW} at the *switching* (or coercive) field $H_S = 2K/\mu_0 M_S$ [275], forming a hysteresis loop. In contrast, for $\alpha = 90°$, one observes no hysteresis, but a smooth and continuous rotation of $\mathbf{M}$ towards the hard axis.

9.2. Spintronic devices and magnetoresistance effects

The field of *spintronics* aims to actively control and manipulate also the spin degree of freedom in electronic devices, and exploits the influence of the electron spin on electric currents [22–24]. Pure 'spin currents' could ultimately replace charge currents for a fast and efficient transfer and processing of information in quantum computation schemes [25]. We briefly introduce some of the most important concepts in spintronics, and the relevant magnetoresistance effects observed in the spintronic devices studied in this thesis. For a coherent review, we refer to Refs. [26, 277] which we partially follow.

9.2.1. Spin polarization, spin injection and detection

One of the most important cornerstones of spintronics is the concept of *spin-polarized currents* [22]. Due to the exchange-split spin-bands of a ferromagnet

the DOS of the spin species at the Fermi energy is different, and one can define a *spin polarization* of the ferromagnet's conduction electrons as

$$P_{\mathrm{N}} = \frac{N^{\uparrow}(E_{\mathrm{F}}) - N^{\downarrow}(E_{\mathrm{F}})}{N^{\uparrow}(E_{\mathrm{F}}) + N^{\downarrow}(E_{\mathrm{F}})}, \tag{9.2}$$

which can have absolute values of 0 (unpolarized, normal metal) to 1 (completely polarized, ferromagnetic half-metal) [278]. Figure 9.1(a) illustrates that the terms majority and minority spins can refer both to the DOS at E_{F} important for the spin polarization and transport ($N^{\uparrow}(E_{\mathrm{F}}) > N^{\downarrow}(E_{\mathrm{F}})$, red and blue arrows), or to the larger total number of spins relevant for the magnetization ($n^{\uparrow} < n^{\downarrow}$, light red and blue, chosen opposite in this example). This spin polarization consequently leads to a spin-polarized current in a ferromagnet: in itinerant ferromagnets such as Fe, Co and Ni, both 4s and 3d bands contribute to the DOS at E_{F} [279]. While magnetism originates from the exchange-split 3d bands, conductivity is mostly determined by the light electrons of the unsplit 4s-band. Since the main source of s-electron scattering are spin-conserving s-d interband transitions, the different DOS of the spin-species result in strongly spin-dependent scattering probabilities. If spin-flip scattering is negligible, one can hence describe transport in a two-current model with two spin channels j_σ, $\sigma = \uparrow, \downarrow$ of different resistivity, first proposed by Mott [279] and later experimentally verified by Fert and Campbell [280]. The separation in a total spin current $j_\uparrow - j_\downarrow$ and charge current $j_\uparrow + j_\downarrow$ allows to define a *transport or current spin polarization* [22]

$$P_{\mathrm{j}} = \frac{j_\uparrow - j_\downarrow}{j_\uparrow + j_\downarrow}, \tag{9.3}$$

much more suitable for transport experiments than Eq. (9.2). Note that the transport spin polarization determined by an experiment also depends on the experimental conditions, i.e. on the transport regime [278], and care has to be taken when comparing absolute values. In the ballistic transport regime relevant for point contact spectroscopy (PCS), one finds $j_\sigma \propto N^\sigma(E_{\mathrm{F}}) v_{\mathrm{F}\sigma}$ and $P_{\mathrm{j}} = P_{\mathrm{Nv}}$ with Fermi velocity v_{F} [278]. In the diffusive (e.g. also PCS) or tunneling (e.g. magnetic tunnel junctions) regime, one finds $j_\sigma \propto N^\sigma(E_{\mathrm{F}})(v_{\mathrm{F}\sigma})^2\tau$ and $P_{\mathrm{j}} = P_{\mathrm{Nv}^2}$ (assuming same relaxation times τ for both spin species), or $j_\sigma \propto N^\sigma(E_{\mathrm{F}})|T_\sigma|^2$ and $P_{\mathrm{j}} = P_{\mathrm{T}}$, respectively, with a spin-dependent tunneling matrix element T_σ [278, 281]. Hence, one does not only probe the spin polarization (9.2) defined by the DOS alone in a transport experiment, but rather a DOS weighted with a spin-dependent carrier velocity or tunnel matrix element. Typical transport spin polarizations for the 3d transition metals are $P_{\mathrm{j}} \sim 0.4$ [281–283].

Ferromagnets (F) can thus be used as fundamental elements in spintronic devices by, for example, driving a spin-polarized current across the interface into

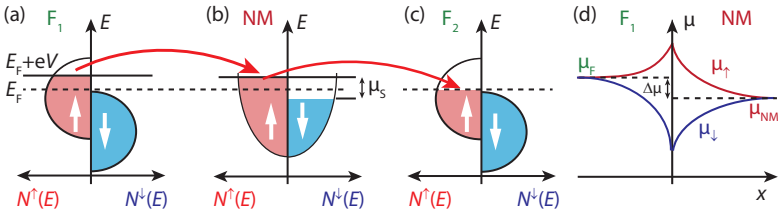

Figure 9.2.: (a,b) Spin injection into a non-magnetic (NM) material. A spin-polarized current is injected into a NM material from a ferromagnet F_1, causing a non-equilibrium spin accumulation μ_s in NM. (c) This spin accumulation can be detected with a second ferromagnet F_2. (d) Schematic spin accumulation $\mu_s = \mu_\uparrow - \mu_\downarrow$ at a ferromagnet-normal metal interface. $\Delta\mu$ denotes the step of the averaged electrochemical potentials μ_F and μ_{NM} across the interface. Adapted from Refs. [58, 277, 284] (a-c) and [285, 286] (d).

a non-magnetic material (NM) such as a normal metal (N), superconductor (S) or a semiconductor (SC). This process is called *spin injection* and induces a non-equilibrium spin-band population in NM [284, 285, 287, 288], schematically depicted in Fig. 9.2(a-b). The so-caused *spin accumulation* $\mu_s = \mu_\uparrow - \mu_\downarrow$ at the interface, defined by the induced difference in the electrochemical potentials of spin-up and down carriers, decays with increasing distance $|x|$ from the interface due to spin-flip processes [Fig. 9.2(d)], to reach its equilibrium $\mu_s = 0$ far away from the interface in NM [289, 290]. In a diffusive transport regime, this decay is exponential, which can be obtained from a solution of the diffusion equation for the non-equilibrium spin accumulation μ_s [277, 285],

$$\frac{\partial^2 \mu_s}{\partial x^2} = \frac{\mu_s}{L_s^2}. \tag{9.4}$$

Here, $L_s = \sqrt{D\tau_s}$ denotes the spin diffusion length or characteristic length scale for spin-flip processes, D a spin-averaged diffusion coefficient and τ_s the spin relaxation time. In the absence of magnetic impurities, spin relaxation and spin-flip processes are mainly due to spin-orbit (SOI) and hyperfine interactions [277]. The spin accumulation and the remaining spin-polarized current can e.g. be *detected* with a second ferromagnetic contact as shown in Fig. 9.2(c) [284]. In typical spin-valve experiments on graphene, for example, one uses this second ferromagnet to detect the non-equilibrium spin accumulation injected from a ferromagnetic contact by a non-local voltage measurement [135].

Generally, when one combines a ferromagnet with a material of sufficiently larger resistivity such as a SC or graphene, spin injection is largely suppressed due to a *conductivity mismatch* [291]. This mismatch leads to a depolarization of the current already in F before passing the interface. The conductivity mismatch can be circumvented by using a half-metallic ferromagnet with $P_N = 1$, or by a large interface resistance due to an implemented tunnel barrier [292–

294]. Then, the spin-dependent resistance is dominated by the tunnel barrier and the decay of spin accumulation shifted to NM. In case of CNTs, the contact interfaces typically provide a tunnel barrier, as discussed in Sec. 1.2.

9.2.2. Magnetoresistance effects

As just illustrated, ferromagnetic materials can be used as a source and detector of spin-polarized currents, which makes them an obvious choice to study spin transport phenomena in mesoscopic devices. Here, we briefly discuss the influence of $\mathbf{M}$ and $\mathbf{H}$ on the resistance, i.e. the magnetoresistance (MR) effects most relevant for the spintronic devices of this thesis.

Anisotropic magnetoresistance (AMR)

Already the resistance of a ferromagnet itself depends on the relative orientation of a current $\mathbf{j}$ and the magnetization $\mathbf{M}$, discovered by Lord Kelvin in 1856 [295]. This *anisotropic magnetoresistance (AMR)* can only be understood as a consequence of spin-orbit interactions and resulting anisotropic s-d spin-flip scattering processes [296] in Mott's two current model: resistivity in a ferromagnet is mainly caused by s-d intra-band scattering, and the scattering cross section or resistivity depends on the number of empty d states. Inclusion of spin-orbit interactions increases this scattering cross-section due to now also allowed spin-flip s-d scattering processes. Because of the d bands' orbital anisotropy, the scattering becomes dependent on the angle between current (s electrons) and magnetization (determined by the d-bands) [296]. In a simplified intuitive picture, s-electrons can only scatter into empty 3d-states, when their momentum direction $\mathbf{k}$ lies in the plane of the classical d-orbitals [297]. Empty d-states always have a component of the angular momentum $\mathbf{L}$ perpendicular to $\mathbf{M}$. Thus if $\mathbf{j} \parallel \mathbf{M}$ (e.g. in x-y-plane), the s-electrons $\mathbf{k}$-vector lies within the plane of classical d-orbits (big component L_z, e.g. $3d_{x^2-y^2}$) and an increased s-d-scattering and resistance is the consequence [Fig. 9.3(a), bottom]. If, however, $\mathbf{j} \perp \mathbf{M}$ (e.g. $\mathbf{M}$ in z-direction), the probability of empty states with $\mathbf{L} \parallel \mathbf{j}$ is increased and scattering is reduced because the classical d-orbits (e.g. $3d_{z^2-r^2}$) are incompatible with the $\mathbf{k}$-vector of the s-electrons [Fig. 9.3(a), top]. As illustrated in Fig. 9.3(a), we observe an anisotropic scattering cross-section or resistivity ρ larger for $\mathbf{k}, \mathbf{j} \parallel \mathbf{M}$ than for $\mathbf{k}, \mathbf{j} \perp \mathbf{M}$ [297]. Typically, this dependence is phenomenologically described as [296]

$$\rho(\varphi) = \rho_\perp + (\rho_\parallel - \rho_\perp) \cos^2 \varphi, \tag{9.5}$$

with the angle φ between $\mathbf{j}$ and $\mathbf{M}$ and the resistivities $\rho_\parallel$ ($\rho_\perp$) for $\mathbf{j} \parallel \mathbf{M}$ ($\mathbf{j} \perp \mathbf{M}$). While the simplified picture discussed here holds for most common materials, a correct description requires a microscopic treatment of the scattering matrix elements and the spin-orbit interaction, which can also result

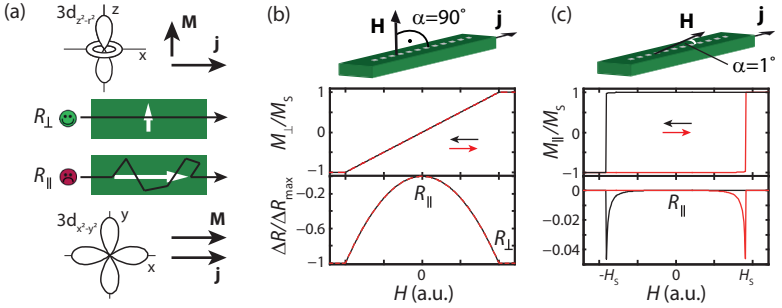

Figure 9.3.: (a) Phenomenology and intuitive explanation of AMR. (b,c) Resistance change ΔR and magnetization M of a rectangular single-domain strip as function of the external field H calculated from the Stoner-Wolfarth model, for angles $\alpha = 90°$ (b) and $\alpha = 1°$ (c) between $\mathbf{H}$ and the strips easy axis (white dashed line). The symbols $\parallel$ and $\perp$ label the component (alignment) of $\mathbf{M}$ relative to $\mathbf{j}$ and the easy axis. Adapted from Refs. [58, 299].

in $\rho_\parallel < \rho_\perp$ [296]. One typically observes resistance changes of a few percent in AMR measurements on common ferromagnetic materials, but AMR has already been applied in hard drive read-heads [26] and can be further exploited in tunneling AMR (T-AMR) spintronic devices [298].

We employ AMR measurements on single-domain strips to determine their switching fields H_S in external magnetic fields $\mathbf{H}$ (Chap. 10) [36]. Using the single-domain Stoner-Wolfarth model (9.1) to determine $\mathbf{M}(\mathbf{H})$, we can find the angle φ between the fixed current direction $\mathbf{j}$ along the easy axis and $\mathbf{M}$ and calculate the resistance change (9.5) caused by the external field H. This is schematically depicted in Fig. 9.3(b) and (c) for two angles α between $\mathbf{H}$ and the easy axis. If the external field is applied perpendicular to the easy axis ($\alpha = 90°$), the magnetization continuously rotates towards the hard axis and a continuous decrease of the resistivity to the value $\rho_\perp$ ($\mathbf{j} \perp \mathbf{M}$) is observed. If $\alpha = 0°$, i.e. the external field is applied parallel to the easy axis, a sudden switching of the magnetization occurs. Ideally, one would not expect any resistance change in AMR because always $\mathbf{M} \parallel \mathbf{j}$. A small misalignment $\alpha \sim 1°$ of the external field with the easy axis leads however to a brief rotation of $\mathbf{M}$ towards the hard axis before inverting its sign, and a detectable resistance change with a sharp sudden jump at the switching fields. This characteristic resistance dip obtained in AMR measurements is shown in Fig. 9.3(b), and allows to determine the switching fields H_S of single-domain ferromagnetic strips, or draw conclusions on single- or multi-domain behavior in magnetization reversal.

Magnetoresistance in spin-valve structures

Spintronic devices and particularly *spin-valve structures* have played a key role in recent industrial applications, such as read/write heads of hard drives, magnetoresistive random-access memory (MRAM), and many more [26]. A spin-valve generally consists of two ferromagnets (F) separated by a non-magnetic material (NM), and allows to control the device resistance by the magnetization configuration of F or by external magnetic fields. While many different geometries and materials can be implemented, Fig. 9.4(a) shows the lateral spin-valve geometry most relevant for the nanospintronic devices of this thesis. Two narrow F strips of varying widths have different coercive fields due to shape anisotropy, and allow for a parallel (P) and anti-parallel (AP) magnetization configuration tunable by external magnetic fields. Due to the effects discussed below, the P and AP configuration result in different device resistances or conductances $G_\mathrm{P}/G_\mathrm{AP}$ in electronic transport through the spin-valve structure. Figure 9.4(b) plots the conductance of such a device as function of the external magnetic field, where one observes a step-like conductance change at the switching fields of the electrodes. This characteristic step-like change in conductance, or more precisely the normalized difference between G_P and G_AP, is defined as *magnetoresistance* (MR)[4]

$$\mathrm{MR} = \frac{G_\mathrm{P} - G_\mathrm{AP}}{G_\mathrm{P} + G_\mathrm{AP}}. \tag{9.6}$$

Magnetoresistance can have different physical origins. If, for example, a conducting material is implemented as NM spacing layer, the *giant magnetoresistance* (GMR) originates from spin-dependent scattering rates in the ferromagnets [300, 301]. We focus here on so-called *magnetic tunnel junctions* (MTJ) [302], where the NM material is an insulator (I) and represents a tunnel barrier (F-I-F), and the corresponding MR is called *tunneling magnetoresistance* (TMR). This TMR is determined by spin-dependent tunneling processes. The most simple and commonly used model developed by Jullière [303] assumes that the electron spin is conserved in tunneling, so that the current is the sum of two independent spin channels. Second, it presumes spin and energy-independent tunneling matrix elements $T_\sigma(E) = T$, so that the tunneling current is determined only by the product of the spin-dependent DOS $N^\sigma(E_\mathrm{F})$ at the Fermi energy. Hence, the conductance in the parallel and anti-parallel magnetization configuration can be written as

$$\begin{aligned} G_\mathrm{P} = G_{P,\uparrow} + G_{P,\downarrow} &\propto N^\uparrow_{1+}(E_\mathrm{F})N^\uparrow_{2+}(E_\mathrm{F}) + N^\downarrow_{1+}(E_\mathrm{F})N^\downarrow_{2+}(E_\mathrm{F}) \\ G_\mathrm{AP} = G_{AP,\uparrow} + G_{AP,\downarrow} &\propto N^\uparrow_{1+}(E_\mathrm{F})N^\uparrow_{2-}(E_\mathrm{F}) + N^\downarrow_{1+}(E_\mathrm{F})N^\downarrow_{2-}(E_\mathrm{F}), \end{aligned} \tag{9.7}$$

[4]Here, we use a symmetric definition most suited for the later presented QD spin-valve experiments, while often only $G_{\mathrm{P/AP}}$ are used for normalization in the denominator. When comparing values, one has to pay attention to the used definition.

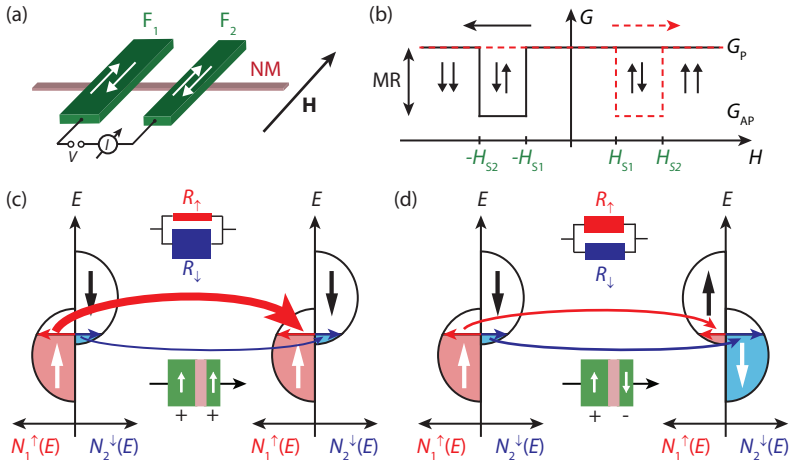

Figure 9.4.: (a) Lateral spin-valve geometry with two ferromagnetic contacts (F_1, F_2) and a non-magnetic material (NM). (b) Typical spin-valve magnetoconductance curve, assuming different switching fields H_{S1} and H_{S2} of the contacts. Horizontal (vertical) arrows denote the sweep direction of H (magnetization configuration). (c,d) Illustration of Jullières model for the tunneling magnetoresistance (TMR). Conductances are determined by the DOS of two independent spin-channels, so that a higher conductance occurs for the parallel magnetization configuration ++ (c, inset) than for the antiparallel (+−, d) case (resistor models). Adapted from Ref. [58].

where the + (-) denotes the direction of the magnetization. Figure 9.4(c) and (d) illustrate the reduced conductance G_{AP} in the anti-parallel magnetization state in the Jullière model. Because majority[5] (minority) spins have to tunnel into empty minority (majority) states in the AP case, the total conductance of the two spin channels is reduced compared to the conductance in the parallel magnetization state dominated by the majority spin current (larger arrow). Using the identity $N_{2-}^{\sigma}(E_F) = N_{2+}^{-\sigma}(E_F)$, $\sigma = \uparrow, \downarrow$ and the definition (9.2) of the spin polarization P_N, we find the tunneling magnetoresistance as function of the contacts spin polarization P_1 and P_2 as

$$\mathrm{TMR} = \frac{G_P - G_{AP}}{G_P + G_{AP}} = P_1 P_2. \tag{9.8}$$

In this definition, TMR can vary between 0 (normal metal) and 1 (ferromagnetic half-metals, $P_N = 1$). While the simple Jullière model provides an intuitive approach to TMR and described early F-I-F experiments with Al_2O_3 tunnel barriers quite well [283, 302], it has severe limitations. These

[5] We refer here to the total number of spins (majority = ↑ for +).

concern especially the neglected spin-flip processes at the interfaces and during tunneling, and the assumption of spin- and energy independent tunneling matrix elements $T_\sigma(E) = T$. We note, for example, that the spin polarization entering Eq. (9.8) is the density of states definition from Eq. (9.2), which is equivalent to the (tunneling) transport spin polarization P_T defined earlier only for $T_\sigma(E) = T$. In case of highly single crystalline, epitaxially grown MgO tunnel barriers, for example, unusually high TMR values [304] not consistent with the polarizations P_N have been observed. Similarly, for two different ferromagnetic materials (F1-I1-F2) or two different barriers (F-I1-I2-F) negative values of TMR and one of the contact polarizations P [305, 306] have been found, even if the same materials yielded a positive value of TMR in the F1-I2-F2 or F-I2-F configuration. These effects can be explained by a symmetry selection (s,p,d-like) of the tunneling electrons contributing most to the tunnel current, depending on the particular F-I interface [306–308]. Thus, the relevant spin polarization entering here is the tunneling transport spin polarization $P_\mathrm{T} = \frac{N^\uparrow|T_\uparrow|^2 - N^\downarrow|T_\downarrow|^2}{N^\uparrow|T_\uparrow|^2 + N^\downarrow|T_\downarrow|^2}$, and the symmetry selection is captured by spin-dependent tunneling matrix elements T_σ, effectively introducing a spin-filter effect at the F-I interface [307].

9.3. Magnetoresistance signals in CNT spin-valve devices

Merging the exquisite tunability of electronic nanostructures with ferromagnetic materials in nanospintronic devices bears great potential for applications and fundamental investigations. To use the electron spin directly, for example in a spin-transistor [309] or as a spin quantum bit [2, 310], it is necessary to fabricate nanostructures with the required long coherence times and electrical tunability. CNTs (and graphene) are in principle ideally suited for spintronic devices due to the large intrinsic coherence and expected long spin relaxation times (due to the weak spin-orbit coupling and hyperfine interaction), tunable electron density and large maximum current densities. Already the earliest CNT spin-valve experiments [35], or non-local spin-accumulation experiments in graphene [135] demonstrated the great potential of carbon-based nanostructures. To obtain an electrically tunable spin signal, one strategy is to fabricate a nanostructure with a gate-tunable conductance, e.g. a QD in a CNT [27]. For such structures, the magnetoresistance is still calculated from Eq. (9.6), i.e. from the difference of the now gate-dependent conductances in the parallel and anti-parallel magnetization configurations. However, the electrical tunability introduces additional complexity to the data analysis compared to the previously discussed TMR, since the MR signal now depends on the position, amplitude and broadening of a conductance feature [see e.g. Fig. 9.5(b)], which all can vary with the magnetizations of the contacts, as we will discuss in the following and in Chap. 11. In this section, we briefly review some im-

portant findings in the field of spin transport in CNTs, with a particular focus on the QD transport regime most relevant for this thesis. We mostly discuss results obtained in a local spin-valve transport geometry shown in Fig. 9.4(a), where the non-magnetic medium is a CNT connected to two ferromagnetic source-drain contacts of different switching fields, and the magnetoresistance is measured as function of an external field as discussed previously. This brief overview over the rather complex and diverse field is far from complete (e.g. we omit a discussion of the Kondo effect with ferromagnetic leads) and rather represents the view of the author: For a more detailed and thorough review, we refer to Ref. [29].

Experiments in standard CNT spin-valve structures While the first experiments could already demonstrate magnetoresistance signals with a hysteretic spin-valve characteristics and the potential of the field, they also illustrated already the manifold challenges one is facing when combining CNTs with ferromagnetic contacts: both consistently positive [35, 311, 312] and surprisingly also negative MR signals [313, 314] were reported, as well as varying MR (positive and negative) depending on the gate voltage region or sample [37, 315, 316] – hence significantly deviating from a simple Jullière picture. Most of the devices typically lacked reproducible signals, some showed single switching characteristics [314] and huge variations were reported both from sample-to-sample [35, 37, 313] and within a device [37]. MR signals with a spin-valve characteristics were partially even observed for only a single ferromagnetic and a normal metal contact [37], at least questioning a spin injection and detection picture. These early experiments typically lacked a clear identification of the device transport regime and at least partially employed multi-wall CNTs, and both a systematic gate-control for electrical tunability as well as a clear understanding and control of magnetization reversal by shape anisotropy were usually missing. Nevertheless, these studies already highlighted the importance of the interface between a ferromagnetic material and the CNT, e.g. for reliable contacts, and an engineered and reliably controllable magnetization reversal of the ferromagnetic contacts. These two main crucial points, that we also address in later chapters, are certainly made difficult due to the oxidative nature of ferromagnetic materials. The landmark experiments by Sahoo *et al.* [27] and Man *et al.* [317] finally demonstrated an electric field control of spin transport by a gate voltage both in the QD and the Fabry-Perot transport regime, and triggered significant experimental and theoretical efforts for an improved understanding. In both cases, a MR signal oscillating with the gate voltage was observed, which is clearly correlated to the conductance pattern.

In the case of Sahoo *et al.*, an asymmetric MR signal was reported with negative MR on resonance, while MR was positive off-resonance. This negative MR on resonance can be intuitively understood from the schematics depicted

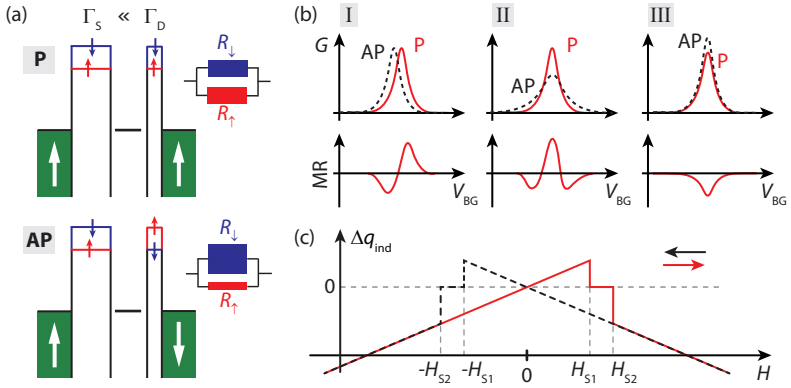

Figure 9.5.: (a) Intuitive schematic to explain negative MR ($G_{AP} > G_P$) on resonance for asymmetric coupling strengths $\Gamma_D \gg \Gamma_S$, and corresponding two spin-channel resistor model (text). Adapted from Ref. [27]. (b) Sources of negative MR, adapted from Refs. [318, 319]. Changes in position (I), width (II) and amplitude (III) of the CB resonances depending on the magnetization configuration (P/AP) can all result in oscillating or negative MR. (c) Expected induced gate charge Δq_{ind} due to the MCE as function of the external field H for a QD spin-valve with two F contacts of different switching fields $H_{S1/2}$, adapted from Ref. [320].

in Fig. 9.5(a) [27]: for a device with very asymmetric source-drain (S/D) tunnel coupling strengths $\Gamma_S \ll \Gamma_D$ [represented by the width of the barriers in Fig. 9.5(a)], the conductance amplitude on resonance for a Breit-Wigner lineshape is $\propto \Gamma_S/\Gamma_D$ [cf. Eq. (1.10), with $\Delta E = 0$ and $\Gamma_S \ll \Gamma_D$] and the resistance $\propto \Gamma_D/\Gamma_S$. For ferromagnetic contacts, the electron lifetime on the QD becomes spin-dependent, hence also Γ_S^σ and Γ_D^σ are spin-dependent, with $\sigma = \uparrow, \downarrow$ [see also detailed discussion below, represented by spin-dependent barrier heights in Fig. 9.5(a)]. Using now the two spin-channel resistor model depicted in Fig. 9.5(a), where $R_\sigma \propto \Gamma_D^\sigma/\Gamma_S^\sigma$, we find $R_\uparrow < R_\downarrow$ in the antiparallel (AP) configuration due to $\Gamma_D^\uparrow < \Gamma_D^\downarrow$ and $\Gamma_S^\uparrow > \Gamma_S^\downarrow$, whereas $R_\uparrow = R_\downarrow$ in the parallel (P) configuration. Due to the dominance of the smaller resistor in the antiparallel resistor circuit, the conductance is thus larger in the antiparallel case and one obtains a negative MR. Off-resonance, the conductance is $\propto \Gamma_S^\sigma \Gamma_D^\sigma$ [cf. Eq. (1.10), with $\Delta E \gg \Gamma$] and one recovers a positive MR.

Both experiments by Sahoo *et al.* [27] and Man *et al.* [317] could very well be accounted for with theoretical models as described below, but employed the well-coupling F alloy PdNi which was later shown to exhibit complex multi-domain characteristics and magnetization reversal [321–323]. Following studies have hence focussed on [324] and achieved a controlled magnetization reversal and more reproducible spin-valve MR signals with Permalloy contacts

[36, 114, 319]. Nevertheless, progress in this field is rather demanding and significant challenges remain, as we will see in the following chapters.

Theoretical description of spin transport in CNT QD spin-valves From a theoretical perspective, to lowest order in perturbation theory (the sequential tunneling limit) the MR of a CNT QD with two ferromagnetic leads is predicted to be purely positive [325, 326], i.e. the conductance is always larger in the parallel magnetization configuration. This picture changes if higher order processes are taken into account, as necessary in the lifetime broadening or strong coupling regime of a QD ($\Gamma > kT$) most relevant for the experiments in this thesis. As illustrated in Fig. 9.5(b), for such an 'intermediate' coupling strength of the contacts, negative MR and MR oscillations as a function of gate voltage are predicted to occur due to changes of the resonance position (situation I), width (situation II) and amplitude (situation III), depending on the contacts magnetization configuration (parallel or anti-parallel) [318, 319]. These changes can be due to different mechanisms, i.e. spin-dependent interfacial phase shifts (SDIPS) [29, 325, 327] and virtual charge fluctuation processes [318, 319] have been proposed, which we will briefly discuss in the following.

To understand the origin of the SDIPS, a non-interacting picture based on a scattering approach is instructive [327], which for example also describes the spin-dependent interference modulation of the MR in Ref. [317] very well. For such a device with highly transparent barriers, e.g. in the Fabry-Perot transport regime of a CNT, spin-up and spin-down electrons will 'feel' a different scattering potential during reflection at a contact due to the ferromagnetic exchange field, which depends on the contact's magnetization [327]. Hence, the phase acquired during reflection will depend on the contact's magnetization direction and the electron spin. Finally, due to the quantum mechanical resonance condition of a Fabry-Perot cavity, also the resonant energy position will depend on this phase. This leads to "spin-dependent interfacial phase shifts" (SDIPS) of the resonant energies for spin-up and spin-down electrons – and a spin-splitting of their resonant energies $E^{\mathrm{c}}_{\uparrow} - E^{\mathrm{c}}_{\downarrow} = g\mu_{\mathrm{B}} h^{\mathrm{c}}_{\mathrm{SDIPS}}$ described by an effective Zeeman field $h^{\mathrm{c}}_{\mathrm{SDIPS}}$. Because this Zeeman field also depends on the magnetization configuration $\mathrm{c} \in \{\mathrm{P}, \mathrm{AP}\}$ of the contacts [327], a shift of the resonance position can occur between the parallel and anti-parallel magnetization configurations. This can be similarly implemented in the interacting QD description, where the ferromagnetic exchange field leads to spin-dependent electron confinement potentials [see Fig. 9.5(a)], which naturally accounts for spin-dependent orbital energies of the QD [29]. Such a scenario corresponds to situation I in Fig. 9.5(b) and an oscillating MR, and has been used to describe both the sign and magnitude of the MR oscillations observed by Sahoo *et al.* qualitatively and quantitatively very well [325].

Similarly, the concept of virtual charge fluctuation processes (between the

leads and the QD) also leads to an effective Zeeman field h^{c} modifying the resonance positions due to level renormalization [318]. Recently, it was found that such virtual charge fluctuation processes can also be responsible for a width change according to situation II in Fig. 9.5(b), which has been used to qualitatively describe the observed MR gate dependence obtained on a CNT device with Py contacts [319].

More generally, we note that the concept of spin-dependent energy level shifts, present in both so far discussed mechanisms, is also closely related to the well-understood energy level shifts and exchange fields in the Kondo regime [328–330]. Finally, a negative MR according to situation III in Fig. 9.5(b) can occur in both models even if the effective Zeeman field is the same for both magnetization configurations [318, 325], i.e. $h^{\mathrm{P}} = h^{\mathrm{AP}} \neq 0$ (e.g. only accounting for the "background" due to the external magnetic field). The underlying effective magnetic field removes the spin-degeneracy of the QD ground states and favors a ground state of maximum total spin. Hence, for a sequential filling of a four-electron CNT QD shell, the transitions 0e $\leftrightarrow$ 1e $\leftrightarrow$ 2e will be dominated by spin-up electrons, whereas the transitions 2e $\leftrightarrow$ 3e $\leftrightarrow$ 4e will be dominated by spin-down electrons [318, 325]. Assuming e.g. a high DOS for spin-up carriers in both contacts for the parallel magnetization configuration, the AP conductance might exceed the P conductance for the third or fourth CB peak of a CNT shell [situation III in Fig. 9.5(b) with negative MR]. This is due to the fact that the dominantly transferred spin-down electrons for these transitions have a higher DOS at least in one of the contacts for the AP configuration, whereas the DOS for spin-down electrons is lower for both contacts in the P configuration [318, 325].

While these theoretical concepts show good agreement with some data and certainly lead to an improved understanding of spin-transport and the origin of magnetoresistance in CNT QD spin-valve devices, the author is at least skeptical if a quantitative comparison to the experiments is always justified. Here, one has to bear in mind that the QD resonance position and width can also strongly vary due to external effects such as charge rearrangements in the substrate, mimicking a magnetic origin. Typically, the observed shifts in resonance position between the parallel and anti-parallel configuration are hardly reproducible among several identical repeated magnetic field sweeps, and even the conductance base lines might change in repetitive experiments (see e.g. also Chap. 11).

Other magnetoresistive effects in QD spin-valves In the so far discussed *local* measurement geometry, other magnetoresistive effects might mimic or contribute to the spin-valve characteristics. While stray field field effects or influences of TAMR effects [298] can usually be excluded due to their small magnitude and expected gate-independence [29], the *Magneto-Coulomb effect*

(MCE) [331] might indeed contribute or even be partially responsible for the magnetoresistance signals [320]. In a ferromagnet, the spin-split DOS are shifted in opposite directions by the Zeeman energy in an external magnetic field. Due to the different DOS of the spin species at the Fermi energy, the chemical potential of the ferromagnet has to change in order for the total number of charges to be conserved. Because the ferromagnetic electrode is connected to a normal metal and also capacitively coupled to the QD, the resulting change in work-function translates to an induced gate charge Δq_{ind} on the island, acting like a gate voltage [320]. For a QD spin-valve with two ferromagnetic contacts the expected induced gate charge due to the external field magnetic field H is qualitatively depicted in Fig. 9.5(c). The induced charge changes linearly with the field (due to the linear dependence of the Zeeman term on H), except at the switching fields of the contacts where the magnetization reversal leads to an abrupt sign change of the spin polarization and a jump in the induced charge. Depending on the slope of the conductance $\mathrm{d}G/\mathrm{d}V_{\mathrm{BG}}(V_{\mathrm{BG}})$, this can lead either to a similar positive, negative or zero conductance change proportional to Δq_{ind}. The MR signal obtained from a MCE can hence also oscillate with the gate voltage and will be correlated with $\mathrm{d}G/\mathrm{d}V_{\mathrm{BG}}(V_{\mathrm{BG}})$. Such MCEs can also be obtained with a single ferromagnetic contact, and can possibly be identified due to the energy scale of the MR oscillations and the MR signal shape [320]. Indeed, MCEs have been unambiguously identified in a CNT filled with magnetic particles [332], or in InP nanowires [333], individual gold nano-particles [334] and CNTs [208] connected to F contacts.

To exclude the influences of effects not originating from spin injection into the CNT QD, one would ideally prefer non-local multi-terminal measurements, similar to experiments on graphene [135], where the spin can be separated from the charge signal. While this is in principle feasible also on CNTs, at least in the Fabry-Perot or open transport regime with transparent contacts, leading to unambiguous typical [335] or unusual novel [321, 336] non-local spin signals even for so-called 'minor' hysteresis loops, the observation of spin signals and the interpretation of the experiments becomes significantly more involved or even impossible if multiple QDs form [337], one between each contact pair.

Conclusion To summarize, while there is ample of evidence that the observed magnetoresistance signals are due to spin injection and detection in QD spin valves, the experiments typically suffer from a lack of reproducibility. Mostly due to these experimental difficulties, a completely coherent picture of spin transport through QD spin valves has unfortunately not evolved yet, also making more complex experiments or applications, e.g. as detectors of electron spin entanglement [38, 39], difficult.

10

Fabrication and characterization of Permalloy contacts for nanospintronic devices[1]

As we have seen in the previous chapter, the most fundamental CNT spin transport device is a spin valve with two ferromagnetic (F) contacts to the CNT, where the F contacts serve as injector and detector of a spin-polarized current. Figure 10.1(a) shows an SEM picture of such a device. Ideally, the contacts can be either magnetized parallel or anti-parallel to each other by an external magnetic field, in order to obtain a measurable and reproducible magnetoresistance (MR) signal. Compared to other carbon based nanoscale devices with normal metal or superconducting leads, the contact material has to be chosen from a very limited range of readily available and processable magnetic metals, which limits the optimization of the contacts. In addition, most ferromagnetic materials form oxides when exposed to air [338], which diminishes the electrical contact yield. To obtain low-ohmic contacts with non-magnetic materials, one often chooses large contact areas, which, however, is in conflict with using narrow contact geometries to control the shape anisotropy [36] and thus the magnetic field at which the magnetization is reversed (switching field). Even the thickness of the deposited material is limited to avoid the formation of vertical, more complex magnetic domains [324]. No adhesion or contact layer can be used because the equilibrium spin polarization decays very rapidly in non-magnetic metals (on the scale of the exchange interaction, typically $< 1\,\mathrm{nm}$). For a reproducible MR signal in

[1] Parts of this chapter have been published in similar form in Ref. [114].

CNT spin-valve devices, ferromagnetic contacts should hence allow for a well defined anti-parallel magnetization state with at best clearly separated switching fields tunable by shape anisotropy, and have a large enough transport spin polarization to obtain a measurable spin signal [36]. An in-plane magnetization and single domain characteristics of the contacts are highly relevant for reproducible magnetization reversal, for spin injection and detection in a controlled domain state, and for reduced stray-fields. Finally, large enough yields of low-ohmic contacts to the CNT are a prerequisite for any experiment.

Significant efforts have been already undertaken to find suitable ferromagnetic contact materials for CNT spin-valve devices [36, 323, 324], and many contact materials have already been implemented in CNT spin-valve devices, including Co [35, 311–314, 335], Ni [314, 316, 328], Fe [37], half-metallic ferromagnet lanthanum strontium manganite (LSMO) [339], ferromagnetic semiconductor (Ga,Mn)As [37], diluted alloys such as PdNi [27, 315, 317, 321, 330, 340], PdFe [324], PdCo [341], CoFe [342], NiFe [36, 114, 130, 319], or multilayers [329, 337]. Most of these materials have one or more disadvantages, in either controlling the magnetic domain states and reproducible magnetization reversal in nanoscale ferromagnetic strips, or in obtaining low-ohmic electrical contacts. The often implemented PdNi alloy, for example, allows for reproducibly transparent contacts to CNTs [315, 317], but a multi-domain state and a favored in-plane easy axis perpendicular to the strips long axis render spin-valve experiments with reproducible MR signals difficult [321–323]. While we have also tested Co (for conclusions see Appendix E), our choice of contact material is the well-studied $Ni_{80}Fe_{20}$ alloy Permalloy (Py), for which one can obtain single-domain contacts and control over the magnetic easy axis by the shape of the contacts [36, 58, 324, 343]. Py also fulfills the prerequisite of a large transport spin polarization, typically $P_j \sim 45\%$ [281, 283]. We have already demonstrated in Sec. 2.2.1 – in contrast to previous studies [324] – that we reproducibly obtain low-ohmic electrical contact to CNTs with narrow Py contacts when using an optimized, essentially residue-free EBL based on the low-density polymer ZEP. In this chapter, we hence focus on the micromagnetism of ferromagnetic Py contacts, and illustrate reproducible magnetic characteristics also for sub-micrometer scale Py contacts fabricated by ZEP EBL and thermal evaporation or sputter deposition. The latter also allows to deposit magnetic multi-layer structures, e.g. anti-ferromagnetic exchange-bias layers [319].

10.1. Optimized fabrication scheme

Following Refs. [36, 324, 343] and shown in the SEM image of Fig. 10.1(a), our approach to obtain reproducible magnetic domains and switching characteristics for the ferromagnetic contacts is to fabricate rectangular, 25 nm thick,

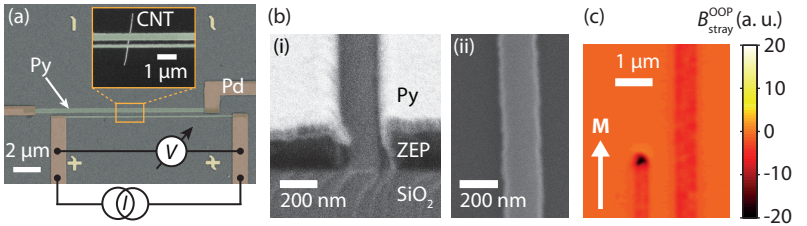

Figure 10.1.: (a) False color SEM image of a lateral CNT QD spin-valve with rectangular Py contacts and Pd leads, and measurement scheme for AMR measurements of an individual Py strip of the device. (b) Optimized sputter deposition of Py strips, using the ZEP EBL process with 10 kV acceleration voltage. SEM image of a (i) cross section of the metallized strip structure, and (ii) top view of Py strip after lift-off. (c) MFM image of the out-of-plane stray field $B_{\text{stray}}^{\text{OOP}}$ created by a narrow and broader Py strip, by courtesy of S. Zihlmann and P. Makk. The arrow indicates the in-plane easy axis of **M**.

ferromagnetic Py strips with a large aspect ratio (~ 100) in a ZEP EBL process. To deposit Py we use two techniques: (1) thermal e-beam evaporation of Py in a UHV chamber at a base pressure of $\sim 10^{-9}$ mbar, sample cooling to -30°C and a deposition rate of ~ 0.2 Å/s. (2) DC sputter deposition using an Ar plasma at a power of 35 W and an Ar pressure/flow of $\sim 6 \times 10^{-3}$ mbar (5 mTorr)/35 sccm in a UHV chamber with a base pressure of $\sim 10^{-9}$ mbar. In Sec. 2.2.1, we have already extensively discussed the optimized fabrication of nanoscale Py strips by thermal evaporation, and demonstrated that we obtain clean and well-defined Py strips without significant residual metal particles (from lift-off) closeby [see e.g. Fig. 2.5(c)]. In this process, we evaporate Py thermally from a commercially available target of correct stoichiometric composition. Nevertheless, such a target is susceptible for metal contamination from the surrounding vacuum chamber and different evaporation processes, and the stoichiometric composition of both the target and evaporated strips might vary. We hence regularly monitored both the target and evaporated test films for the correct stoichiometry by energy dispersive X-ray spectroscopy (EDX), and adjusted the target accordingly. A correct stoichiometry of Py strips can be easily[2] achieved by sputter deposition [344]. The fabrication of nanostructures by sputter deposition is however often difficult because the sputtered material is scattered at gas particles in the chamber, which leads to a large angular spread that can fill the lithographically defined polymer trench and lead to lift-off problems. To overcome such problems, the sputter deposition was systematically optimized by co-worker J. Samm, including a magnetic characterization of sputtered Py strips. The author of this thesis did

[2] All target components are physically sputtered with very similar rates (maintaining stoichiometry of the target), whereas the rates for individual target material components in thermal evaporation might vary due to different vapor pressures at high temperature.

not contribute significantly to this process, which is why we only summarize the results and refer to Ref. [344] for more details. Sufficient directionality for the sputter deposition of Py can be achieved by working with a relatively low Ar pressure and no sample rotation, at a deposition rate of $\sim 0.5\,\text{Å/s}$. The sample resides directly above the Py target at a distance of $\sim 10\,\text{cm}$ from the plasma at room temperature. Similarly clean Py strips as for thermal evaporation (cf. Fig. 2.5(c) and Sec. 2.2.1) with a slightly increased surface roughness can be obtained using the ZEP recipe and sputter deposition of Py, as demonstrated in Fig. 10.1(b). Using this recipe, one even obtains slightly increased yields of low-ohmic contacts to CNTs than for thermal evaporation of Py [344], possibly due to the larger kinetic energies of the deposited material and an associated improved metal wetting of the CNT surface, or a creation of defects in the CNT. We fabricate long ($10\,\mu\text{m}$), thin ($25\,\text{nm}$) Py strips with a small width w, which forces the magnetization of the ferromagnetic contacts to lie along the strip axis [324]. Figure 10.1(c) shows a magnetic force microscopy (MFM) image[3] of such a strip, indicating a significant stray field only at the ends of the strip and supporting a single-domain magnetization with the easy axis along the strip direction. The magnetization direction can be inverted by an external magnetic field along the strip axis that switches the magnetization to the opposite orientation at a characteristic switching field H_S tunable by the width w of the strip [36, 343].

10.2. Anisotropic magnetoresistance measurements

To assess the magnetic properties and material quality of an individual Py strip, we follow the techniques of Refs. [36, 58] and contact the Py strip with Pd contacts to measure the anisotropic magnetoresistance (AMR, Sec. 9.2.2) in the measurement set-up[4] depicted in Fig. 10.1(a). We performed a systematic study of AMR on thermally evaporated Py test strips of widths ranging from 90 to 450 nm, contacted as single strips in a 4-terminal measurement geometry and fabricated by ZEP EBL. Because the AMR signals can be detected both in 4-terminal and 2-terminal measurements, one can also monitor and assess the AMR of individual contact strips by 2-terminal measurements in a CNT spin-valve device as depicted in Fig. 10.1(a). This proves very useful for the interpretation of spin-valve signals due to the possibility to determine the expected switching fields H_S of the strips. Non-magnetic (Pd) leads are of crucial importance to obtain reproducible switching characteristics [324]. From the 4-terminal measurements, we deduce transparent metallic contacts of the Pd leads to Py, a resistivity of Py at low temperatures $\rho(T = 1.5\,\text{K}) \sim 4.5 \cdot$

[3] By courtesy of P. Makk & S. Zihlmann, collaboration with H.-J. Hug, EMPA.

[4] A home-built resistance bridge (or Picowatt AVS-47) is employed to substract the large strip resistance background, in order to resolve resistance changes $\lesssim 0.1\%$ in a lock-in measurement.

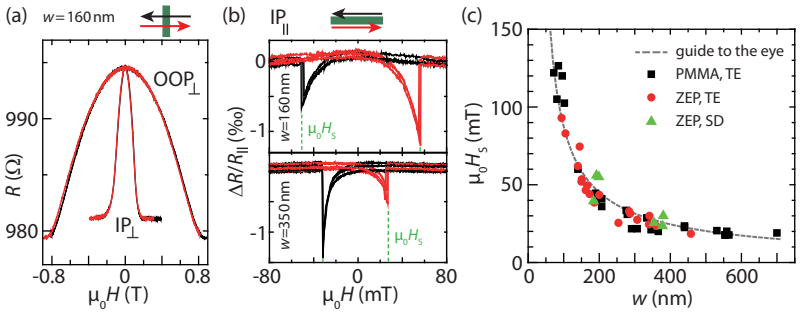

Figure 10.2.: (a) AMR measurement of a $w = 160\,\text{nm}$ wide, thermally evaporated Py strip. The external magnetic field $\mu_0 H$ is applied perpendicular ($\perp$) to the current direction $\mathbf{j}$ and easy axis, both in-plane ($\text{IP}_\perp$, bottom) and out of the sample plane ($\text{OOP}_\perp$, top). Color-coded arrows in (a) and (b) denote the respective sweep direction of H, relative to the (green) Py strips easy (long) axis. (b) AMR measurements of $w = 160\,\text{nm}$ (top) and $w = 350\,\text{nm}$ (bottom) wide, thermally evaporated Py strips with H applied in plane parallel to the current direction $\mathbf{j}$ ($\text{IP}_\parallel$). Switching fields $\mu_0 H_\text{S}$ can be read off from the sharp resistance jumps, a small asymmetry in H_S is due to the hysteresis of the superconducting magnet. (c) Switching fields $\mu_0 H_\text{S}$ as a function of strip width w, extracted from AMR measurements at $T \lesssim 1.5\,\text{K}$ similar to (b) on individual, 25 nm thick and 10 μm long Py strips. The symbols represent values for strips obtained by ● thermal evaporation (TE) and ZEP recipe (this thesis), ▲ optimized sputter deposition (SD) and ZEP masks (J. Samm, [344]), and ■ thermal evaporation and a PMMA/MA recipe (from Ref. [36, 58]). The dashed line is a guide to the eye.

$10^{-7}\,\Omega\text{m}$ and from temperature dependent measurements a residual resistance ratio $RRR = R_{298\,\text{K}}/R_{1.5\,\text{K}} \sim 1.3$. These values compare reasonably well with previous findings [58] and are typical for slightly oxidized ferromagnetic thin films [343, 345].

Figure 10.2(a) and (b) show typical AMR measurements of individual, thermally evaporated Py strips at low temperatures, for the external magnetic field $\mathbf{H}$ applied perpendicular [(a), out-of-plane ($\text{OOP}_\perp$, top) and in-plane, ($\text{IP}_\perp$, bottom)] and parallel [(b), $\text{IP}_\parallel$] to the strips easy axis and current direction. As explained in Sec. 9.2.2, we observe a continuous decrease of the resistance to a certain value for the $\text{OOP}_\perp$ and $\text{IP}_\perp$ configurations, consistent with the rotation of a single domain magnetization towards the hard axis until $\mathbf{M}$ is aligned with $\mathbf{H}$ and $\mathbf{M} \perp \mathbf{j}$. The larger fields needed for the alignment of $\mathbf{M}$ with $\mathbf{H}$ in the $\text{OOP}_\perp$ measurement agree with a favored in-plane easy axis and the strip dimensions. Also consistent with our previous discussion in Sec. 9.2.2, Fig. 10.2(b) shows sharp characteristic changes in the resistance on a flat background at $\mu_0 H_\text{S} = 28$ and 53 mT for a 350 (bottom) and 160 nm (top) wide Py strip, respectively, when $\mathbf{H}$ is aligned nearly parallel to the strips long axis. These switching fields indicate the reversal of the magnetization [36, 343]. The four plotted consecutive measurements, separated in

time by several days, demonstrate reproducible magnetization reversal and switching fields within a range of 3 mT. We observe similar characteristics in parallel and perpendicular magnetic fields for all studied Py strips, also for sputtered strips [344], and do not find differences in the switching fields of individual Py strips or pairs of Py strips located close to each other as in Fig. 10.1(a). Figure 10.2(c) shows the switching fields $\mu_0 H_S$ as a function of w for strips obtained by different fabrication techniques. We find that the sputtered and thermally evaporated contacts defined using ZEP exhibit the same dependence on w as the PMMA processed and thermally evaporated Py contacts studied previously [36]. The switching fields can be distinguished reliably for widths $w < 400$ nm, for which H_S increases strongly for smaller w. This allows to design contacts with an experimentally accessible antiparallel magnetization state, i.e. with well separated switching fields $\Delta\mu_0 H_S > 10$ mT. The AMR studies strongly support a single-domain magnetization of the Py strips, aligned with the long (easy) strip axis. This is further supported by recent x-ray circular dichroism (XMCD) studies of Py strips in our group [346], demonstrating mainly single domain characteristics for 120 nm $< w <$ 1 μm. For much smaller strips, multiple domains can occur in the unmagnetized strip state e.g. due to edge roughness or surface corrugation, while for larger strips magnetic closure domains may form near the tips of the strips.

10.3. Conclusions

In conclusion, the achievable low-ohmic contacts with narrow Py strips, their expected single-domain behavior with reproducible magnetization reversal tunable by shape anisotropy, and a magnetic easy axis along the strip ideally fulfill all prerequisites for CNT QD spin-valve experiments. While the AMR curves of individual Py strips are very reproducible, the resulting MR in a spin valve are more problematic, as we will discuss in the next chapters. We note already here that AMR experiments are sensitive to the bulk of the material, while in spin valve configurations the last few atomic layers are crucial.

11

Magnetoresistance signals in conventional CNT QD spin-valve devices[1]

This chapter presents experimental results and magnetoresistance signals obtained on 'conventional' CNT QD devices with ferromagnetic contacts fabricated by e-beam lithography on substrate. Due to the aforementioned difficulties in interpreting multi-terminal experiments with multiple QDs, we choose a local two-terminal spin-valve geometry as the most basic QD structure, also to analyze the suitability of the ferromagnetic contacts for more complex experiments or applications, e.g. as detectors of electron spin entanglement [38, 39] in Cooper pair splitting device geometries [40].

In the first part, we demonstrate the need for an extended data analysis due to the typically occurring instabilities in QD spin-valve MR experiments, that can for example be due to magnetic particles from incomplete lift-off or imperfect CNT-metal interfaces with resist residues originating from unoptimized fabrication. Using the previously introduced optimized fabrication of CNT spin-valves based on ZEP resist (cf. Sec. 2.2.1 and Chap. 10), we report spin-valve experiments with significantly improved characteristics in terms of both electrical stability and reproducible magnetic switching between the parallel and anti-parallel magnetization state in Sec. 11.2. These results were obtained on two devices both fabricated by co-worker J. Samm, and details of the analysis were already reported in Ref. [344]. Although the main work was carried out by J. Samm, at least for the first device, we briefly summarize the findings because the author of this thesis contributed significantly to data analysis and interpretation, performed most of the measurements for the 2nd

[1] Parts of this chapter have been published in similar form in Ref. [114].

device and its here presented data analysis, and in developing the optimized EBL process (cf. Sec. 2.2.1) and characterizing the Py strips (Chap. 10) as a crucial prerequisite for the discussed experiments. Finally, we conclude and sketch future perspectives and experiments in Sec. 11.3.

11.1. Nanospintronic magnetoresistance experiments

In this section we demonstrate the need of extended data acquisition and analysis for nanospintronic devices with non-trivial conductance characteristics. In the QD spin-valves discussed here, the conductance depends on the gate voltage, which tunes the QD level energies. The charging energy and level separation lead to characteristic Coulomb blockade (CB) conductance maxima, with a strongly reduced conductance in between. Figure 11.1(a) shows the employed device geometry and measurement set-up of a conventional CNT QD spin-valve on substrate with Py contacts, fabricated as discussed previously in Chap. 2 and Sec. 10.1. The magnetoresistance (MR) of a spin-valve device is defined in terms of its conductances G_{P} and G_{AP} when the magnetizations in the two contact strips are either parallel (P) or anti-parallel (AP). Here, the symmetric definition (9.6) with a maximum MR value of 100% is used, which is more adequate for our purpose because it provides an equal measure for positive and negative MR. We investigate the CNT spin-valve devices at low temperatures, where a QD forms between the ferromagnetic Py contacts. The base temperature in most experiments presented here is $\sim 230\,\mathrm{mK}$, and we only present data recorded at $V_{\mathrm{SD}} = 0$. Prior to the cool-down, devices are usually either pre-magnetized at RT or field-cooled to base temperature with a magnetic field of 1 T applied parallel to the strips easy axis. This serves likely to reduce magnetization pinning and formation of multiple domains due to possible exchange-coupled anti-ferromagnetic oxide top layers.

In the color-scale image in Fig. 11.1(b), the QD conductance is plotted as a function of the backgate voltage V_{BG} and an increasing external magnetic field $\mu_0 H$ (up-sweep) applied parallel to the Py strips for a QD fabricated with standard PMMA-based lithography. The QD conductance has a maximum at $V_{\mathrm{BG}} \approx -6.48\,\mathrm{V}$ and decays rapidly away from this value. A cross section at constant magnetic field is plotted in white. When the magnetic field is increased from negative values beyond $\mu_0 H = 0$, a first sharp ($\Delta\mu_0 H < 1\,\mathrm{mT}$) change in the conductance pattern occurs at $\mu_0 H_1 \approx 20\,\mathrm{mT}$, and another at $\mu_0 H_2 \approx 30\,\mathrm{mT}$. These fields correspond well to the contact switching fields of the two Py strips.

At $\mu_0 H_1$ the amplitude of the CB resonance increases by a factor of ~ 2 and the peak position shifts by about $\Delta V_{\mathrm{BG}} \approx 4\,\mathrm{mV}$, which corresponds to an energy shift of $\Delta E \approx 400\,\mu\mathrm{eV}$ or to almost the resonance width. While the amplitude of the CB resonance increases by almost a factor of 2 at $\mu_0 H_1$

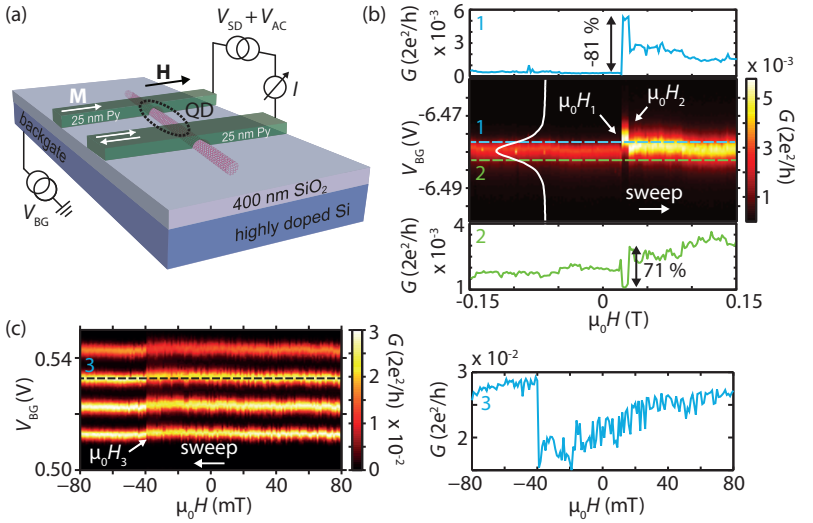

Figure 11.1.: (a) Schematic and measurement scheme of a lateral CNT QD spin-valve with Py leads. (b) Differential conductance map $G(V_{\rm BG}, \mu_0 H)$ of a CNT spin-valve fabricated by standard PMMA-based lithography and thermal Py evaporation. The top and bottom MR curves are cross-sections at the gate voltages indicated by the dashed lines (1,2) in the main graph. (c) Similar conductance map obtained at $T = 1.5\,\mathrm{K}$ for a CNT spin-valve fabricated by optimized ZEP lithography and thermal Py evaporation. The right panel shows a cross-section of the conductance map at the gate voltage indicated by the dashed line (3).

starting at the low field side, it does not change at $\mu_0 H_2$ and is reduced slightly only at higher fields. At $\mu_0 H_2$ the resonance position switches back roughly to the same gate position as for $H < H_1$. In a standard MR measurement the conductance is recorded as a function of $\mu_0 H$ alone, which corresponds to cross sections in Fig.11.1(b) at a fixed gate voltage. Two examples for slightly off-resonance voltages are shown on top and below the main figure: at a more negative gate voltage (green dashed line, 2) we find a decrease in conductance for the anti-parallel magnetizations, $H_1 < H < H_2$, which corresponds to an increased resistance and a positive MR of $\sim 70\%$. Off-resonance for a more positive gate voltage (blue dashed line, 1) the MR at fixed voltage is negative, MR $\approx -80\%$. These large values of the MR are almost exclusively due to the large shift of the resonance position. In the simplest model by Jullière for tunneling MR discussed previously one would expect MR $= P_1 P_2 \approx 9 - 25\%$ when using $P_{\rm T} = 0.3 - 0.5$ for the tunneling transport spin polarizations in the two F contacts. These values rather correspond to the amplitude modulation (MR $< 30\%$) than to the MR observed in cross-sections with a major contri-

bution due to resonance position shifts. Hence, since the MR in QD devices not only depends on the magnetic orientation of the contacts, but also on the electrostatic environment (e.g. gates), it is necessary to expand the standard magnetic field sweeps to three-dimensional maps that also contain a variable gate voltage to track the origin of the observed MR.

We will discuss shifts of the conductance features in the MR later, and only point out that while the MR at H_1 and H_2 might be described by a simple spin-valve model, the increase of G for $H > H_2$ with respect to $H < H_1$ is more difficult to explain since it suggests a difference between the two parallel configurations, a phenomenon possibly related to the single switching behavior reported before [208, 314]. Such single-switching characteristics at a field $\mu_0 H_3$ is illustrated in Fig. 11.1(c) for a device fabricated by optimized ZEP EBL and thermal evaporation, and possibly due to the previously discussed magneto-Coulomb effect (MCE) [208], or a pinned (interface) magnetization direction of one of the F contacts [314].

Generally, the electrical stability and reproducibility of the QD spin-valve signals is considerably improved for devices fabricated using the ZEP recipe introduced in Sec. 2.2.1. As discussed there, this is on the one hand most likely due to the reduced number of magnetic particles close to the active device structure (obviously not ideal for MR experiments) compared to non-optimized, PMMA-based fabrication. On the other hand, the considerably improved interface quality with less resist residues possibly results in smaller resonance position fluctuations due to e.g. charge rearrangements. During this thesis, however, we still did not obtain devices with clear spin-valve characteristics for devices with thermally evaporated Py contacts. The results presented in the following were hence obtained on two devices fabricated with Py sputter deposition by co-worker J. Samm. The reason for this finding remains unclear at present. We speculate that the slightly increased yield of low-ohmic devices, as well as the stoichiometric material composition, and an improved CNT interface wetting due to the higher kinetic energies in sputter deposition might play a role. Particularly a better wetting could play a significant role in an improved interface stability and CNT-metal bonding [65].

11.2. Spin-valve signals in stable devices

We now analyze in more detail the data measured on two devices with sputtered Py contacts, fabricated as discussed in Chap. 10.

11.2.1. Negative magnetoresistance over complete orbital

In Fig. 11.2(a) the QD spin-valve conductance G of device A with a RT resistance of $\sim 50\,k\Omega$ is plotted for a large backgate voltage interval at a base temperature of $\sim 230\,\mathrm{mK}$. The CB peaks occur in groups of four consistent

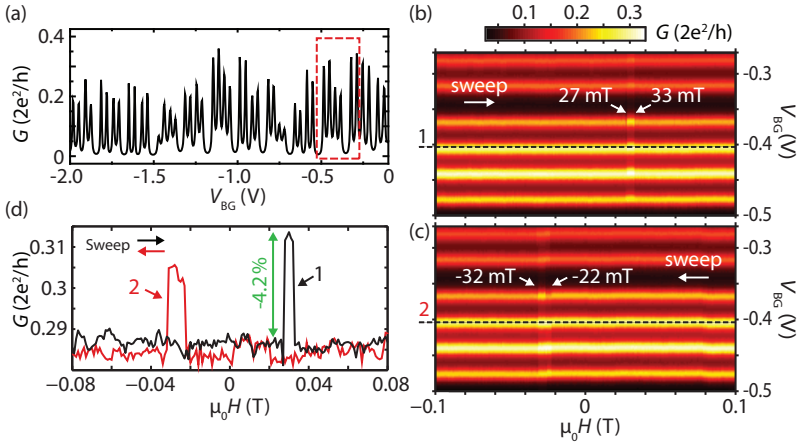

Figure 11.2.: (a) Differential conductance G of CNT spin-valve A for a large backgate voltage interval. (b), (c) G as a function of the backgate voltage V_{BG} for increasing (b) and decreasing (c) external magnetic field H. (d) Up and down sweeps at fixed V_{BG}, indicated as dashed lines in (b) and (c).

with the spin and valley degeneracy of a CNT orbital. Such a pattern suggests that the CNT segment forming the QD is relatively clean [102]. From charge stability diagrams (not shown, see Ref. [344] for details) we find the lever arm of the backgate to the QD $\alpha_{\mathrm{BG}} \approx 0.14$, a charging energy of $\sim 4.5\,\mathrm{meV}$ and a level spacing of $\sim 3.5\,\mathrm{meV}$. We estimate the source, drain and backgate capacitances as $C_{\mathrm{S}} \approx 23.6\,\mathrm{aF}$, $C_{\mathrm{D}} \approx 6.3\,\mathrm{aF}$ and $C_{\mathrm{BG}} \approx 4.9\,\mathrm{aF}$. From the CB maxima of $\sim 0.25\frac{2e^2}{h}$, the average broadening of the peaks $\sim 2.4\,\mathrm{meV}$ and using the Breit-Wigner form (1.10) for resonant tunneling at low temperatures ($kT \ll \Gamma$), we find for the tunnel couplings of the QD to source and drain $\Gamma_{\mathrm{S}} \approx 2.0\,\mathrm{meV}$ and $\Gamma_{\mathrm{D}} \approx 0.4\,\mathrm{meV}$, which gives a relatively small coupling asymmetry of $\Gamma_{\mathrm{S}}/\Gamma_{\mathrm{D}} \approx 5$ (we chose the larger value as Γ_{S}).

We now focus on the four CB peaks highlighted in Fig. 11.2(a) by the red rectangle, which originate from the same four-fold degenerate QD orbital. In Fig. 11.2(b) and (c) the QD conductance G is plotted for this gate voltage interval and as a function of an external magnetic field H along the Py contact strips. In Fig. 11.2(b) the field is increased from negative values (up sweep), while in 11.2(c) it is decreased, starting from positive values (down sweep). The magnetizations were saturated at $\pm 150\,\mathrm{mT}$ before the respective sweep. In the up sweep in Fig. 11.2(b), G is larger for $27 \leq B \leq 33\,\mathrm{mT}$, which usually is identified as the anti-parallel configuration of the contact magnetizations. In the down sweep the magnetization switching occurs at negative fields and

we find an increased conductance for $-32 \leq B \leq -22\,\mathrm{mT}$. The variation between the absolute values of the switching fields in the up and down sweeps are compatible with the variation observed in the corresponding AMR curves. Apart from the expected conductance changes in the parallel and anti-parallel magnetization configuration, almost no random resonance position shifts or conductance changes can be observed. Figure 11.2(d) shows the up and down sweeps in cross-sections at a fixed backgate voltage, indicated by the dashed lines in Figs. 11.2(b) and (c). We find a sharp switching of the conductance at the Py strip switching fields, which corresponds to a MR of $\sim -4\%$. The MR is negative for all gate voltages, which we now discuss in more detail.

In devices with a variable conductance $G(V_{\mathrm{BG}})$, the origin of the MR signal can lie in changes of the width, position and amplitude of the conductance feature as discussed in Chap. 9. In Fig. 11.3(a) we plot the CB oscillations indicated in Fig. 11.2(a) as a function of V_{BG} for the different magnetization configurations. The two parallel configurations lead to identical conductances (red line), which demonstrates the reproducibility of both, the magnetic and electronic structures in the device. The anti-parallel configuration (black dashed line), however, deviates significantly from the parallel. The resulting MR vs V_{BG} curve is plotted in Fig. 11.3(b) (full red line). The MR is negative for almost all backgate voltages and shows a MR modulation of $\sim 10\%$ on an offset of about -5%. The modulation is correlated with the gradient $\mathrm{d}G/\mathrm{d}V_{\mathrm{BG}}$ of G, i.e. it is largest at the gate voltages where G has the largest slopes, which suggests that the MR is caused mainly by a shift of the CB resonances.

In the next step we fit the data with multiple Lorentzians to extract the amplitude, width and position of the individual CB peaks (no background is subtracted), which is exemplary demonstrated for the AP configuration in Fig. 11.2(a) as green (individual Lorentzians) and orange lines (fit). The resulting parameters for the up sweep are plotted in Figs. 11.3(c-e) for the third CB peak highlighted by an asterisk in Fig. 11.3(a). Compared to the parallel magnetization configurations, the anti-parallel shows an increase in amplitude and width by $\sim 4\%$ and 4.5%, respectively, and a shift of $\sim 1.0\,\mathrm{mV}$, which corresponds to $\sim 140\,\mu\mathrm{eV}$ or $\sim 6\%$ of the peak width. We obtain similar values for the other CB peaks (for details see Ref. [344]). All peaks are shifted by the same absolute value within experimental errors.

The extracted parameters allow us to investigate the respective impact on the MR, for example by calculating the MR from the measured curve for the parallel magnetizations and a shifted curve in the anti-parallel case. The result is plotted in Fig. 11.3(b) as blue dashed line (cor. MR). The corrected MR is negative for all gate voltages and has MR maxima at gate voltages where also G has maxima, as expected if the shifts were corrected precisely enough. The MR variation on this curve is only $\sim 3\%$ with a slightly smaller negative offset than in the original data. The remaining modulation possibly arises from changes in the peak widths.

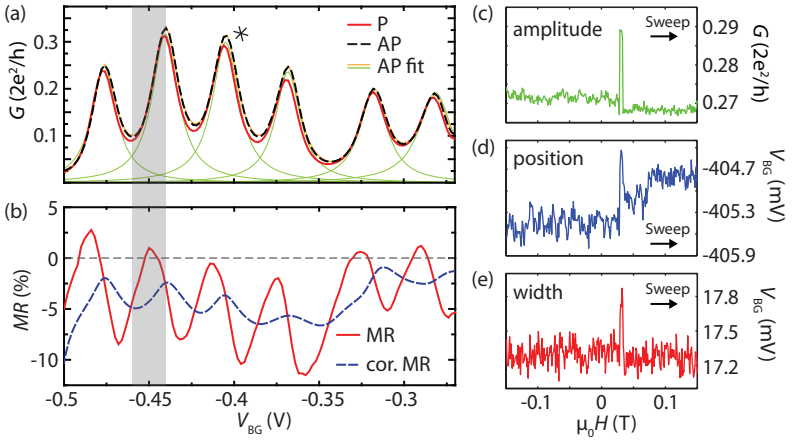

Figure 11.3.: (a) Conductance G as a function of the backgate voltage V_{BG} for the magnetization configurations both parallel [↑↑, ↓↓, red line], and antiparallel [↑↓, black dashed line]. The corresponding MR curves are shown in (b). (c)-(e) Amplitude, position and width of the third CB resonance peak (asterisk) as a function of the applied magnetic field H for the up sweep, extracted from the fits described in the text and exemplary shown as green lines (individual Lorentzians) and orange curve (sum, fit) in (a) for the AP configuration.

11.2.2. Similar characteristics for a second device

A second, similarly stable CNT spin-valve device B with a RT resistance of $\sim 70\,\mathrm{k\Omega}$ was studied at a base temperature of $T \approx 1.5\,\mathrm{K}$. Also this device exhibits a four-fold symmetric CB pattern in the conductance as a function of backgate voltage shown in Fig. 11.4(a), suggesting a clean CNT. From charge stability diagrams (not shown, see Ref. [344]), one can extract the lever arm of the backgate $\alpha_{\mathrm{BG}} \approx 0.07$, a charging energy of $\sim 4\,\mathrm{meV}$, a level spacing of $\sim 3.8\,\mathrm{meV}$, and an average CB peak width of $\sim 1.75\,\mathrm{meV}$ – quite comparable to device A. Following the analysis scheme for the previous device, Fig. 11.4(b) and (c) show magnetoconductance maps of the four peaks labeled by a rectangle in Fig. 11.4(a) for the up and down sweep of the external magnetic field H. We identify the anti-parallel magnetization configuration for $20 \leq |\mu_0 H| \leq 40\,\mathrm{mT}$, for which a significant conductance change compared to the parallel state is visible. The sharp switching fields agree with the AMR measurements on the individual, 200 and 400 nm wide Py strips. To demonstrate the extremely reproducible switching characteristics of this device, Fig. 11.2(d) and (e) show the up and down sweeps in cross-sections at a fixed backgate voltage for peak 1 and 2. Three repetitive measurements are plotted in different colors, extracted from three independent color maps as in-

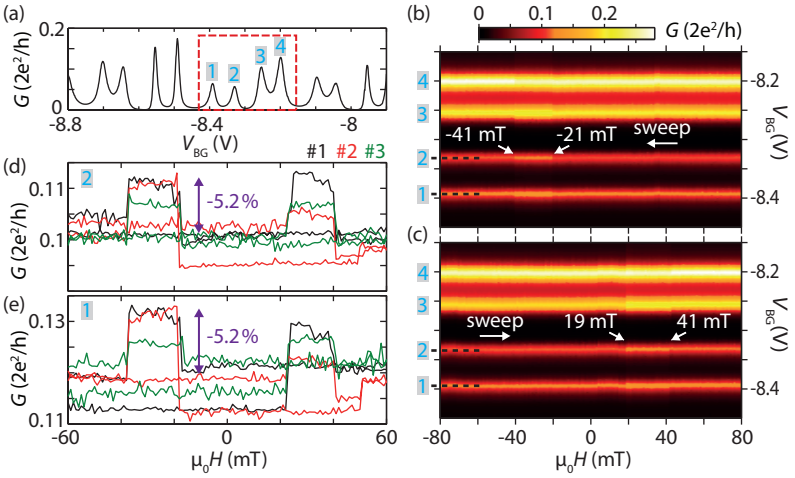

Figure 11.4.: (a) $G(V_{\mathrm{BG}})$ of CNT spin-valve B. (b), (c) $G(V_{\mathrm{BG}}, \mu_0 H)$ conductance maps for increasing (b) and decreasing field (c). (d,e) Up and down sweeps in cross-sections of $G(V_{\mathrm{BG}}, \mu_0 H)$ at fixed V_{BG} for the peaks 1 and 2, indicated as dashed lines in (b) and (c). The color-coded numbers #1-#3 label repeated, independent measurements.

dicated by the dashed lines in Fig. 11.2(b) and (c). While the conductance base line changes slightly from repetition to repetition, clear conductance changes are visible for every repetition at the same switching fields, clearly correlating the magnetization reversal with the observed conductance changes. Again, we find a negative MR for most gate voltages, i.e. $\sim -5\%$ for peaks 1 and 2.

To investigate this further, we repeat the analysis for the previous device. Figure 11.5(a) plots the conductance of the four selected CB peaks in the parallel (red line) and anti-parallel (black dashed line) configurations as a function of V_{BG} for the up sweep. For this device, we find again a small consistent gate voltage shift of $\sim 1\,\mathrm{mV}$ (or $\sim 70\,\mu\mathrm{eV}$, corresponding to $\sim 4\%$ of the peak width) of the CB maxima between the different magnetization configurations, and significantly different amplitudes. The resulting MR vs V_{BG} curve is plotted in Fig. 11.5(b) (full red line). Again, we find a negative MR for almost all backgate voltages and a MR modulation of $\sim 10\%$ on an offset of about -5%. The blue dashed line shows a shift-corrected MR curve, where the AP conductance was shifted with the experimentally extracted separation of CB maxima from above. The corrected MR is again negative for almost all gate voltages with a slightly smaller offset than in the original data. Due to the larger temperatures, temperature broadening of the CB resonances already plays a role. Hence, the data is not described well by a fit with multiple

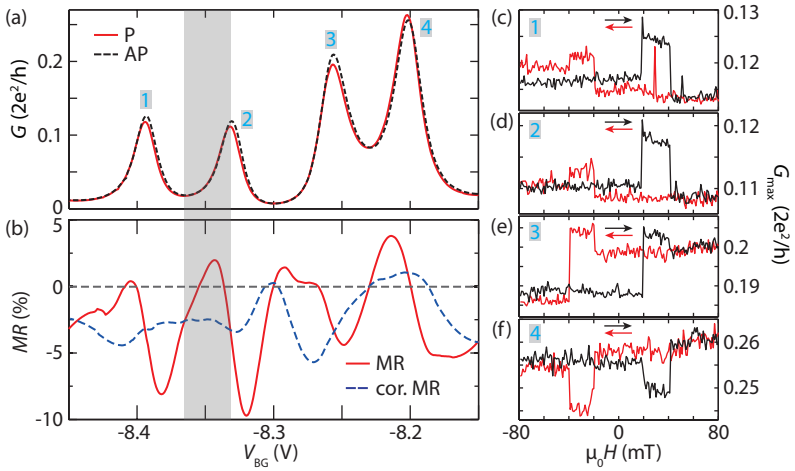

Figure 11.5.: (a) $G(V_{\mathrm{BG}})$ for the P and AP magnetization configurations in the up sweep. The corresponding MR curves are shown in (b). (c)-(f) Maximum amplitude G_{max} of the CB resonance peaks 1-4 as a function of the applied magnetic field H for up (black line) and down sweep (red line), extracted from the measurements.

Lorentzians or temperature-broadened CB resonances alone, and does not allow for a precise enough quantitative analysis of the position and width of individual resonances. We therefore only extract the maximum amplitude of the four peaks labeled 1-4 for the up and down sweep of the external magnetic field, which is plotted in Fig. 11.5(c-f). Peak 1-3 show a negative MR with increased conductance in the anti-parallel state, with a superimposed change of the conductance base-line for peak 3, possibly due to a small resonance position shift. Only peak 4 shows a different characteristics, with a regular positive MR signal and reduced conductance in the anti-parallel state. Due to the changing conductance base-lines and differing absolute values of the MR [see Fig. 11.4(d,e)] between repetitive sweeps, we omit a more quantitative analysis as for the previous device. In any case, the very similar MR vs V_{BG} curve also for device B [cf. Fig. 11.5(b) and Fig. 11.3(b)] suggests a generic origin of the negative MR in our CNT QD spin-valve devices with sputtered Py contacts.

11.2.3. Discussion

The observation of a mostly negative MR and a consistent position shift of the CB resonances over a complete orbital depending on the magnetization configuration is in strong contrast to previous findings (cf. Sec. 9.3).

As discussed previously, a periodic modulation of the MR with the CB oscillations was already observed by Sahoo *et al.* [27] and modelled by spin-dependent effective tunnel rates. In their simple intuitive picture [Sec. 9.3, Fig. 9.5(a)], one can construct negative MR signals for a strongly asymmetric QD coupling to the contacts, which can lead to a negative offset for strongly overlapping resonances. The change of the effective tunnel couplings at the switching fields could in principle also result in a change of the resonance widths. However, this model requires strongly asymmetric tunnel couplings and predicts that the MR maxima occur near the conductance minima, both in contrast to our observations. This intuitive picture does not produce shifts in the CB resonance energies, either. The more elaborate models reviewed in Sec. 9.3 predict a purely positive MR offset in the sequential tunneling limit [325, 326], and inclusion of higher order contributions leads to major MR contributions from shifts of the CB resonances in an effective magnetic field, caused either by spin dependent electron scattering at the QD-contact interfaces (SDIPS) [325, 325, 327] or by a spin-dependent renormalization of the QD energy levels [318, 319]. Characteristic for both mechanisms is that the sign of the shifts depends on the spin state of the CB resonance. Specifically, as dicussed in Sec. 9.3, of the four states in a CNT orbital two should be shifted in energy opposite to the other two, which we do not observe. None of the models predicts identical shifts for all four peaks, nor a generally negative offset of the MR. Nevertheless, the sign change of MR observed on resonance for peak 4 of device B at least suggests an occupation dependent MR, as also discussed in the theoretical models. Also note that even if the MR modulation could be described by the models, a quantitative comparison would be hardly justified due to the observed variations of the resonance amplitudes and positions in the parallel and anti-parallel configuration in repetitive experiments, see e.g. Fig. 11.4(d,e). This rather points to external small random potential fluctuations as source of the shifts, e.g. at the metal-CNT interface and possibly triggered by magnetization reversal.

Another mechanism that results in a constant shift in the anti-parallel configuration is the magneto-Coulomb effect (MCE) [320, 331] introduced in Sec. 9.3. For the extracted capacitances of device A, we estimate a MCE shift of the QD resonances in an external magnetic field H of $\Delta V_{\mathrm{BG}}/\mu_0 H = \frac{1}{2e}\frac{C_{\mathrm{S}}+C_{\mathrm{D}}}{C_{\mathrm{BG}}} P_{\mathrm{N}} g \mu_{\mathrm{B}} \approx 300\,\mu\mathrm{V/T}$. In the last step we used $P_{\mathrm{N}} = 0.8$ as an upper limit of the (thermodynamic) Py polarization in both leads, the Landé g-factor in thick ($> 15\,\mathrm{nm}$) Py films of $g = 2.1$ [347] and the Bohr Magneton μ_{B}. With the same parameters one obtains a total change in position of $\Delta V_{\mathrm{BG}} \approx 15\,\mu\mathrm{V}$ when sweeping the field beyond both switching fields. The negligible slope observed for the peak positions is consistent with the small value obtained in these estimates, but the predicted change at the switching fields is far too small to account for the observed shifts of 1 mV. We note that also the quali-

tative curve shape observed in the experiments does not follow the triangular characteristics of the MCE at the switching fields [cf. Fig. 9.5(c)].

A quite natural explanation of our experimental findings is an inversion of majority and minority spin carriers at the CNT interface to only one of the Py strips, and hence an effective sign change of this contact's transport spin polarization. Similar effects have been observed for magnetic tunnel junctions and are ascribed to the symmetry selection of the tunneling electrons (cf. Sec. 9.2.2) by the chemical bonds at the metal/CNT interface [305, 306]. Another possibility is an anti-ferromagnetically coupled contact area, e.g. due to an oxidized Py interface layer [338, 348] that is strongly coupled to the bulk, effectively introducing a spin-filter effect [307]. Here, the coupling of the interface layer to the bulk could depend on the thickness of the oxide and explain why the two contacts of different widths are not coupled identically to the CNT, a phenomenon well known from non-magnetic metal contacts to CNTs. This scenario would explain the sign reversal of the MR gate modulation and offset, but not the peak shifts at the switching fields which are possibly due to random potential fluctuations triggered by magnetization reversal. Even if this is not shown and substantiated in great detail, we note also that Cottet *et al.* mention in a side remark of Ref. [325] that negative MR could occur in their model (interacting case, without SDIPS) for an enhanced spin polarization. While certainly further theoretical and experimental efforts are required for an improved understanding of the observed negative MR, we remark that negative MR has also occasionally been found for graphene spin-valves and is explained with similar mechanisms as discussed above [349–352].

11.3. Conclusions and outlook

In conclusion, we generally find a better electrical stability, improved yields of electrical contacts and more reproducible magnetoresistance signals in CNT QD spin-valves fabricated by optimized EBL and sputtered Py contacts. While the optimized fabrication techniques and detailed characterization of nanoscale Py contacts certainly lead to improved device characteristics, allowing to observe some of the most stable magnetoresistance signals with reproducible switching characteristics in CNT QD spin-valves reported so far, we note that also these devices still show gate voltage shifts of the conductance features that are possibly due to external potential fluctuations. Three-dimensional magnetoconductance maps $G(V_{\mathrm{BG}}, \mu_0 H)$ allowed to track the origin of the observed magnetoresistance, with major contributions stemming from these shifts in the conductance features. From the observed magnitude of the signals and a discussion of several mechanisms specific to nanospintronic devices we exclude other effects like the magneto-Coulomb effect or anisotropic magnetoresistance in the contacts as source of the observed signals, and tentatively conclude that

interface properties might be crucial to explain the presented magnetoresistance characteristics. The consistently observed negative magnetoresistance offset stands however in contradiction to existing theories and experiments. Due to this still incoherent picture of spin transport in CNT QD spin-valves and the not yet reproducible enough device characteristics, we hence also conclude that ferromagnetic contacts connected to CNT QDs are not yet suited as detectors of electron spin entanglement [38–40].

The reported results point to the insufficient control over the CNT-metal interface as main issue, a problem persisting in CNT devices from early on. To improve this aspect and significantly advance the field of spin transport through CNT QDs, novel experimental ideas and techniques are hence required, also to provide a deepened understanding of spin transport in these devices. One approach to achieve a better control over the CNT-metal interface and the associated tunnel barriers is to implement atomically thin tunnel barriers such as hexagonal boron nitride at the interface, an idea currently pursued in our group and also demonstrating great promise for longer spin-life times in graphene spin-valves [121, 353, 354]. Alternatively, one could merge ultra-clean fabrication techniques for CNT devices with ferromagnetic contacts in a spin-valve device geometry, a technique we will discuss intensively in the next chapter. The possible tunability of the QD tunnel coupling strengths in these devices could ultimately provide the necessary prerequisite for a Hanle experiment [110] similar to graphene spin-valve devices [135, 354], offering useful and required insights into spin transport and relaxation mechanisms in CNT QD spin-valves. In such an experiment, an external magnetic field $H_\perp$ is applied perpendicular to the leads magnetization direction or easy axis, causing a precession of the quantum-dot spins about the external field, which gives rise to a characteristic transport signature [110]. For the devices reported here, a Hanle experiment is of limited use due to the large tunnel coupling strengths $\Gamma \sim 2\,\mathrm{meV}$ and associated short electron lifetimes $\tau_\mathrm{el} \sim \hbar/\Gamma \approx 3 \times 10^{-13}\,\mathrm{s}$ on the QD. A simple estimate shows that a magnetic field of $\mu_0 H_\perp = \pi\Gamma/g\mu_\mathrm{B} \approx 54\,\mathrm{T}$ would be required for an electrical signal associated with a spin precession of $\omega_\mathrm{L}\tau_\mathrm{el} = \pi$, where we used the Larmor frequency $\omega_\mathrm{L} = g\mu_\mathrm{B}\mu_0 H_\perp/\hbar$ with the Bohr magneton μ_B and an electron g-factor $g = 2$. This magnetic field scale is of course inaccessible and not compatible with the rotation of the Py strips magnetization direction out of plane already at fields of $\mu_0 H_\perp \sim 1\,\mathrm{T}$, as shown in Fig. 10.2(a). Hence, much longer electron lifetimes on the QD are required to provide a reasonable parameter range for the proposed experiment. Very recently two conceptionally similar experiments, relying both on a non-collinear spin-valve geometry, and for one additionally on a artificially engineered spin-orbit interaction in a double QD and a microwave cavity read-out [310], claimed an out-of-equilibrium spin precession and a mostly contact-induced spin relaxation [355], and a promising lower bound of $\sim 60\,\mathrm{ns}$ for the intrinsic spin decoherence time in CNTs [340].

12

Towards ultra-clean, tunable CNT spin-valve devices with gate-defined QDs

We have seen in the previous chapter, that tunnel barriers and the ferromagnet-CNT interface play a key role in CNT spin-valve devices and might also be responsible for the observed negative MR. A high electrical stability of CNT QD spin-valve devices is a crucial prerequisite for any reliable and reproducible MR experiment [114], also to implement ferromagnetic contacts in entanglement detection schemes [38–40]. As already introduced in Sec. 2.2, one approach to improve CNT spin-valve device characteristics with respect to the above points and allowing fundamental investigations of spin transport is to integrate CNT spin-valve structures in ultra-clean fabrication approaches. Apart from using pristine CNTs, these schemes most importantly employ an elaborate gating scheme to electro-statically define QDs, in contrast to contact-defined QDs. Previous experiments with normal metal contacts have already demonstrated unprecedented quality, improved electrical stability and robustness of gate-defined CNT QDs, permitting to tune tunnel-couplings from the open Fabry-Perot regime to the few-electron QD regime [101, 102]. A combination of these benefits with a CNT spin-valve structure would hence allow to investigate spin-transport in electrically stable devices with tunable tunnel-barriers, shedding more light on previously discussed issues and leading to a deeper understanding of spin-transport in CNT QDs. Such devices could ultimately permit a 'smoking-gun' Hanle-type experiment [110], proving spin transport through a CNT QD by tuning the tunnel barriers to the required transport regime.

As already discussed extensively in Chap. 2, it is however quite challenging

to integrate ferromagnetic contacts in such ultra-clean processing schemes. This chapter is hence intended as an outlook, summarizes the results of our first attempts to combine ultra-clean processing schemes with F contacts, and gives an overview of the challenges and prospects one is facing. We start by discussing the results obtained with the more conventional device fabrication scheme employing partially suspended CNTs and recessed Re bottomgates (cf. Sec. 2.2.3), before we summarize our study on fork stamping of CNTs onto spin-valve structures (cf. Sec. 2.2.4). Section 12.3 gives a brief conclusion and lists possible changes and improvements.

12.1. Spin-valve structures with semi-suspended CNTs and recessed Re bottomgates

We briefly review transport measurements on spin-valve structures with semi-suspended CNTs and recessed Re bottomgates, fabricated as discussed in Sec. 2.2.3. A schematic and an example of such a spin-valve device with thermally evaporated Py contacts is depicted in Fig. 2.9. The semi-suspended CNT can be tuned by a backgate (BG) and additionally by a recessed Re bottomgate (Bot), and the devices are studied in the measurement set-up of Fig. 11.1(a). AMR measurements allow to determine the expected switching fields of the electrodes, and similar yields of low-ohmic contacts than for conventionally fabricated samples enabled us to study a number of devices. For an easier lift-off process, we only employed devices with thermally evaporated Py electrodes, due to the slightly disturbed resist mask profiles in the vicinity of the Re trenches. Hence, for ease of fabrication, the Py contacts are also placed at a distance $d \sim 100\,\mathrm{nm}$ away from the trench in the SiO_2 as depicted in Fig. 2.9(b), so that the CNT is only semi-suspended and a part of it still resides on substrate. According to Ref. [102], this should allow to electrostatically define a QD in the suspended CNT part by the bottomgate as illustrated in Sec. 2.2.3, even if it is *a priori* at least questionable how efficient spin injection would work from the ferromagnet via the piece of 'CNT lead' on substrate into the suspended CNT QD in this device scheme.

We nevertheless tested this approach, and studied 8 promising devices (out of ~ 60 successfully fabricated samples in this scheme) at low temperatures of $T \sim 1.5\,\mathrm{K}$. Data of two typical devices A and B is shown in Fig. 12.1. All of the 8 studied devices fulfilled the prerequisite of semi-conducting or narrow band-gap CNT characteristics at RT as exemplary shown in Fig. 12.1(a), and had a RT resistance in the 'ON'-state of the CNT transistor of $R_{\mathrm{RT}} < 1\,\mathrm{M\Omega}$. For devices with broad, $w \gtrsim 120\,\mathrm{nm}$ wide bottomgates, it was impossible to form a QD electro-statically. This is possibly due to the employed rather broad and distant gates, leading to relatively small lever arms and a rather smooth than sharp confinement potential in the p-n-junctions. Still, often

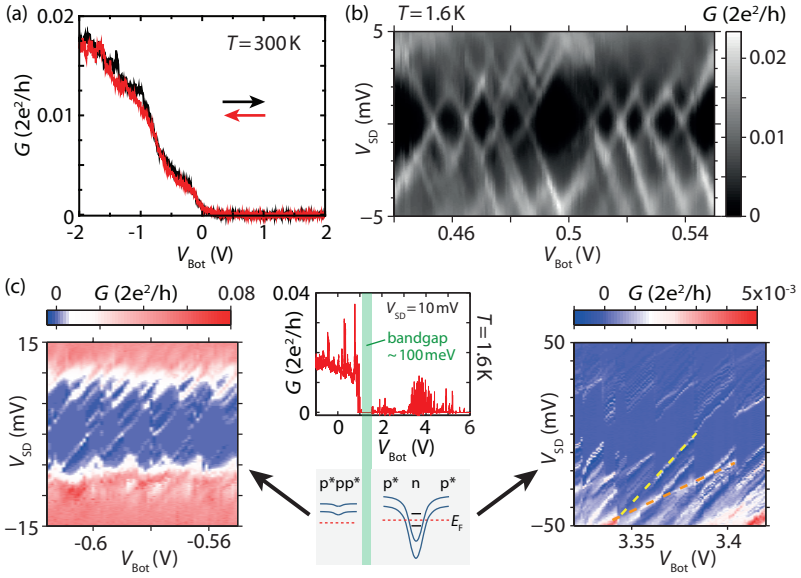

Figure 12.1.: (a) Typical $G(V_{\mathrm{Bot}})$ trace of a p-type semiconducting CNT (device A) recorded at RT and in vacuum. (b) Charge stability diagram $G(V_{\mathrm{SD}}, V_{\mathrm{Bot}})$ of a small bandgap CNT (device B) obtained at $V_{\mathrm{BG}} = -8.7\,\mathrm{V}$. (c) Left, right: $G(V_{\mathrm{SD}}, V_{\mathrm{Bot}})$ maps at $V_{\mathrm{BG}} = -10\,\mathrm{V}$ in different device transport regimes of device A. The middle panel illustrates these different regimes separated by a $\sim 100\,\mathrm{meV}$ bandgap in a conductance trace obtained at $V_{\mathrm{BG}} = -10\,\mathrm{V}$ and a bias voltage of $V_{\mathrm{SD}} = 10\,\mathrm{mV}$. One observes single-dot features in the p*pp* regime (left), and multi-dot characteristics (orange/yellow dashed line) in the p*np* region (right).

quite regular Coulomb blockade (CB) diamonds with a four-fold shell filling pattern were found as for device B in Fig. 12.1(b), suggesting clean CNTs. The small observed charging energies and level spacings, in this case $\sim 1.1\,\mathrm{meV}$ and $\sim 1.7\,\mathrm{meV}$, respectively, indicate a QD formed by the contact barriers, and not by the gate. For devices with more narrow, $\lesssim 80\,\mathrm{nm}$ wide bottomgates, achieved e.g. by cold development as discussed in Sec. 2.2.3, we observed clear indications of gate-defined QDs. Figure 12.1(c) illustrates this for device A with the corresponding RT conductance trace plotted in Fig. 12.1(a). The conductance curve in the middle panel, plotted as a function of the bottomgate voltage V_{Bot} at a fixed $V_{\mathrm{BG}} = -10\,\mathrm{V}$ and bias $V_{\mathrm{SD}} = 10\,\mathrm{mV}$, demonstrates that one can smoothly tune the device from a p*-p-p* doping across a bandgap of $\sim 100\,\mathrm{meV}$ to a p*-n-p* junction with the bottomgate. Here, p* (p/n) denotes the doping of the CNT part on substrate (suspended CNT part), with respect to the Fermi energy E_{F}. While one recognizes CB diamonds with four-fold

symmetry and charging energies of $\sim 4\,\mathrm{meV}$ typical for a single QD in the p*-p-p* region (left panel), the CB diamond pattern in the p*-n-p* regime (right panel) becomes more complex and changes significantly, with increased charging energies of $\sim 25\,\mathrm{meV}$ (up to $\sim 55\,\mathrm{meV}$, depending on the region). This clearly corroborates a smaller, gate-defined QD. One notes however lines of significantly different slopes (yellow and orange dashed line) in the charge stability diagram on the right, indicative of multiple dots or resonances in the CNT leads. This is most likely due to a too weak coupling of the Py contacts to the CNT leads, i.e. we also observe clear QD characteristics in the p*-p-p* regime (probably contact-defined), whereas in Ref. [102] for normal metal contacts Fabry-Perot resonances or an open regime were observed in this p*-p-p* regime. Unfortunately, similar multi-dot features appeared for all studied devices, rendering stable and reproducible MR experiments and signals in the desired regime difficult. We note that the devices studied here had RT resistances down to $\sim 100\,\mathrm{k\Omega}$, still much larger than the quantum resistance $h/e^2 \sim 25.8\,\mathrm{k\Omega}$, so that residual QDs could still form in the leads due to the contact tunnel barriers. Hence, we conclude that we did not achieve sufficiently well-coupled, transparent enough Py contacts to the CNT yet. Generally, these symmetrically well-coupled Py contacts seem necessary to obtain a single bottomgate-defined QD, the major prerequisite for reproducible MR experiments in this device scheme.

12.2. Spin-valve devices with fork-stamped pristine CNTs[1]

In this section, we discuss transport measurements on spin-valve devices, where a pristine CNT is stamped last onto predefined ferromagnetic contacts. The fabrication of these devices was already introduced in Sec. 2.2.4, and Fig. 12.2(b) shows a device schematic and the used measurement set-up. In total, we studied ~ 15 of these devices at low temperatures, that showed all a more or less similar characteristics.

12.2.1. Electrical characterization

The already wire-bonded CNT devices are built into a cryogenic variable temperature insert allowing measurements in the range of $T = 1.5 - 300\,\mathrm{K}$. As discussed previously in Sec. 2.2.4, samples usually degrade and have a relatively high resistance compared to the values directly after CNT transfer. To measure a signal at low temperatures, the devices have first to be annealed in the cryostat at room temperature and in low-pressure He atmosphere at $p \sim 5\,\mathrm{mbar}$. Fig. 12.2(a) shows the electrical circuit for annealing and a typical 'annealing trace'. A DC voltage V_{appl} is applied over an external resistor

[1] Parts of this chapter have been published in similar form in Ref. [130].

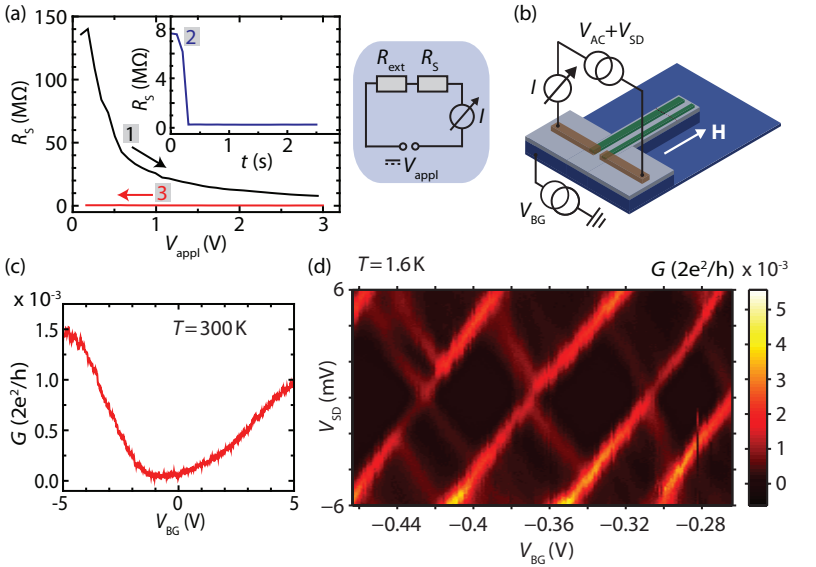

Figure 12.2.: (a) Typical contact annealing trace of a stamped CNT device with Py contacts, recorded at RT in low-pressure He-atmosphere with the annealing circuit depicted on the right. The sample resistance R_S is plotted as a function of the voltage V_{appl} applied over the sample and a pre-resistor $R_{ext} = 100\,k\Omega$ for the up- (1) and downsweep (3). The inset shows the waiting trace (2) at $V_{appl} = 3\,V$. (b) Measurement scheme for electrical measurements. (c) $G(V_{BG})$ trace for an annealed device at RT. (d) $G(V_{BG}, V_{SD})$ map for an annealed device at $T = 1.6\,K$.

R_{ext} in series with the sample R_S, measuring the current, from which R_S can be calculated. A typical annealing cycle consists of ramping the voltage up to some predefined value V_{max} (black trace 1), a waiting trace at V_{max} for a given time (blue trace 2) and the backtrace (red curve 3). This is repeated several times with increasing V_{max} until a device resistance change to reasonable values in the $< 1\,M\Omega$ range is observed. Figure 12.2(a) shows the traces of a successful annealing, with a large device resistance at the start and a final device resistance of $R_S = 250\,k\Omega$ originating from the abrupt change in the waiting trace (2) at $V_{max} = 3\,V$ (inset). In contrast to the current annealing usually applied for suspended graphene devices where the cleaning and device changes are ascribed to Joule heating [356], it is evident that such large resistance changes can only be caused by the contact resistance, showing that the annealing is actually not only cleaning the CNT, but changes mainly the contact resistance. We note that the currents through the device prior to the resistance change are in the sub-μA regime. These characteristics are similar

for most samples with device resistance changes often occurring after a certain waiting time at $V_{\max}$ and agree very well with previous findings on surface-oxidized Pd/PdO contacts to CNTs [357]. We speculate that a large voltage portion drops across the contact interfaces, leading to an irreversible dielectric breakdown in the oxide barrier on the Py surface, possibly creating permanent percolation paths to the CNT [357, 358]. This results in a low impedance CNT device with relatively transparent contacts. For further electrical characterization, we use the set-up depicted in Fig. 12.2(b) to measure the differential conductance G. To characterize the metallic or semiconducting nature of the stamped CNT, G is measured at RT as a function of the backgate voltage V_{BG}, seen in Fig. 12.2(c) for a semiconducting CNT. Figure 12.2(d) shows the charge stability diagram $G(V_{\mathrm{BG}}, V_{\mathrm{SD}})$ of such a device at $T = 1.6\,\mathrm{K}$. Clear CB diamonds are visible, indicating that a single QD forms in the CNT suspended over the two source-drain (SD) contacts. From the measurements, we can extract a backgate leverarm of $\eta \sim 0.082\,\mathrm{eV/V}$ only slightly smaller than for CNTs on substrate, a charging energy $E_{\mathrm{c}} \sim 4\,\mathrm{meV}$ and from the excited states a level spacing of $\delta E = 1.9\,\mathrm{meV}$. From the extracted level spacing, we can roughly estimate an effective QD size of $L = 1\,\mu\mathrm{m}/\delta E\,(\mathrm{meV}) = 0.52\,\mu\mathrm{m}$ [50], in reasonable agreement with the designed contact pitch and center-to-center separation of 400 nm, respectively 670 nm.

12.2.2. Magnetoresistance

We perform local magnetoresistance measurements at $T = 1.6\,\mathrm{K}$ in a standard QD spin-valve geometry as discussed earlier. Following Chap. 10, to characterize the quality of the ferromagnetic Py strips after processing and RIE etching, we first measure the AMR of individual strips with the sample geometry and measurement set-up depicted in Fig. 12.3(a). Here, the 35 μm long Py strips reside on a mesa bridge structure surrounded by trenches in the SiO_2/Si on two sides only, enabling transport measurements through each strip separately. It is possible to transfer CNTs also on this structure by tilting the transfer forks. Figure 12.3(a) shows the AMR of a 160 (red/orange) and 380 nm (black/grey) wide Py strip for the external magnetic field $\mu_0 H$ applied parallel to the strip. Sharp resistance changes at $\mu_0 H_{\mathrm{S1}} = 21\,\mathrm{mT}$ (wide strip) and $\mu_0 H_{\mathrm{S2}} = 52\,\mathrm{mT}$ (narrow strip) are consistent with our previous characterization in Chap. 10, indicate a sign reversal of the magnetization, and confirm that the bulk behavior of the magnetization remains intact after processing and RIE etching. To assess the magnetoresistance (MR) through the CNT, we measure MR maps over a single CB conductance maximum [114], see Fig. 12.3(b). Here, the conductance G through the CNT is plotted as a function of the backgate voltage for the up-sweep of H (large arrow). For this peculiar device with 380 and 500 nm wide Py strips, we expect switching fields of $\mu_0 H_{\mathrm{S1}} = 12 - 15\,\mathrm{mT}$ and $\mu_0 H_{\mathrm{S2}} = 21\,\mathrm{mT}$, indicated by vertical arrows

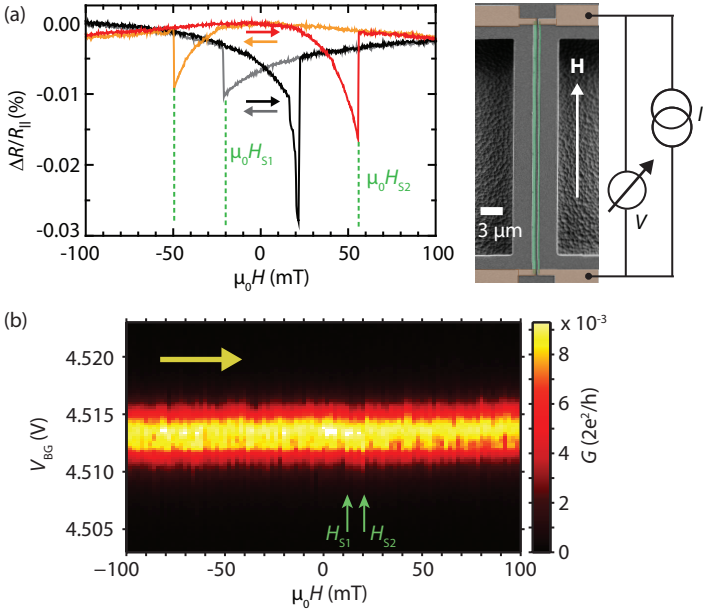

Figure 12.3.: (a) AMR of individual, 35 μm long, 160/380 nm wide (red and orange/black and grey curve) Py strips on a mesa structure. The right panel shows the measurement set-up and sample geometry with Py strips on a mesa bridge. (b) $G(\mu_0 H, V_{\mathrm{BG}})$ map at $V_{\mathrm{SD}} = 0$ of a stamped CNT device with H applied parallel to the Py strips. Small vertical arrows denote the expected switching fields $\mu_0 H_{\mathrm{S1}}$ and $\mu_0 H_{\mathrm{S2}}$ for this device, horizontal arrows in (a) and (b) the (color-coded) sweep direction of H.

in Fig. 12.3(b). A small change in amplitude and position of the CB conductance maximum might be visible at these positions, but the data remain inclusive for a reliable interpretation. We would expect a MR signal for the amplitude change alone of $MR = (G_{\mathrm{P}} - G_{\mathrm{AP}})/(G_{\mathrm{P}} + G_{\mathrm{AP}}) \sim 10\%$ for Py as discussed previously, not accounting for MR effects due to shifts of CB resonances, but the conductance noise of the device coming from both amplitude and position fluctuations of the CB resonances is on the same order of magnitude or larger. Further repetitions of up- and downsweeps on the same and other devices show similar features also with different switching fields. The conductance noise and instability of the devices, also apparent in the charge stability diagram of Fig. 12.2(d), are still too large to detect reliably any spin signals in the CNT spin-valves. We speculate that these fluctuations of the CB resonances are caused by instabilities in the contact interfaces. The annealing curves clearly show that the ferromagnetic contact interfaces are not

completely stable due to oxidation and might have inherent charge traps in the oxide, possibly close to the contact area.

12.3. Conclusions and prospects

While we have demonstrated some crucial steps towards integrating ferromagnetic contacts in ultra-clean processing schemes, significant challenges remain and demand further research. Nevertheless, the presented fabrication schemes could be beneficial in combining ultra-clean QD systems with hybrid-CNT devices, especially because both approaches can be readily extended to other contact materials, including complicated device layouts with several gates and superconducting as well as ferromagnetic electrodes.

For the first approach with semi-suspended CNTs and recessed bottomgates, the stringent requirement of highly transparent ferromagnetic contacts did not allow stable MR experiments in a single, electrostatically defined QD yet. Larger sample statistics should finally allow to obtain such a low-ohmic device. Further, the yield of low-ohmic devices and the contact coupling could possibly be improved by employing sputtered Py contacts [344], or using well-coupling diluted ferromagnetic alloys such as PdNi [315, 317] or PdFe [324], even if their magnetization reversal and domain structure is not ideal.

In the second approach, we report a fabrication scheme suited for the mechanical transfer of individual CNTs onto ferromagnetic contacts, leading to pristine, as-grown CNTs suspended over ferromagnetic electrodes in a spin-valve geometry. Using these recipes, we demonstrate that single CNTs can be contacted on top of ferromagnetic contacts with reasonable device resistances achieved by an electrical contact annealing, and that we are able to form single QDs suited for transport studies at low temperatures. No clear spin-valve signal could be found yet in magnetoresistance experiments at low temperatures, which we tentatively ascribe to interface properties resulting in an increased conductance noise. These current difficulties in magnetoresistance experiments could possibly be overcome by using an in-situ setup similar to the one used in Ref. [101], using less oxidizing ferromagnetic materials as e.g. PdNi alloys or implementing atomically thin, oxygen tight tunnel barriers [346] in-situ on top of the plasma cleaned ferromagnetic contacts prior to a CNT transfer. Hexagonal boron nitride (hBN), for example, holds great promise for longer spin-life times in bottom-up fabricated CNT spin-valve devices, an approach currently followed intensively for graphene spin-valves [121, 354].

PART III

CONCLUSIONS AND APPENDIX

13

Summary and outlook

In this thesis, we investigated carbon nanotube (CNT) quantum dot (QD) hybrid devices, in which a single CNT is coupled either to superconducting (S) and normal metal (N) electrodes or to ferromagnetic (F) contacts, by means of low-temperature transport spectroscopy experiments.

As a major technical prerequisite for the reported results, we systematically developed and optimized different fabrication approaches with the aim to improve (i) the device yield and quality, and (ii) the for experiments with S or F contacts especially relevant CNT-metal interface cleanliness. To this end, an essentially residue-free e-beam lithography (EBL) based on ZEP resist proved particularly useful.

Using such fabrication techniques, we first studied CNT QDs coupled to one S and either one or two N contacts in a two- or three-terminal device geometry. These devices are characterized by the QD life-time broadening Γ, the coupling strengths Γ_S (Γ_N) of the S (N) contacts to the QD, the charging energy E_C of the QD, and the superconducting energy gap Δ. Due to the improved interface quality, optimized Pb- or Nb-based S contacts enabled us to reliably obtain large and "clean" superconducting transport gaps of $\Delta \sim 1\,\mathrm{meV}$ in S-QD devices also for varying Γ_S, with satisfying characteristics of the S contacts for transport spectroscopy experiments. The achievable large gaps pose a major advantage for the future study of S-QD hybrid devices, particularly due to the straight-forward adaption of the fabrication scheme to other low-dimensional material systems. Our experiments suggest that we simply probe the gap of the metallic S contacts, and hence also contribute to the recent discussion about "hard gaps"/"soft gaps" and the superconducting proximity effect in mesoscopic QD or nanowire structures [227, 243–245]. Due to the enhanced

spectroscopic resolution for subgap bias voltages, i.e. $\Gamma \ll \Delta$, we could analyze novel subgap transport phenomena. Depending on the coupling Γ_S and the other relevant energy scales, we investigated N-QD-S devices in three very distinct regimes, where different transport mechanisms dominate.

For devices with weak couplings Γ_S, the conductance was dominated by quasiparticle transport only, which allowed us to demonstrate the impact of Δ on the Coulomb blockade diamond structure. Additionally occurring transport resonances at bias voltages below Δ are either due to the thermal excitation of quasiparticles in S for temperatures $kT \sim \Delta$, or due to the peculiar three-terminal QD geometry and the extra transport channel between the two N contacts. In such a three-terminal device, a floating N contact also generates extra subgap transport resonances, potentially useful to unravel higher-order subgap transport processes [226].

For a device with an intermediate coupling Γ_S, i.e. $\Gamma_N \lesssim \Gamma_S < \Delta \ll E_C$, we could for the first time spectroscopically identify resonant (elastic) and inelastic Andreev tunneling (AT) on a QD. This fundamental sequential transport process provides the so far missing analogies to the Andreev reflection in metallic N-S structures and to the multiple Andreev reflections found in S-QD-S devices [359], and accounts for a competing local transport channel in Cooper pair splitter (CPS) devices [19, 33]. While a 'smearing' of the observed discrete resonances might also be an alternative origin of "soft gaps" in superconductor nanostructures, devices with a more controlled coupling to engineered bosonic environments could shed more light on the nature of the observed inelastic processes. For example, the CNT stamping technique investigated in this thesis gives access to well-controlled phonons [48] in suspended CNTs coupled to S electrodes, or a radio frequency cavity coupled to the S-QD system might provide discrete electromagnetic modes [104]. Such engineered hybrid quantum devices pave the way for future experiments, and are predicted to generate also inelastic replicas of Andreev bound states (ABS) [264], or to allow the ground state cooling of a suspended CNT mechanical resonator by means of inelastic AT [360].

In devices with a sufficiently strong coupling $\Gamma_S \sim \Delta$, we investigated transport through ABS. Our peculiar three-terminal QD geometry enabled us to identify the finite coupling to the N contacts as main source for the broadening of the Andreev resonances (AR), and to ascribe 'excited' AR to the detailed energy level spectrum of the QD. Peculiar sign changes in the conductance through Andreev resonances between two N contacts allow us to qualitatively probe the gate-evolution of the ABS' Bogoliubov-de-Gennes amplitudes, and to identify the competition between the direct transport of a single electron through the AR ("resonant ABS tunneling") and the non-local creation of a Cooper pair in S (or a CPS process) as origin of the sign changes. Our experiments with a floating S contact constitute a novel experimental probe for the superconducting proximity effect in S-QD systems, and potentially probe

the strength of the coupling between S and the QD. Recently, such a single QD system coupled to one S and two N terminals has also been the subject of intriguing proposals, which predict very similar non-local transport signatures [177, 200].

Since we obtained mostly a single QD object in our Pb-based three-terminal devices, we also proposed and already demonstrated some first steps to reproducibly implement a double QD (DQD) in such large-gap CPS devices. Such devices still open a wide range of experimental prospects: While the large gaps are beneficial to gain a deeper understanding of Cooper pair splitting (CPS) and its relation to competing subgap transport mechanisms [19, 33, 216], it was recently suggested that a supercurrent through S with a momentum component parallel to the CNT could enhance the CPS efficiency [271]. With the large critical current densities of the Pb contacts, this might prove a valuable asset to reliably achieve the high CPS efficiencies needed for entanglement detection proposals. One of the most promising proposals to implement such a so far missing Bell test in CPS devices employs different spin quantization axes in the two QDs due to the spin-orbit interaction in a bent CNT and an external magnetic field, to allow for non-collinear spin projection measurements [113]. In contrast to the optimal operating regime for CPS discussed so far, a strong coupling of the two QDs to S and only a weak coupling to the N contacts enables to study an even richer interplay of local (ABS) and non-local transport (CPS) channels. The non-local CPS mixes the ABS of each individual QD, so that a new molecular state or *Andreev molecule* could form. Such DQD systems are currently investigated intensively [41, 207], and researchers constantly propose new ideas, such as "poor man's Majorana bound states" [361], to couple spin qubits non-locally via a superconductor [212], or to exploit a triplet blockade [202].

In a much wider context, our study of the N-QD-S model system also contributes to the continuing progress to understand subgap transport in superconductor hybrid devices, relevant also in the current quest to reveal and manipulate solid-state versions of Majorana fermions [10, 12, 13] with a potential use in topological quantum computation schemes [14]. Similar superconductor-semiconductor hybrid devices have recently also been implemented in superconducting qubits or "gatemons", where a gate-tunable nanowire provided the weak link in a Josephson junction [17, 18]. For future experiments in such superconductor hybrid devices, also the investigated three- or multi-terminal device geometry might prove extremely valuable. This geometry allows to unambiguously determine all contact tunnel couplings, and could hence also give further insight into proximity-induced gaps in low-dimensional material systems with the help of a weakly coupled "density of states (DOS)" probe, while simultaneously studying subgap transport with another probe.

In a second part of this thesis, we studied CNT QDs coupled to two ferromagnetic contacts in a spin-valve device geometry, also to analyze the suitabil-

ity of ferromagnetic leads as detectors of electron spin entanglement in CPS devices [38–41]. With an optimized fabrication and characterization scheme, we obtained more reproducible magnetoresistance (MR) signals in these devices. Nevertheless, the consistently observed MR modulation on a *negative* MR offset stands in contrast to previous findings and orthodox theories of spin transport through QD devices, and is most likely due to the CNT-metal interface properties. Due to this still incoherent picture of spin transport in CNT QD spin-valves and the still not reproducible enough device characteristics, further optimization and experiments are needed to be able to employ ferromagnetic contacts for entanglement detection purposes, or other complex applications.

To overcome these challenges, we proposed to integrate the ferromagnetic contacts in ultra-clean processing schemes, and demonstrated some crucial first steps to achieve this challenging goal. A combination of these schemes with a CNT spin-valve structure possibly allows to investigate spin-transport in electrically stable devices with tunable tunnel barriers, to perform Hanle-type experiments on a QD [110, 355], or to achieve the ground-state cooling of a suspended CNT mechanical resonator with spin-polarized currents [112].

Finally, using such novel fabrication schemes, and further technical advancements to the ones discussed here, a combination of both superconducting and ferromagnetic contacts would further enrich the various experimental possibilities in future hybrid QD devices [40, 41, 200, 329]. Here, particularly the exchange fields induced on the QD by strongly coupled ferromagnetic contacts might prove very useful [328–330], to enable a spin-resolved analysis of subgap transport [41], or for spin correlation studies [40, 329]. Altogether, the investigated QD hybrid devices with superconducting, ferromagnetic and normal metal contacts still provide a major playground to explore fundamental physics, or to come yet another step closer to applications of these devices in quantum technology.

Bibliography

[1] M. Mitchell Waldrop, Nature News **530**, 144 (2016).

[2] D. Loss and D. P. DiVincenzo, Phys. Rev. A **57**, 120 (1998).

[3] D. P. DiVincenzo, Fortschritte der Physik **48**, 771 (2000).

[4] M. Nielsen and I. Chuang, *Quantum Computation and Quantum Information*, 10th ed. (Cambridge University Press, 2010).

[5] M. W. Johnson *et al.*, Nature **473**, 194 (2011).

[6] T. Lanting *et al.*, Phys. Rev. X **4**, 021041 (2014).

[7] L. P. Kouwenhoven, C. M. Marcus, P. L. McEuen, S. Tarucha, R. M. Westervelt, and N. S. Wingreen, *Mesoscopic Electron Transport* (Springer Netherlands, Dordrecht, 1997) Chap. Electron Transport in Quantum Dots, pp. 105–214.

[8] L. P. Kouwenhoven, D. G. Austing, and S. Tarucha, Rep. Prog. Phys. **64**, 701 (2001).

[9] S. De Franceschi, L. Kouwenhoven, C. Schönenberger, and W. Wernsdorfer, Nat. Nanotechnol. **5**, 703 (2010).

[10] V. Mourik, K. Zuo, S. M. Frolov, S. R. Plissard, E. P. A. M. Bakkers, and L. P. Kouwenhoven, Science **336**, 1003 (2012).

[11] A. Das, Y. Ronen, Y. Most, Y. Oreg, M. Heiblum, and H. Shtrikman, Nat. Phys. **8**, 887 (2012).

[12] S. Nadj-Perge, I. K. Drozdov, J. Li, H. Chen, S. Jeon, J. Seo, A. H. MacDonald, B. A. Bernevig, and A. Yazdani, Science **346**, 602 (2014).

[13] T. D. Stanescu and S. Tewari, J. Phys. Condens. Matter **25**, 233201 (2013).

[14] S. Das Sarma, M. Freedman, and C. Nayak, NPJ Quantum Information **1**, 15001 (2015).

[15] C. Janvier, L. Tosi, L. Bretheau, Ç. Ö. Girit, M. Stern, P. Bertet, P. Joyez, D. Vion, D. Esteve, M. F. Goffman, H. Pothier, and C. Urbina, Science **349**, 1199 (2015).

[16] A. Zazunov, V. S. Shumeiko, E. N. Bratus', J. Lantz, and G. Wendin, Phys. Rev. Lett. **90**, 087003 (2003).

[17] T. W. Larsen, K. D. Petersson, F. Kuemmeth, T. S. Jespersen, P. Krogstrup, J. Nygård, and C. M. Marcus, Phys. Rev. Lett. **115**, 127001 (2015).

[18] G. de Lange, B. van Heck, A. Bruno, D. J. van Woerkom, A. Geresdi, S. R. Plissard, E. P. A. M. Bakkers, A. R. Akhmerov, and L. DiCarlo, Phys. Rev. Lett. **115**, 127002 (2015).

[19] P. Recher, E. V. Sukhorukov, and D. Loss, Phys. Rev. B **63**, 165314 (2001).

[20] L. Hofstetter, S. Csonka, J. Nygård, and C. Schönenberger, Nature **461**, 960 (2009).

[21] L. G. Herrmann, F. Portier, P. Roche, A. Levy Yeyati, T. Kontos, and C. Strunk, Phys. Rev. Lett. **104**, 026801 (2010).

[22] G. A. Prinz, Phys. Today **48**, 58 (1995).

[23] G. A. Prinz, Science **282**, 1660 (1998).

[24] A. Fert, Rev. Mod. Phys. **80**, 1517 (2007).

[25] S. A. Wolf, D. D. Awschalom, R. A. Buhrman, J. M. Daughton, S. von Molnár, M. L. Roukes, A. Y. Chtchelkanova, and D. M. Treger, Science **294**, 1488 (2001).

[26] C. Chappert, A. Fert, and F. N. Van Dau, Nat. Mater. **6**, 813 (2007).

[27] S. Sahoo, T. Kontos, J. Furer, C. Hoffmann, M. Gräber, A. Cottet, and C. Schönenberger, Nat. Phys. **1**, 99 (2005).

[28] C. Schönenberger, Semicond. Sci. Technol. **21**, S1 (2006).

[29] A. Cottet, T. Kontos, S. Sahoo, H. T. Man, M.-S. Choi, W. Belzig, C. Bruder, A. F. Morpurgo, and C. Schönenberger, Semicond. Sci. Technol. **21**, S78 (2006).

[30] M. R. Gräber, T. Nussbaumer, W. Belzig, and C. Schönenberger, Nanotechnology **15**, S479 (2004).

[31] R. S. Deacon, Y. Tanaka, A. Oiwa, R. Sakano, K. Yoshida, K. Shibata, K. Hirakawa, and S. Tarucha, Phys. Rev. Lett. **104**, 076805 (2010).

[32] A. Das, Y. Ronen, M. Heiblum, D. Mahalu, A. V. Kretinin, and H. Shtrikman, Nat. Commun. **3**, 1165 (2012).

[33] J. Schindele, A. Baumgartner, and C. Schönenberger, Phys. Rev. Lett. **109**, 157002 (2012).

[34] R. Leturcq, D. Graf, T. Ihn, K. Ensslin, D. D. Driscoll, and A. C. Gossard, Europhys. Lett. **67**, 439 (2004).

[35] K. Tsukagoshi, B. W. Alphenaar, and H. Ago, Nature **401**, 572 (1999).

[36] H. Aurich, A. Baumgartner, F. Freitag, A. Eichler, J. Trbovic, and C. Schönenberger, Appl. Phys. Lett. **97**, 153116 (2010).

[37] A. Jensen, J. R. Hauptmann, J. Nygård, and P. E. Lindelof, Phys. Rev. B **72**, 035419 (2005).

[38] S. Kawabata, J. Phys. Soc. Jap. **70**, 1210 (2001).

[39] W. Kłobus, A. Grudka, A. Baumgartner, D. Tomaszewski, C. Schönenberger, and J. Martinek, Phys. Rev. B **89**, 125404 (2014).

[40] O. Malkoc, C. Bergenfeldt, and P. Samuelsson, Europhys. Lett. **105**, 47013 (2014).

[41] P. Trocha and I. Weymann, Phys. Rev. B **91**, 235424 (2015).

[42] R. Hanson, L. P. Kouwenhoven, J. R. Petta, S. Tarucha, and L. M. K. Vandersypen, Rev. Mod. Phys. **79**, 1217 (2007).

[43] S. Iijima, Nature **354**, 56 (1991).

[44] B. J. LeRoy, S. G. Lemay, J. Kong, and C. Dekker, Nature **432**, 371 (2004).

[45] S. Sapmaz, P. Jarillo-Herrero, Y. M. Blanter, C. Dekker, and H. S. J. van der Zant, Phys. Rev. Lett. **96**, 026801 (2006).

[46] R. Leturcq, C. Stampfer, K. Inderbitzin, L. Durrer, C. Hierold, E. Mariani, M. G. Schultz, F. von Oppen, and K. Ensslin, Nat. Phys. **5**, 327 (2009).

[47] A. K. Hüttel, G. A. Steele, B. Witkamp, M. Poot, L. P. Kouwenhoven, and H. S. J. van der Zant, Nano Lett. **9**, 2547 (2009).

[48] A. Benyamini, A. Hamo, S. V. Kusminskiy, F. von Oppen, and S. Ilani, Nat. Phys. **10**, 151 (2014).

[49] S. Ilani and P. L. McEuen, Annu. Rev. Condens. Matter Phys. **1**, 1 (2010).

[50] J. Nygård, D. H. Cobden, M. Bockrath, P. L. McEuen, and P. E. Lindelof, Appl. Phys. A **69**, 297 (1999).

[51] S. Sapmaz, P. Jarillo-Herrero, L. P. Kouwenhoven, and H. S. J. van der Zant, Semicond. Sci. Technol. **21**, S52 (2006).

[52] J.-C. Charlier, X. Blase, and S. Roche, Rev. Mod. Phys. **79**, 677 (2007).

[53] E. A. Laird, F. Kuemmeth, G. A. Steele, K. Grove-Rasmussen, J. Nygård, K. Flensberg, and L. P. Kouwenhoven, Rev. Mod. Phys. **87**, 703 (2015).

[54] C. Schönenberger, *Bandstructure of graphene and carbon nanotubes : An exercise in condensed matter physics*, Lecture notes (2000), online available: http://www.nanoelectronics.ch/education/Nanotubes/cnt.php.

[55] K. S. Novoselov, A. K. Geim, S. V. Morozov, D. Jiang, Y. Zhang, S. V. Dubonos, I. V. Grigorieva, and A. A. Firsov, Science **306**, 666 (2004).

[56] A. H. Castro Neto, F. Guinea, N. M. R. Peres, K. S. Novoselov, and A. K. Geim, Rev. Mod. Phys. **81**, 109 (2009).

[57] P. R. Wallace, Phys. Rev. **71**, 622 (1947).

[58] H. Aurich, *Carbon nanotube spin-valve with optimized ferromagnetic contacts*, Ph.D. thesis, University of Basel (2012).

[59] J. Svensson and E. E. B. Campbell, J. Appl. Phys. **110**, 111101 (2011).

[60] S. Heinze, J. Tersoff, R. Martel, V. Derycke, J. Appenzeller, and P. Avouris, Phys. Rev. Lett. **89**, 106801 (2002).

[61] A. Javey, J. Guo, Q. Wang, M. Lundstrom, and H. Dai, Nature **424**, 654 (2003).

[62] X. Cui, M. Freitag, R. Martel, L. Brus, and P. Avouris, Nano Lett. **3**, 783 (2003).

[63] L. Ding, S. Wang, Z. Zhang, Q. Zeng, Z. Wang, T. Pei, L. Yang, X. Liang, J. Shen, Q. Chen, R. Cui, Y. Li, and L.-M. Peng, Nano Lett. **9**, 4209 (2009).

[64] W. Kim, A. Javey, R. Tu, J. Cao, Q. Wang, and H. Dai, Appl. Phys. Lett. **87**, 173101 (2005).

[65] V. Vitale, A. Curioni, and W. Andreoni, J. Am. Chem. Soc. **130**, 5848 (2008).

[66] J. W. G. Wilder, L. C. Venema, A. G. Rinzler, R. E. Smalley, and C. Dekker, Nature **391**, 59 (1998).

[67] C. Zhou, J. Kong, and H. Dai, Phys. Rev. Lett. **84**, 5604 (2000).

[68] M. Ouyang, J.-L. Huang, C. L. Cheung, and C. M. Lieber, Science **292**, 702 (2001).

[69] V. V. Deshpande, B. Chandra, R. Caldwell, D. S. Novikov, J. Hone, and M. Bockrath, Science **323**, 106 (2009).

[70] J. Cao, Q. Wang, and H. Dai, Nat. Mater. **4**, 745 (2005).

[71] M. Rontani, Phys. Rev. B **90**, 195415 (2014).

[72] T. Ando, J. Phys. Soc. Jap. **69**, 1757 (2000).

[73] W. Izumida, K. Sato, and R. Saito, J. Phys. Soc. Jap. **78**, 074707 (2009).

[74] J. Klinovaja, M. J. Schmidt, B. Braunecker, and D. Loss, Phys. Rev. B **84**, 085452 (2011).

[75] F. Kuemmeth, S. Ilani, D. C. Ralph, and P. L. McEuen, Nature **452**, 448 (2008).

[76] T. S. Jespersen, K. Grove-Rasmussen, J. Paaske, K. Muraki, T. Fujisawa, J. Nygard, and K. Flensberg, Nat. Phys. **7**, 348 (2011).

[77] W. Liang, M. Bockrath, D. Bozovic, J. H. Hafner, M. Tinkham, and H. Park, Nature **411**, 665 (2001).

[78] J. Schindele, *Observation of Cooper Pair Splitting and Andreev Bound States in Carbon Nanotubes*, Ph.D. thesis, University of Basel (2014).

[79] T. Ihn, *Semiconductor Nanostructures: Quantum States and Electronic Transport* (Oxford University Press, 2010).

[80] C. W. J. Beenakker, Phys. Rev. B **44**, 1646 (1991).

[81] S. De Franceschi, S. Sasaki, J. M. Elzerman, W. G. van der Wiel, S. Tarucha, and L. P. Kouwenhoven, Phys. Rev. Lett. **86**, 878 (2001).

[82] T. Dirks, Y.-F. Chen, N. O. Birge, and N. Mason, Appl. Phys. Lett. **95**, 192103 (2009).

[83] M. Gaass, S. Pfaller, T. Geiger, A. Donarini, M. Grifoni, A. K. Hüttel, and C. Strunk, Phys. Rev. B **89**, 241405 (2014).

[84] C. C. Escott, F. A. Zwanenburg, and A. Morello, Nanotechnology **21**, 274018 (2010).

[85] G. A. Steele, A. K. Hüttel, B. Witkamp, M. Poot, H. B. Meerwaldt, L. P. Kouwenhoven, and H. S. J. van der Zant, Science **325**, 1103 (2009).

[86] W. G. van der Wiel, T. H. Oosterkamp, S. de Franceschi, C. J. P. M. Harmans, and L. P. Kouwenhoven, in *Strongly Correlated Fermions and Bosons in Low-Dimensional Disordered Systems*, NATO Science Series, Vol. 72, edited by I. V. Lerner, B. L. Althsuler, V. I. Fal'ko, and T. Giamarchi (Springer Netherlands, 2002) pp. 43–68.

[87] C. Meyer, J. M. Elzerman, and L. P. Kouwenhoven, Nano Lett. **7**, 295 (2007).

[88] J. Kong, H. T. Soh, A. M. Cassell, C. F. Quate, and H. Dai, Nature **395**, 878 (1998).

[89] J. Furer, *Growth of Single-Wall Carbon Nanotubes by Chemical Vapor Deposition for Electrical Devices*, Ph.D. thesis, University of Basel (2006).

[90] X. Li, X. Tu, S. Zaric, K. Welsher, W. S. Seo, W. Zhao, and H. Dai, J. Am. Chem. Soc. **129**, 15770 (2007).

[91] M. Burkhardt, *Carbon Nanotubes Blockcourse Report* (2008), unpublished.

[92] H. Dai, Acc. Chem. Res. **35**, 1035 (2002).

[93] B. Babić, J. Furer, M. Iqbal, and C. Schönenberger, AIP Conf. Proc. **723**, 574 (2004).

[94] M. A. Mohammad, M. Muhammad, S. Dew, and M. Stepanova, in *Nanofabrication*, edited by M. Stepanova and S. Dew (Springer Vienna, 2012) pp. 11–41.

[95] T. Brintlinger, Y.-F. Chen, T. Dürkop, E. Cobas, M. S. Fuhrer, J. D. Barry, and J. Melngailis, Appl. Phys. Lett. **81**, 2454 (2002).

[96] J. Lefebvre, D. G. Austing, J. Bond, and P. Finnie, Nano Lett. **6**, 1603 (2006).

[97] G. A. Steele, G. Gotz, and L. P. Kouwenhoven, Nat. Nanotechnol. **4**, 363 (2009).

[98] C. C. Wu, C. H. Liu, and Z. Zhong, Nano Lett. **10**, 1032 (2010).

[99] M. Muoth and C. Hierold, in *IEEE 25th International Conference on Micro Electro Mechanical Systems (MEMS), Paris* (IEEE, 2012) pp. 1352–1355.

[100] F. Pei, E. A. Laird, G. A. Steele, and L. P. Kouwenhoven, Nat. Nanotechnol. **7**, 630 (2012).

[101] J. Waissman, M. Honig, S. Pecker, A. Benyamini, A. Hamo, and S. Ilani, Nat. Nanotechnol. **8**, 569 (2013).

[102] M. Jung, J. Schindele, S. Nau, M. Weiss, A. Baumgartner, and C. Schönenberger, Nano Lett. **13**, 4522 (2013).

[103] J. J. Viennot, J. Palomo, and T. Kontos, Appl. Phys. Lett. **104**, 113108 (2014).

[104] V. Ranjan, G. Puebla-Hellmann, M. Jung, T. Hasler, A. Nunnenkamp, M. Muoth, C. Hierold, A. Wallraff, and C. Schönenberger, Nat. Commun. **6**, 7165 (2015).

[105] J. Cao, Q. Wang, M. Rolandi, and H. Dai, Phys. Rev. Lett. **93**, 216803 (2004).

[106] G. A. Steele, F. Pei, E. A. Laird, J. M. Jol, H. B. Meerwaldt, and L. P. Kouwenhoven, Nat. Commun. **4**, 1573 (2013).

[107] V. V. Deshpande and M. Bockrath, Nat. Phys. **4**, 314 (2008).

[108] S. Pecker, F. Kuemmeth, A. Secchi, M. Rontani, D. C. Ralph, P. L. McEuen, and S. Ilani, Nat. Phys. **9**, 576 (2013).

[109] E. A. Laird, F. Pei, and L. P. Kouwenhoven, Nat. Nanotechnol. **8**, 565 (2013).

[110] M. Braun, J. König, and J. Martinek, Europhys. Lett. **72**, 294 (2005).

[111] S.-N. Zhang, W. Pei, T.-F. Fang, and Q.-f. Sun, Phys. Rev. B **86**, 104513 (2012).

[112] P. Stadler, W. Belzig, and G. Rastelli, Phys. Rev. Lett. **113**, 047201 (2014).

[113] B. Braunecker, P. Burset, and A. Levy Yeyati, Phys. Rev. Lett. **111**, 136806 (2013).

[114] J. Samm, J. Gramich, A. Baumgartner, M. Weiss, and C. Schönenberger, J. Appl. Phys. **115**, 174309 (2014).

[115] I. Maximov, A. A. Zakharov, T. Holmqvist, L. Montelius, and I. Lindau, J. Vac. Sci. Technol. B **20**, 1139 (2002).

[116] D. S. Macintyre, O. Ignatova, S. Thoms, and I. G. Thayne, J. Vac. Sci. Technol. B **27**, 2597 (2009).

[117] Q. Hang, D. A. Hill, and G. H. Bernstein, J. Vac. Sci. Technol. B **21**, 91 (2003).

[118] W. W. Hu, K. Sarveswaran, M. Lieberman, and G. Bernstein, J. Vac. Sci. Technol. B **22**, 1711 (2004).

[119] J. S. Wi and K. B. Kim, Electron. Mater. Lett. **3**, 1 (2007).

[120] ZEON Corporation, Electronics Materials Division, *ZEP520A Technical Report* (2010), online available: https://www.zeonchemicals.com/pdfs/ZEP520A.pdf.

[121] W. Fu, P. Makk, R. Maurand, M. Bräuninger, and C. Schönenberger, J. Appl. Phys. **116**, 074306 (2014).

[122] A. Baumgartner, G. Abulizi, K. Watanabe, T. Taniguchi, J. Gramich, and C. Schönenberger, Appl. Phys. Lett. **105**, 023111 (2014).

[123] J.-N. Longchamp, C. Escher, and H.-W. Fink, ArXiv:1408.6114 (2014).

[124] C. Kanai, K. Watanabe, and Y. Takakuwa, Phys. Rev. B **63**, 235311 (2001).

[125] R. Yang, L. Zhang, Y. Wang, Z. Shi, D. Shi, H. Gao, E. Wang, and G. Zhang, Adv. Mat. **22**, 4014 (2010).

[126] L. Xie, L. Jiao, and H. Dai, J. Am. Chem. Soc. **132**, 14751 (2010).

[127] D. Hug, *Zigzag Edges in Graphene and Graphite Defined with a Cold Hydrogen Plasma*, Ph.D. thesis, University of Basel (2013).

[128] S. Zihlmann, *Hydrogen plasma etching of graphene*, Master's thesis, University of Basel (2013).

[129] G. Zhang, P. Qi, X. Wang, Y. Lu, D. Mann, X. Li, and H. Dai, J. Am. Chem. Soc. **128**, 6026 (2006).

[130] J. Gramich, A. Baumgartner, M. Muoth, C. Hierold, and C. Schönenberger, Phys. Status Solidi B **252**, 2496 (2015).

[131] M. Muoth, T. Helbling, L. Durrer, S.-W. Lee, C. Roman, and C. Hierold, Nat. Nanotechnol. **5**, 589 (2010).

[132] L. Durrer, J. Greenwald, T. Helbling, M. Muoth, R. Riek, and C. Hierold, Nanotechnology **20**, 355601 (2009).

[133] R. Legtenberg, H. Jansen, M. de Boer, and M. Elwenspoek, J. Electrochem. Soc. **142**, 2020 (1995).

[134] S. B. Kim and H. Jeon, J. Korean Phys. Soc. **49**, 1991 (2006).

[135] N. Tombros, C. Jozsa, M. Popinciuc, H. T. Jonkman, and B. J. van Wees, Nature **448**, 571 (2007).

[136] C. Enss and S. Hunklinger, *Low-Temperature Physics* (Springer, 2005).

[137] H. Bluhm and K. A. Moler, Rev. Sci. Instrum. **79**, 014703 (2008).

[138] M. Tinkham, *Introduction to Superconductivity*, 2nd ed. (Dover, 2004).

[139] H. Ibach and H. Lüth, *Festkörperphysik*, 7th ed. (Springer, 2008).

[140] J. Bardeen, L. N. Cooper, and J. R. Schrieffer, Phys. Rev. **108**, 1175 (1957).

[141] D. J. Thouless, Phys. Rev. **117**, 1256 (1960).

[142] D. H. Douglass Jr. and L. M. Falicov, in *The Superconducting Energy Gap*, Progress in Low Temperature Physics, Vol. 4, edited by C. Gorter (Elsevier, 1964) pp. 97 – 193.

[143] C. Beenakker, in *Quantum Mesoscopic Phenomena and Mesoscopic Devices in Microelectronics*, NATO Science Series, Vol. 559, edited by I. O. Kulik and R. Ellialtioğlu (Springer Netherlands, 2000) pp. 51–60.

[144] A. F. Andreev, Sov. Phys. JETP **19**, 1228 (1964).

[145] G. E. Blonder, M. Tinkham, and T. M. Klapwijk, Phys. Rev. B **25**, 4515 (1982).

[146] B. Pannetier and H. Courtois, J. Low Temp. Phys. **118**, 599 (2000).

[147] T. Klapwijk, J. Supercond. Nov. Magn. **17**, 593 (2004).

[148] D. Beckmann, H. B. Weber, and H. v. Löhneysen, Phys. Rev. Lett. **93**, 197003 (2004).

[149] S. Russo, M. Kroug, T. M. Klapwijk, and A. F. Morpurgo, Phys. Rev. Lett. **95**, 027002 (2005).

[150] A. Kleine, A. Baumgartner, J. Trbovic, and C. Schönenberger, Europhys. Lett. **87**, 27011 (2009).

[151] G. Falci, D. Feinberg, and F. W. J. Hekking, Europhys. Lett. **54**, 255 (2001).

[152] P. Joyez, *Probing the DOS in Proximity Systems*, Lecture notes Capri Spring School (2012), online available: http://tfp1.physik.uni-freiburg.de/Capri12/lectures.php.

[153] C. W. J. Beenakker, in *Transport Phenomena in Mesoscopic Systems*, Springer Series in Solid-State Sciences, Vol. 109, edited by H. Fukuyama and T. Ando (Springer, 1992) pp. 235–253.

[154] H. le Sueur, P. Joyez, H. Pothier, C. Urbina, and D. Esteve, Phys. Rev. Lett. **100**, 197002 (2008).

[155] A. Martín-Rodero and A. Levy Yeyati, *Advances in Physics*, Adv. Phys. **60**, 899 (2011).

[156] A. Y. Kasumov, R. Deblock, M. Kociak, B. Reulet, H. Bouchiat, I. I. Khodos, Y. B. Gorbatov, V. T. Volkov, C. Journet, and M. Burghard, Science **284**, 1508 (1999).

[157] Y. J. Doh, J. A. van Dam, A. L. Roest, E. Bakkers, L. P. Kouwenhoven, and S. De Franceschi, Science **309**, 272 (2005).

[158] P. Jarillo-Herrero, J. A. van Dam, and L. P. Kouwenhoven, Nature **439**, 953 (2006).

[159] J. A. van Dam, Y. V. Nazarov, E. P. A. M. Bakkers, S. de Franceschi, and L. P. Kouwenhoven, Nature **442**, 667 (2006).

[160] H. I. Jørgensen, T. Novotný, K. Grove-Rasmussen, K. Flensberg, and P. E. Lindelof, Nano Lett. **7**, 2441 (2007).

[161] A. Eichler, R. Deblock, M. Weiss, C. Karrasch, V. Meden, C. Schönenberger, and H. Bouchiat, Phys. Rev. B **79**, 161407 (2009).

[162] R. Maurand, T. Meng, E. Bonet, S. Florens, L. Marty, and W. Wernsdorfer, Phys. Rev. X **2**, 011009 (2012).

[163] R. Delagrange, D. J. Luitz, R. Weil, A. Kasumov, V. Meden, H. Bouchiat, and R. Deblock, Phys. Rev. B **91**, 241401 (2015).

[164] R. Delagrange, R. Weil, A. Kasumov, M. Ferrier, H. Bouchiat, and R. Deblock, ArXiv:1601.03878 (2016).

[165] J.-D. Pillet, C. H. L. Quay, P. Morfin, C. Bena, A. Levy Yeyati, and P. Joyez, Nat. Phys. **6**, 965 (2010).

[166] T. Dirks, T. L. Hughes, S. Lal, B. Uchoa, Y.-F. Chen, C. Chialvo, P. M. Goldbart, and N. Mason, Nat. Phys. **7**, 386 (2011).

[167] L. Bretheau, Ç. Ö. Girit, H. Pothier, D. Esteve, and C. Urbina, Nature **499**, 312 (2013).

[168] B.-K. Kim, Y.-H. Ahn, J.-J. Kim, M.-S. Choi, M.-H. Bae, K. Kang, J. S. Lim, R. López, and N. Kim, Phys. Rev. Lett. **110**, 076803 (2013).

[169] J.-D. Pillet, P. Joyez, R. Žitko, and M. F. Goffman, Phys. Rev. B **88**, 045101 (2013).

[170] A. Kumar, M. Gaim, D. Steininger, A. L. Yeyati, A. Martín-Rodero, A. K. Hüttel, and C. Strunk, Phys. Rev. B **89**, 075428 (2014).

[171] E. J. H. Lee, X. Jiang, M. Houzet, R. Aguado, C. M. Lieber, and S. De Franceschi, Nat. Nanotechnol. **9**, 79 (2014).

[172] J. Schindele, A. Baumgartner, R. Maurand, M. Weiss, and C. Schönenberger, Phys. Rev. B **89**, 045422 (2014).

[173] A. P. Higginbotham, S. M. Albrecht, G. Kiršanskas, W. Chang, F. Kuemmeth, P. Krogstrup, T. S. Jespersen, J. Nygård, K. Flensberg, and C. M. Marcus, Nat. Phys. **11**, 1017 (2015).

[174] J.-P. Cleuziou, W. Wernsdorfer, V. Bouchiat, T. Ondarcuhu, and M. Monthioux, Nat. Nanotechnol. **1**, 53 (2006).

[175] M. R. Buitelaar, T. Nussbaumer, and C. Schönenberger, Phys. Rev. Lett. **89**, 256801 (2002).

[176] W. Chang, V. E. Manucharyan, T. S. Jespersen, J. Nygård, and C. M. Marcus, Phys. Rev. Lett. **110**, 217005 (2013).

[177] G. Michałek, T. Domański, B. Bułka, and K. Wysokiński, Sci. Rep. **5**, 14572 (2015).

[178] J. S. Lim, R. López, and R. Aguado, Phys. Rev. Lett. **107**, 196801 (2011).

[179] J. Gramich, A. Baumgartner, and C. Schönenberger, Phys. Rev. Lett. **115**, 216801 (2015).

[180] J. Gramich, A. Baumgartner, and C. Schönenberger, ArXiv:1601.00672 (2016).

[181] A. Levy Yeyati, J. C. Cuevas, A. López-Dávalos, and A. Martín-Rodero, Phys. Rev. B **55**, R6137 (1997).

[182] K. Grove-Rasmussen, H. I. Jørgensen, B. M. Andersen, J. Paaske, T. S. Jespersen, J. Nygård, K. Flensberg, and P. E. Lindelof, Phys. Rev. B **79**, 134518 (2009).

[183] C. B. Whan and T. P. Orlando, Phys. Rev. B **54**, R5255 (1996).

[184] S. Datta, *Electronic Transport in Mesoscopic Systems*, reprint of the 1st ed. (Cambridge University Press, Cambridge, 2009).

[185] C. W. J. Beenakker, Phys. Rev. B **46**, 12841 (1992).

[186] N. R. Claughton, M. Leadbeater, and C. J. Lambert, J. Phys. Condens. Matter **7**, 8757 (1995).

[187] Q.-f. Sun, J. Wang, and T.-h. Lin, Phys. Rev. B **59**, 3831 (1999).

[188] Y. Zhu, Q.-f. Sun, and T.-h. Lin, Phys. Rev. B **64**, 134521 (2001).

[189] J. C. Cuevas, A. Levy Yeyati, and A. Martín-Rodero, Phys. Rev. B **63**, 094515 (2001).

[190] R. Fazio and R. Raimondi, Phys. Rev. Lett. **80**, 2913 (1998).

[191] P. Schwab and R. Raimondi, Phys. Rev. B **59**, 1637 (1999).

[192] K. Kang, Phys. Rev. B **58**, 9641 (1998).

[193] S. D'Hollosy, *Locally Tunable InAs Nanowire Quantum Dots for Cooper Pair Splitting*, Ph.D. thesis, University of Basel (2014).

[194] Q.-f. Sun, J. Wang, and T.-h. Lin, Phys. Rev. B **59**, 13126 (1999).

[195] R. Deblock, E. Onac, L. Gurevich, and L. P. Kouwenhoven, Science **301**, 203 (2003).

[196] A. Eichler, M. Weiss, S. Oberholzer, C. Schönenberger, A. Levy Yeyati, J. C. Cuevas, and A. Martín-Rodero, Phys. Rev. Lett. **99**, 126602 (2007).

[197] E. Vecino, A. Martín-Rodero, and A. L. Yeyati, Phys. Rev. B **68**, 035105 (2003).

[198] J. Bauer, A. Oguri, and A. Hewson, J. Phys. Condens. Matter **19**, 486211 (2007).

[199] Y. Tanaka, N. Kawakami, and A. Oguri, J. Phys. Soc. Jap. **76**, 074701 (2007).

[200] D. Futterer, M. Governale, M. G. Pala, and J. König, Phys. Rev. B **79**, 054505 (2009).

[201] T. Meng, S. Florens, and P. Simon, Phys. Rev. B **79**, 224521 (2009).

[202] J. Eldridge, M. G. Pala, M. Governale, and J. König, Phys. Rev. B **82**, 184507 (2010).

[203] A. Braggio, M. Governale, M. G. Pala, and J. König, Solid State Commun. **151**, 155 (2011).

[204] A. Martín-Rodero and A. Levy Yeyati, J. Phys. Condens. Matter **24**, 385303 (2012).

[205] J. Barański and T. Domański, J. Phys. Condens. Matter **25**, 435305 (2013).

[206] D. Futterer, J. Swiebodzinski, M. Governale, and J. König, Phys. Rev. B **87**, 014509 (2013).

[207] R. Žitko, Phys. Rev. B **91**, 165116 (2015).

[208] J. S. Lee, J.-W. Park, J. Y. Song, and J. Kim, Nanotechnology **24**, 195201 (2013).

[209] L. Hofstetter, *Hybrid Quantum Dots in InAs Nanowires*, Ph.D. thesis, University of Basel (2011).

[210] P. Recher, D. Saraga, and D. Loss, in *Fundamental Problems of Mesoscopic Physics*, NATO Science Series II: Mathematics, Physics and Chemistry, Vol. 154, edited by I. Lerner, B. Altshuler, and Y. Gefen (Springer Netherlands, 2004) pp. 179–202.

[211] D. S. Golubev, M. S. Kalenkov, and A. D. Zaikin, Phys. Rev. Lett. **103**, 067006 (2009).

[212] M. Leijnse and K. Flensberg, Phys. Rev. Lett. **111**, 060501 (2013).

[213] O. Sauret, D. Feinberg, and T. Martin, Phys. Rev. B **70**, 245313 (2004).

[214] P. Burset, W. J. Herrera, and A. L. Yeyati, Phys. Rev. B **84**, 115448 (2011).

[215] D. Chevallier, J. Rech, T. Jonckheere, and T. Martin, Phys. Rev. B **83**, 125421 (2011).

[216] L. Hofstetter, S. Csonka, A. Baumgartner, G. Fülöp, S. d'Hollosy, J. Nygård, and C. Schönenberger, Phys. Rev. Lett. **107**, 136801 (2011).

[217] G. Fülöp, S. d'Hollosy, A. Baumgartner, P. Makk, V. A. Guzenko, M. H. Madsen, J. Nygård, C. Schönenberger, and S. Csonka, Phys. Rev. B **90**, 235412 (2014).

[218] Z. B. Tan, D. Cox, T. Nieminen, P. Lähteenmäki, D. Golubev, G. B. Lesovik, and P. J. Hakonen, Phys. Rev. Lett. **114**, 096602 (2015).

[219] I. V. Borzenets, Y. Shimazaki, G. F. Jones, M. F. Craciun, S. Russo, Y. Yamamoto, and S. Tarucha, arXiv:1506.04597 (2015).

[220] R. S. Deacon, A. Oiwa, J. Sailer, S. Baba, Y. Kanai, K. Shibata, K. Hirakawa, and S. Tarucha, Nat. Commun. **6**, (2015).

[221] G. Burkard, J. Phys. Condens. Matter **19**, 233202 (2007).

[222] P. Samuelsson and A. Brataas, Phys. Rev. B **81**, 184422 (2010).

[223] N. M. Chtchelkatchev, G. Blatter, G. B. Lesovik, and T. Martin, Phys. Rev. B **66**, 161320 (2002).

[224] P. Samuelsson, E. V. Sukhorukov, and M. Büttiker, Phys. Rev. Lett. **91**, 157002 (2003).

[225] A. Bednorz and W. Belzig, Phys. Rev. B **83**, 125304 (2011).

[226] S. Ratz, A. Donarini, D. Steininger, T. Geiger, A. Kumar, A. K. Hüttel, C. Strunk, and M. Grifoni, New J. Phys. **16**, 123040 (2014).

[227] W. Chang, S. M. Albrecht, T. S. Jespersen, F. Kuemmeth, P. Krogstrup, J. Nygård, and C. M. Marcus, Nat. Nanotechnol. **10**, 232 (2015).

[228] C. P. Poole, Jr., *Handbook of Superconductivity* (Academic Press, San Diego, 2000).

[229] G. Fülöp, F. Domínguez, S. d'Hollosy, A. Baumgartner, P. Makk, M. H. Madsen, V. A. Guzenko, J. Nygård, C. Schönenberger, A. Levy Yeyati, and S. Csonka, Phys. Rev. Lett. **115**, 227003 (2015).

[230] R. Flükiger, S. Y. Hariharan, R. Küntzler, H. L. Luo, F. Weiss, T. Wolf, and J. Q. Xu, *Landolt-Börnstein - Group III Condensed Matter (Springer Materials)* (Springer-Verlag GmbH, 1993).

[231] M. Palma, D. Maradan, and D. Zumbühl, *Private communication* (2015).

[232] Y.-F. Chen, T. Dirks, G. Al-Zoubi, N. O. Birge, and N. Mason, Phys. Rev. Lett. **102**, 036804 (2009).

[233] N. Bronn and N. Mason, Phys. Rev. B **88**, 161409 (2013).

[234] I. V. Borzenets, U. C. Coskun, S. J. Jones, and G. Finkelstein, Phys. Rev. Lett. **107**, 137005 (2011).

[235] J. Paajaste, M. Amado, S. Roddaro, F. S. Bergeret, D. Ercolani, L. Sorba, and F. Giazotto, Nano Lett. **15**, 1803 (2015).

[236] J. M. Eldridge, Y. J. Van der Meulen, and D. W. Dong, Thin Solid Films **12**, 447 (1972).

[237] J. Kim, V. Chua, G. A. Fiete, H. Nam, A. H. MacDonald, and C.-K. Shih, Nat. Phys. **8**, 464 (2012).

[238] L. Serrier-Garcia, J. C. Cuevas, T. Cren, C. Brun, V. Cherkez, F. Debontridder, D. Fokin, F. S. Bergeret, and D. Roditchev, Phys. Rev. Lett. **110**, 157003 (2013).

[239] D. H. Douglass Jr., Phys. Rev. Lett. **6**, 346 (1961).

[240] D. H. Douglass Jr., Phys. Rev. Lett. **7**, 14 (1961).

[241] R. Meservey and D. H. Douglass Jr., Phys. Rev. **135**, A24 (1964).

[242] R. F. Gasparovic, B. N. Taylor, and R. E. Eck, Solid State Commun. **4**, 59 (1966).

[243] G. Fagas, G. Tkachov, A. Pfund, and K. Richter, Phys. Rev. B **71**, 224510 (2005).

[244] T. D. Stanescu and S. Das Sarma, Phys. Rev. B **87**, 180504 (2013).

[245] S. Takei, B. M. Fregoso, H.-Y. Hui, A. M. Lobos, and S. Das Sarma, Phys. Rev. Lett. **110**, 186803 (2013).

[246] S. Pfaller, A. Donarini, and M. Grifoni, Phys. Rev. B **87**, 155439 (2013).

[247] J. P. Morten, A. Brataas, and W. Belzig, Phys. Rev. B **74**, 214510 (2006).

[248] D. S. Golubev and A. D. Zaikin, Phys. Rev. B **76**, 184510 (2007).

[249] C. A. Stafford, Phys. Rev. Lett. **77**, 2770 (1996).

[250] D. Sánchez and R. López, Phys. Rev. B **71**, 035315 (2005).

[251] R. Leturcq, L. Schmid, K. Ensslin, Y. Meir, D. C. Driscoll, and A. C. Gossard, Phys. Rev. Lett. **95**, 126603 (2005).

[252] A. Jacobsen, P. Simonet, K. Ensslin, and T. Ihn, New J. Phys. **14**, 023052 (2012).

[253] A. Jacobsen, P. Simonet, K. Ensslin, and T. Ihn, Phys. Rev. B **89**, 165413 (2014).

[254] J. Hölzl and F. K. Schulte, *Solid Surface Physics* (Springer, Berlin, Heidelberg, 1979) Chap. Work function of metals, pp. 1–150.

[255] C. Livermore, C. H. Crouch, R. M. Westervelt, K. L. Campman, and A. C. Gossard, Science **274**, 1332 (1996).

[256] W. G. van der Wiel, S. De Franceschi, J. M. Elzerman, T. Fujisawa, S. Tarucha, and L. P. Kouwenhoven, Rev. Mod. Phys. **75**, 1 (2002).

[257] M. R. Gräber, W. A. Coish, C. Hoffmann, M. Weiss, J. Furer, S. Oberholzer, D. Loss, and C. Schönenberger, Phys. Rev. B **74**, 075427 (2006).

[258] B. Camarota, F. Parage, F. Balestro, P. Delsing, and O. Buisson, Phys. Rev. Lett. **86**, 480 (2001).

[259] M. Dresselhaus, G. Dresselhaus, R. Saito, and A. Jorio, Phys. Rep. **409**, 47 (2005).

[260] K. Watanabe, K. Yoshida, T. Aoki, and S. Kohjiro, Jpn. J. Appl. Phys. **33**, 5708 (1994).

[261] T. Greibe, T. Bauch, C. Wilson, and P. Delsing, J. Phys.: Conf. Ser. **150**, 052063 (2009).

[262] T. Greibe, M. P. V. Stenberg, C. M. Wilson, T. Bauch, V. S. Shumeiko, and P. Delsing, Phys. Rev. Lett. **106**, 097001 (2011).

[263] J. P. Pekola, V. F. Maisi, S. Kafanov, N. Chekurov, A. Kemppinen, Y. A. Pashkin, O.-P. Saira, M. Möttönen, and J. S. Tsai, Phys. Rev. Lett. **105**, 026803 (2010).

[264] J. Barański and T. Domański, J. Phys. Condens. Matter **27**, 305302 (2015).

[265] J. Nygård, D. H. Cobden, and P. E. Lindelof, Nature **408**, 342 (2000).

[266] B. Babić, T. Kontos, and C. Schönenberger, Phys. Rev. B **70**, 235419 (2004).

[267] F. D. M. Haldane, Phys. Rev. Lett. **40**, 416 (1978).

[268] P. Jarillo-Herrero, J. Kong, H. S. van der Zant, C. Dekker, L. P. Kouwenhoven, and S. De Franceschi, Nature **434**, 484 (2005).

[269] K. Izydor Wysokiński, J. Phys. Condens. Matter **24**, 335303 (2012).

[270] C. Thiele, H. Vieker, A. Beyer, B. S. Flavel, F. Hennrich, D. Munoz Torres, T. R. Eaton, M. Mayor, M. M. Kappes, A. Gölzhäuser, H. v. Löhneysen, and R. Krupke, Appl. Phys. Lett. **104**, 103102 (2014).

[271] W. Chen, D. N. Shi, and D. Y. Xing, Sci. Rep. **5**, 7607 (2015).

[272] J. Stöhr and H. Siegmann, *Magnetism - From Fundamentals to Nanoscale Dynamics*, Springer Series in Solid-State Sciences (Springer, 2006).

[273] M. Getzlaff, *Fundamentals of Magnetism* (Springer, 2007).

[274] W. Brown, Jr., *Micromagnetics* (Interscience (Wiley), New York, 1963).

[275] C. Tannous and J. Gieraltowski, Eur. J. Phys. **29**, 475 (2008).

[276] E. Stoner and E. Wohlfarth, Phil. Trans. R. Soc. A **240**, 599 (1948).

[277] I. Žutić, J. Fabian, and S. Das Sarma, Rev. Mod. Phys. **76**, 323 (2004).

[278] I. I. Mazin, Phys. Rev. Lett. **83**, 1427 (1999).

[279] N. F. Mott, Adv. Phys. **13**, 325 (1964).

[280] A. Fert and I. A. Campbell, Phys. Rev. Lett. **21**, 1190 (1968).

[281] B. Nadgorny, R. J. Soulen, M. S. Osofsky, I. I. Mazin, G. Laprade, R. J. M. van de Veerdonk, A. A. Smits, S. F. Cheng, E. F. Skelton, and S. B. Qadri, Phys. Rev. B **61**, R3788 (2000).

[282] R. Meservey and P. Tedrow, Phys. Rep. **238**, 173 (1994).

[283] J. S. Moodera, , J. Nassar, and G. Mathon, Annu. Rev. Mater. Sci. **29**, 381 (1999).

[284] M. Johnson and R. Silsbee, Phys. Rev. B **37**, 5312 (1988).

[285] P. C. van Son, H. van Kempen, and P. Wyder, Phys. Rev. Lett. **58**, 2271 (1987).

[286] T. Heinzel, *Mesoscopic Electronics in Solid State Nanostructures*, 3rd ed. (Wiley, 2010).

[287] M. Johnson and R. Silsbee, Phys. Rev. Lett. **55**, 1790 (1985).

[288] T. Valet and A. Fert, Phys. Rev. B **48**, 7099 (1993).

[289] F. Jedema, A. Filip, and B. van Wees, Nature **410**, 345 (2001).

[290] F. Jedema, M. Nijboer, A. Filip, and B. van Wees, Phys. Rev. B **67**, 085319 (2003).

[291] G. Schmidt, D. Ferrand, L. Molenkamp, A. Filip, and B. van Wees, Phys. Rev. B **62**, 4790 (2000).

[292] E. I. Rashba, Phys. Rev. B **62**, R16267 (2000).

[293] A. Fert and H. Jaffrès, Phys. Rev. B **64**, 184420 (2001).

[294] D. Smith and R. Silver, Phys. Rev. B **64**, 045323 (2001).

[295] W. Thomson, Proc. R. Soc. London **8**, 546 (1856).

[296] T. McGuire and R. Potter, IEEE Trans. Magn. **11**, 1018 (1975).

[297] R. Gross and A. Marx, *Spinelektronik*, Lecture Notes (2004), online available: http://www.wmi.badw.de/teaching/Lecturenotes/.

[298] C. Gould, C. Rüster, T. Jungwirth, E. Girgis, G. M. Schott, R. Giraud, K. Brunner, G. Schmidt, and L. W. Molenkamp, Phys. Rev. Lett. **93**, 117203 (2004).

[299] G. Fábián, *Engineered Magnetoconductance in InAs Nanowire Quantum Dots*, Ph.D. thesis, University of Basel (2015).

[300] M. N. Baibich, J. M. Broto, A. Fert, F. N. Van Dau, F. Petroff, P. Etienne, G. Creuzet, A. Friederich, and J. Chazelas, Phys. Rev. Lett. **61**, 2472 (1988).

[301] G. Binasch, P. Grünberg, F. Saurenbach, and W. Zinn, Phys. Rev. B **39**, 4828 (1989).

[302] J. S. Moodera, L. R. Kinder, T. M. Wong, and R. Meservey, Phys. Rev. Lett. **74**, 3273 (1995).

[303] M. Julliere, Phys. Lett. A **54**, 225 (1975).

[304] S. S. Parkin, C. Kaiser, A. Panchula, P. M. Rice, B. Hughes, M. Samant, and S.-H. Yang, Nat. Mater. **3**, 862 (2004).

[305] M. Sharma, S. X. Wang, and J. H. Nickel, Phys. Rev. Lett. **82**, 616 (1999).

[306] J. M. De Teresa, A. Barthélémy, A. Fert, J. P. Contour, F. Montaigne, and P. Seneor, Science **286**, 507 (1999).

[307] J. S. Moodera, G.-X. Miao, and T. S. Santos, Phys. Today **63**, 46 (2010).

[308] G.-X. Miao, M. Münzenberg, and J. S. Moodera, Rep. Prog. Phys. **74**, 036501 (2011).

[309] S. Datta and B. Das, Appl. Phys. Lett. **56**, 665 (1990).

[310] A. Cottet and T. Kontos, Phys. Rev. Lett. **105**, 160502 (2010).

[311] K. Tsukagoshi, B. Alphenaar, and M. Wagner, Mat. Sci. and Engin. B **84**, 26 (2001).

[312] J.-R. Kim, H. M. So, J.-J. Kim, and J. Kim, Phys. Rev. B **66**, 233401 (2002).

[313] B. Zhao, I. Mönch, T. Mühl, H. Vinzelberg, and C. M. Schneider, J. Appl. Phys. **91**, 7026 (2002).

[314] R. Thamankar, S. Niyogi, B. Yoo, Y. Rheem, N. Myung, R. Haddon, and R. Kawakami, Appl. Phys. Lett. **89**, 033119 (2006).

[315] S. Sahoo, T. Kontos, C. Schönenberger, and C. Sürgers, Appl. Phys. Lett. **86**, 112109 (2005).

[316] B. Nagabhirava, T. Bansal, G. Sumanasekara, and B. Alphenaar, Appl. Phys. Lett. **88**, 023503 (2006).

[317] H. T. Man, I. J. W. Wever, and A. F. Morpurgo, Phys. Rev. B **73**, 241401 (2006).

[318] S. Koller, M. Grifoni, and J. Paaske, Phys. Rev. B **85**, 045313 (2012).

[319] A. Dirnaichner, M. Grifoni, A. Prüfling, D. Steininger, A. K. Hüttel, and C. Strunk, Phys. Rev. B **91**, 195402 (2015).

[320] S. J. van der Molen, N. Tombros, and B. J. van Wees, Phys. Rev. B **73**, 220406 (2006).

[321] C. Feuillet-Palma, T. Delattre, P. Morfin, J.-M. Berroir, G. Fève, D. C. Glattli, B. Plaçais, A. Cottet, and T. Kontos, Phys. Rev. B **81**, 115414 (2010).

[322] J.-Y. Chauleau, B. McMorran, R. Belhou, N. Bergeard, T. Mentes, M. Nino, A. Locatelli, J. Unguris, S. Rohart, J. Miltat, and A. Thiaville, Phys. Rev. B **84**, 094416 (2011).

[323] D. Steininger, A. K. Hüttel, M. Ziola, M. Kiessling, M. Sperl, G. Bayreuther, and C. Strunk, J. Appl. Phys. **113**, 034303 (2013).

[324] D. Preusche, S. Schmidmeier, E. Pallecchi, C. Dietrich, A. K. Hüttel, J. Zweck, and C. Strunk, J. Appl. Phys. **106**, 084314 (2009).

[325] A. Cottet and M.-S. Choi, Phys. Rev. B **74**, 235316 (2006).

[326] S. Koller, L. Mayrhofer, and M. Grifoni, New J. Phys. **9**, 348 (2007).

[327] A. Cottet, T. Kontos, W. Belzig, C. Schönenberger, and C. Bruder, Europhys. Lett. **74**, 320 (2006).

[328] J. R. Hauptmann, J. Paaske, and P. E. Lindelof, Nat. Phys. **4**, 373 (2008).

[329] L. Hofstetter, A. Geresdi, M. Aagesen, J. Nygård, C. Schönenberger, and S. Csonka, Phys. Rev. Lett. **104**, 246804 (2010).

[330] M. Gaass, A. K. Hüttel, K. Kang, I. Weymann, J. von Delft, and C. Strunk, Phys. Rev. Lett. **107**, 176808 (2011).

[331] K. Ono, H. Shimada, and Y. Ootuka, J. Phys. Soc. Jap. **66**, 1261 (1997).

[332] S. Datta, L. Marty, J. P. Cleuziou, C. Tilmaciu, B. Soula, E. Flahaut, and W. Wernsdorfer, Phys. Rev. Lett. **107**, 186804 (2011).

[333] F. A. Zwanenburg, D. W. van der Mast, H. B. Heersche, and L. P. Kouwenhoven, Nano Lett. **9**, 2704 (2009).

[334] A. Bernand-Mantel, P. Seneor, K. Bouzehouane, S. Fusil, C. Deranlot, F. Petroff, and A. Fert, Nat. Phys. **5**, 920 (2009).

[335] N. Tombros, S. J. van der Molen, and B. J. van Wees, Phys. Rev. B **73**, 233403 (2006).

[336] A. Cottet, C. Feuillet-Palma, and T. Kontos, Phys. Rev. B **79**, 125422 (2009).

[337] G. Gunnarsson, J. Trbovic, and C. Schönenberger, Phys. Rev. B **77**, 201405 (2008).

[338] M. R. Fitzsimmons, T. J. Silva, and T. M. Crawford, Phys. Rev. B **73**, 014420 (2006).

[339] L. E. Hueso, J. M. Pruneda, V. Ferrari, G. Burnell, J. P. Valdes-Herrera, B. D. Simons, P. B. Littlewood, E. Artacho, A. Fert, and N. D. Mathur, Nature **445**, 410 (2007).

[340] J. J. Viennot, M. C. Dartiailh, A. Cottet, and T. Kontos, Science **349**, 408 (2015).

[341] C. Morgan, M. Misiorny, D. Metten, S. Heedt, T. Schäpers, C. M. Schneider, and C. Meyer, ArXiv:1511.03058 (2015).

[342] H. Yang, M. E. Itkis, R. Moriya, C. Rettner, J.-S. Jeong, D. S. Pickard, R. C. Haddon, and S. S. P. Parkin, Phys. Rev. B **85**, 052401 (2012).

[343] S. Hacia, T. Last, S. Fischer, and U. Kunze, J. Phys. D: Appl. Phys. **37**, 1310 (2004).

[344] J. Samm, *Investigation of Carbon Nanotube Quantum Dots connected to Ferromagnetic Leads*, Ph.D. thesis, University of Basel (2014).

[345] J. Stankiewicz, F. Jiménez-Villacorta, and C. Prieto, Phys. Rev. B **73**, 014429 (2006).

[346] S. Zihlmann, P. Makk, C. A. F. Vaz, and C. Schönenberger, 2D Materials **3**, 011008 (2015).

[347] J. P. Nibarger, R. Lopusnik, Z. Celinski, and T. J. Silva, Appl. Phys. Lett. **83**, 93 (2003).

[348] G. Mihaujlovic, D. K. Schreiber, Y. Liu, J. E. Pearson, S. D. Bader, A. K. Petford-Long, and A. Hoffmann, Appl. Phys. Lett. **97**, 112502 (2010).

[349] A. K. Singh and J. Eom, ACS Appl. Mater. Interfaces **6**, 2493 (2014).

[350] M. Z. Iqbal, M. W. Iqbal, X. Jin, C. Hwang, and J. Eom, J. Mater. Chem. C **3**, 298 (2015).

[351] B. Dlubak, M.-B. Martin, R. S. Weatherup, H. Yang, C. Deranlot, R. Blume, R. Schloegl, A. Fert, A. Anane, S. Hofmann, P. Seneor, and J. Robertson, ACS Nano **6**, 10930 (2012).

[352] J. Maassen, W. Ji, and H. Guo, Nano Lett. **11**, 151 (2011).

[353] M. V. Kamalakar, A. Dankert, J. Bergsten, T. Ive, and S. P. Dash, Sci. Rep. **4**, 6146 (2014).

[354] M. Drögeler, F. Volmer, M. Wolter, B. Terrés, K. Watanabe, T. Taniguchi, G. Güntherodt, C. Stampfer, and B. Beschoten, Nano Lett. **14**, 6050 (2014).

[355] A. D. Crisan, S. Datta, J. J. Viennot, M. R. Delbecq, A. Cottet, and T. Kontos, Nat. Commun. **7**, 10451 (2016).

[356] J. Moser, A. Barreiro, and A. Bachtold, Appl. Phys. Lett. **91**, 163513 (2007).

[357] F. E. Jones, A. A. Talin, F. Léonard, P. M. Dentinger, and W. M. Clift, J. Electron. Mater. **35**, 1641 (2006).

[358] S. Lombardo, J. H. Stathis, B. P. Linder, K. L. Pey, F. Palumbo, and C. H. Tung, J. Appl. Phys. **98**, 121301 (2005).

[359] M. R. Buitelaar, W. Belzig, T. Nussbaumer, B. Babich, C. Bruder, and C. Schönenberger, Phys. Rev. Lett. **91**, 057005 (2003).

[360] P. Stadler, W. Belzig, and G. Rastelli, ArXiv:1511.04858 (2015).

[361] M. Leijnse and K. Flensberg, Phys. Rev. B **86**, 134528 (2012).

[362] A. Fert and L. Piraux, J. Magn. Magn. Mat. **200**, 338 (1999).

A

Detailed fabrication recipes

A.1. Wafer properties

- highly boron p-doped Si wafer
- resistivity $\sim 10\,\mu\Omega$cm
- 400 nm thick thermally grown, polished SiO_2 top layer

A.2. Substrate preparation

1. Break wafer into $1 \times 1\,cm^2$ substrate pieces with diamond cutter.
2. Sonication for ~ 60 min. in acetone.
3. Sonication for ~ 30 min. in IPA, N_2 blow-dry.
4. 30 min. UV ozone cleaning (Model 42-220, Jelight Company, USA).

A.3. FeRu or FeMo CVD catalyst solution

1. Two hour long sonication of the 3 constituent stock solutions for the FeMo or FeRu CVD catalyst:
   - 30 mg of Al_2O_3 (particle size: 4 nm) solved in 20 ml IPA
   - 93 mg of $Fe(NO_3)_3 \cdot 9H_2O$ solved in 20 ml IPA
   - 27 mg of MoO_2Cl_2 solved in 20 ml IPA for FeMo catalyst *or*
     48 mg of $RuCl_3{\cdot}H_2O$ solved in 20 ml IPA for FeRu catalyst
2. Mix 0.5 ml of each solution and add 38-50 ml IPA (depending on the desired CNT density).

A.4. CVD growth

1. Sonicate catalyst solution for 3 h in pulsed high power sonicator (power 100%, pulse duration 0.5 s, pause 0.5 s) to break up catalysts clusters.
2. Spin-coat 1-2 droplets of catalyst solution on already spinning substrate (40 s, 4000 rpm).
3. Place 3-4 growth substrates in the middle of the CVD reactor's quartz tube, control leak tightness and set/control the flow rates for the growth process:
   - 1500 sccm for Ar (= 104 l/h at the air-gauged flow meter)
   - 1000 sccm for CH_4 (= 44.7 l/h at the flow meter)
   - 500 sccm for H_2 (= 8 l/h at the flow meter)
4. Heat up furnace to $T = 850°C$ (FeRu) or $T = 950°C$ (FeMo) under constant Ar flow.
5. CNT growth: Replace Ar flow by CH_4 and H_2 for 10 min.
6. Turn off CH_4 and furnace heating, cool down under H_2 and Ar flow.
7. At $T < 500°C$ turn off H_2 flow, at $T < 250°C$ turn off Ar flow and take out wafer.
8. Quickly control the wafers in the SEM to preselect suited substrates for further processing, the density of grown CNTs can strongly vary within a growth batch of 3-4 substrates.

A.5. E-beam lithography for conventional devices

We systematically analyzed different resist systems with an optimization of exposure parameters for clean interfaces and resulting undercut resist profiles. Below we only give parameters for the optimized EBL process based on ZEP resist, which is most suited for the fabrication of conventional CNT devices (convenient electrical contact yield, ideal lift-off).

ZEP resist

1. Spin-coat 300 nm ZEP520A (ZEP, Zeon Cooperation) diluted in anisole (ramp/spreading cycle 4 s, speed 4000 rpm, time 40 s).
2. Bake for 3 min on a hot plate at 180°C.

The resist thickness (adjust with resist dilution or spinning frequency) is measured after the resist bake with a profilometer. Undiluted ZEP results in a 380 nm thick resist layer. Anisole evaporates very slowly, so that the resist thickness of a given dilution changes hardly over a year or two. For improving the surface adhesion, an adhesion promoter (e.g. HMDS, Allresist GmbH) may be used, which we omitted due to the desired lift-off properties.

Exposure parameters

All EBL has been carried out with a Supra 35 or Supra 40 SEM (Carl Zeiss AG) and an Elphy EBL attachment (Raith GmbH). Typically, a working distance of $\sim 17\,\mathrm{mm}$ was used, and a $10\,\mu\mathrm{m}$ aperture for the exposure of small structures in a $200\,\mu\mathrm{m}$ write-field, while the largest aperture $120\,\mu\mathrm{m}$ was used for the exposure of large-scale bond pads etc. in a coarse $2000\,\mu\mathrm{m}$ write-field. We always chose the smallest possible exposure step-size, corresponding to $\sim 3\,\mathrm{nm}$ ($200\,\mu\mathrm{m}$ write-field) and $\sim 60\,\mathrm{nm}$ ($2000\,\mu\mathrm{m}$ write-field). All given doses are optimized for no remaining resist residues after development, but also that no severe widening of structures is observed compared to the design mask. To reduce occurring 'sudden charge-up jumps' during EBL on the insulating resist and hence resulting undesired gaps in structured leads, we recommend to use the built-in 'ordering function' of the Elphy lithography software starting from the smallest structures close to the CNT, and sufficient design overlaps for the outer, larger structures.

Optimized EBL with ideal undercut resist profile

- *Acceleration voltage* $10\,\mathrm{kV}$
- *Area dose* $34\,\mu\mathrm{C/cm^2}$
- *Line dose* $350\,\mathrm{pC/cm}$, resulting line-width $\sim 130\,\mathrm{nm}$

Straight resist profile, useful for increased resolution

- *Acceleration voltage* $20\,\mathrm{kV}$
- *Area dose* $68\,\mu\mathrm{C/cm^2}$
- *Line dose* $550\,\mathrm{pC/cm}$, resulting line-width $\sim 100\,\mathrm{nm}$

Room-temperature development

1. Develop for 60 s in n-Amyl acetate (pentyl acetate).
2. Stop development by dipping for 10 s in 9:1 mixture of MIBK:IPA.
3. Rinse in pure IPA, blow dry with N_2.

Ar plasma etching

An optional Ar plasma etching (*in-situ*, loadlock UHV Bestec evaporation system) is done prior to contacting ferromagnetic Py strips with metallic Pd leads to remove surface oxides and achieve metallic contacts. We use a plasma source current of 20 mA, an extraction voltage 0.6 kV, an anode voltage (ion energy) 1 kV and an Ar chamber pressure of $5 \cdot 10^{-5}$ mbar, resulting in an anode (ion etching) current of $\sim 0.1\,\mathrm{mA}$. A $1-2\,\mathrm{min}$. long etching is sufficient to achieve metallic contacts, and removes $\sim 2-5\,\mathrm{nm}$ resist.

Metallization

Detailed parameters for the deposition of Pd, Ti/Au, Py, Co, Ti/Nb and Pd/Pb/In can be found in the respective chapters in the main text.

Lift-off process

1. Remove resist in a $15-30$ min. long bath in NMP at $T = 70°C$ on a hotplate, support if necessary with turbulent flow (syringe).
2. Rinse for $30-60$ min. in acetone at $T = 50°C$ to remove NMP residues.
3. Dip in IPA, blow dry with N_2.

A.6. Partially suspended CNT devices with recessed Re bottomgates

Recessed Re bottomgates

1. E-beam lithography of bottom-gate structures and markers

- Spin-Coat 260 nm PMMA(950k) (AR-P 671.09, Allresist GmbH) diluted in chlorobenzene (4000 rpm, 40 s, 4 s ramp), bake for 3 min on a hot plate at 180°C.
- Exposure: Acceleration voltage 20 kV, aperture 10 μm, area dose 280 $\mu C/cm^2$ (markers), line dose 1300 pC/cm (bottomgates, resulting resist line-width $\sim$ 50 nm).
- Development at RT: 60 s in 1:3 mixture of MIBK:IPA, stop in pure IPA, blow-dry, post-bake for 3 min on a hot plate at 120°C.

2. RIE etching of trenches in the SiO_2, using an inductively coupled plasma (ICP-RIE, SI-500, Sentech GmbH):

- O_2 chamber cleaning process, without sample
- 10 min. long CF_4 plasma for chamber conditioning on a pure Si wafer, without sample
- Sample etch: flow 30 sccm CF_4, pressure $p = 0.4$ Pa, RF power 45 W, ICP power 50 W. This process results in an anisotropic etch profile, and a plasma bias voltage of $\sim$ 170 V should be obtained (control). A $85-90$s long etching creates a $\sim 60-70$ nm deep trench in the SiO_2. Etch rates: PMMA $\sim$ 110 nm/min., SiO_2 $\sim$ 45 nm/min.

3. HF etching: Dip for 1 min. in buffered hydrofluoric acid (BHF, 1:20 conc., etch rate SiO_2 $\sim$ 35 nm/min., does not etch resist significantly) to create an undercut below the resist and deepen/widen the trench further, stop etching in deionized water, dip in IPA, blow-dry.

4. Sputter deposition (Orion-8-UHV, AjA, USA) of 35 nm Re in the trenches: base pressure $\sim 5 \cdot 10^{-9}$ torr, sample position 40 mm (height of the crystal for thickness measurement), flow 40 sccm Ar, pressure $p = 20$ mTorr, power 30 W, for $t = 4$ min. with a rate of 1.47 Å/s.
5. Lift-off for 30 min. in 50°C warm acetone, IPA, blow dry. This results in ~ 100 nm deep trenches, and ~ 90 nm wide Re bottomgates. Trench width top ~ 280 nm, trench width bottom ~ 150 nm.

Cold development

With a cold development at $T = 5$°C (measured in the developer + stopper with a thermometer) and an increased line dose of 1900 pC/cm, one achieves a reduced line-width of ~ 25 nm in the 260 nm thick resist with the above parameters, and a reduced bottomgate width of $\sim 50 - 80$ nm.

Device fabrication

For the final device, CNTs are grown via CVD over the trenches and bottomgates, located and a device is fabricated by standard EBL.

A.7. Fork stamping of pristine CNTs onto predefined contact structures

Mesa fabrication

1. E-beam lithography of etching mask for mesa structure

– After the fabrication of a contact structure (3 EBL steps), spin-coat 1.2 μm PMMA(950k) (4000 rpm, 40 s, 4 s ramp), bake for 3 min on a hot plate at 180°C.
– Exposure: Acceleration voltage 20 kV, aperture 20 μm, area dose 220 μC/cm^2.
– Development at RT: 40 s in 1:3 mixture of MIBK:IPA, stop in pure IPA, blow-dry.

2. RIE etching into the SiO_2/Si (Oxford Plasmalab 80 Plus):

– Long (~ 2 h) chamber cleaning process, without sample. Either Ar/O_2 plasma, flow 6 sccm (6%)/16 sccm (16%) Ar/O_2, pressure 300 mTorr, power 30 W, until a plasma bias voltage of ~ 90 V is reached (control). Alternatively, pure O_2 plasma, flow 16 sccm (16%), pressure 300 mTorr, power 50 W, until a plasma bias voltage of ~ 120 V is reached (control). A clean chamber is of crucial importance, without it no reproducible SiO_2/Si etching process (very sensitive to chamber chemistry!) can be

achieved. In worst case, a prior mechanical cleaning of visible chamber polymer residues using acetone, IPA and ethanol helps.
- Individual, 1 min. long CHF_3/SF_6 chamber conditioning with the below processes, without sample.
- Sample etch: First, a 10 min. long CHF_3 etching is used for the removal of the 400 nm thick SiO_2 layer: flow 8 sccm (16%) CHF_3, pressure 50 mTorr, power 200 W (etch selectivity ~ 2.5, etch rates PMMA ~ 20 nm/min., $SiO_2 \sim 50$ nm/min., plasma bias voltage ~ 470 V). A subsequent 2.5 min. long anisotropic and selective SF_6/O_2 RIE creates a 3 μm deep trench in the p-doped Si: flow 13 sccm (50%)/5 sccm (5%) SF_6/O_2, pressure 75 mTorr, power 100 W (etch selectivity ~ 7, etch rates PMMA ~ 215 nm/min., $SiO_2 \sim 1.35 - 1.5$ μm/min., plasma bias voltage ~ 110 V).
- Minimize polymer residues from etch process: etch remaining resist mask ($\sim 500 - 600$ nm) down to $\sim 200 - 300$ nm by alternating the above Ar/O_2 (PMMA etch rate ~ 55 nm/min) and pure O_2 (PMMA etch rate ~ 80 nm/min) RIE step. Control resist thickness individually with a profilometer, typically $\sim 2 + 3$ min. long etching steps are required.

3. Resist removal in warm NMP or acetone, IPA, blow dry.
4. Removal of remaining carbon-fluor polymer residues (5^{th} EBL, RIE):

- Spin-coat 450 nm thick ZEP resist (3500 rpm, 40 s, 4 s ramp), bake 3 min on a hot plate at 180°C. The resist thickness will not be homogeneous at the edge of the mesa.
- Exposure: expose only at the edge of the mesa, where carbon-fluor polymer residues remain. Acceleration voltage 20 kV, aperture 10 μm, area dose 90 μC/cm^2 (overexposed due to varying resist thickness at mesa edge).
- Development at RT: 60 s in n-amylacetate, stop 10 s in 9:1 mixture of MIBK:IPA, rinse in IPA, blow-dry.
- RIE sample etch for $\sim 4 - 6$ min. in above Ar/O_2 plasma, control in light microscope if residues are gone, otherwise repeat, but the contact structure has still to be protected by resist from the plasma.
- Resist removal in 70°C warm NMP, 50°C warm acetone, IPA, blow dry. Clean mesa structures (with contact structures that have always been protected during processing) are the result.

5. Glue 'electrical circuit' chips into chip-carrier and perform wire-bonding.

CNT transfer in FIRST cleanroom, ETH Zurich

1. Immediately prior to CNT transfer, a 25 s long Ar plasma RIE etching (Oxford RIE 76, flow 50 sccm, pressure 50 μbar, power 200 W, plasma bias voltage $\sim$ 410 V) removes surface oxides. Special attention has to be paid that the chip-carrier with the already wire-bonded electrical circuit chips lies flat on the RIE electrode, otherwise electrostatic discharges (ESD) can destroy the metallic contact structure.
2. CNT transfer: CNTs are transferred from the forks onto the device structure using a micromanipulator set-up as described in the main text. A home-built electrical circuit set-up and flow-box allow for a steady N_2 flow around the devices to prevent oxidation during transfer. After successful CNT deposition, the in general very sensitive, suspended CNT devices are 'soft-grounded' via a 1 MΩ pre-resistor to prevent ESD and limit the device currents, and immediately stored in vacuum.
3. Transport of the finished devices in ESD-safe boxes to Basel in a home-built metallic desiccator system, pumped to a base pressure $\sim 10^{-6}$ mbar at ETH Zurich for the transport.

B

Additional data to Chapter 5.2

In this appendix, we present and analyze additional data for the device discussed in Sec. 5.2.

Single QD

Figure B.1(a) and (b) show the measured differential conductance G_1 and G_2 of the device as a function of the sidegate voltages V_{SG1} and V_{SG2}, for the ac bias applied to S, at $V_{\mathrm{S}} = 0.95\,\mathrm{meV} \gtrapprox \Delta_0/e$ and $B = 0$. We observe mostly a single dominant resonance slope visible in both G_1 and G_2, with only small

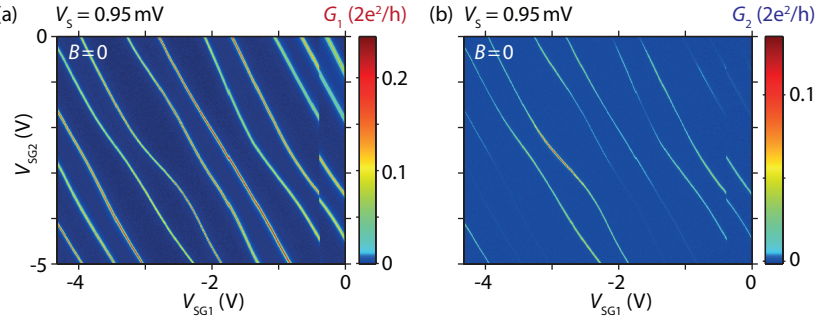

Figure B.1.: Differential conductance G_1 (a) and G_2 (b) as a function of the sidegate voltages V_{SG1} and V_{SG2}, for $V_{\mathrm{S}} = 0.95\,\mathrm{mV}$, $V_{21} = 0$, and $V_{\mathrm{BG}} = -1\,\mathrm{V}$, at $B = 0$. The abrupt jump at $V_{\mathrm{SG1}} \approx -0.4\,\mathrm{V}$ is due to a sudden rearrangement of the gate charge.

variations of the distance between adjacent resonance lines. Hence, transport through this device can be captured to first approximation by a single QD [255, 256] coupled to three contact terminals, thus supporting our arguments given in the main text.

"Hardness" of the superconducting transport gap

To analyze the "hardness" of the superconducting transport gap Δ_0 in our experiments, i.e. the degree of conductance suppression for bias voltages below the superconducting gap, we study conductance traces along a CB resonance $\mu_{\mathrm{QD}} = \mu_{\mathrm{N}}$. Since the device is very weakly coupled to S and transport is dominated by quasiparticle transport only, this effectively probes the single-particle DOS in the S contact. Such conductance traces are shown in Fig. B.2, where the differential conductance G_1 between S and N1 has been measured at $\sim 30\,\mathrm{mK}$ base temperature for identical electrical potentials of the N contacts, i.e. $V_{21} = 0$. We find a suppression of ~ 100 for the subgap conductance compared to the normal state ($B > B_{\mathrm{c}}$) or the above-gap conductance $G_{1\mathrm{n}}$, suggesting a clean and hard superconducting transport gap. While this suppression is similar to the one found in Ref. [227] for epitaxial Al-semiconductor nanowires, we note that our experiment most likely probes the superconducting gap of the metallic Pd-Pb system, whereas Ref. [227] potentially probes the proximity-induced gap in the InAs nanowire.

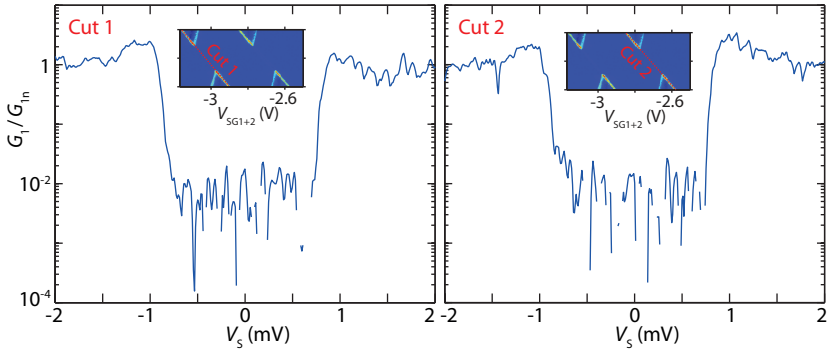

Figure B.2.: Conductance G_1 in the superconducting state of S at $B = 0$ as a function of the bias voltage V_{S}, along the resonance line where $\mu_{\mathrm{QD}} = \mu_1$ (indicated in the insets), normalized to the conductance value above the superconducting transport gap $G_{1\mathrm{n}} = G_1(|eV_{\mathrm{S}}| \gg \Delta_0)$ along the resonance. The insets indicate the gate position of the studied resonances in a conductance map, recorded for identical electrical potentials of the N contacts, i.e. $V_{21} = 0$, at $V_{\mathrm{BG}} = -1\,\mathrm{V}$ and $\sim 30\,\mathrm{mK}$ base temperature.

C

Additional data to Chapter 6

In this appendix, we present additional data and supplementary information to Chap. 6, which has been published in similar form in the supplementary material of Ref. [179].

C.1. Sample characteristics

No Cooper pair splitting or QD hybridization

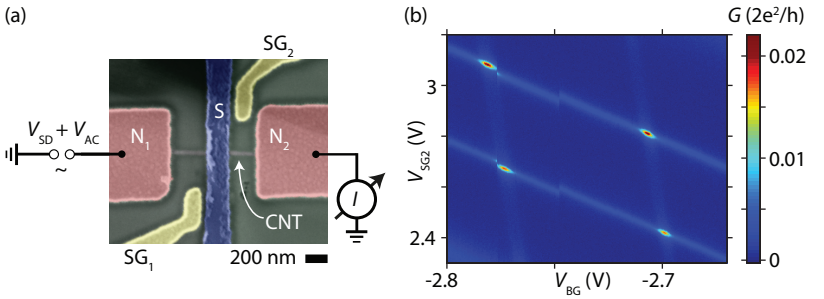

Figure C.1.: (a) Experimental setup to measure the two QDs in series. The superconductor is floating (not connected to ground). (b) Serial double-QD conductance map of SG2 voltage vs backgate voltage at $V_{\mathrm{SD}} = 0\,\mathrm{mV}$, $B = 5\,\mathrm{T}$ and $T = 110\,\mathrm{mK}$.

To exclude any effects due to the second QD of the device, we measured G

vs. sidegate and backgate voltage with the two QDs in series, see Fig. C.1(a). The resulting double-QD charge stability diagram in Fig. C.1(b) confirms that the two QDs are well decoupled by the superconducting contact in between. In particular, we do not observe the typical honeycomb pattern or any anti-crossings, but solely an increased conductance at the resonance crossing points. This suggests that the inter-dot coupling is much smaller than the individual QD life times, $\Gamma_{12} \ll \Gamma_{\mathrm{QD1}}, \Gamma_{\mathrm{QD2}}$, and that also capacitive cross-talk is negligible [255–257]. In experiments with the two QDs in parallel, we do not find any conductance features that depend on both QDs, excluding effects due to Cooper pair splitting.

No dependence of subgap features on the QD charge state

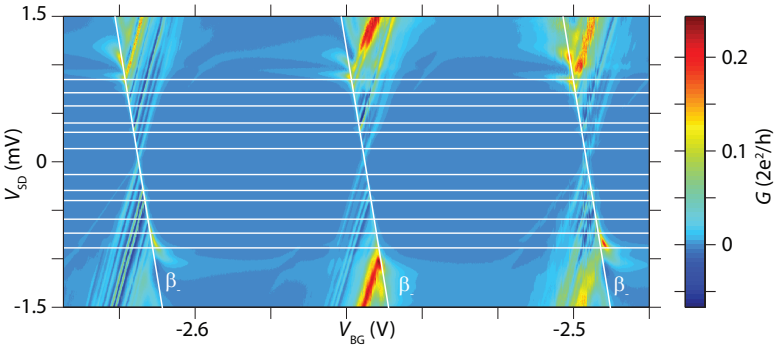

Figure C.2.: G as function of V_{BG} and V_{SD} over 3 CB resonances. The horizontal white lines mark the position ε_n of the IE replica states determined in Fig. 6.3, the line with slope β_- is drawn for better orientation.

Figure C.2 demonstrates that neither the position nor the spacing of the IE replicas depends on the electronic charge state of the QD within experimental error. The relative intensities of the replica lines are also similar, even if the total conductance of the replicas change for different CB resonances.

Line shape fits at finite bias

To confirm that our fits in Fig. 6.2 at $V_{\mathrm{SD}} = 0$ are independent of an overlapping Andreev bound state (ABS), we fit the expressions for a Breit-Wigner (BW), the resonant AT and of a thermally broadened CB resonance to the conductance data at a small bias $|V_{\mathrm{SD}}| \ll \Delta_0/e$. Figure C.3 shows such fits for a cross-section at $V_{\mathrm{SD}} = -0.25\,\mathrm{mV}$. The data points to the right of the resonance R are ignored (not shown) because of the inelastic AT features. The

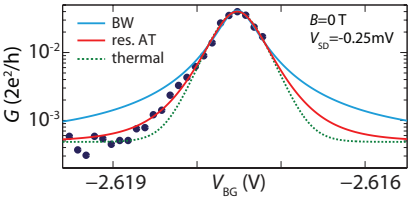

Figure C.3.: Conductance G of the resonant Andreev line R as function of V_{BG} (blue points) at a bias of $V_{\mathrm{SD}} = -0.25\,\mathrm{mV}$, $B = 0$ and $T = 110\,\mathrm{mK}$. The blue, red and dashed green lines are best fits according to the Breit-Wigner, resonant AT and thermally broadenend CB line shape, respectively.

resonant AT line shape (red line) agrees very well with the data. From this fit, we extract $\Gamma_1 \approx 6.9\,\mu\mathrm{eV}$, $\Gamma_2 \approx 68.3\,\mu\mathrm{eV}$ and $\Gamma = \Gamma_1 + \Gamma_2 \approx 75.2\,\mu\mathrm{eV}$, in very good agreement with the values obtained in Sec. 6.2.1 for $V_{\mathrm{SD}} = 0$. To control our fits in the normal state at larger magnetic fields, we also performed fits at $B = 0$ and finite bias $|V_{\mathrm{SD}}| > \Delta_0/e$ of the quasiparticle tunneling lines of the CB diamonds (not shown). Again the Breit-Wigner line shape agrees best with the data and we obtain very similar Γ-values compared to the fit at $B = 5\,\mathrm{T}$ shown in Sec. 6.2.1.

Evolution with temperature

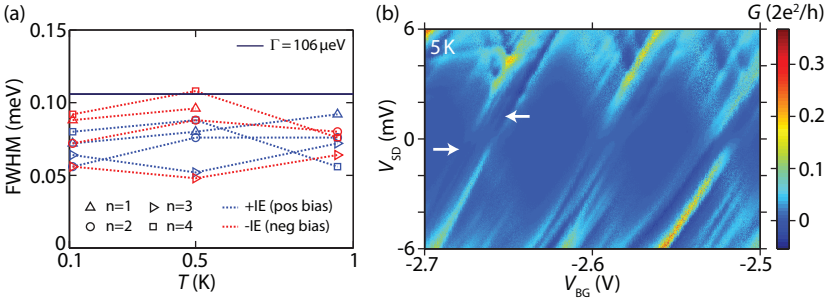

Figure C.4.: (a) Extracted FWHM vs temperature for the $n = 1...4$ IE replicas for positive (blue) and negative (red) bias, the dark blue line marks the extracted QD life-time broadening $\Gamma = 106\,\mu\mathrm{eV}$. (b) G vs V_{BG} and V_{SD} at $T \approx 5\,\mathrm{K}$, white arrows mark some still visible subgap features.

From a similar analysis as in Sec. 6.2.1, we can conclude that both the position and the spacing of the IE replicas stays constant within the studied temperature range up to $T = 1\,\mathrm{K}$. Figure C.4(a) shows the extracted FWHM of the IE replica lines as a function of temperature. The FWHM of the resonant line R (not shown) and the replicas stay roughly constant and FWHM $\lesssim \Gamma$, in agreement with the prediction FWHM $< \sqrt{2}\Gamma$ independent of T [111]. Figure C.4(b) shows a conductance map recorded at $T \approx 5\,\mathrm{K} < T_{\mathrm{c1}} = 7.7\,\mathrm{K}$

(cf. Sec. 4.1). Even if most features and the superconducting gap are already smeared with temperature, one still observes pronounced lines and features in the subgap region running parallel to the positive slope of the CB diamonds, marked by white arrows in the figure.

Evolution with magnetic field

Figure C.5 shows some $G(V_{\mathrm{BG}}, V_{\mathrm{SD}})$ maps for a series of external magnetic fields applied perpendicular to the sample plane. Such conductance maps were used for the data analysis in Sec. 6.2.3, from which the following quantities were extracted for each field in Sec. 6.2.3: (i) the transport gap Δ from the tips of the shifted diamonds which is plotted and discussed in Sec. 4.1, (ii) the Zeeman splitting of the ground and (electronic) excited states of the QD, indicated in Fig. C.5(d), (iii) the B-field dependence of resonant Andreev tunneling from horizontal cross-sections at $V_{\mathrm{SD}} = 0\,\mathrm{mV}$, (iv) the position, spacing, conductance maximum G_{max} and FWHM of IE replica lines from an analysis similar to Sec. 6.2.1. We now discuss some additional results in more detail.

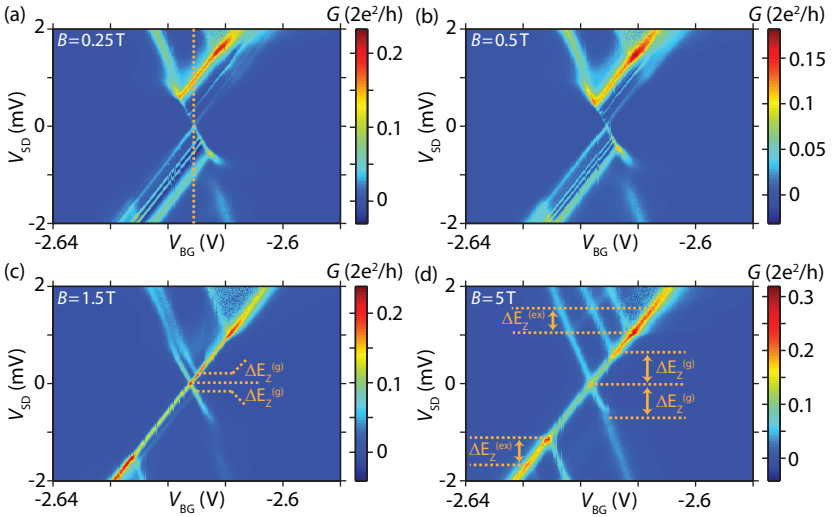

Figure C.5.: Example data for the B-field analysis: $G(V_{\mathrm{BG}}, V_{\mathrm{SD}})$ colormaps for (a) $B = 0.25\,\mathrm{T}$, (b) $B = 0.5\,\mathrm{T}$, (c) $B = 1.5\,\mathrm{T}$ and (d) $B = 5\,\mathrm{T}$. The magnetic field is applied perpendicular to the sample plane and CNT. The vertical dashed line in (a) indicates the position of the measurement in Fig. 6.5(a). In (c) and (d), the marked $\Delta E_{\mathrm{Z}}^{(\mathrm{g})}$ and $\Delta E_{\mathrm{Z}}^{(\mathrm{ex})}$ correspond to the Zeeman splitting of the ground and (electronic) excited states for positive and negative bias, respectively.

Figure C.6(a) and (b) show the analysis of the Zeeman splitting $\Delta E_Z = g\mu_B B$ of the ground and first (electronic) excited state of QD1. We obtain a g-factor of $g \approx 1.9$.

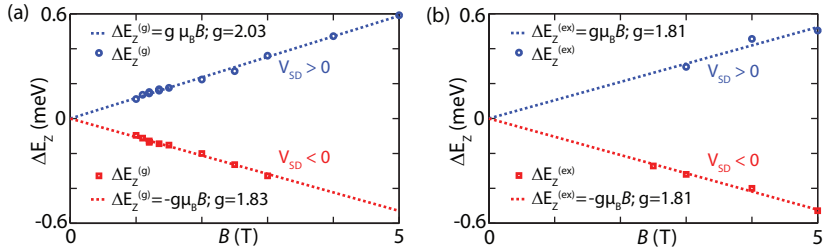

Figure C.6.: Zeeman splitting $\Delta E_Z^{(g)}$ (a) and $\Delta E_Z^{(ex)}$ (b) of the ground and first (elctronic) excited state for positive and negative bias, respectively, read-out from the B-field colormaps as demonstrated in Fig. C.5. We obtain a g-factor of roughly $g \approx 1.9$ from the fits $\Delta E_Z = g\mu_B B$.

Figure C.7 shows the magnetic field dependence of the resonant Andreev tunneling peak R, for (a) the conductance maximum $G_{\max}$ and (b) the extracted Γ_1 from individual fits to the resonant AT and the Breit-Wigner (BW) line shape (see Sec. 6.2.1). Γ_1 is the most sensitive parameter in these fits. In both plots, we observe a clear transition (marked on top of the plots with a colorscale) with contributions from resonant AT only (red, up to $B \approx 1\,\mathrm{T}$) to an intermediate region where both processes coexist ($B \approx 1-3\,\mathrm{T}$) to contributions from normal electron tunneling alone (blue, $B \approx 3.5-5\,\mathrm{T}$). This is immediately evident when one looks at the range of Γ_1 for acceptable deviations from

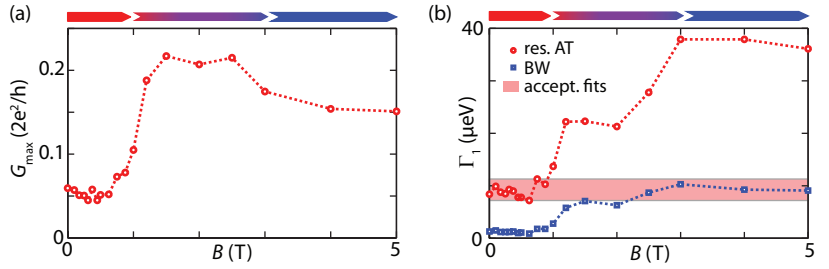

Figure C.7.: B dependence of resonant AT. We study horizontal cross-sections at $V_{\mathrm{SD}} = 0$ as function of B, extracted from individual colormaps. (a) Conductance maximum $G_{\max}$ of the resonant line (R) vs B. (b) Γ_1 extracted from fits to the expressions for resonant AT (red circles) and the Breit-Wigner line shape (blue squares). The shaded red area indicates the Γ_1 values for fits in good agreement with the data.

the high-field BW values in Fig. C.7(b). The values for small B extracted from resonant AT and for large B from normal tunneling agree very well. Similarly, one observes an increase in the conductance from $G_{\max} \sim 0.06 \times 2e^2/h$ to $G_{\max} \sim 0.22 \times 2e^2/h$ in the intermediate region where both processes coexist, followed by a decrease of conductance to $G_{\max} \sim 0.16 \times 2e^2/h$ at high fields.

As an extension to the analysis of the position, amplitude and spacing of the IE replica lines in a magnetic field discussed in Sec. 6.2.3, we note that the FWHM of these resonances stays also constant as function of B and FWHM $<$ Γ holds (not shown).

C.2. Second QD and a different CNT device

Figure C.8 shows supporting data with very similar findings for QD2 of the same device and for a second sample fabricated in the same geometry. In both cases, one clearly sees straight lines running parallel to the edge of the CB diamond as discussed in detail for the first sample.

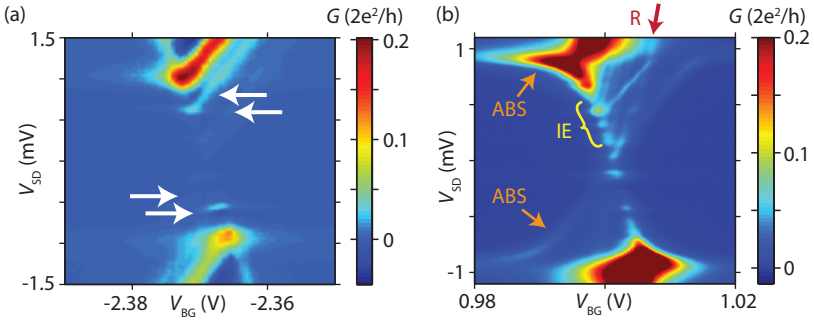

Figure C.8.: $G(V_{\mathrm{BG}}, V_{\mathrm{SD}})$ conductance map for (a) QD2 of the same device (b) an independent sample with the same geometry, recorded at $T = 60\,\mathrm{mK}$. In (a), weak conductance lines running parallel to the CB diamond are labeled with white arrows. In (b), an Andreev bound state (ABS, orange arrows) is more pronounced, but a set of lines running parallel to one edge of the diamond are still visible. The resonant Andreev line R and inelastic replicas IE can be clearly identified here.

D

Additional data to Chapter 7

In this appendix, we present and analyze additional data for the devices A, B and C discussed in Chap. 7. In particular, we discuss the most likely electronic configuration of each device, using conductance maps as a function of both sidegate voltages.

Device A

Figure D.1(a) and (b) show the measured differential conductance G_1 and G_2 of device A as a function of the sidegate voltages V_{SG1} and V_{SG2}, for the ac bias applied to S, but with $V_{\mathrm{S}} = V_{21} = V_{\mathrm{BG}} = 0$, and in the normal state of the device at $B = 0.3\,\mathrm{T}$. There are only very few features visible that are reminiscent of a double dot charge stability diagram, i.e. only a slight conductance modulation with some features stronger (weaker) in one (the other) arm, and only slight changes in the slopes or the spacing between neighboring resonance lines. We observe the same resonance lines in both arms N1 and N2 of the device when applying the ac bias at S, and one dominant slope which is tuned mostly with V_{SG2}. We hence conclude that if there would be two separate QDs, their inter-dot coupling must be so large that transport can be described to first approximation [255, 256] by a single, large QD [inset in Fig. (a)]. Particularly in the region studied in the main text [orange line in Fig. (b)], this assumption should be justified. In Fig. D.1(c), we plot the differential conductance in the normal state of S along the yellow dashed line of Fig. (b), as a function of the bias V_{S} and one sidegate voltage only. Here, we also clearly observe the same diamond structure in both arms of the device, further supporting the above claim.

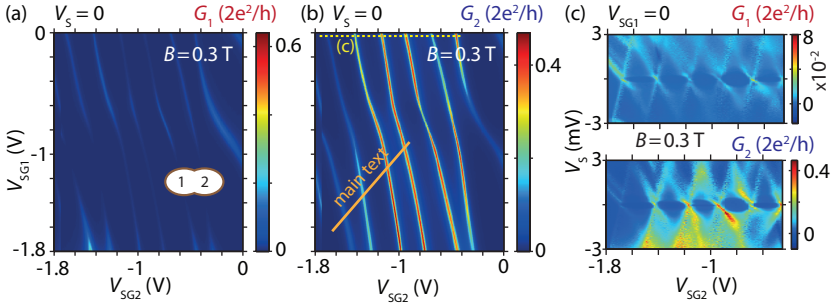

Figure D.1.: (a-b) Differential conductance G_1 and G_2 of device A as a function of the sidegate voltages V_{SG1} and V_{SG2}, for $V_S = 0$, $V_{21} = 0$, and $V_{BG} = 0$, at an external magnetic field $B = 0.3\,\mathrm{T}$ applied out-of-plane. The orange [dashed yellow] line in (b) indicate the studied gate voltages in the main text [Fig. (c)]. The inset in (a) sketches the assumed electronic QD configuration in arms 1 and 2 of the device. (c) G_1 and G_2 as function of V_S and V_{SG2} only, at $B = 0.3\,\mathrm{T}$ and $V_{SG1} = V_{21} = V_{BG} = 0$.

Next, we briefly demonstrate the fitting procedure to determine the individual Γ_i of the contacts. In Fig. D.2, the simultaneously measured zero-bias conductance G_1 and G_2 of resonance 1 (main text) is plotted as a function of the gate voltage V_{SG1+2} in the normal state of the device. Fits with a Breit-Wigner resonance line-shape for a three-terminal device (Sec. 5.2) agree very well with the data, and yield $\Gamma = \Gamma_1 + \Gamma_2 + \Gamma_S \approx 205\,\mu\mathrm{eV}$, $\Gamma_S\Gamma_1 \approx 198\,\mu\mathrm{eV}^2$ and $\Gamma_S\Gamma_2 \approx 7945\,\mu\mathrm{eV}^2$. From these equations, all parameters are determined for $\Gamma_S > \Gamma_1, \Gamma_2$. This assumption can be directly justified from a similar analysis of measurements with the bias applied to N1, while measuring G_S and G_2 (not shown).

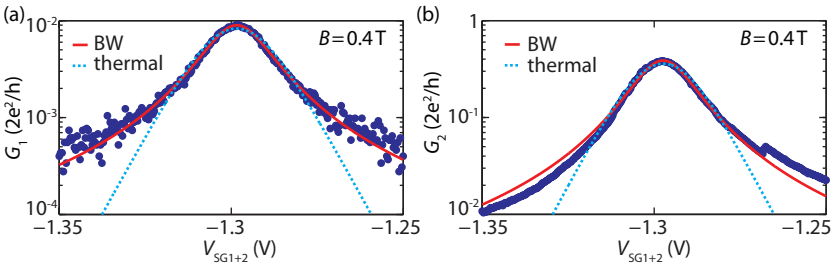

Figure D.2.: Differential conductance G_1 (a) and G_2 (b) of resonance 1 (main text) as a function of the combined sidegate voltage V_{SG1+2}, at $V_S = V_{21} = V_{BG} = 0$ and $B = 0.4\,\mathrm{T}$. Red (blue dashed) lines represent the best fits obtained for a Breit-Wigner lineshape (thermally broadened CB resonance).

Device B

Figure D.3(a) and (b) show again G_1 and G_2 of device B as a function of the sidegate voltages V_{SG1} and V_{SG2}, for the ac bias applied to S, but with $V_S = V_{21} = V_{BG} = 0$, and in the normal state of the device at $B = 0.4\,T$. In the conductance map of G_1, we observe a single dominant slope which is tuned mostly with V_{SG1}, suggesting a QD located between S and N1 of the device. In contrast, in Fig. D.3(b) we observe very high conductance with a weak and only slow amplitude variation as function of V_{SG2}, characteristic for a more open CNT regime with highly transmissive contacts. Particularly, G_2 never approaches zero. Additionally, imprints of the resonances from G_1 can be observed in G_2, which we ascribe to resistive cross-talk similar to a voltage divider [20]. Hence, we assume an electronic configuration of the CNT device as depicted in the geometry of Fig. D.3(c), with a larger QD on the left side of the device mostly tunable by V_{SG1}, and an 'open' CNT lead to the right.

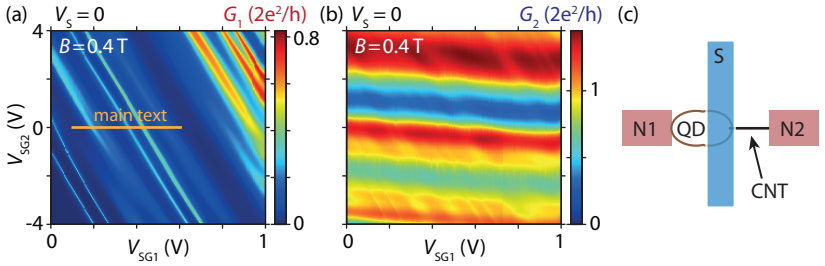

Figure D.3.: (a-b) G_1 and G_2 of device B as a function of the sidegate voltages V_{SG1} and V_{SG2}, for $V_S = 0$, $V_{21} = 0$, and $V_{BG} = 0$, at $B = 0.4\,T$. The orange line in (a) indicates the studied gate voltage region in the main text. (c) Possible electronic configuration of the CNT device.

Device C

In Fig. D.4, G_1 and G_2 of device C are plotted as a function of the sidegate voltages V_{SG1} and V_{SG2}, for the ac bias applied to S, but with $V_S = V_{21} = V_{BG} = 0$, for S in the normal state at $B = 0.4\,T$ (a-b) and in the superconducting state of S at $B = 0$ (c-d). In contrast to both previous devices, a charge stability diagram with anti-crossings characteristic for a double quantum dot with strong inter-dot coupling and hybridization is observed in the normal state of S. The dominant conductance lines of different slopes in each arm of the device are consistent with resonances of QD1 or QD2 [Fig. D.4(a)]. An apparent 'smearing' of resonances in every second charge state both for QD1 and QD2 resonances is due to pronounced Kondo ridges. In particular, the broad

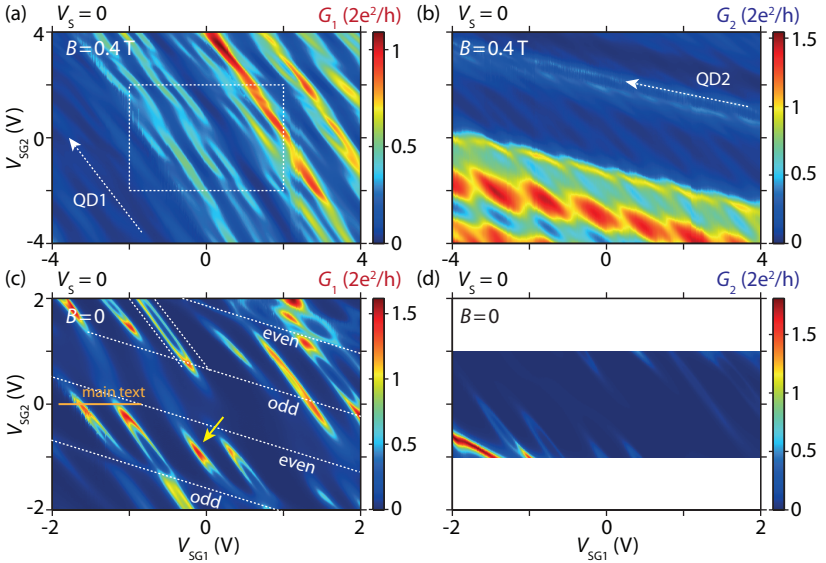

Figure D.4.: G_1 and G_2 of device C as a function of the sidegate voltages V_{SG1} and V_{SG2}, for $V_S = V_{21} = V_{BG} = 0$, at $B = 0.4$ T (a-b) and at $B = 0$ (c-d). White dashed arrows in (a,b) denote different slopes consistent with resonances of QD1 or QD2. The white rectangle marks the region studied in (c,d). In (c), the orange line corresponds to the gate voltage region studied in the main text, and dashed lines denote the charge states of QD2 (even/odd).

resonances which we ascribe to QD1 [Fig. D.4(a)] indicate an odd charge state with a Kondo ridge. This is more obvious when one closely inspects the region indicated by a dashed rectangle in Fig. D.4(a) in the superconducting state of S, which is plotted in Fig. D.4(c). Here one observes a pair of Andreev resonance lines in the even charge state of QD2 (yellow arrow), corresponding to the two singlet-doublet quantum phase transitions (QPT) observed in the odd charge states of QD1. Most surprisingly, this QPT vanishes close to the boundary and in the odd charge state of QD2, which can for example be seen by following the Andreev resonances marked with a yellow arrow. While such a feature could be due to a possible coupling of Andreev resonances in the left and right QD (see also Chap. 8), we refrain here from speculating on the origin and do not analyze this finding further. In the main text, we focus on Andreev states in QD1 for a fixed even charge state of QD2, but close to its charge degeneracy point [orange line in Fig. D.4(a)].

E

Co contacts for CNT spin-valve devices

Convincing non-local spin signals with sharp switchings have already been observed for Co-based graphene spin-valves [135], and Co contacts have also been employed in early CNT QD spin-valve experiments [35, 311–314, 335]. We therefore also investigated Co as contact material for CNT QD spin-valve structures, and fabricated 16 CNT spin-valve devices with 25 nm thick, thermally evaporated Co contacts, using the optimized ZEP EBL and similar design guidelines (e.g. aspect ratio) as for Py strips. As indicated in Fig. 2.6, we obtained a comparable yield of low-ohmic CNT devices than with thermally evaporated Py contacts in contrast to previous conclusions [58]. This underlines the importance of an optimized EBL as key for a good contact yield of low-ohmic devices, independent of the used contact material. In disagreement with former work in our group, all of the devices were stable enough and could be cooled down without loosing contact. As visible in Fig. E.1(a), SEM images of spin-valve devices illustrate clean and well-defined Co contacts, a QD formed in all cases at low temperatures, and devices had high conductances up to $\sim 0.45 \times 2e^2/h$. In total, the magnetoresistance and AMR of 6 CNT devices were studied. On most devices, one could observe some magnetization reversal related switching features in the magnetoresistance as indicated by the green arrows in Fig. E.1(d) and (e), i.e. changes of the conductance amplitude on resonance in the anti-parallel magnetization state relative to the parallel configuration. All of the QDs were however electrically too unstable to investigate this further in detail. Partially, it was already impossible to stabilize a single resonance. The AMR measurements turned out to be even less promising: While in best case, one could observe a clear and reproducible switching as in Fig. E.1(b), we also observed very irreproducible, multi-step like resistance

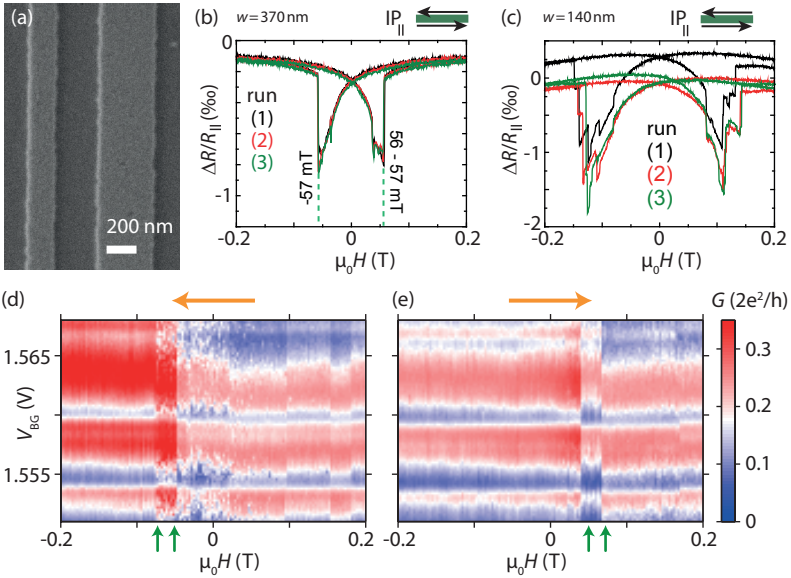

Figure E.1.: (a) SEM image of 180/370 nm wide Co strips of a CNT spin-valve device. (b, c) AMR measurements of single Co strips, with the external field H aligned parallel to the strip axis for a 370 nm (b) and a 140 nm (c) broad strip. Color-coded numbers indicate several repetitions. (d, e) Magnetoconductance $G(V_{\mathrm{BG}}, \mu_0 \mathrm{H})$ maps at $V_{\mathrm{SD}} = 0$ for downsweep (d) and upsweep (e) – the sweep direction of the magnetic field is indicated by orange arrows. Green arrows below the graphs mark the expected switching fields from AMR measurements for this particular sample (55 mT & $75 - 80$ mT).

changes as visible in Fig. E.1(c). This is a clear indication of a multi-domain strip state and magnetization reversal via several domains, and possibly due to the fact that for Co the free energy associated with magnetocrystalline anisotropy is of the same order of magnitude as for the shape anisotropy [362]. We did not find a clear correlation between multi-domain characteristics and the strip width. While the presented study is hardly representative due to the small number of devices, the occasionally occurring multi-domain characteristics even for perfectly well defined Co contacts, in combination with the observed electrically unstable QDs, make it much more complex to reliably control and interpret spin transport in devices with Co contacts. We hence decided to not use Co contacts for spin-valve devices in this thesis.

Curriculum Vitae

Jörg Benedikt Gramich
Born 3 October 1987 in Leonberg (Germany)

Education

2012–2016	PhD in experimental physics at the University of Basel PhD thesis in the group of Prof. C. Schönenberger: "Andreev and spin transport in carbon nanotube quantum dot hybrid devices"
10/2011	Diploma in physics at the Karlsruhe Institute of Technology (KIT), Germany Diploma thesis at the Center for Functional Nanostructures in the groups of Prof. G. Goll and Prof. H. v. Löhneysen: "Fabrication, characterization and electronic transport properties of nanostructured Pb/Fe point contacts"
2006–2011	Studies of physics at the Karlsruhe Institute of Technology (KIT), Germany (10/2006–07/2009, 03/2010–10/2011) and at the University of California, Berkeley, USA (08/2009–02/2010) Project work in the group of Prof. D.-H. Lee at UC Berkeley, "Surface states of topological insulators – Dirac fermions in a slab geometry".
1993–2006	Primary and secondary school, Abitur (high school diploma), Gymnasium Renningen

Positions

2012–2016	Teaching assistant for physics at the University of Basel
12/2011–04/2012	Research assistant at the Center for Functional Nanostructures, KIT
10/2008–04/2009	Teaching assistant for physical chemistry at the Karlsruhe Institute of Technology (KIT)
08/2006–09/2006	Internship in the group of Prof. W. Dietsche, Prof. K. v. Klitzing's department, Max Planck Institute for Solid State Research, Stuttgart

Scholarships and Awards

12/2015	Teaching award for the best assistant in fall semester 2015, Department of Physics, University of Basel
2006–2011	Student scholarship of the "Studienstiftung des deutschen Volkes", including an individual research scholarship for studies at the UC Berkeley (08/2009-02/2010)
04/2008	Youth laboratory award of the German hightech industry association "Spectaris", for the development of an industrially usable microwave lab reactor
05/2006	1st place on federal level ("Bundessieger") in the German youth research competition "Jugend forscht", for the project "Plasmabased cracking in the microwave"
04/2006	Gold medal as captain of team Germany in the international youth science competition "International Conference of Young Scientists (ICYS)"

Publications

Experimental verification of contact-size estimates in point-contact spectroscopy on superconductor/ferromagnet heterocontacts, J. Gramich, P. Brenner, C. Sürgers, H. v. Löhneysen and G. Goll, Phys. Rev. B **86**, 155402 (2012).

Optimized fabrication and characterization of carbon nanotube spin valves, J. Samm, J. Gramich, A. Baumgartner, M. Weiss and C. Schönenberger, J. Appl. Phys. **115**, 174309 (2014).

Carbon nanotube quantum dots on hexagonal boron nitride, A. Baumgartner, G. Abulizi, K. Watanabe, T. Taniguchi, J. Gramich and C. Schönenberger, Appl. Phys. Lett. **105**, 023111 (2014).

Fork stamping of pristine carbon nanotubes onto ferromagnetic contacts for spin-valve devices, J. Gramich, A. Baumgartner, M. Muoth, C. Hierold and C. Schönenberger, Phys. Status Solidi B **252**, 2496 (2015).

Resonant and inelastic Andreev tunneling observed on a carbon nanotube quantum dot, J. Gramich, A. Baumgartner and C. Schönenberger, Phys. Rev. Lett. **115**, 216801 (2015).

Cooper-Paare tunneln durch einen Quantenpunkt, A. Baumgartner, J. Gramich, and C. Schönenberger, Physik in unserer Zeit **47**, 62 (2016).

Subgap resonant quasiparticle transport in normal-superconductor quantum dot devices, J. Gramich, A. Baumgartner and C. Schönenberger, submitted, arXiv:1601.00672 (2016).

Subgap quasiparticle transport due to a three-terminal superconductor/normal metal carbon nanotube quantum dot, J. Gramich, A. Baumgartner and C. Schönenberger, in preparation.

Andreev bound states probed in a three-terminal superconductor/normal metal carbon nanotube quantum dot, J. Gramich, A. Baumgartner and C. Schönenberger, in preparation.

Talks

Characterization and electronic transport properties of nanostructured Pb/Fe point contacts, Talk at the DPG Spring Meeting, Berlin, 30 March 2012.

Spin transport in carbon-based nanodevices, Talk at the QSIT Junior Meeting, Passugg (GR), 14 June 2013.

Resonant and inelastic Andreev tunneling observed on a CNT QD, Talk at the QSIT Lunch Seminar, ETH Zürich, 1 October 2015.

Poster Contributions

Permalloy contacts for carbon-based spintronic devices, J. Samm, J. Gramich, M. Weiss, A. Baumgartner, C. Schönenberger. Poster at the Swiss Nanoconvention, Basel, 23 May 2013.

Permalloy contacts for carbon-based spintronic devices, J. Gramich, J. Samm, M. Weiss, A. Baumgartner, C. Schönenberger. Poster at the QSIT Junior Meeting, Passugg (GR), 12 June 2013.

Permalloy contacts for carbon-based spintronics, J. Samm, J. Gramich, M. Weiss, A. Baumgartner, C. Schönenberger. Poster at the Conference "Frontiers in Quantum Engineered Devices", Obergurgl (Austria), 21 August 2013.

Fabrication and characterization of nanospintronic devices, J. Gramich, J. Samm, A. Baumgartner, M. Weiss, M. Muoth, C. Hierold, C. Schönenberger. Poster at the 4th QSIT General Meeting, Arosa (GR), 5 February 2014.

Optimized fabrication and characterization of CNT spin-valve devices, J. Gramich, J. Samm, A. Baumgartner, M. Weiss, M. Muoth, C. Hierold, C. Schönenberger. Poster at the 9th Advanced Research Workshop "Fundamentals of Electronic Nanosystems", St. Petersburg (Russia), 25 June 2014.

Multiple subgap states in a superconductor–CNT hybrid device, J. Gramich, A. Baumgartner, C. Schönenberger. Poster at the International Winterschool on Electronic Properties of Novel Materials, Kirchberg (Austria), 9 March 2015.

Boson-assisted and resonant Andreev tunneling observed on a CNT QD, J. Gramich, A. Baumgartner, C. Schönenberger. Poster at the SpinTech VIII International School & Conference, Basel, 11 August 2015.

Art is I, science is we.
Claude Bernard (1813-1878)

Acknowledgements

This PhD thesis would not have been possible without the guidance and support from many exceptional scientists, colleagues and friends. Hence, it is time to thank all people that contributed in various ways to this work.

First of all, my deepest gratitude is directed towards my thesis advisor Prof. Christian Schönenberger. He has guided me throughout this thesis with a never ending drive and enthusiasm for nanoscale science, and an inspiring openness and support for exploring new avenues. Only by sharing his vast scientific expertise and posing the right questions, he enabled me to successfully tackle various challenging experiments. I especially admire his clear-sighted view on projects, and his mind's sharpness to immediately pinpoint to the critical problem. I also gratefully acknowledge the given freedom to develop own ideas in "Friday afternoon" projects, Christian's appreciation of only small progress in challenging problems and his motivational skills to still push me onwards, but also the various collaborations and international conferences he enabled me to be part of. It has truly been a pleasure to be part of his research group and to work in such a stimulating environment.

Second, I would like to thank Prof. Christoph Strunk and Prof. Richard Deblock for making the effort to read my thesis. It is an honor to have two so distinguished scientists in my PhD committee.

I am also immensely grateful to Andreas Baumgartner for the constant supervision and guidance during my whole PhD project, and for always lending an open ear to all of my questions. Particularly, I thank Andreas for sharing all his experience in nanoelectronics and low-temperature experiments with me, for his inspiring enthusiasm about new findings and experiments, for teaching me how to "streamline" scientific writing, and for all his time and support – be it in the laboratory or in countless insightful discussions. A special thanks goes also to Péter Makk, for always having time for discussions and advice in spite of a usually busy schedule, for being a good friend, and for pushing me to join him in various sports activities. Along this line, I'd like to acknowledge also

the great support of the other post-docs, Markus Weiss, Minkyung Jung, and Romain Maurand. I thank both Andreas Baumgartner and Péter Makk for proof-reading (parts of) this thesis, and for valuable feedback and comments.

Further, I want to express my deep gratitude towards all with whom I collaborated very closely: Julia Samm, with whom I shared not only many hours in the lab, but all the ups and downs one encounters with ferromagnetic contacts; Matthias Muoth and Prof. Christofer Hierold for the fork stamping collaboration, for introducing me to the art of CNT stamping and the continuous supply of fork structures with pre-grown CNTs; and Jens Schindele, for the many fruitful discussions, and the collaboration in the H radical etching. I am also looking forward to the ongoing collaborations with Pb contacts, with Gergö Fülöp and Prof. Szabolcs Csonka (Budapest university) in InAs nanowires, and with Simon Zihlmann and Péter Makk in graphene devices.

I also want to thank all (further) current and former members of the nanoelectronics group, the best fellow scientists, office mates and colleagues one could have hoped for. These are Gulibusitan Abulizi, Maria El Abbassi, Masoud Baghernejad, Matthias Bräuniger, Jan Brunner, Michel Calame, Gábor Fábián, Axel Fanget, Frank Freitag, Toni Fröhlich, Wangyang Fu, Clevin Handschin, Cezar Harabula, Thomas Hasler, Samuel d'Hollosy, Christian Jünger, Stefan Nau, Cornelia Nef, Jan Overbeck, Vishal Ranjan, Peter Rickhaus, Ralph Stoop, Alexey Tarasov, Kishan Thodkar, Anton Vladyka, Lujun Wang, Mathias Wipf, as well as all the other project or external students during my time here. With many I collaborated in the one or other way, with some friendships developed, but all contributed to the lively discussions about and beyond physics, and the many common social activities that made life and working in this group so enjoyable!

I am also very grateful to many people of the department: Astrid Kalt and Barbara Kammermann, who had a solution to any administrative problem, Daniel Sacker, who fixed countless technical problems, Dominik Sifrig, who provided me with liquid Helium even when resources were scarce, Monica Schönenberger for her assistance at the AFM, and the teams of the mechanical and electronic workshop for all the support, where I want to mention particularly Patrick Stöcklin, Michael Steinacher, Heinz Breitenstein and Silvester Jakob. I also gratefully acknowledge the support of the operation team of FIRST cleanroom at ETH Zurich, and for granting me access to this facility.

Finally, I am greatly indebted to all people who reminded me that there still exists a life beyond science. Here, I want to thank especially my sports fellows from running, and all my friends from Karlsruhe and Basel, many of whom accompanied me on various outdoor activities – be it climbing, mountaineering, trekking or windsurfing. These trips helped me to regain a wider perspective, see the problems in nanoscience as small as they are, and find new inspiration and motivation. My deepest thanks, however, go to my family who supported me throughout the years and without whom I wouldn't be where I am today.